CHARACTERIZATION OF HEAT EXCHANGE FOR ADDITIVELY MANUFACTURED COMPONENTS

AHMED ELKHOLY

A DISSERTATION SUBMITTED TO THE FACULTY OF GRADUATE STUDIES IN PARTIAL FULFILLMENT OF THE REQUIREMENTS FOR THE DEGREE OF DOCTOR OF PHILOSOPHY*

GRADUATE PROGRAM IN MECHANICAL ENGINEERING
YORK UNIVERSITY
TORONTO, ONTARIO

April 2021

ABSTRACT

The current work aims to develop a fundamental understanding of thermal transport mechanisms within and on AM components and structures, which is addressed through three specific objectives. The first objective is to characterize the effect of the process parameters, of FFF and SLM, on the effective thermal conductivity of AM components. Secondly, to improve the pool boiling heat transfer coefficient (HTC) using AM-based structures. Finally, to investigate the application of SLM 3D-printed evaporators in a two-phase loop thermosyphon.

To achieve the first objective, a high-accuracy steady-state guarded method was developed to measure the effective conductivity of AM components. First, this apparatus was employed to measure the thermal conductivity of several PLA polymer-composites, either metal or carbon fiber. The experimental results showed that all samples featured high anisotropy in thermal conductivity, reaching up to 2 in the carbon fiber composite. Thereafter, the apparatus was modified to quantify the effect of the SLM process parameters, such as the laser power, hatch spacing, etc., on the effective thermal conductivity of AlSi10Mg, which were found to significantly decrease the resulting thermal conductivity up to 22%.

With respect to the second objective, an FFF-based polymer fixture was proposed to enhance the pool boiling characteristics from copper surfaces. Due to the low conductivity of the fixture, it could create a spatial temperature distribution at the boiling surface, initiating the bubbles earlier and enhancing the HTC.

A high-precision pool boiling apparatus was then built, addressing most of the experimentation issues found in the literature, such as repeatability, surface aging, and the heater's small size. This device was subsequently used to examine novel 3D re-entrant cavities fabricated using SLM on the pool boiling performance. It was observed that the surface with re-entrant

cavities increased the nucleation site density and the bubble departure frequency, enhancing the HTC 2.8 times compared to the plain 3D-printed surface.

The last objective was achieved by investigating the difference in the thermal performance of closed-loop thermosyphon between two surfaces: machined and additively manufactured via SLM. It was shown that the 3D-evaporator slightly increased the loop thermal resistance; however, it mitigated the temperature instabilities.

ACKNOWLEDGMENTS

I would like to express my sincere gratitude to my academic supervisor Dr. Roger Kempers for his guidance and motivation during this study. I would like to extend my appreciation to Dr. Hossam Sadek for his support and his valuable insights.

I would like to thank all TF-Lab members for their valuable scientific discussions and assistance in many technical matters.

I also appreciate the technical support provided by the South Eastern Applied Materials Research Centre (SEAM) for printing my 3D-printed metal samples and helping in performing the required microstructure analysis.

Finally, I sincerely thank my wife and family, especially my parents, to deserve all the credit for the encouragement in carrying out this work.

TABLE OF CONTENTS

LIST OF TABLES

LIST OF FIGURES

NOMENCLATURE

q''	[W/cm^2]	Heat flux
Δz	[mm]	The distance between the location of the measured temperature and the boiling surface
A	[cm^2]	Boiling heat transfer area or the conductivity sample cross sectional area
CHF	[W/cm^2]	Critical heat flux
Co		Confinement number
D	[mm]	Diameter
E	J/mm^3	Energy density
f	[HZ]	Frequency
g	[m/s^2]	Gravitational acceleration
H	[mm]	Fixture height
h	[mm]	The height difference between the evaporator and the condenser in the loop thermosyphon or the layer height setting in printing with FFF in chapter 2 or the ethanol level rise in chapter 4
HTC	[W/cm^{2}K]	Boiling heat transfer coefficient
I	[Amp]	Measured current
k	[W/m K]	Thermal conductivity
K	[m^2]	Fixture permeability
n	[-]	The number of cells or channels of the polymer fixture or the number of the embedded re-entrant cavities in the boiling surface
OL	%	The overlap between the printed rasters

p	[pa]	pressure
P	[W]	Power
R	[K/W]	Thermal resistance
r	[mm]	the effective capillary radius of the 3D-printed wick sample.
Ra	[μm]	Roughness
S	[mm]	Polymer fixture unit cell size or spacing between re-entrant cavities.
SD	[pa or °C]	Fluctuation standard deviation
T	[K]	Temperature
t	[s]	time
v	[mm/s]	Printing speed
v	[%]	volume fraction
V	[Volt]	The input voltage to the main heaters
w	[mm]	raster width
X		Lockhart and Martinelli parameter
α		Two phase flow void fraction
L	[mm]	The thickness of tested polymer samples fabricated by FFF or the distance between the RTD in the thermal conductivity sample printed via SLM
Q	[W]	Thermal power
l	[mm]	The heater size
β	°	The boiling surface orientation angle
δ	[mm]	Fixture wall thickness
ε	[%]	The 3D-printed wick sample porosity

θ	$\circ$	Raster angle of the printed components via FFF or the fluid contact angle
λ	[mm]	Working fluid capillary length
μ	[kg/m s]	Viscosity
ρ	[kg/m^3]	density
σ	[N/m]	Surface tension

Abbreviations

ABS	Acrylonitrile butadiene styrene
AM	Additive manufacturing
CPHE	Composite polymer heat exchanger
DMLS	Direct metal laser sintering
DOE	Design of experiment
DSC	Differential scanning calorimetry
FDM	Fused deposition modelling
FFF	Fused filament fabrication
GBP	Geyser boiling phenomenon
HIP	Hot isostatic pressing
LOM	Laminated object manufacturing
LPBF	Laser powder bed fusion
MEMS	Microelectromechanical systems
OES	Optical emission spectroscopy

ONB	Onset of nucleate boiling
PLA	Polylactic acid
SEM	Scanning electron microscopy
SLA	Stereolithography
SLM	Selective laser melting
SLS	Selective laser sintering
SMA	Shape memory alloy
TPLT	Two-phase loop thermosyphon
TPS	Transient Plane Source

Subscripts

a	Acceleration or air
amb	Ambient
b	Bed
C	Copper
c	Condenser or Capillary
calc	Calculated
cap	Capillary
con	Contact
conv	Convection
e	Evaporator
eff	Effective
exp	Experimental

f	Fraction or friction
g	Gravitational
h	Hatch spacing
in	Inlet
l	Liquid
m	Measured or matrix or mixture
mom	Momentum
N	Nozzle
out	Outlet
p	Pore or point wise
P	Polymer
S	Surface
s	Solid
Sat	Saturation
T	Temperature
t	Total or thickness of printed layer with SLM
v	Vapour
W	Wetted
w	Wall
x	Vapor quality

Chapter 1 Introduction and Motivation

1.1 Additive Manufacturing Heat Transfer Applications

Additive manufacturing (AM) has garnered extensive attention in the last decade due to its capability to build innovative and functional end products at a low cost compared with conventional subtractive methods. The rapid evolution of AM has impacted sectors such as aerospace, automotive, microelectromechanical systems (MEMS), biomedical applications, and numerous other areas [1]–[3]. AM covers several techniques such as selective laser melting (SLM), stereolithography (SLA), fused deposition modelling (FDM) or fused filament fabrication (FFF), and laminated object manufacturing (LOM) [4]. In each case, parts are fabricated in subsequent layers through the deposition of the build material on a controlled, pre-programmed moving substrate according to a G-code generated from slicing software. For heat exchange applications, AM facilitates the fabrication of complex structures for single-phase and two-phase flows. Of these AM techniques, SLM and FFF methods were commonly utilized through the literature in several single-phase and two heat transfer applications, as discussed in the following subsections.

1.1.1 Fused Filament Fabrication (FFF)

Over the last decade, fused filament fabrication has been one of the widely popular polymer AM techniques because it is commercially accessible, open-source, low cost, and has a wide range of feedstock materials. Through this process, the polymer is melted through the extrusion nozzle that travels across the build plate to build the part layer by layer. Polylactic acid (PLA) and acrylonitrile butadiene styrene (ABS) are among the most popular feedstock polymers used by FFF. The employment of polymers for heat transfer applications offers many favorable properties such as flexibility, low weight, antifouling, and corrosion resistance. Besides the ability to create intricate surface structures that AM offers, which can play an essential factor in enhancing the fluid-solid interaction. Generally, polymers have low melting points and thermal conductivities compared to metals, which limits their use for many applications. Therefore, several studies attempted to increase the thermal conductivity of the 3D-printed parts by FFF using either composite filament [5], [6] or continuous fiber printing [7], [8] methods, as discussed in more detail in Chapter 2.

Very few recent studies have shown the ability to produce final prototypes of single-phase polymer heat exchangers using the FFF method. Cevallos [9] was the first to build a water-to-air webbed-tube from polymer composite by FFF. Jia et al. [10] employed the FFF process to produce a heat sink made of a thermally conductive graphite-polymer composite using a 3D printer extruder. Their results showed that it achieved a similar temperature compared with the conventional aluminum heat exchanger. In the same direction, Hymas et al. [11] established a new hybrid approach of FDM and embedded metallic strips to fabricate a composite polymer heat exchanger (CPHE).

1.1.2 Selective Laser Melting (SLM)

Among AM methods, SLM is a laser powder bed method where high-density laser energy is employed to selectively fuse metal powder in specific regions of the bed according to the sliced CAD model by the machine software. Once a layer is complete, the build platform lowers, and a new layer of metal powder is spread over the build region, and the process is repeated until the whole part is built as instructed. SLM is also commercially referred to as laser powder bed fusion (LPBF) or direct metal laser sintering (DMLS). SLM has significant benefits over other AM methods, such as the superior thermal characteristics of most of its feedstock materials, and high resolution. These features make it a notable candidate for the fabrication of components for heat transfer applications compared to other AM methods. Consequently, several studies adopted SLM to enhance the heat transfer performance of single-phase systems, such as heat sinks and heat exchangers, and two-phase systems, including heat pipes and thermosyphons. Some of these studies are discussed here.

For single-phase heat exchange, Hutter et al. [12] used selective laser sintering (SLS) to construct the organized shape of a porous metal insert for tube reactors, which is analogous to commercially available metal foam. They demonstrated that building a fully sintered reactor and integrating the metal foam and pipe wall yield heat transfer enhancement up to three orders of magnitude compared with a traditional reactor. Wong et al. [13] investigated three different novel designs of heat sinks manufactured by SLM – elliptic staggered fin array, latticed, and round-cornered rectangular arrays – and compared them with the conventional design of pin fins and rectangular fins. Ho et al. [14] went in the same direction and proposed further innovative heat sinks made by SLM, such as airfoil-shaped fins. Robinson et al. [15] and Kempers et al. [16] used a micro-additive manufacturing approach to develop, fabricate, and test a single-phase, hybrid micro-jet/microchannel heat sink, which achieved a maximum conductance of 350 kW/m^{2}K. Kirsch and Thole [17] optimized the thermal and hydraulic performance of AM wavy microchannels by SLM for cooling gas turbine blades. Their experimental results demonstrated the enhancement of the heat transfer performance; however, the printed channels resulted in high surface roughness which increased the pressure loss. Other studies examined the improvement of the overall heat transfer coefficient of many types of heat exchangers enabled by SLM, such as plate-fin heat exchangers [18] and twisted shell and tube [19].

SLM has also been employed for two-phase heat transfer to build a novel design of flat-plate oscillating heat pipes [20]. Regarding pool boiling, Wong et al. [21] adopted SLM to create porous lattices to increase the heat transfer rate for saturated FC-72. The additively manufactured latticed surfaces showed notable improvement in the nucleation regime and deferment of the critical heat flux (CHF) compared with plain surfaces. Hayes et al. [22] used SLM to manufacture a porous hollow conical structure to separate between the liquid and vapor paths. These shapes were equipped with one opening at the top, and another one on the side. According to the ratio between the geometric parameters of these openings and the bubble departure diameter, these shapes regulated the directions of the vapour and the liquid flow, which resulted in a twofold increase in the CHF and a fourfold increase in boiling the heat transfer coefficient (HTC) compared with the plain flat surface.

1.2 Technological Opportunity

While both SLM and FFF offer many potential opportunities to enhancing the performance of two-phase heat exchange technologies, a key challenge is an understanding of how the AM fabrication process parameters contribute to the thermal performance of the printed part from different aspects: the thermal conductivity, the structure wickability, and the associated boiling heat transfer coefficient with its surface morphology. Improving this understanding allows for the optimization of AM process parameters for a given application and directly supports the design of a new generation of AM two-phase heat transfer technologies, and may inform the direction of AM technologies themselves.

Moreover, many researchers showed a drastic improvement of HTC and CHF by altering heating surfaces' characteristics, whether by changing their wettability, porosity, or attaching a 3D structure to regulate both liquid and vapor phases. As such, AM represents an excellent candidate to tailor and fabricate new intricate structures and wicks for improving the performance of two-phase heat exchange applications.

1.3 Objectives

The overarching goal of my research is to develop a fundamental understanding of thermal transport mechanisms in and on AM solids and structures to support the design fabrication of novel AM heat exchangers. This is addressed through three shorter-term specific objectives as follows:

Objective 1: To Characterize the Thermal Properties of AM Components Fabricated by FFF and SLM.

This objective is achieved through the following steps:

- Develop accurate experimental facilities and techniques for characterizing the thermal conductivity of AM components and materials.
- Characterize the effect of process parameters of the FFF and SLM methods on the thermal conductivity of AM-parts.
- Establish numerical models that can predict the effective thermal conductivity of AM-components for a range of fabrication parameters.
- Develop reliable thermal conductivity data for the available commercially composite materials for printing with the FFF technique.

Objective 2: To Characterize the Pool Boiling Heat Transfer on AM Surfaces with Water as the Working Fluid.

This objective is achieved through the following steps:

- Develop a pool boiling apparatus to permit simultaneous flow visualization and characterization of the HTC and the CHF for a range of AM material and fluid combinations.

- Enhance the pool boiling heat transfer rate from bare copper surfaces by attaching 3D-printed fixtures fabricated by FFF.
- Explore opportunities to enhance the boiling heat transfer by taking advantage of the unique material properties and fabrication techniques offered by SLM surfaces and structures.

Objective 3: To Leverage Additively Manufacturing Evaporators to Increase the Performance in a Closed-Loop Two-Phase Loop Thermosyphon.

This objective is achieved through the following steps:

- Investigate the thermal performance and the geyser boiling phenomenon (GBP) in an air-cooled, two-phase loop thermosyphon, having a conventionally CNC-machined evaporator.
- Study the influence of the operational parameters such as the heating load, working fluid, fill ratio, and the evaporator surface design on thermosyphon thermal performance and the associated instabilities.
- Examine the thermal performance of the thermosyphon with SLM-evaporator for different operational parameters and comparing it with the conventional CNC-machined one.

1.4 Thesis Layout

The first step towards achieving the research objectives was to build an accurate apparatus for characterizing the thermal conductivity of a range of materials. This apparatus was utilized to characterize the effect of geometric printing parameters such as the layer height, raster width, and fill ratio on the anisotropic effective thermal conductivities of FFF-printed components. It was further employed to characterize composite FFF feedstocks' thermal performance as they pertain to potential heat transfer applications. This work is detailed in **Chapter 2** and was published as a peer-reviewed journal paper titled "Characterization of the Anisotropic Thermal Conductivity of Additively Manufactured Components by Fused Filament Fabrication" in *Progress in Additive Manufacturing* [23].

Chapter 3 presents the results of an investigation using a modified version of the thermal conductivity facility for examining the influence of the SLM process parameters on the effective bulk thermal conductivity of metal 3D-printed parts. All the samples were printed from an aluminum alloy (AlSi10Mg) due to its high thermal conductivity and low specific gravity, demonstrating excellent potential in heat transfer applications. The experimental results of this chapter have been submitted as a peer-reviewed article titled "Characterization and Analysis of the Thermal Conductivity of AlSi10Mg Fabricated by Selective Laser Melting (SLM)" in *Additive Manufacturing*. This work was performed in collaboration with the South Eastern Applied Materials Research Centre (SEAM).

Chapter 4 describes a proof-of-concept study to enhance the two-phase pool boiling heat transfer rate from copper surfaces through the attachment of 3D-printed polymer fixtures fabricated by the FFF technique. This chapter also provides the construction of a simple experimental pool boiling facility used in the testing, which helped to understand the challenges associated with such type of experimentation. A version of this chapter has been presented in the *HEFAT2019* conference [24] and subsequently published in a peer-reviewed article titled "Enhancement of Pool Boiling Heat Transfer Using 3D-Printed Polymer Fixture" in *Experimental Thermal and Fluid Science* [25].

Chapter 5 describes the design and development of a highly functional and accurate pool boiling apparatus for characterizing the HTC and the CHF for any fluid and solid surface combination. This apparatus incorporates many key features, such as swapping the surface and testing different orientations. Firstly, this device was used to investigate the measurement repeatability challenge associated with pool boiling heat transfer research. It was then employed to show an exciting future opportunity to understand, enhance, and control boiling mechanisms using the new SLM-3d printed surfaces. A version of this chapter has been presented at the *ITherm 2020* [26].

Chapter 6 and **Chapter 7** work together to develop a fundamental understanding of the thermal performance of a two-phase closed-loop thermosyphon with a 3D-printed evaporator by SLM, where **Chapter 6** describe the details of a baseline study of the loop performance with machined evaporators while **Chapter 7** shows a comparison between the machine surface and the AM surface. Initially, the impact of the loop geometrical and operational parameters, such as the heating load, working fluid, fill ratio, and the evaporator surface design, on thermosyphon thermal performance and the associated instabilities were initially studied in **Chapter 6**. Then, the developed loop was a bit modified in **Chapter 7** to investigates the performance and the associated geysering instabilities at different fill ratios and working fluids for the SLM-3D evaporator surface and compare it to the conventionally machined surface. The experimental outcomes investigated in **Chapter 6** has been published in a peer-reviewed journal titled "Experimental investigation of geyser boiling in a small diameter two-phase loop thermosyphon" in *Experimental Thermal and Fluid Science* [27]. Furthermore, the findings of **Chapter 7** are drafted in a journal paper and have been submitted to *Applied Thermal Engineering*.

Chapter 8 presents the current work's main conclusions and discusses the potential future studies for using AM in heat transfer applications.

Please note that this thesis is paper-based, in which Chapters 2-7 represents a different investigations, whether published as a journal paper or submitted for publication. Consequently, each chapter includes its relevant literature, test rig, methodology, and outcome results.

1.5 References

[1] H. Wang, S. Masood, P. Iovenitti, and E. C. Harvey, "Application of fused deposition modeling rapid prototyping system to the development of microchannels," in BioMEMS and Smart Nanostructures, 2001, vol. 4590, pp. 213–221.

[2] S. Guessasma, W. Zhang, J. Zhu, S. Belhabib, and H. Nouri, "Challenges of additive manufacturing technologies from an optimisation perspective," Int. J. Simul. Multidiscip. Des. Optim., vol. 6, no. Figure 1, p. A9, 2015, doi: 10.1051/smdo/2016001.

[3] B. Berman and F. G. Zarb, "3-D printing: The new industrial revolution 1. A multi-faceted technology: 3-D printing," Bus. Horiz., vol. 55, pp. 155–162, 2011, doi: 10.1016/j.bushor.2011.11.003.

[4] K. V. Wong and A. Hernandez, "A Review of Additive Manufacturing," ISRN Mech. Eng., vol. 2012, pp. 1–10, 2012, doi: 10.5402/2012/208760.

[5] M. Nikzad, S. H. Masood, and I. Sbarski, "Thermo-mechanical properties of a highly filled polymeric composites for Fused Deposition Modeling," Mater. Des., 2011, doi: 10.1016/j.matdes.2011.01.056.

[6] S. Hwang, E. I. Reyes, K. sik Moon, R. C. Rumpf, and N. S. Kim, "Thermo-mechanical Characterization of Metal/Polymer Composite Filaments and Printing Parameter Study for Fused Deposition Modeling in the 3D Printing Process," J. Electron. Mater., 2015, doi: 10.1007/s11664-014-3425-6.

[7] F. Zhang, G. Ma, and Y. Tan, "The Nozzle Structure Design and Analysis for Continuous Carbon Fiber Composite 3D Printing," Adv. Eng. Res., vol. 136, no. Icadme, pp. 193–199, 2017.

[8] A. N. Dickson, J. N. Barry, K. A. Mcdonnell, and D. P. Dowling, "Fabrication of continuous carbon , glass and Kevlar fibre reinforced polymer composites using additive manufacturing," Addit. Manuf., vol. 16, pp. 146–152, 2017, doi: 10.1016/j.addma.2017.06.004.

[9] J. Cevallos, "Thermal and manufacturing design of polymer composite heat exchangers," Dr. Philos. Univ. Maryl., 2014.

[10] Y. Jia, H. He, Y. Geng, B. Huang, and X. Peng, "High through-plane thermal conductivity of polymer based product with vertical alignment of graphite flakes achieved via 3D printing," Compos. Sci. Technol., vol. 145, pp. 55–61, 2017, doi: 10.1016/j.compscitech.2017.03.035.

[11] D. M. Hymas, M. A. Arie, F. Singer, A. H. Shooshtari, and M. M. Ohadi, "Enhanced Air-Side Heat Transfer i n a n Additively Manufactured Polymer Composite Heat Exchanger," 2017.

[12] C. Hutter, D. Büchi, V. Zuber, and P. R. von Rohr, “Heat transfer in metal foams and designed porous media,” Chem. Eng. Sci., vol. 66, no. 17, pp. 3806–3814, 2011.

[13] M. Wong, I. Owen, C. J. Sutcliffe, and A. Puri, “Convective heat transfer and pressure losses across novel heat sinks fabricated by Selective Laser Melting,” Int. J. Heat Mass Transf., vol. 52, no. 1–2, pp. 281–288, 2009.

[14] J. Y. Ho, K. K. Wong, K. C. Leong, and T. N. Wong, “Convective heat transfer performance of airfoil heat sinks fabricated by selective laser melting,” Int. J. Therm. Sci., vol. 114, pp. 213–228, 2017, doi: 10.1016/j.ijthermalsci.2016.12.016.

[15] A. J. Robinson, R. Kempers, J. Colenbrander, N. Bushnell, and R. Chen, “A single phase hybrid micro heat sink using impinging micro-jet arrays and microchannels,” Appl. Therm. Eng., vol. 136, 2018, doi: 10.1016/j.applthermaleng.2018.02.058.

[16] R. Kempers, J. Colenbrander, W. Tan, R. Chen, and A. J. Robinson, “Experimental Characterization of a Hybrid Impinging Microjet-Microchannel Heat Sink Fabricated using High-Volume Metal Additive Manufacturing,” J. Thermofluids, vol. 5, p. 100029, 2020.

[17] K. L. Kirsch and K. A. Thole, “Experimental investigation of numerically optimized wavy microchannels created through additive manufacturing,” J. Turbomach., vol. 140, no. 2, p. V05CT21A004, 2018, doi: 10.1115/1.4038180.

[18] B. J. Hathaway, K. Garde, S. C. Mantell, and J. H. Davidson, “Design and characterization of an additive manufactured hydraulic oil cooler,” Int. J. Heat Mass Transf., vol. 117, pp. 188–200, 2018, doi: 10.1016/j.ijheatmasstransfer.2017.10.013.

[19] J. D. Bernardin, K. Ferguson, D. Sattler, and S. J. Kim, “The design, analysis, and fabrication of an additively manufactured twisted tube heat exchanger,” ASME 2017 Heat Transf. Summer Conf. HT 2017, vol. 2, pp. 1–8, 2017, doi: 10.1115/HT2017-4866.

[20] S. M. Thompson, Z. S. Aspin, N. Shamsaei, A. Elwany, and L. Bian, “Additive manufacturing of heat exchangers: A case study on a multi-layered Ti-6Al-4V oscillating heat pipe,” Addit. Manuf., 2015, doi: 10.1016/j.addma.2015.09.003.

[21] K. K. Wong and K. C. Leong, “Saturated pool boiling enhancement using porous lattice structures produced by Selective Laser Melting,” Int. J. Heat Mass Transf., vol. 121, pp. 46–63, 2018, doi: 10.1016/j.ijheatmasstransfer.2017.12.148.

[22] A. Hayes, P. A. Raghupathi, T. S. Emery, and S. G. Kandlikar, “Regulating Flow of Vapor to Enhance Pool Boiling,” Appl. Therm. Eng., 2018, doi: 10.1016/j.applthermaleng.2018.12.091.

[23] A. Elkholy, M. Rouby, and R. Kempers, “Characterization of the anisotropic thermal conductivity of additively manufactured components by fused filament fabrication,” Prog. Addit. Manuf., vol. 4, no. 4, pp. 497–515, 2019, doi: 10.1007/s40964-019-00098-2.

[24] A. Elkholy and R. Kempers, “Enhancement of Pool Boiling Heat Transfer using 3D-Printed Polymer Fixtures,” in 14th International Conference on Heat Transfer, Fluid Mechanics and Thermodynamics, 2019, p. 6.

[25] A. Elkholy and R. Kempers, “Enhancement of pool boiling heat transfer using 3D-printed polymer fixtures,” Exp. Therm. Fluid Sci., vol. 114, no. January, p. 110056, 2020, doi: 10.1016/j.expthermflusci.2020.110056.

[26] A. Elkholy and R. Kempers, “Investigation of Surface Aging Effects on the Repeatability of Saturated Pool Boiling Heat Transfer,” in ITherm 2020 The Intersociety Conference on Thermal and Thermomechanical Phenomena in Electronic Systems, 2020, pp. 893–899.

[27] A. Elkholy and R. Kempers, “Experimental investigation of geyser boiling in a small diameter two-phase loop thermosyphon,” Exp. Therm. Fluid Sci., vol. 118, no. May, p. 110170, 2020, doi: 10.1016/j.expthermflusci.2020.110170.

Chapter 2 Characterization of the Thermal Conductivity of 3D-Printed Components by FFF[1]

The effect of process parameters on the mechanical properties of FFF 3D-printed parts has been studied extensively. However, there are limited reliable data for the thermal conductivity of 3D-printed components which has impeded the development of additively manufactured heat exchangers. In this chapter, the effect of the layer height and raster width have been investigated experimentally and numerically to characterize the effective thermal conductivity of 3D-printed components and investigate the thermal anisotropic nature of unidirectional printed parts. The unidirectional effective conductivity model was subsequently modified to characterize the common cross-hatched layer fill configuration, and the influence of fill ratio on the effective thermal conductivity was investigated. Finally, the effective thermal conductivity of several commercially available PLA composite filaments was characterized experimentally.

2.1 Introduction

The FFF process depends on depositing the molten material layer by layer on a heated bed using a continuous filament of thermoplastic feedstock, which passes through a heated nozzle moving in the X–Y plane. The nozzle motion is controlled according to the data generated by slicing software, which divides the original CAD model into separate layers. Once one layer is completed, the bed is lowered to begin another until the component is complete. This process has many

[1] This chapter has been published as a peer-reviewed journal paper titled "Characterization of the Anisotropic Thermal Conductivity of Additively Manufactured Components by Fused Filament Fabrication" in *Progress in Additive Manufacturing.*

parameters, such as layer height, raster width, the overlap between rasters, infill pattern, and raster angle, as shown in Figure 2-1. Several studies have investigated the influence of these parameters on dimensional accuracy and printing resolution [1–3]. Other work has addressed the influence of these parameters on the mechanical properties of pure polymer using a design of experiment (DOE) approach and the Taguchi method [4–11]. For instance, Cantrell et al. [5] characterized the tensile and shear properties of 3D-printed parts made of acrylonitrile-butadiene-styrene (ABS) and polycarbonate at various raster angles and different build directions. These studies generally demonstrate the anisotropic behavior present in the 3D-printed components that can be altered by changing the printing parameters. Moreover, they show that their mechanical properties are inferior compared with pure polymers due to the air voids generated inside the polymer matrix.

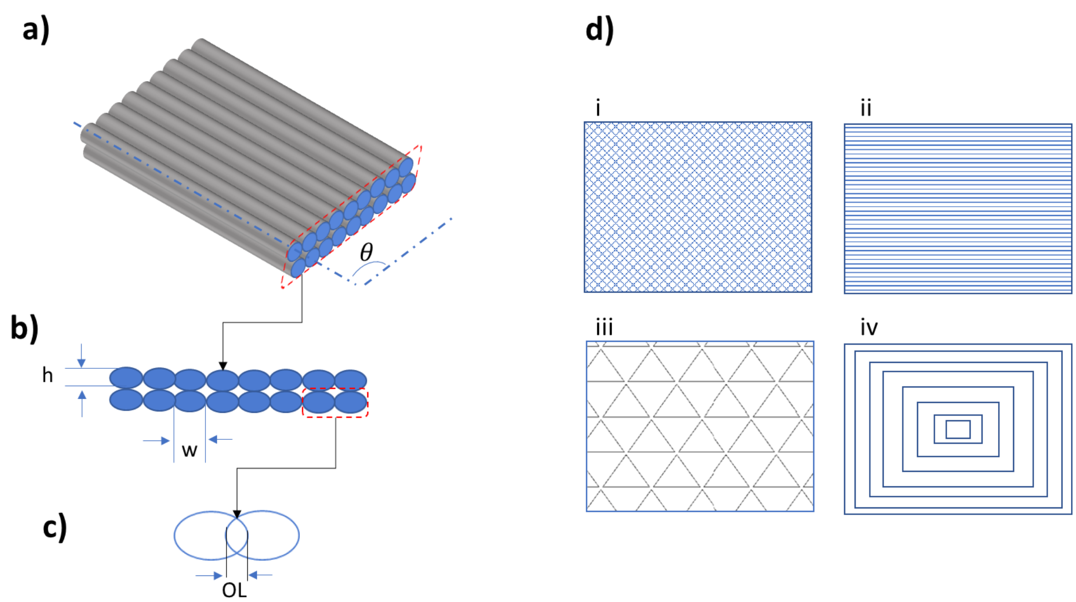

Figure 2-1. FFF process parameters: (a) raster angle, θ; (b) layer height, h, and raster width, w; (c) overlap, OL; (d) infill pattern (i. hatched layers, ii. unidirectional or lines, iii. triangles, iv. concentric).

To address these deficiencies, Nikzad et al. [12,13] found that the mechanical and thermal properties of ABS-printed components could be improved by including metallic filler particles of iron or copper into the FDM filament. They utilized the transient line source technique and differential scanning calorimetry (DSC) to measure thermal conductivity and the thermal capacity of the resultant polymer composite. Their results showed the thermal conductivity improved markedly above 30 % volume fraction of filler. However, the thermal capacity deteriorated by incorporating the metallic fillers at any volume percentage. They also examined the dynamic mechanical properties of the printed composites and showed that high filler percentage reduced the material strength due to poor filler distribution, agglomeration, and the development of voids. Hwang et al. [14] examined similar feedstocks and characterized the effect of printing parameters, such as printing temperature and fill density, on the mechanical properties of pure ABS. Masood et al. [15] manufactured a nylon–iron FDM filament for direct rapid tooling of injection dies and inserts. Laureto et al. [16] used the guarded heat flow meter TCA300 to quantify the through-plane thermal conductivity of 3D-printed parts made from the commercially available polylactic acid (PLA) filament and its metal composites. They quantified the particles size, their volume fraction, and also the air void fraction using backscattered electron (BSE) microscopic photos; these measurements were employed in three analytical models: Maxwell–Eucken [17], Lichtenecker [18], and Landauer [19], and compared to the experimental measurements. It was shown that these models are deficient in predicting the experimental measurements.

Shemelya et al. [20] utilized the Transient Plane Source (TPS) technique to characterize the anisotropic thermal properties of 3D-printed ABS composites filled with graphite, carbon fiber, and silver. Flaata et al. [21] developed a steady-state apparatus explicitly designed to measure the thermal conductivity of 3D-printed composites and used it to test some feedstock materials available commercially for FDM, such as PLA, ABS, brass PLA, bronze PLA, and stainless-steel PLA. However, there is a large discrepancy between the measured values by Laureto [27], Shemelya et al. [20], and Flaata et al. [21]. For instance, ABS has a thermal conductivity of 0.35 W/mK, according to [21] when it was tested by [20], and suggested to have a value range from 0.15 W/mK to 0.2 W/mK, depending on the direction of measurements which represents a deviation of 57%–75%. The same discrepancy applies to PLA and its composites. Prajapati et al. [22] studied the effect of the air gap on the anisotropic thermal conductivity ratio for unidirectional FDM 3D-printed parts made from ABS and ULTEM. They utilized a Stratasys Fortus 450mc printer and successfully characterized effective thermal conductivity as a function of the spacing between the rasters. They concluded the anisotropic ratio could reach up to 1.7 for both materials, depending on the air gap between the rasters. However, this printer is not open-source, and therefore they had limited control over the process parameters or materials.

The composites in these studies can be classified as discontinuous fiber composites because the fillers exist as discrete particles inside the polymer matrix. Most have demonstrated improved mechanical and thermal properties; however, there are limits to their performance, such as porosity generation in the case of metal fillers. Other limitations are associated with the discontinuous nature of the composite, especially at low filler concentrations below the percolation limit, such as the filler distribution and the interfacial heat resistance between the two phases. Generally, filler orientation is not considered a problem because Shofner et al. [23] proved that the vapor-grown carbon fibers (VGCFs) are aligned well in the material feedstock and after printing in the FDM traces due to the shear effect happening through the extrusion process. To address these limitations, other researchers have investigated the printing of continuous fiber composites using FDM [24–29]. This process rests on impregnating a continuous filler into the polymer matrix, using a modified nozzle that can liquify the thermoplastic and wrap it around the filler filament while printing.

In summary, while the effects of printing parameters on the mechanical properties of 3D-printed components have been studied extensively, there is a limited understanding of the effective thermal conductivity of 3D-printed components. The development of effective 3D-printed composite polymer heat exchangers requires an understanding of the anisotropic nature of the printed parts with respect to process variables to produce reliable thermal conductivity data and performance models. Therefore, the objectives of this work are to characterize the effect of geometric printing parameters such as the layer height, raster width, and fill ratio on the anisotropic effective thermal conductivities of FFF-printed components and to develop and validate numerical models which can be used to further predict thermal performance for other printing configurations and process variables. Other printing parameters such as temperature and print speed have more of an indirect effect on the effective thermal conductivity through their influence on the internal geometry. As such, these parameters were not considered in the current work, and only the basic geometry parameters were investigated. A further objective is to characterize the thermal performance of composite FFF feedstocks as they pertain to potential heat transfer applications.

2.2 Sample Design and Preparation

A popular infill pattern for printing with FFF or FDM is to print using a cross-hatched layer configuration [30]. This requires printing a layer at an angle and the subsequent one at another angle, most usually perpendicular to it, such as the one shown in Figure 2-1d(i). The effect of the process variables on the anisotropic thermal conductivity of FFF or FDM 3D-printed parts was characterized by first experimentally measuring how these parameters will alter heat transfer within unidirectional printed parts, using this experimental data to validate a numerical model and subsequently using the validated model to characterize thermal conductivity at any angle.

Investigation of the anisotropic nature of unidirectional parts requires specimens of the same size, printed in three different configurations, as shown in Figure 2-2. The first is used to quantify the thermal conductivity in the z-direction, k_{zz}, the second is for the y-direction, k_{yy}, and the third is for the x-direction, k_{xx}. In the present study, the first direction, k_{zz}, was printed and measured experimentally and used to validate a numerical model. Numerical and analytical models were subsequently used to characterize thermal conductivity in the other directions. The influence of the layer height was studied by printing the specimens with different values ranging from 0.1 mm to 0.3 mm, while keeping the raster width and overlap constant at 0.4 mm and zero, respectively, which are the default printer settings. As for the layer width, its value was varied from 0.4 mm to 0.8 mm while maintaining the layer height and overlap at 0.15 mm and zero. All other process parameters, such as nozzle temperature, speed, etc., were preserved constant as shown in Table 2-1. All samples were printed using 100% fill of PLA filament using an Ultimaker® 2 printer. Each sample was printed to the size 40 mm x 40 mm x 3 mm to facilitate thermal conductivity measurement. An automatic ULTRAPOL polishing machine was utilized to ensure that the sample surfaces were parallel and that its surface roughness was very small to minimize thermal contact resistance. The sample surface roughness was measured after polishing at several spots by means of a profilometer (Bruker ContourGT-K). It was found to have an average Ra of 0.912±0.1 µm. The sample thickness was measured again at different locations after polishing using a micrometer to quantify any uncertainties in thickness.

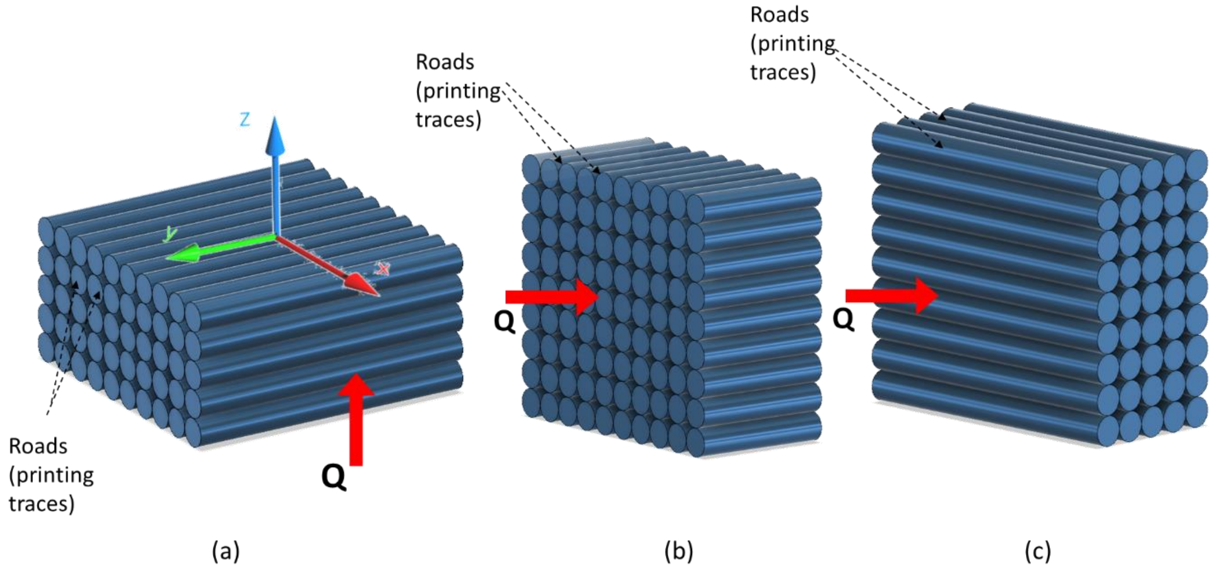

Figure 2-2. Different configurations of FFF 3D-printed samples to measure the thermal conductivity in: (a) z-direction, k_{zz}, (b) y-direction, k_{yy}, (c) x-direction, k_{xx}.

Table 2-1. The parameters used to print the FFF samples.

Parameter	Value
Sample size	40 mm x 40 mm x 3 mm
Layer height	0.1 mm–0.3 mm
Raster width	0.4 mm–0.8 mm
Overlap	0 %
Fill %	100 %
Nozzle temperature, T_N	200 °C
Bed temperature, T_b	60 °C
Printing speed, v	60 mm/s
Pattern	Lines

Numerical or analytical determination of the thermal conductivity for the other directions requires an investigation of the pattern of layers after printing, which was carried out by means of a microscopic study. Also, this study was used to obtain the air volume fraction inside the matrix. Preparation of the samples for the microscopic study was achieved by installing them through an epoxy well and letting them cure for a day. Then, they were cut using an abrasive cutting wheel and polished in two sequential steps with silica carbide sandpapers of 180–1200/400 on the same polishing machine.

2.3 Experimental Measurement of Effective Thermal Conductivity

Several methods have been used to measure the thermal conductivity of polymer composites manufactured either by AM or by conventional methods. These include the transient plane source (TPS) technique [20], transient line source for homogeneous molten composite mixture [12], steady-state [21], and laser flash method [31]. Laser flash and TPS techniques quantify thermal diffusivity and require additional digital scanning calorimetry DSC measurements to quantify thermal capacity and therefore measure the anisotropic thermal conductivity. Consequently, the apparatus developed in the current work is a steady-state device that can directly measure effective thermal conductivity in all directions.

Oftentimes, steady-state thermal conductivity apparatuses characterize thermal conductivity by sandwiching the sample between two instrumented and calibrated meter bars to measure heat flux through the sample and temperature at the contacting surfaces [32]. These types of apparatuses are typically used to characterize thin, conductive samples. However, for relatively thick, low conductivity materials, such as those in the present study, it was found that an appreciable fraction of the heat can bypass the sample through the insulation surrounding the bars, thereby limiting measurement accuracy.

To achieve the accurate and precise measurements required to characterize these materials, an apparatus was developed which is based upon a modified guarded hot plate technique outlined in ASTM C177 [33] and is shown schematically in Figure 2-3a. A known thermal power from the electrical heaters embedded in the primary heater block was conducted through the sample to a temperature-controlled primary cold block. The resultant steady-state temperature difference across the sample was measured using the resistance temperature detectors (RTDs) embedded in each block and the measured thermal resistance of the sample, R_{meas}, is given by:

$$R_{meas} = \frac{(T_a - T_b)}{Q} \tag{2.1}$$

where, $(T_a - T_b)$ is the temperature difference across the sample and Q is the measured input electric power to the primary heaters ($P = IV$).

The measured thermal resistance represents the summation of the bulk sample resistance and the thermal contact resistance between the sample and the apparatus is given by:

$$R_{meas} = R_{c,1} + R_{c,2} + R_{sample} = R_c + R_{sample} \tag{2.2}$$

$$= R_c + \frac{L}{k_{sample}A} \tag{2.3}$$

where $R_{c,1}$is the contact resistance between the sample and the primary heater, while $R_{c,2}$ is the contact resistance between the sample and the primary cooler.

The thermal conductivity of the sample can be calculated by rearranging this as:

$$k_{sample} = \frac{L}{A\left[\frac{(T_a - T_b)}{Q} - R_c\right]} \tag{2.4}$$

where, L is the specimen thickness, and A is the sample cross-section area.

The contact resistance was obtained by measuring the total thermal resistance for several samples with the same surface conditions and different thicknesses and then fitting the measured values against the samples' thicknesses to obtain the *y*-intercept.

The key elements in designing an accurate, guarded, steady-state method rests on creating two hot-and-cold isothermal plates and ensuring all supplied, and measured input power flows through the sample. This was achieved by guarding the heat source with another independent secondary heater block which surrounds the primary block whose temperature was controlled to be identical to the primary heater block. By ensuring identical temperatures between the primary and secondary (guard) heater blocks, the heat going through the sample can be quantified by measuring the electric power to the primary heater block. Similarly, the cold plate was guarded from its top surface by another secondary cooling block, as shown in Figure 2-3a.

Numerical simulations were carried out to design the primary and secondary heating and cooling blocks, to ensure all primary heater input power flowed through the sample, and to quantify any heat loss when measuring relatively low conductivity materials. Overall, for representative operating conditions and sample properties, thermal simulations demonstrated that over 99% of the input power to the primary heater block flowed through the sample and that the surface temperatures of the hot and cold blocks were isothermal to within 0.04 K, as shown in Figure 2-3b. Also, the temperature difference between the primary and secondary blocks was about 0.06 K, as shown in Figure 2-3b.

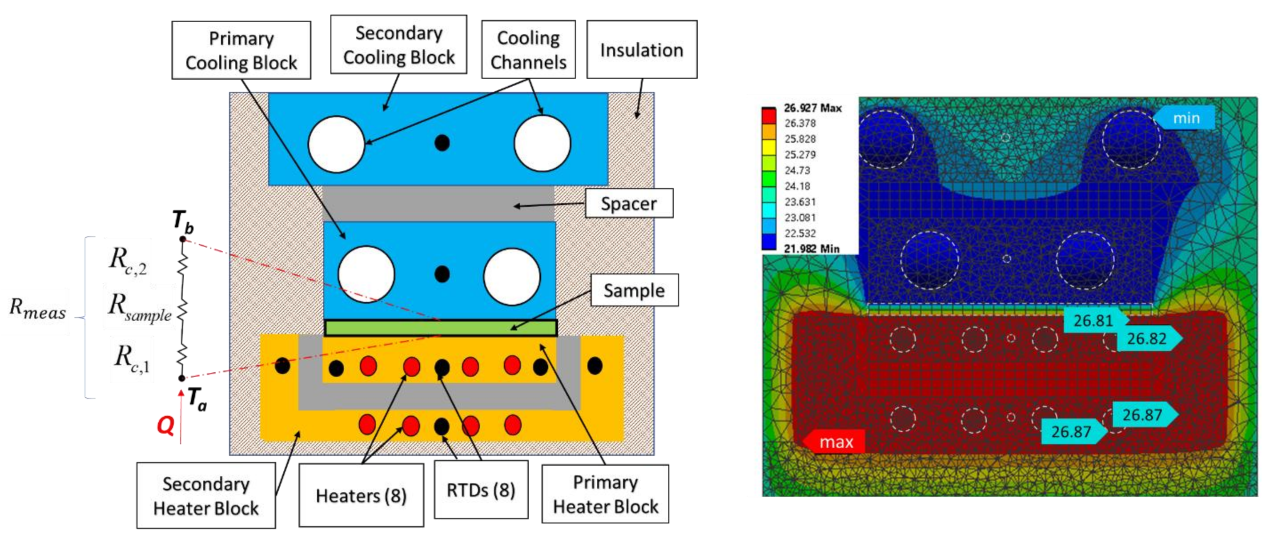

(a) (b)

Figure 2-3. (a) Schematic of experimental thermal conductivity apparatus (b) numerical simulation of the experimental apparatus.

The overall experimental setup is shown in Figure 2-4a. The primary and secondary (guard) blocks were machined from copper because of its high thermal conductivity to help ensure uniform temperature within each block. The primary heater block was 40 mm x 40 mm x 6.35 mm. Four cartridge heaters (Sun Electric Heater), with a diameter of 3.1 mm (1/8 inch) and a length of 38 mm (1.5 in), were inserted into holes drilled through the block. The secondary heater block had overall dimensions of 70 mm x 70 mm x 15.7 mm and had a 55 mm x 55 mm x 9.35 mm cutout, into which a plastic spacer and the primary heater block were inserted. An additional four 3.1 mm x 50 mm (1/8-inch x 2 inches) cartridge heaters were installed into the secondary heater block.

The temperature of each block was measured using three RTDs 1 mm x 15 mm (Omega, 1PT100KN1510) inserted into holes at the locations shown in Figure 2-3 such that each sensor from the primary block was opposite a corresponding sensor on the secondary heater block. The input power to each block was supplied using two independent DC supplies (Aim TTi, CPX400D) and controlled by varying the supplied voltage.

The primary cooling block measured 40 mm x 40 mm x 12 mm, while the secondary block was 80 mm x 80 mm x 12 mm. Each was drilled with 8.5 mm diameter holes in a U-channel configuration to permit cooling water to flow through them. Temperature-controlled water supplied from a circulator (Julabo F32-HE) flowed through the primary block and then to the secondary one. Both blocks had a single RTD inserted near the center to monitor block temperatures. An additional RTD was inserted in the water channel to provide feedback to the circulator. During testing, the chiller temperature was tuned to keep the sample average temperature close to the ambient temperature to minimize the heat loss or gain from or to the sample sidewalls. The heat loss was further estimated using the numerical simulation and was found to be less than 2% of the input power to the primary heater. The secondary cooling block function was to help isolate the system from temperature fluctuations in the surrounding environment.

The sample under test was clamped between the primary and secondary heating and cooling blocks using a clamping screw, device frame, and the load cell (AST, KAF-S/500/0.1), as shown in Figure 2-4. Samples were clamped with a pressure of approximately 3 bars, and a few droplets of thermal paste (ARCTIC, MX-4) were used to minimize thermal contact resistance and to help ensure reparability of results.

The entire assembly was encased in silica aerogel insulating material with a thermal conductivity of 0.014 W/m K. The ambient temperature was monitored using a T-type thermocouple.

Once assembled into the heater blocks, the RTDs were simultaneously calibrated using a 50 mm-long Fluke PRT full immersion reference probe (Model 5606), which was certified from -200°C to 160°C. The calibration was carried out using an isothermal-controlled copper chamber from 5°C to 30°C using the approach described in [33]. Upon calibration, the uncertainty in temperature difference between the sensors was ±0.012 K.

The temperature sensors were monitored using an Agilent 34970A data acquisition system, while the input power to the primary heater block of the heater side was carried out by measuring the voltage and current using independent Agilent 34401A digital multimeters. A MATLAB script was used to log measurements and control the secondary heater block power. The criteria for secondary power control was to ensure the temperature difference between the primary and secondary heater blocks did not exceed 0.01 K at a steady-state. The system was considered a steady-state when the time gradient of the temperature for each sensor was less than 1e-5 K/s.

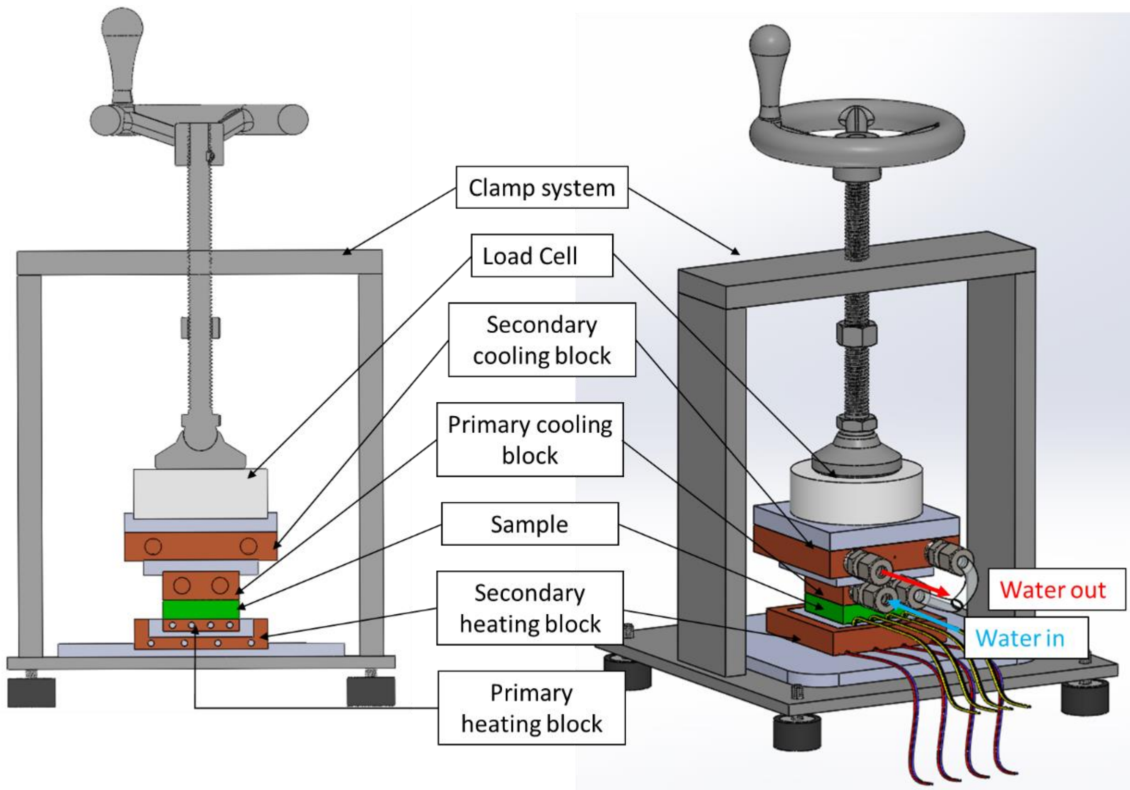
Clamp system
Load Cell
Secondary cooling block
Primary cooling block
Sample
Secondary heating block
Primary heating block
Water out
Water in

(a)

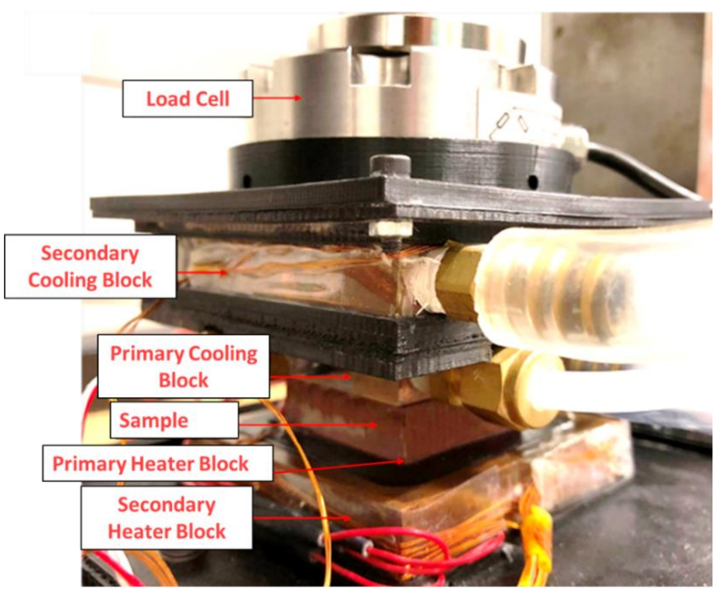
Load Cell
Secondary Cooling Block
Primary Cooling Block
Sample
Primary Heater Block
Secondary Heater Block

(b)

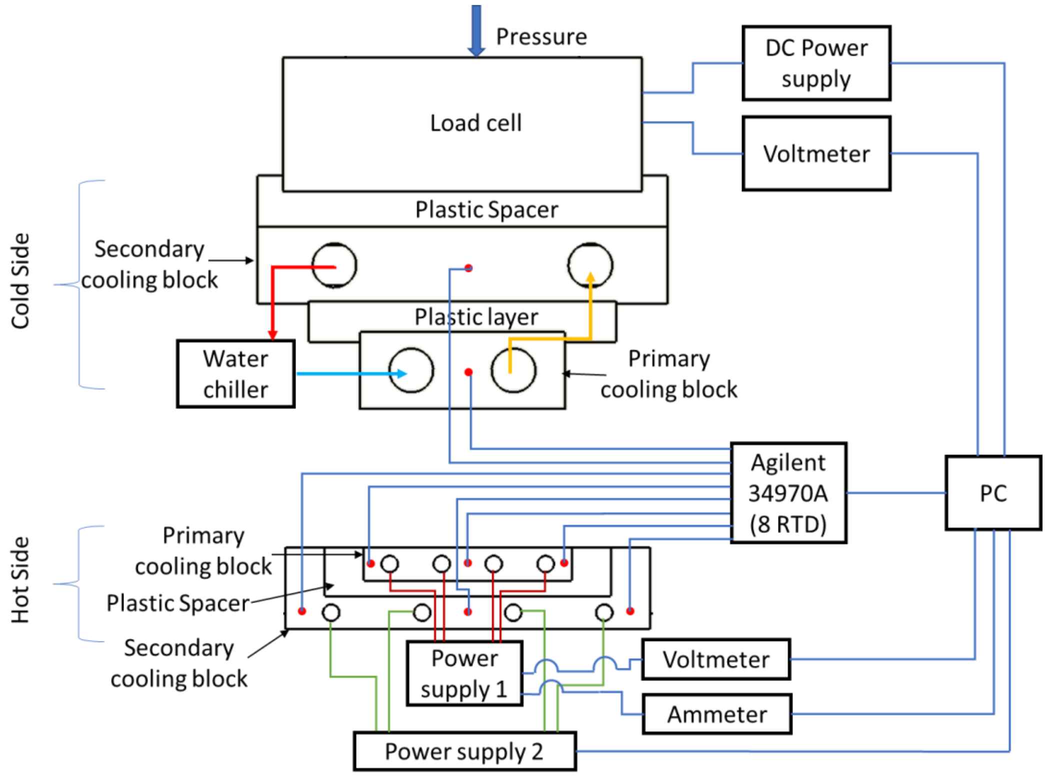

(c)

Figure 2-4. Experimental thermal conductivity apparatus: (a) overall Schematic (b) photograph of test section (c) instrumentation and control.

2.3.1 Uncertainty Analysis

The resulting uncertainty in measuring the thermal conductivity was a combination of two types: device bias uncertainty and the precision uncertainty. The bias uncertainty of the device was predicted by the error propagation method detailed in [34]. The uncertainties for all input parameters are shown in Table 2-2 and the precision uncertainty was determined by repeating the measurement three times using the same device under the same conditions. The maximum uncertainty originating from the repeatability test was less than 1.8 %.

$$U_k = \sqrt{\left(\frac{\partial k}{\partial V}U_V\right)^2 + \left(\frac{\partial I}{\partial I}U_I\right)^2 + \left(\frac{\partial k}{\partial L}U_L\right)^2 + \left(\frac{\partial k}{\partial T}U_T\right)^2 + \left(\frac{\partial k}{\partial A}U_A\right)^2} \tag{2.5}$$

where V is the applied voltage, and I is the resultant current which was utilized to obtain the imposed heater power.

Table 2-2. Uncertainties for the measured quantities of the thermal conductivity device.

<table>
<tr><th>Parameter</th><th colspan="2">Uncertainty</th></tr>
<tr><td>Sample thickness, L</td><td colspan="2">0.15 mm (Maximum)</td></tr>
<tr><td>Sample area, A</td><td colspan="2">1×10^{-5} (m^2)</td></tr>
<tr><td>Temperature Difference</td><td colspan="2">0.012 K</td></tr>
<tr><td rowspan="2">Voltage</td><td>Range</td><td>± (% of reading + % of range)</td></tr>
<tr><td>100 mV
1 V
10 V
100 V</td><td>0.0050 + 0.0035
0.0040 + 0.0007
0.0035 + 0.0005
0.0045 + 0.0006</td></tr>
<tr><td>Current</td><td>10 mA
100 mA
1 A</td><td>0.050 + 0.020
0.050 + 0.005
0.100 + 0.010</td></tr>
</table>

2.4 Numerical Modeling

The effective thermal conductivity of the printed components in z or x directions was modeled numerically by simplifying the geometry into a 2D cross-section and extracting unit cells to represent the overall geometry, as shown in Figure 2-5. Although the sample's microstructure was not perfectly symmetric, and some of the unit cells or rasters were inconsistent, this simplification allowed for relatively straightforward numerical modeling of the effective thermal conductivity of the structure. The unit cell had a dimension of $h/2$ in the z-direction and $w/2$ in the x-direction, as shown in Figure 2-5a.

ANSYS Fluent 18.2 software [35] was used to model the conduction heat flow through printed parts. The numerical model required inputting the thermal conductivity of pure polymer, which was measured by printing a sample with a small layer height of 0.06 mm and a high percentage of overlap (50%) to ensure that there was no air gap generated inside the part; this was found to be 0.2207 W/m K. The air standard thermal conductivity was defined as 0.0242 W/m K.

The problem boundary conditions were set as follows:

- A temperature boundary condition was applied at the right and left boundaries of the domain. The temperature difference, $T_1 - T_2$, was set equal to 1 K for all cases.
- Adiabatic and symmetry conditions were imposed for the top and bottom boundaries to ensure heat flow through the x-direction, as shown in Figure 2-5b. The symmetry type boundary was assumed based on the simplifications explained boundary. This has been used along with the adiabatic conditions for the other boundaries to force the heat flow through the x-direction.

The effective thermal conductivity was then calculated in x-direction, k_{xx}, by solving the energy equation and quantifying the heat transfer rate in that direction. For effective thermal conductivity in the z-direction, the boundary conditions were reversed, and the temperature difference was imposed in the direction of the thermal conductivity being calculated.

The domain was divided into discrete quadrilateral control volumes, and the energy equation was solved iteratively. The number of cells was increased from 1093 to 1666257 to ensure grid independence. The domain was initialized with a constant temperature of 300 K. The mesh quality was measured using the maximum aspect ratio and the maximum skewness, which were 6 and 0.8, respectively. Convergence was ensured by setting the residuals equal to 1e-10.

The geometry was varied according to the measured cross-sections and the volume fraction calculated by weighing the tested samples in the previous section to determine the air gap distance between the roads, as explained in the following section.

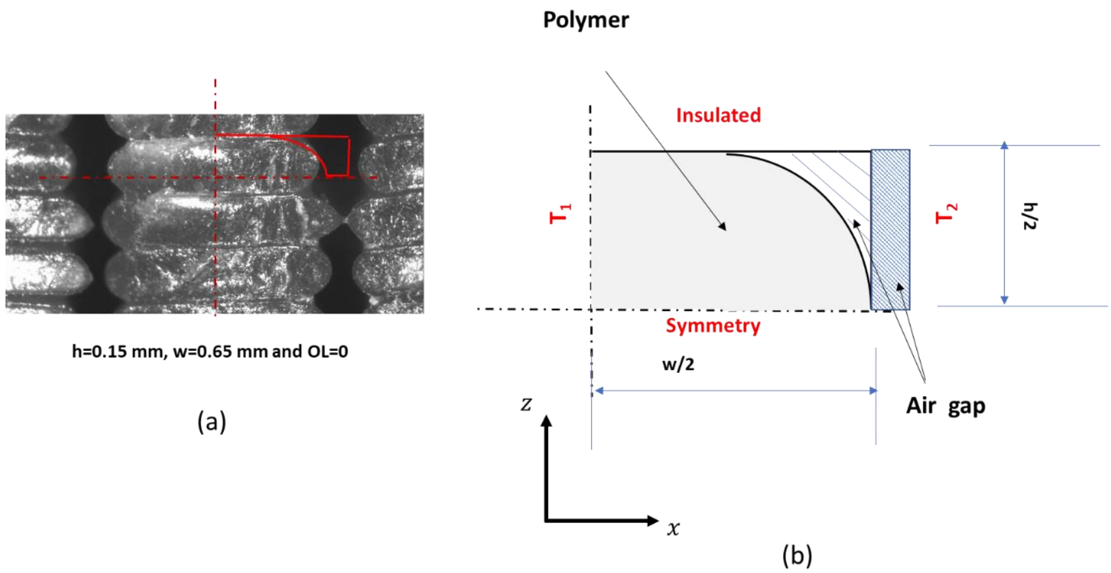

Figure 2-5. Numerical model of FFF process parameters: (a) unit Cell (b) domain.

2.5 Results and Discussion

2.5.1 Microscopic Imaging Results and Sample Characterization

A cross-section of a unidirectionally printed sample is shown in Figure 2-6a, which depicts the effect of changing the layer height from 0.15 mm to 0.3 mm while keeping its width at the default value of 0.4 mm. Here, increasing layer height results in an increase in the air volume fraction within the printed component. A similar effect is apparent when increasing the raster width, as shown in Figure 2-6b, where layer height was held constant at 0.15 mm. We can also see from Figure 2-6 that the pattern is mostly homogeneous except for some roads which are not connected to each other. This phenomenon is more likely to occur at small layer heights. We conjecture this is because the molten polymer, when unconstrained, preferentially flows to either one side or the other. Another important feature to note in Figure 2-6 is that the roads begin to completely disconnect for raster widths greater than 0.5 mm.

The volume fraction for each sample was quantified using two approaches. In the first, each photo was converted into an 8-bit image type to allow thresholding. ImageJ software was employed to carry out the thresholding and calculate the air volume fraction. The second approach to quantifying air volume fraction was accomplished by weighing the sample while postulating that the air mass within the part to be negligible and then applying the following equation:

$$v_f = \frac{v_s - v_p}{v_s} \tag{2.6}$$

where

$$v_p = \frac{m_s}{\rho} \tag{2.7}$$

and where v_f, v_p, v_s are the volume fraction of air, the volume that the polymer occupies inside the printed part, and the printed part volume, respectively. ρ is the polymer density which was measured for the PLA filament feedstock.

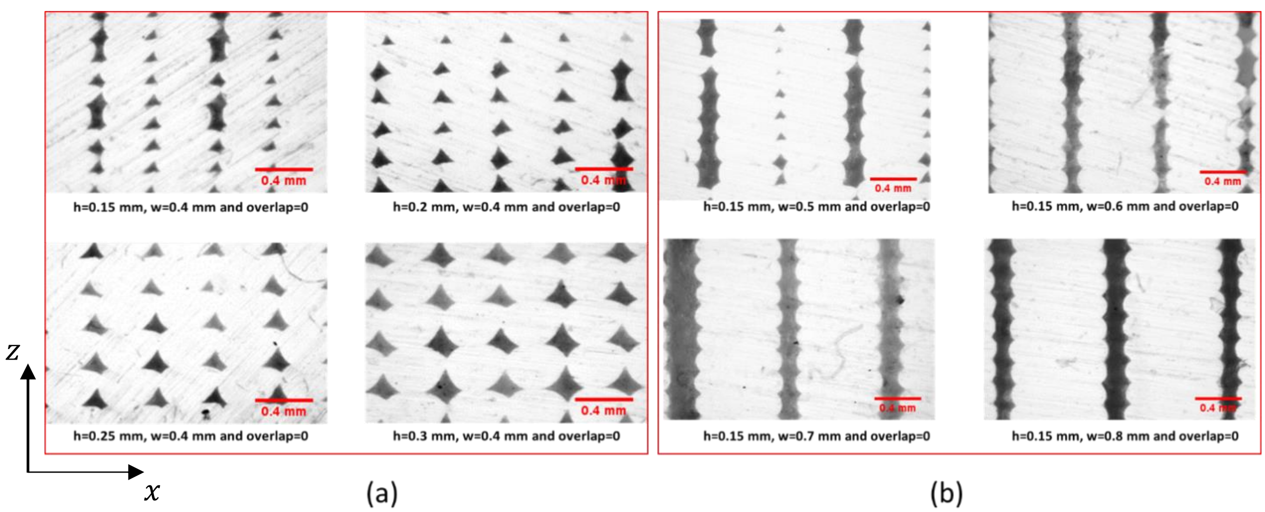

Figure 2-6. Microscopic photos of FFF 3D-printed samples showing the effect of (a) layer height, h, and (b) raster width, w.

Table 2-3 and Table 2-4 show a comparison between the air volume fraction resulting from the ImageJ method and the weighing method. As can be seen from these tables, there is a large deviation between the two methods, especially for the layer height. We suspect this is due to the fact that the sample under the microscope represents only one cross-section, and the photo was captured for part of this section which may not be representative of the whole sample, especially in cases where the layers are somewhat disconnected. The volume fraction measurements were not consistent between different cross-sections; even changing the measurement spot for the same cross-section resulted in different volume fractions. It is worth mentioning that the volume fraction using the weighting method is always greater than the ImageJ method, which we think pertains to the possibility of the existence of smaller pores within the filament itself. Therefore, the weighing method was used to quantify air volume fractions; we believe this better represents the true value of the parts characterized here. However, the photos give a better insight into the internal geometries and served to inform the geometries used when developing the numerical model.

Table 2-3. Air volume fraction at different layer heights at a constant raster width of 0.4 mm for FFF 3D-printed samples.

Layer Height, h (mm)	**Air Volume Fraction %**		
	ImageJ	Weighing Method	
	v_f %	v_f %	Uncertainty %
0.15	4.1	11.7	0.14
0.2	6.5	13.5	0.135
0.25	9.8	14.1	0.134
0.3	14.3	15.92	0.131

Table 2-4. Air volume fraction at different raster widths at a constant layer height of 0.15 mm for FFF 3D-printed samples.

Raster Width, w (mm)	**Air Volume Fraction %**		
	ImageJ	Weighing Method	
	v_f %	v_f %	Uncertainty %
0.4	4.1	11.7	0.137
0.5	11.9	13.7	0.134
0.6	13.7	15.3	0.131
0.7	17.1	19	0.126

2.5.2 Numerical Model Validation

The thermal conductivity in the z-direction, k_{zz}, was measured experimentally and compared with the numerical model, as shown in Figure 2-7 and Figure 2-8. The experimental results, depicted in Figure 2-7, indicate that increasing the layer height reduces the thermal conductivity in the z-direction until it reaches a value of 0.133 W/m K at a layer height of 0.3 mm due to the increase of air volume fraction. This represents a percentage of reduction of about 40 % compared with pure PLA polymer. The thermal conductivity in the z-direction, k_{zz}, also decreased with increasing raster width and resulted in a 14 % reduction of thermal conductivity at a raster width of 0.8 mm, as shown in Figure 2-8.

Overall, the numerical model predictions are in good agreement with the experimental results and predict the effective thermal conductivity within 5 % for 90 % of the data points. The model further captures the trend in the change in thermal conductivity with layer height and width. Slight deviations occur at the largest layer height and the lowest layer width. This is likely due to the simplification of a slightly more complex cross-sectional geometry for these cases into the more idealized shapes which were used as representative unit cells in the numerical model. In addition, in these cases, there exists a greater degree of variability in cross-sections used for geometry input to the numerical model; i.e., sometimes the roads are connected, and sometimes they were not, as discussed in the previous section.

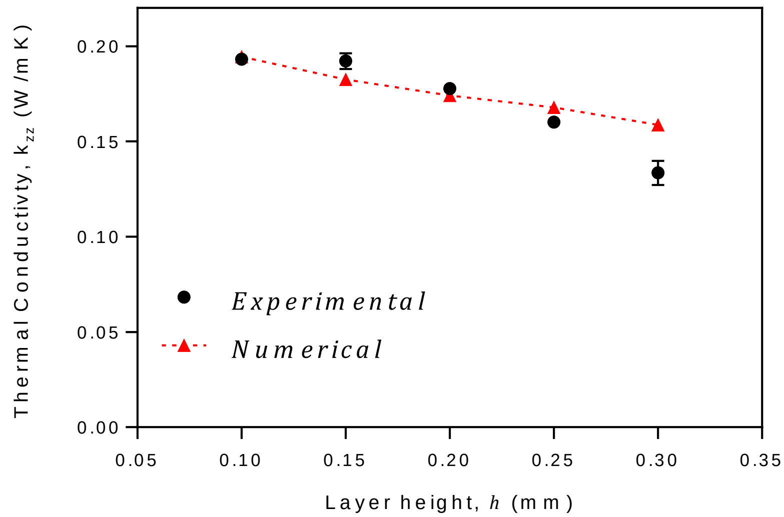

Figure 2-7. Comparison between the experimental results and numerical model for studying the effect of layer height on the thermal conductivity, k_{zz} , of unidirectional FFF 3D-printed part at a constant raster width of 0.4 mm.

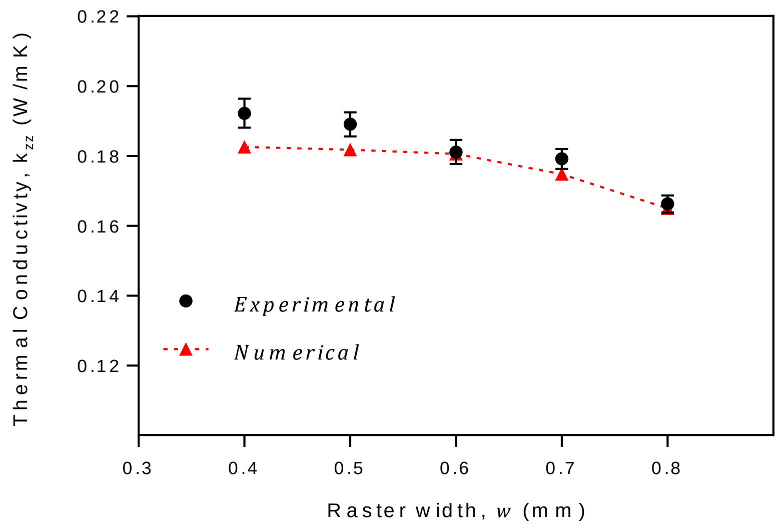

Figure 2-8. Comparison between the experimental results and numerical model for studying the effect of raster width on the thermal conductivity, k_{zz} , of unidirectional FFF 3D-printed part at a constant layer height of 0.15 mm.

2.5.3 Effect of Layer Height

Once the numerical model was established for the relatively complex geometry associated with the z-direction (k_{zz}), this was subsequently used to characterize the effect of printing parameters in the x-direction (k_{xx}). Thermal conductivity in z- and x-directions depends on the raster shape; however, for the relatively straightforward geometry in the y-direction, a parallel analytical model was employed to model the effective thermal conductivity, k_{yy} , given by

$$k_{yy} = (1 - v_f)k_m + v_f\, k_a \tag{2.8}$$

where k_{yy}, is the effective thermal conductivity in y-direction, while k_m and k_a are the conductivities for the matrix and air, respectively. v_f is the air volume fraction inside the PLA matrix, which was measured and tabulated in Table 2-3 and Table 2-4.

The effect of layer height on the thermal conductivity of unidirectional parts in all directions is shown in Figure 2-9, along with the experimental measurements in all directions for the case having a layer height of 0.25 mm. However, the numerical prediction deviation from the experimental measurements is different for all directions, which pertains to the layer disconnection problems that affect the numerical model accuracy differently, as discussed before in Section 2.5.2.

The numerical predictions show that the effect of layer height is more significant in z and x directions, while it is nearly constant for the y-direction. The thermal conductivities are higher in z and y directions than for x-direction. This is because the heat path in x-direction is a series which increases the overall thermal resistance, while it is parallel for the other directions. For the x-direction, the thermal conductivity initially decreases and increases again. This is because when the layer height is small, the layers are not connected.

In summary, the layer height increase causes a decrease in the thermal conductivity, which reaches values of reduction of 42%, 14%, and 28% for x, y, and z, respectively, compared with the pure polymer. The previous percentages were calculated based on the numerical model predictions.

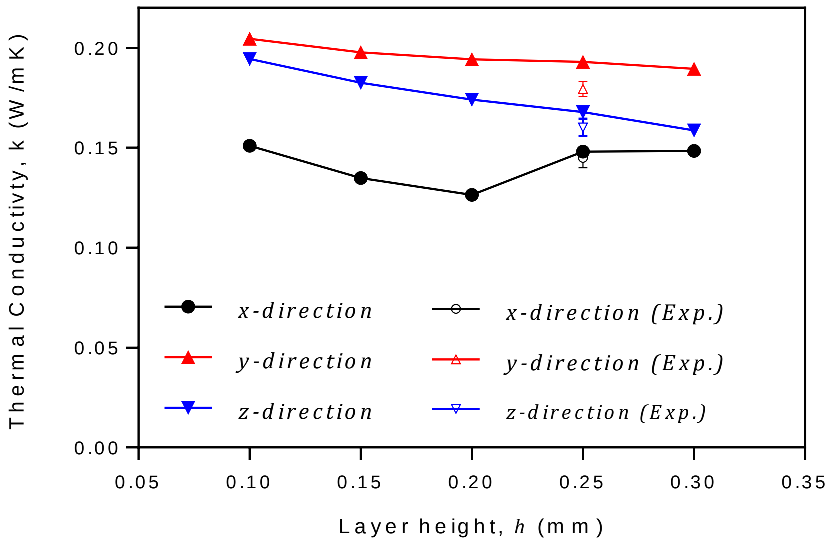

Figure 2-9. The effect of layer height on the thermal conductivity of FFF 3D-printed parts for all directions.

2.5.4 The Effect of Raster Width

The influence of the raster width on thermal conductivity in x and z directions was predicted numerically, while the parallel model was employed for y-direction, as shown in Figure 2-10. Like the layer height, increasing the raster width also causes a decrease in thermal conductivity in all directions. The thermal conductivity in y-direction is higher compared with other directions for the height effect in Figure 2-9 and for the layer width in Figure 2-10. The reason behind this can be explained with the help of the corresponding thermal network in Figure 2-11. Here, the heat flow direction in y-direction is parallel in the air and polymer phases, while it is series in x-direction and partly parallel in z-direction. For this reason, it can be expected that the thermal conductivity in y-direction should be the highest, followed by z-direction, and then, lastly, x-direction.

The raster width has a severe effect on the thermal conductivity in x-direction because the layers are completely disconnected in that direction. The thermal conductivity in x-direction reaches a low thermal conductivity value of 0.077 W/mK at a width of 0.8 mm, representing a 65% reduction compared with pure polymer, while the reduction is 28% and 25% for y and z directions, respectively. This highlights the importance of characterizing these parameters and demonstrates the possibility of tailoring the thermal properties of the printed parts, especially when printing continuous carbon fiber or low-melting-temperature metals.

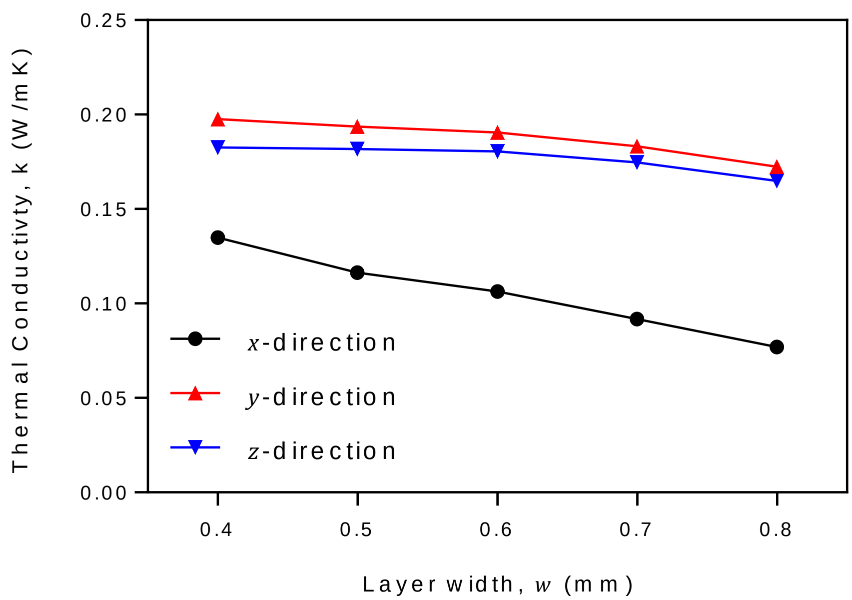

Figure 2-10. The effect of raster width on the thermal anisotropic nature of FFF 3D-printed parts.

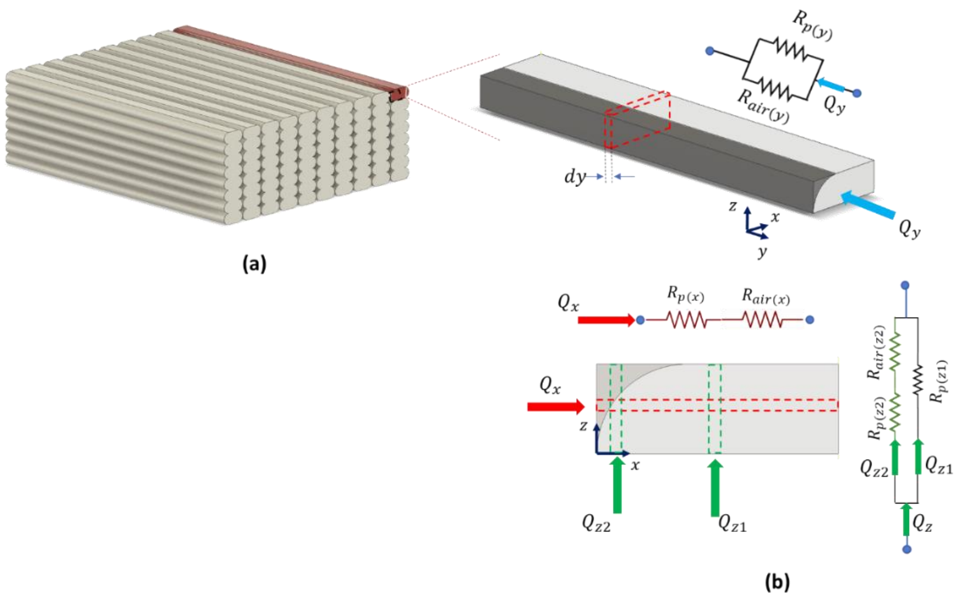

Figure 2-11. The equivalent thermal network for the FFF 3D-printed part unit cell: (a) schematic of the printed part (b) thermal network in all directions.

2.5.5 Thermal Conductivity Modeling for Printing at Cross-Hatched Layer Configuration

The effect of raster width and layer height on the thermal conductivity of unidirectional 3D-printed parts has thus far been characterized. This data is used here as the baseline to build a general model that can predict the thermal conductivity in x and y directions for bi-directional samples or for samples printed at a cross-hatched layer configuration at any angle, as illustrated in Figure 2-12. The thermal conductivity for bi-directional samples was predicted by taking a plane perpendicular to z-direction and applying the same boundary condition as that used in Section 2.4. This depends on inputting the thermal conductivity at the principal axes along with the printing angle to predict the heat transfer rate at the general axes, which can be used to obtain the corresponding thermal conductivities.

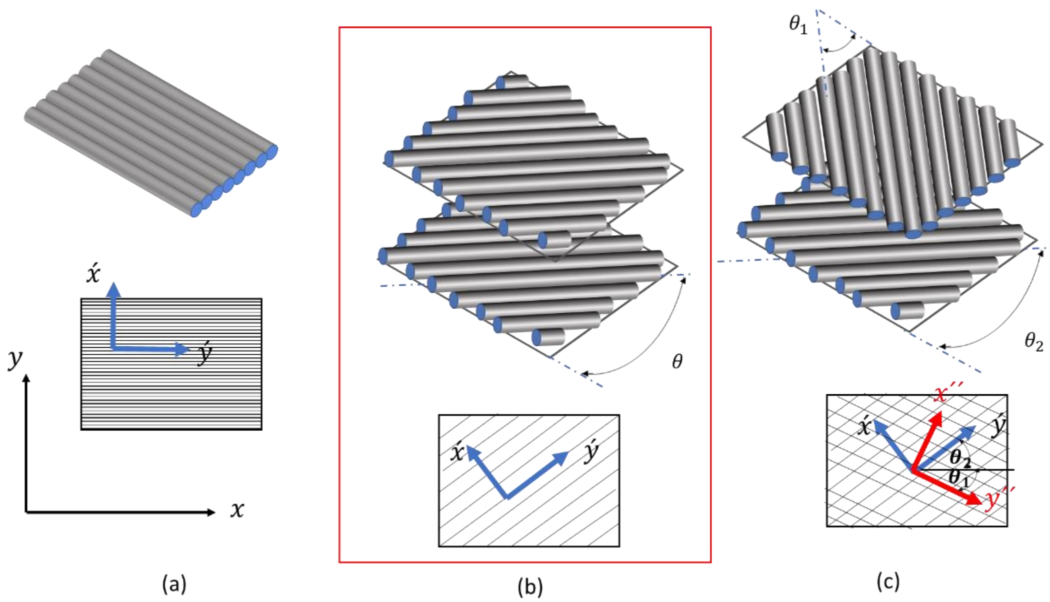

Figure 2-12. Different FFF thermal conductivity models: (a) unidirectional sample, (b) bi-directional sample, (c) cross-hatched layer sample.

Following the unit cell modeling approach described previously, Figure 2-13 shows the simulated temperature contours for a sample of results at a printing angle of 45°. The input thermal conductivities were 0.197 W/mK and 0.1348 W/mK for principal axes $\acute{y}$ and $\acute{x}$, respectively, which were predicted before at a layer height of 0.15 mm and raster width of 0.4 mm for the unidirectional sample in Section 5.2. The thermal conductivity for bi-directional samples in the z-direction will be very close to their unidirectional counterparts because the contact area between the layers has not changed significantly. However, thermal conductivity varies for samples printed using the cross-hatched layer configuration. Figure 2-14 shows the thermal conductivity in the general axes, x and y for bi-directional samples while changing the printing angle from 0° to 90°. The layers for the last sample type, shown in Figure 2-12c, can be interpreted as many bi-directional samples connected in parallel with heat being conducted in the x or y directions. Hence, such types of samples are modelled using the conventional parallel model, and the input thermal conductivity for each layer can be extracted from Figure 2-14 as a bi-directional sample. Since half of the layer is printed at θ_1 and the other half is printed at θ_2, only two resistances are required to model the effective thermal conductivity in both directions, as shown in Figure 2-15.

As discussed previously, the thermal conductivity in the z direction for such samples are different compared with unidirectional or bi-directional samples; therefore, different angle combinations were examined—[20º, 70 º], [30º, 60 º], [45º, -45 º], [0º, 90 º]—as shown in Figure 2-16. The thermal conductivity was similar for the last two combinations because the contact area between the polymer traces through the layers was approximately the same for both. Printing at cross-hatched layer configuration makes the polymer traces though the z direction connected at individual spots instead of having a continuous area of contact. Therefore, all the combinations in this direction were less conductive compared with the unidirectional sample.

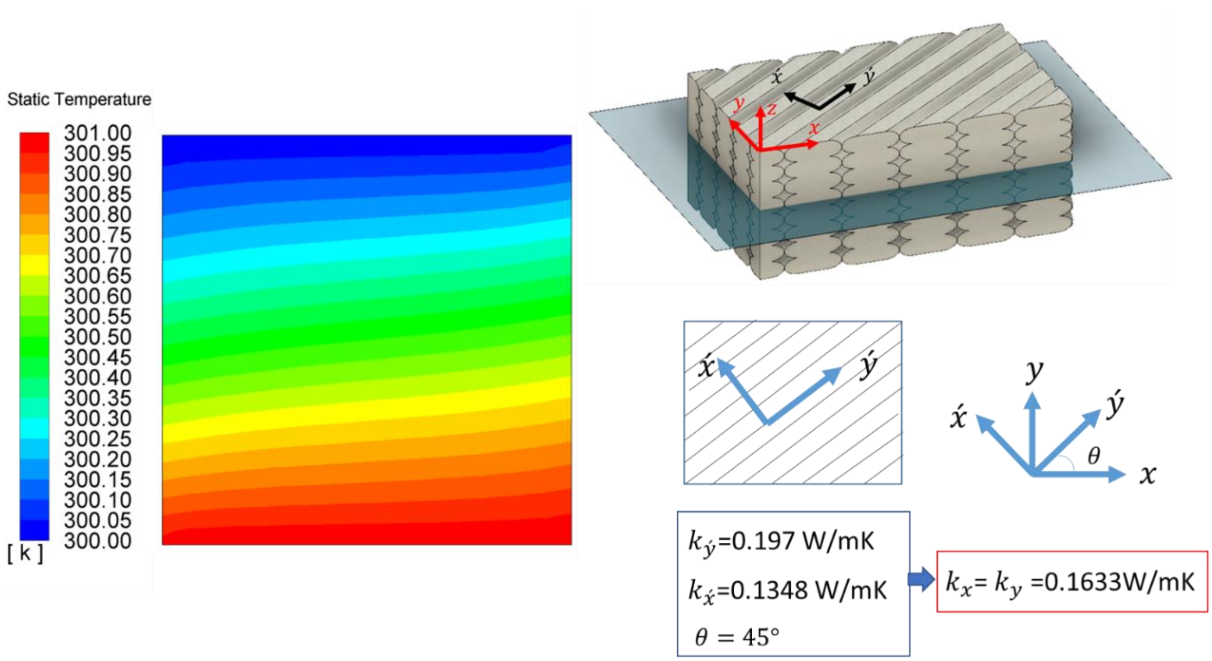

Figure 2-13. Temperature contours for a bi-directional FFF 3D-printed sample at printing angle of 45 º.

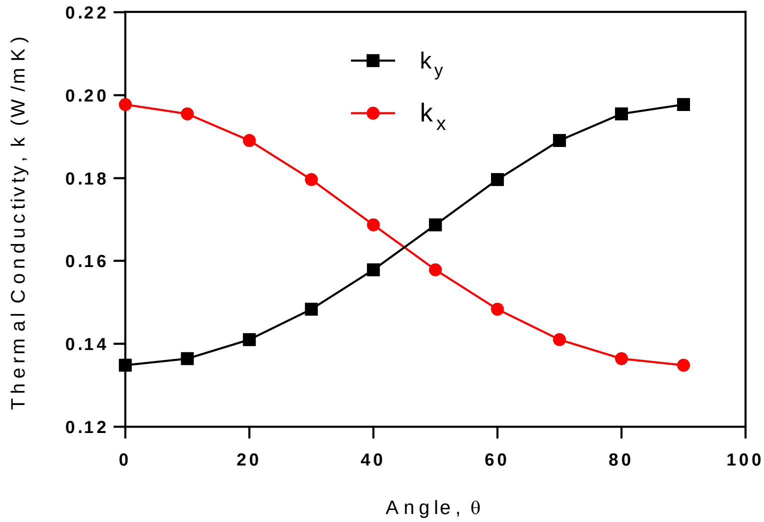

Figure 2-14. The effect of changing the printing angle on the thermal conductivity of FFF 3D-printed samples in x and y directions for cross-hatched layer configuration.

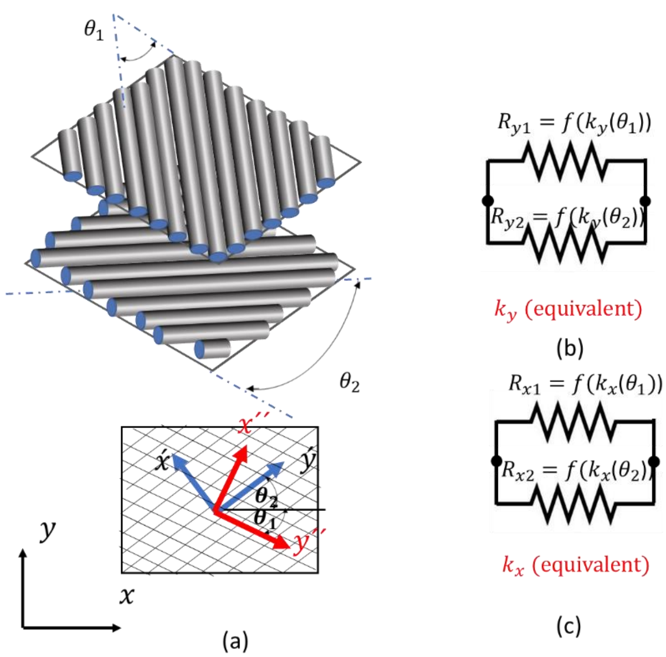

Figure 2-15: Thermal conductivity modeling for cross-hatched layer sample in x and y directions.

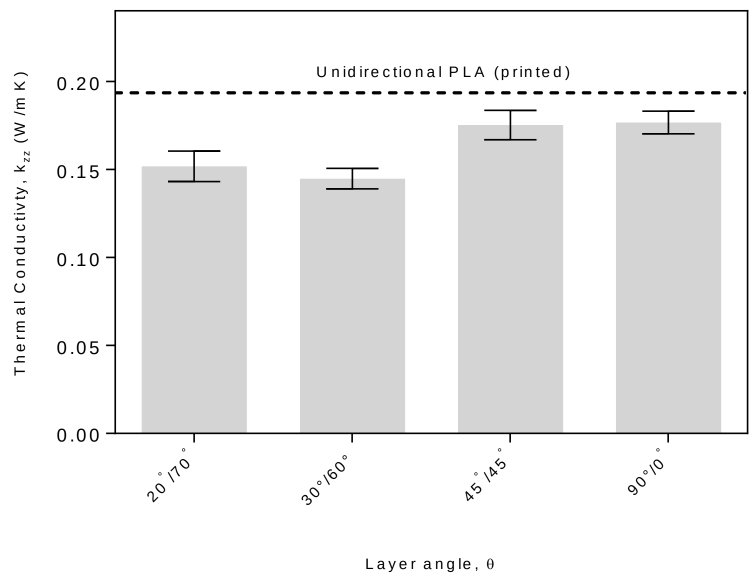

Figure 2-16. Thermal conductivity in z-direction for FFF 3D-printed cross-hatched layer sample.

2.5.6 Effect of Fill Ratio

The last important parameter to be studied was the fill ratio; this is the polymer volume percentage relative to the part volume. This is achieved through intentionally increasing hatch distance between the rasters, i.e., negative overlap. Five samples were printed and tested from pure PLA at 45°/-45° angles with different polymer percentages ranging from 30% to 100%. Figure 2-17 shows the fill ratio effect on the effective thermal conductivity in z-direction. The dash line in this figure represents the thermal conductivity of the pure polymer. The 100% fill sample had a lower thermal conductivity compared with pure polymer due to the generated voids between rasters, as discussed previously in Section 2.5.1. Decreasing the fill ratio has a negative impact on the thermal conductivity in the z-direction, which can reach up to 63% reduction compared with 100%, and 70 % reduction compared to pure polymer due to air volume fraction increase.

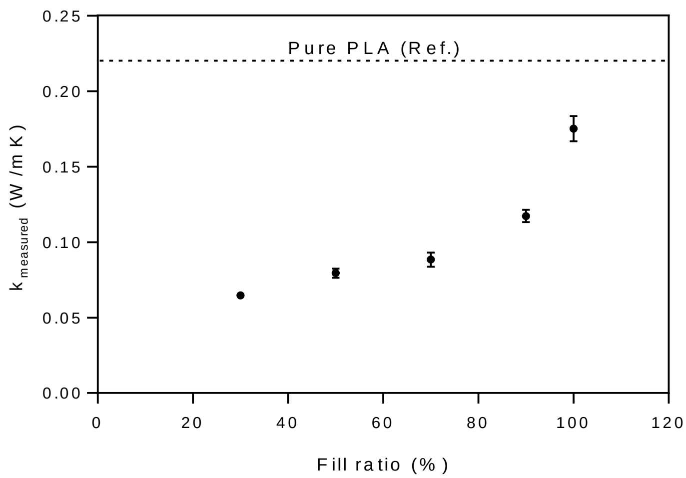

Figure 2-17. Effect of fill ratio on the thermal conductivity of FFF 3D-printed samples in *z*-direction for pure PLA. The dashed line in the figure represents the thermal conductivity of the pure bulk polymer printed with high overlap in Section 2.4.

2.5.7 Polymer Composite

The effective thermal conductivity of several commercially available PLA composite filaments was characterized experimentally by printing unidirectional samples at a layer height of 0.15 mm and raster width of 0.4 mm. Four metal PLA composite filaments were purchased from Sainsmart with different filler types; bronze, brass, copper, and aluminum. Two additional carbon fiber composite filaments (from Robo3D [36] and Proto-Pasta [37]) were measured. Table 2-5 shows the specifications for each filament.

Table 2-5. Materials specifications for FFF 3D-printed composite samples.

Filament	Supplier	Filler Fraction (%)
Pure PLA	Filaments.ca	0
Metal Composites (aluminum, copper, bronze, brass)	Sainsmart	20% (volume-based)
Carbon Fiber (Robo 3D)	Robo3d	unknown
Carbon Fiber (Protopasta)	Proto-pasta	<14.25 (Weight-based)

The samples were prepared in the same manner as shown previously in Section 2.2. It was postulated that thermal conductivity in printing direction (y direction) should be higher than the other directions because the fillers tend to align in the direction of the raster [23], and this may help increase filler connectivity. The thermal conductivity was measured in the y and z directions for these composites and compared with pure PLA, as shown in Figure 2-18. To help interpret these results, the samples were sectioned in two different planes to understand filler distribution in the rasters subsequent to printing. A cross-section of the y-direction is shown in Figure 2-19, and another perpendicular cross-section of the x-direction is shown in Figure 2-20.

As can be seen in Figure 2-18, the thermal conductivity in the z-direction for metallic composites is relatively similar, irrespective of filler type, which indicates that the fillers are poorly connected in the z direction. This imposes a huge thermal interface resistance between the filler and the matrix, compared with the filler resistance, and this indicates that the filler concentration is small and did not reach the percolation limit wherein the fillers form a connected network through the matrix [38]. The carbon fiber composite (Proto-Pasta) has the highest thermal conductivity, representing approximately a 26% increase in thermal conductivity over pure PLA. The carbon fibers inside the matrix are clearly seen to have a cylindrical surface inside the matrix, especially for the Robo3D sample (Figure 2-20).

Another factor that plays a significant role in reducing the thermal conductivity in this direction, besides filler discontinuity, is the porosity generation inside the printed traces, as highlighted by red circles in Figure 2-19. In the printing direction, y-direction, the thermal conductivity showed a reasonable increase for all the samples, especially in the case of carbon fiber which reached up to 162 % compared with pure PLA because the extrusion through the nozzle helped to orient the fillers. This illustrates that the carbon fibers are partially connected compared with the metallic fillers; this is clearly shown in Figure 2-20.

Although the thermal conductivity of metallic fillers is different, there is virtually no corresponding effect on the effective thermal conductivity of the printed composite. This is because the effective thermal conductivity is not only affected by the thermal conductivity of the fillers, but some other factors play an essential role, such as how the fillers are connected, fillers shape, their distribution, their orientation, contact resistance between the two phases, and the resulting voids originating from the filament fabrication. We conjecture that the aluminum composite had a higher thermal conductivity in y-direction despite having lower filler thermal conductivity than copper for one of the abovementioned reasons.

Post-processing techniques such as vapor finish for polymer or sintering for composite filaments can help in boosting the thermal conductivity. Sintering the printed composite part can help to connect the fillers to each other, forming a network of conductive paths for heat flow. Ebrahimi et al. [39] studied the sintering effect on the thermal conductivity only for copper composite. It was demonstrated that sintering improved the effective thermal conductivity by order of magnitude compared with non-sintered samples.

Vapor finishing techniques can be used to smooth outer surfaces of the printed parts and help lower thermal contact resistance with adjacent components; however, it is unclear what effect this would on the interior geometry and thus the effective thermal conductivity of the printed parts.

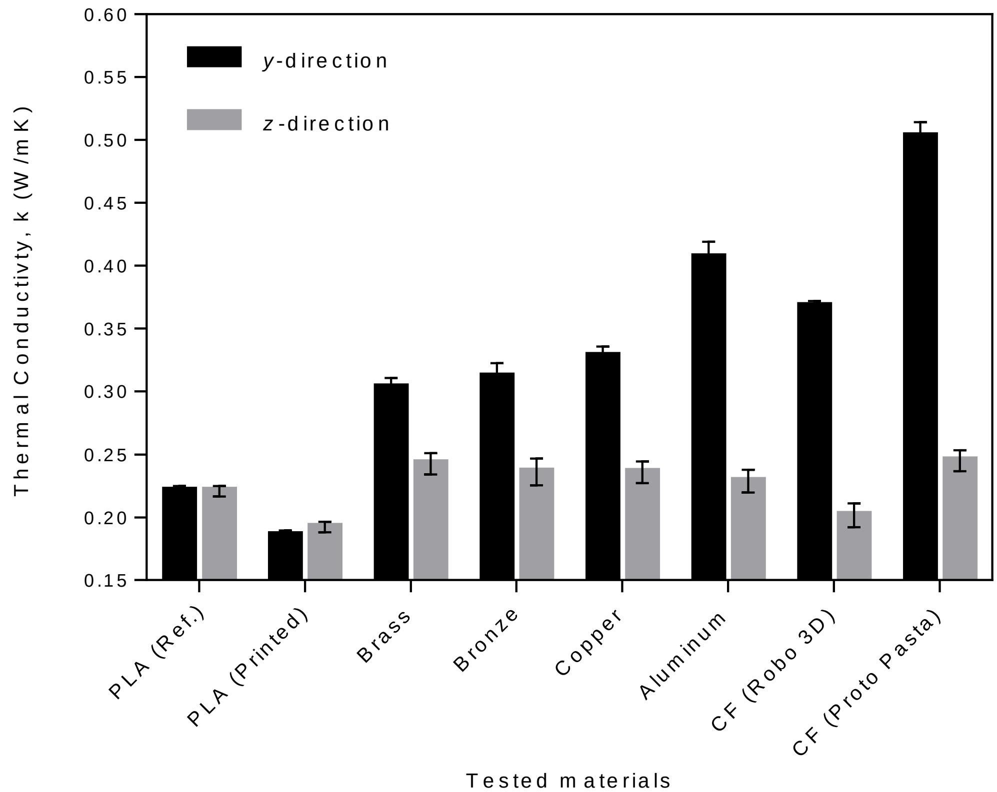

Figure 2-18. Thermal conductivity in *z*-direction for several FFF 3D-printed PLA composites.

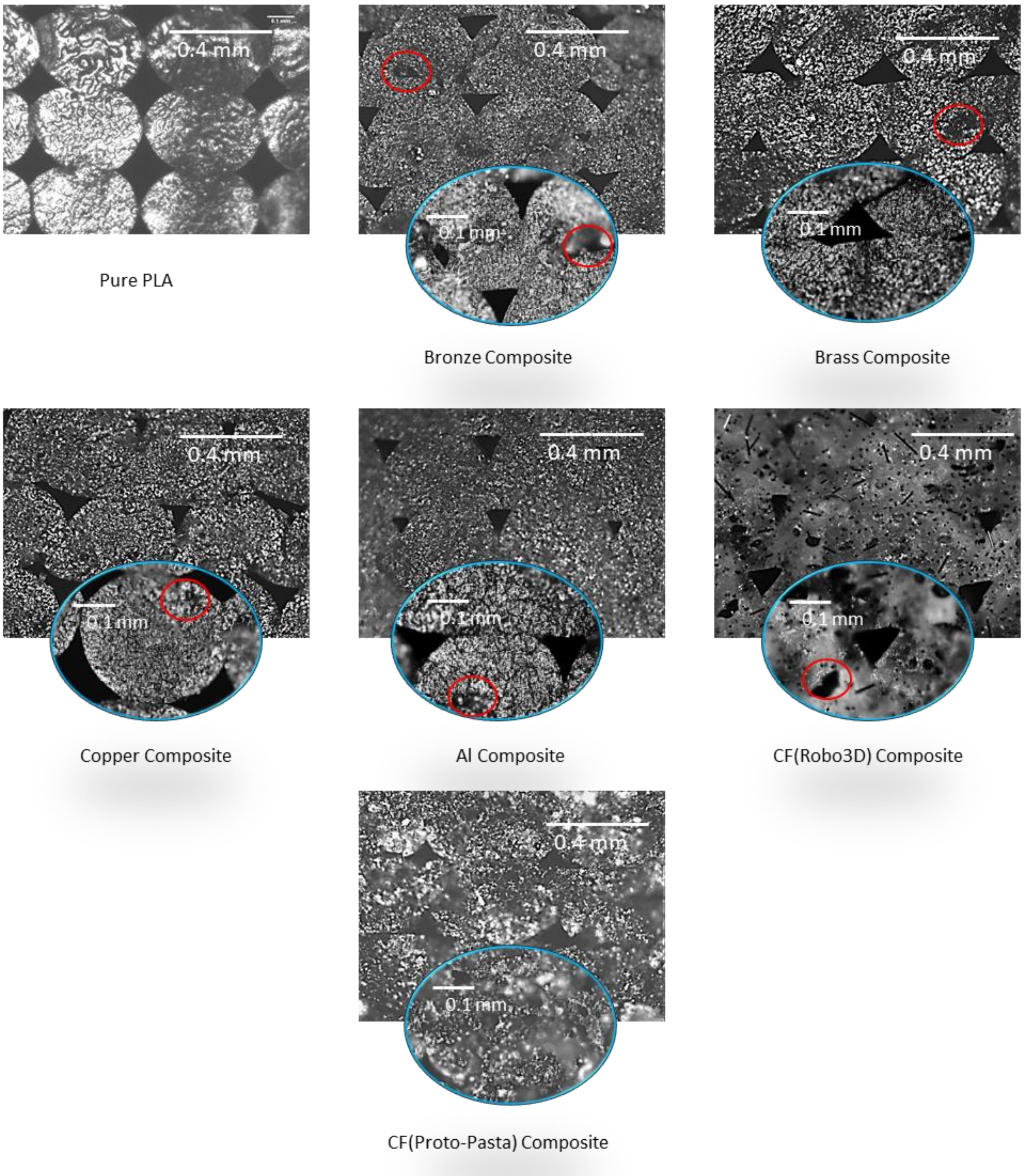

Figure 2-19. Microscopic images for several FFF 3D-printed PLA composites perpendicular to y-direction.

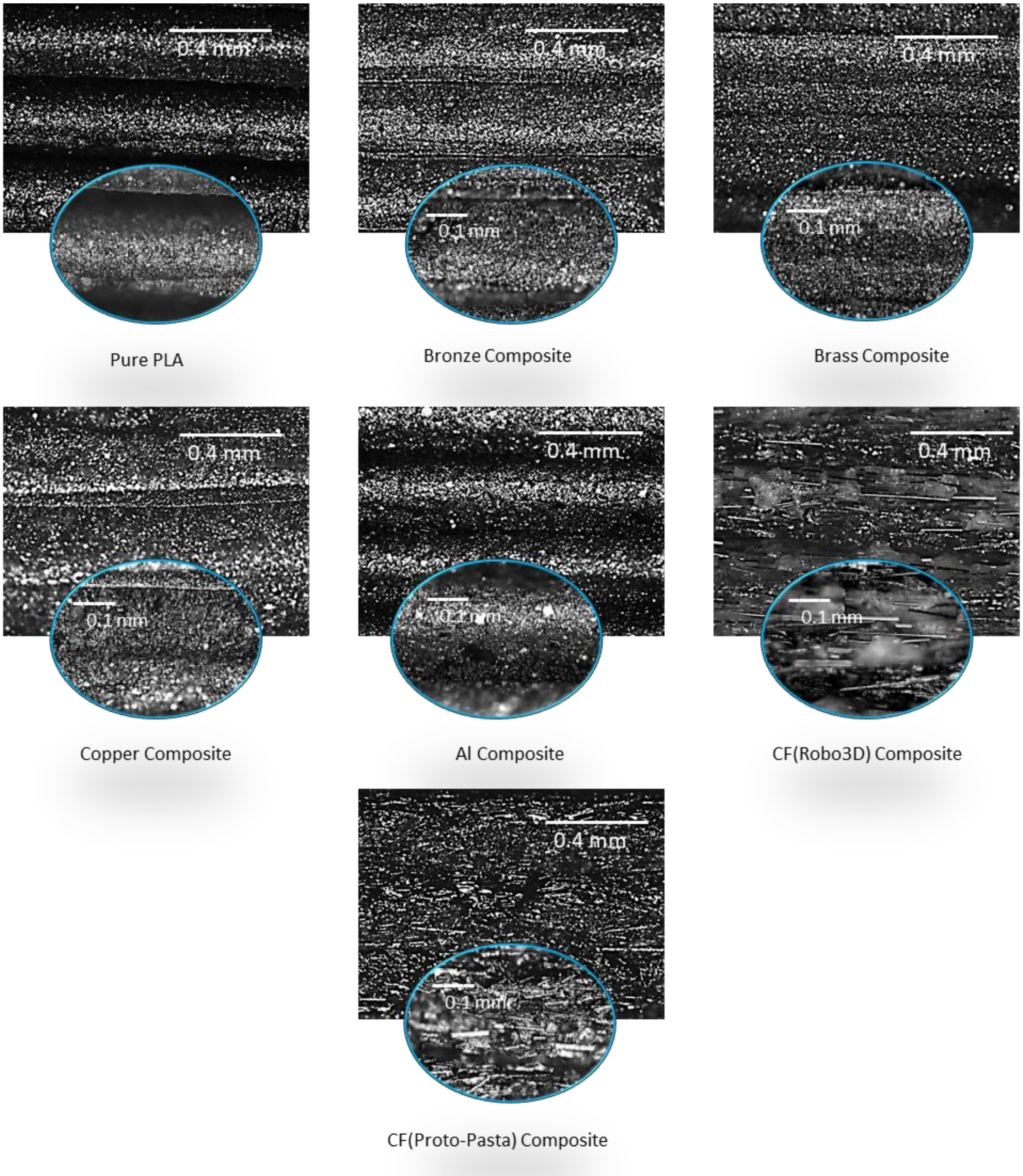

Figure 2-20. Microscopic images for several FFF 3D-printed PLA composites perpendicular to x-direction.

2.6 Summary and Conclusions

This work examined the influence of FFF process parameters on the anisotropic thermal properties of unidirectional 3D-printed parts. An experimental facility was developed to measure the effect of the layer height and raster width on the thermal conductivity in the z-direction and validate a numerical model that was subsequently used, along with an analytical model, to characterize the thermal conductivities in all directions for the unidirectional 3D-printed parts. The thermal performance of the unidirectional samples was used as a baseline dataset to construct a general model able to predict the conductivity of cross-hatched layer configuration at any angle, in addition to investigating the infill ratio effect for this configuration. These modeling approaches can be applied and extended to other 3D-printed geometries or composite printing techniques, especially those which achieve improved effective thermal conductivities such as continuous wire printing [24],[25], continuous fiber-reinforced composite [26],[27], or low melting temperature metals [40], which are all based upon FFF and show good potential for a range of heat exchange applications. Lastly, we examined the anisotropic ratio for some of the commercially available polymer composite filaments also printed in a unidirectional form. The main outcomes can be summarized in the following points:

- Increasing either the layer height or raster width reduces thermal conductivity in all directions as a result of porosity generation.
- The effect of raster width is more significant than the layer height, especially when a layer disconnection problem exists.
- Increasing the layer height while keeping the raster width constant at 0.4 mm results in a drop in the thermal conductivity, which reaches 42%, 14%, and 28% reduction in x, y, and

z directions, respectively, compared with the pure polymer.

- Increasing the raster width at a constant layer height of 0.15 mm, leads to a decline in thermal conductivity, which reaches reduction percentages of 65%, 28%, and 25% in x, y, and z directions, respectively, at a raster width in the layer of 0.8 mm.
- Decreasing the fill ratio for the samples with cross-hatched layer configuration decreases the thermal conductivity in the z-direction, which can reach up to 63% at 30% infill ratio compared with 100% infill due to the porosity fraction growth.
- The polymer composite results showed a reasonable increase in the thermal conductivity, particularly for the carbon fiber filler, which achieved 26% and 162% improvement in z and y directions, respectively, compared with pure polymer. The second direction achieved a higher percentage due to the shear effect happening during the filament extrusion; this tends to orient the fibers and hence help to produce a connected network of the fibers and boost the material heat transfer capability.

2.7 References

[1] N. S. A. Bakar, M. R. Alkahari, and H. Boejang, “Analysis on Fused Deposition Modelling Performance,” J. Zhejiang Univ. Sci. A, vol. 11, no. 12, pp. 972–977, 2010, doi: 10.1631/jzus.A1001365.

[2] J. Santhakumar and R. Maggirwar, “Enhancing Quality of Fused Deposition Modeling Built Parts by Optimizing the Process Variables Using Polycarbonate Material,” vol. 9, no. 37, pp. 173–181, 2016.

[3] B. N. Turner and S. A. Gold, “A review of melt extrusion additive manufacturing processes: II. Materials, dimensional accuracy, and surface roughness,” Rapid Prototyping Journal, vol. 21, no. 3. pp. 250–261, 2015, doi: 10.1108/RPJ-02-2013-0017.

[4] W. Wu, P. Geng, G. Li, D. Zhao, H. Zhang, and J. Zhao, “Influence of layer thickness and raster angle on the mechanical properties of 3D-printed PEEK and a comparative mechanical study between PEEK and ABS,” Materials (Basel)., vol. 8, no. 9, pp. 5834–5846, 2015, doi: 10.3390/ma8095271.

[5] J. Cantrell et al., “Experimental Characterization of the Mechanical Properties of 3D-Printed ABS and Polycarbonate Parts,” Univ. Florida, 2011, doi: 10.1007/978-3-319-41600-7_11.

[6] G. Percoco, F. Lavecchia, and L. M. Galantucci, “Compressive properties of FDM rapid prototypes treated with a low cost chemical finishing,” Res. J. Appl. Sci. Eng. Technol., vol. 4, no. 19, pp. 3838–3842, 2012.

[7] K. M. Ashtankar, A. M. Kuthe, and B. S. Rathour, “Effect of build orientation on mechanical properties of rapid prototyping (fused deposition modelling) made acrylonitrile butadiene styrene (abs) parts,” in Proceedings of the ASME 2013 International Mechanical Engineering Congress and Exposition, 2017, pp. 1–7.

[8] A. Arivazhagan, A. Saleem, S. H. Masood, M. Nikzad, and K. A. Jagadeesh, “Study of Dynamic Mechanical Properties of Fused Deposition Modelling Processed,” Int. J. Eng. Res. Appl., vol. 7, no. 3, pp. 304–312, 2014, doi: 10.3844/ajeassp.2014.304.312.

[9] D. Olivier, S. Borros, and G. Reyes, “Influence of building orientation on failure mechanism and flexural properties of,” vol. 00, 2010.

[10] R. A. Jadav and B. Solanki, “Investigation on Parameter Optimization of Fused Deposition Modeling (FDM) for Better Mechanical Properties – A Review,” IJSRD -International J. Sci. Res. Dev., vol. 3, no. 01online, pp. 2321–613, 2015, [Online]. Available: www.ijsrd.com.

[11] K. Álvarez, R. F. Lagos, and M. Aizpun, “Investigating the influence of infill percentage on the mechanical properties of fused deposition modelled ABS parts,” Ing. e Investig., vol. 36, no. 3, p. 110, 2016, doi: 10.15446/ing.investig.v36n3.56610.

[12] M. Nikzad, S. H. Masood, and I. Sbarski, “Thermo-mechanical properties of a highly filled polymeric composites for Fused Deposition Modeling,” Mater. Des., 2011, doi: 10.1016/j.matdes.2011.01.056.

[13] M. Nikzad, S. H. Masood, I. Sbarski, and a Groth, “Thermo-Mechanical Properties of a Metal-filled Polymer Composite for Fused Deposition Modelling Applications,” 5th Australas. Congr. Appl. Mech. ACAM 2007, vol. 1, no. December, pp. 319–324, 2007, [Online]. Available: http://espace.library.uq.edu.au/view/UQ:132173.

[14] S. Hwang, E. I. Reyes, K. sik Moon, R. C. Rumpf, and N. S. Kim, “Thermo-mechanical Characterization of Metal/Polymer Composite Filaments and Printing Parameter Study for Fused Deposition Modeling in the 3D Printing Process,” J. Electron. Mater., vol. 44, no. 3, pp. 771–777, 2015, doi: 10.1007/s11664-014-3425-6.

[15] S. H. Masood and W. Q. Song, “Assembly Automation Thermal characteristics of a new metal/polymer material for FDM rapid prototyping process Thermal characteristics of a new metal/polymer material for FDM rapid prototyping process,” Assem. Autom. Rapid Prototyp. J. Iss Rapid Prototyp. J., vol. 25, no. 11, pp. 309–315, 2002, [Online]. Available: http://dx.doi.org/10.1108/01445150510626451.

[16] J. Laureto, J. Tomasi, J. A. King, and J. M. Pearce, “Thermal properties of 3-D printed polylactic acid-metal composites,” Prog. Addit. Manuf., vol. 2, no. 1–2, pp. 57–71, 2017, doi: 10.1007/s40964-017-0019-x.

[17] D. S. Smith et al., “Thermal conductivity of porous materials,” J. Mater. Res., vol. 28, no. 17, pp. 2260–2272, 2013, doi: 10.1557/jmr.2013.179.

[18] Y. P. Mamunya, V. V. Davydenko, P. Pissis, and E. V. Lebedev, “Electrical and thermal conductivity of polymers filled with metal powders,” Eur. Polym. J., vol. 38, no. 9, pp. 1887–1897, 2002, doi: 10.1016/S0014-3057(02)00064-2.

[19] R. Landauer, “The electrical resistance of binary metallic mixtures,” J. Appl. Phys., vol. 23, no. 7, pp. 779–784, 1952, doi: 10.1063/1.1702301.

[20] C. Shemelya et al., “Anisotropy of thermal conductivity in 3D printed polymer matrix composites for space based cube satellites,” Addit. Manuf., vol. 16, pp. 186–196, 2017, doi: 10.1016/j.addma.2017.05.012.

[21] T. L. Flaata, Tiffaney, Gregory J. Michna, “Thermal conductivity testing apparatus for 3d printed materials thermal conductivity testing apparatus for 3d printed materials,” no. July, 2017.

[22] H. Prajapati, D. Ravoori, R. L. Woods, and A. Jain, “Measurement of anisotropic thermal conductivity and inter-layer thermal contact resistance in polymer fused deposition modeling (FDM),” Addit. Manuf., vol. 21, no. November 2017, pp. 84–90, 2018, doi: 10.1016/j.addma.2018.02.019.

[23] M. L. Shofner, K. Lozano, F. J. Rodríguez-Macías, and E. V. Barrera, “Nanofiber-reinforced polymers prepared by fused deposition modeling,” J. Appl. Polym. Sci., vol. 89, no. 11, pp. 3081–3090, 2003, doi: 10.1002/app.12496.

[24] Y. Ibrahim, Garrett W. Melenka and Roger Kempers, “Additive Manufacturing of Continuous Wire Polymer Composites,” Manuf. Lett., vol. 16, no. April, pp. 49–51, 2018, doi: 10.1016/j.mfglet.2018.04.001.

[25] K. R. Ibrahim Yehia, . Melenka Garrett W, “Fabrication and Tensile Testing of 3D Printed Continuous Wire Polymer Composites,” Rapid Prototyp. J., 2018, doi: 10.1108/RPJ-11-2017-0222.

[26] C. Yang, X. Tian, T. Liu, Y. Cao, and D. Li, “3D printing for continuous fiber reinforced thermoplastic composites : mechanism,” Rapid Prototyp. J., 2017, doi: 10.1108/RPJ-08-2015-0098.

[27] F. Zhang, G. Ma, and Y. Tan, “The Nozzle Structure Design and Analysis for Continuous Carbon Fiber Composite 3D Printing,” vol. 136, no. Icadme, pp. 193–199, 2017.

[28] X. Tian, T. Liu, C. Yang, Q. Wang, and D. Li, “Interface and performance of 3D printed continuous carbon fiber reinforced PLA composites,” Compos. Part A Appl. Sci. Manuf., vol. 88, pp. 198–205, 2016, doi: 10.1016/j.compositesa.2016.05.032.

[29] M. Namiki, M. Ueda, A. Todoroki, Y. Hirano, and R. Matsuzaki, “3D printing of continuous fiber reinforced plastic,” in International SAMPE Technical Conference, 2014, pp. 187–196.

[30] J. R. C. Dizon, A. H. Espera, Q. Chen, and R. C. Advincula, “Mechanical characterization of 3D-printed polymers,” Addit. Manuf., vol. 20, pp. 44–67, 2018, doi: 10.1016/j.addma.2017.12.002.

[31] H. Y. Ng, X. Lu, and S. K. Lau, “Thermal conductivity of boron nitride-filled thermoplastics: Effect of filler characteristics and composite processing conditions,” Polym. Compos., vol. 26, no. 6, pp. 778–790, 2005, doi: 10.1002/pc.20151.

[32] R. Kempers, P. Kolodner, A. Lyons, and A. J. Robinson, “A high-precision apparatus for the characterization of thermal interface materials,” Rev. Sci. Instrum., vol. 80, no. 9, 2009, doi: 10.1063/1.3193715.

[33] ASTM C177, “Standard Test Method for Steady-State Heat Flux Measurements and Thermal Transmission Properties by Means of the Guarded-Hot-Plate,” ASTM Int., pp. 1–23, 2013, doi: 10.1520/C0177-13.2.

[34] S. J. Kline, “Describing uncertainty in single sample experiments,” Mech. Eng., vol. 75, pp. 3–8, 1953.

[35] ANSYS, “ANSYS Fluent Theory Guide,” ANSYS 16 Documentation, vol. 15317, no. July. p. 80, 2015, doi: 10.1016/0140-3664(87)90311-2.

[36] “Specialty Filament | ROBO 3D.” https://robo3d.com/collections/filament-exotic (accessed Aug. 07, 2018).

[37] “Proto-pasta 3D Printer Filament Made by the Makers at ProtoPlant – ProtoPlant, makers of Proto-pasta.” https://www.proto-pasta.com/ (accessed Aug. 07, 2018).

[38] Y. P. Mamunya, V. V. Davydenko, P. Pissis, and E. V. Lebedev, “Electrical and thermal conductivity of polymers filled with metal powders,” Eur. Polym. J., 2002, doi: 10.1016/S0014-3057(02)00064-2.

[39] N. Dehdari Ebrahimi and Y. S. Ju, “Thermal conductivity of sintered copper samples prepared using 3D printing-compatible polymer composite filaments,” Addit. Manuf., vol. 24, no. August, pp. 479–485, 2018, doi: 10.1016/j.addma.2018.10.025.

[40] M. A. Gibson et al., “3D printing metals like thermoplastics: Fused filament fabrication of metallic glasses,” Mater. Today, vol. 21, no. 7, pp. 697–702, 2018, doi: 10.1016/j.mattod.2018.07.001.

Chapter 3 Characterization of the Thermal Conductivity of 3D-Printed Components by SLM[2]

This chapter characterises the effect of process parameters on the relative density of ALSi10Mg components fabricated by L-PBF to develop and understanding of how these parameter contribute to the thermal conductivity. Four parameters were investigated: the exposure time, laser power, pointwise distance, and build orientation. Overall, it was shown that these parameters can affect the effective thermal conductivity of the printed parts by up to 22%. The pointwise distance had the most considerable impact on the melt pool size and on the effective thermal conductivity compared to other parameters. As the pointwise distance increased, both the conductivity and the melt pool width decreased, whereas the laser power showed negligible effect on both. Also, the effect of exposure time was mainly dependent on the pointwise distance. We showed that thermal conductivity was not only related to the relative density of the samples, but also the intensity of the melt pool boundaries in the microstructure can play a significant role in interrupting the heat flow. A new factor that accounts for the number of melt pool boundaries per unit length in the direction of heat flow, was introduced to quantify the heat distraction associated with the microstructure evolution induced by the process parameters change. This helped understand the thermal conductivity behavior for samples with high energy densities, which had an almost negligible difference in the relative density.

[2] This chapter has been submitted as a peer-reviewed journal paper titled "Characterization and Analysis of the Thermal Conductivity of AlSi10Mg Fabricated by Selective Laser Melting" in *Additive Manufacturing*.

3.1 Introduction & Background

The microstructure of the 3D-printed parts fabricated via SLM is different from the conventionally cast parts due to the involved rapid localized heating and cooling processes, directly affecting the resulting physical properties. Depending on the printing parameters used, the mechanical and thermal properties can vary significantly. As a result, the research into the SLM AM has broadly gone into three directions: The first direction is the development of numerical models for simulating the SLM process at the macroscale for the whole printed part or at the mesoscale for the bead. This can help understand the temperature distribution and evolution associated with the manufacturing process and predict the resulting irregularities of the molten pool, residual stresses, and cold cracks [1]–[3]. The second direction has addressed optimization of printing parameters for improving the quality of the parts, including the dimensional accuracy [4], the surface roughness [5], and density [6], [7]. The third direction has investigated the effect of post-processing, such as heat treatment [8], [9] and hot isostatic pressing [10], [11], for eliminating the internal voids and enhancing the quality of the SLM-printed parts.

According to EOS company, the thermal conductivity of as-built components manufactured using their EOSINT M 280 machine and AlSi10Mg powder is 103 W/mK in the build direction, and 119 W/m K in the transverse direction. It was found that these values increased to 173 W/mK after the heat treatment for both directions [12], which is higher than the conventional aluminum 6061 alloy. To date, a few SLM-related studies have investigated the thermal properties of fabricated AlSi10Mg components. For instance, Yang et al. [13] examined the change of thermal properties, such as heat capacity, thermal expansion, thermal diffusivity, and thermal conductivity of AlSi10Mg parts with temperature and their correlation with the microstructural evolution. Their results indicated the as-built samples suffered from the lower thermal conductivity and diffusivity, due to the formation of the interconnected cellular structure of Al and Si. Strumza et al. [14] investigated the effect of the build orientation on the thermal conductivity, thermal capacity, and thermal diffusivity at temperatures ranging from room temperature to 550 °C. The anisotropic behaviour was evident in all thermal properties, which was found to be linked to some factors such as the preferred orientation of the aluminum grains and the non-uniform distribution of the pores at the melt pool boundaries.

Sélo et al. [15] investigated the effect of annealing and T6 heat treatment on the anisotropic thermal conductivity of AlSi10Mg solid samples and lattice structures. They demonstrated that heat treatment is an effective way to eliminate the anisotropy in the thermal conductivity, similar to its effect on the electrical resistivity [16]. Their results showed that the thermal conductivity increase is related to the microstructure change. Either the annealing or the heat treatment caused the breakdown of the low conductive cellular Si network into circular aggregates, which increased the α-Al matrix connectivity leading to better homogeneity and conductivity of the samples. Similarly, Hirata et al. [11] noticed the same change for the microstructure from fine dendritic cell to granular precipitated Si phases following the hot isostatic pressing (HIP) process. They highlighted this change to be the leading cause for ductility enhancement and tensile strength reduction. These investigations all used a different combination of process parameters, which is usually grouped into the metric parameter energy density. Oftentimes, this parameter is used to combine and optimize the process parameters in the literature, which can be calculated based on a volumetric or linear basis. However, the energy densities used vary from one study to another, which will be discussed here for its effect on the thermal behaviour of SLM 3D-printed components.

Also, most previous research was directed towards the mechanical properties or the impact of heat treatment. To the best of our knowledge, no results have yet been published regarding the influence of process parameters on the thermal conductivity of AlSi10Mg. Therefore, the aim of the current work is to investigate the relationship between the printing parameters and the thermal properties of AlSi10Mg parts. This is examined particularly by predicting the influence of the laser power, point distance, exposure time on the resulting microstructure, and the associated thermal conductivity of SLM- AlSi10Mg 3D-printed parts.

3.2 Experimental Method

3.2.1 Sample Preparation

Aluminum test blocks for the thermal conductivity tests described in Section 3.2.2 were manufactured using Laser Powder Bed Fusion (L-PBF) in a Renishaw AM400 system with a 400W pulsed laser with a 70 µm beam diameter. The LPBF process consists of a layer of metallic powder, in this case, Aluminium (AlSi10Mg) powder, being layered in 30 µm layers by a silicone re-coater blade. This layer is then melted in selected regions by the laser determined by the input slice files. Once the layer melting is complete, a new 30 µm layer is added, and the process is repeated layer-by-layer to manufacture the final test samples.

Samples were manufactured by varying the LPBF processing parameters as represented in Figure 3-1. Variations of these parameters results in varying energy densities being applied to the powder bed, resulting in samples of varying physical properties. The energy density of the samples tested was calculated using as:

$$E_d = \frac{P\ t}{d_p\ d_h\ d_t} \tag{3.1}$$

where P is the laser power, t is the exposure time when the laser is firing on a single location on the powder bed, d_p is the pointwise distance, d_h is the hatch spacing, and d_t is the layer thickness. The default build parameters for AlSi10Mg powder are shown in Table 2-2, with the resulting energy density calculated.

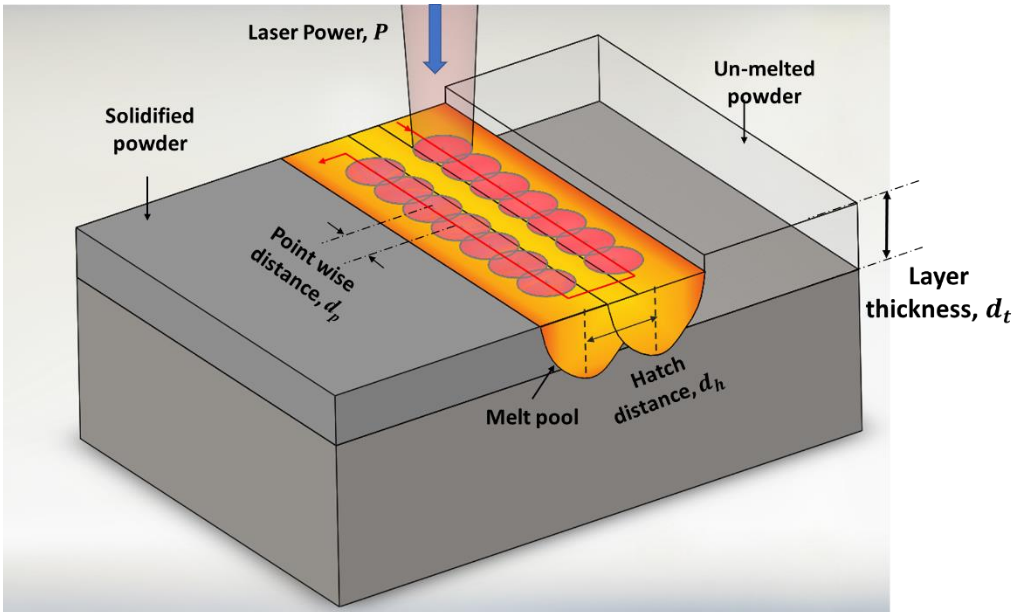

Figure 3-1. Tested process parameters.

Table 3-1. Default laser processing parameters for AlSi10Mg powder.

Parameter	Default Value
Laser Power, P	350 W
Exposure Time, t	40 µs
Point Distance, d_p	90 µm
Hatch Distance, d_h	80 µm
Layer Thickness, d_t	30 µm
Energy Density, E	64.81 J/mm^3

The aluminum powder, AlSi10Mg, used in the current study is a gas atomized powder material supplied by LPW Ltd., with chemical composition as shown in Table 3-2. The powder particle size distribution was determined using dry dispersion laser diffraction on a Microtrac S3500 as well as accompanying scanning electron microscopy (SEM) images from a Hitachi TM3030 Plus Tabletop SEM. Figure 3-2 shows the resulting powder particle size distribution and powder morphology.

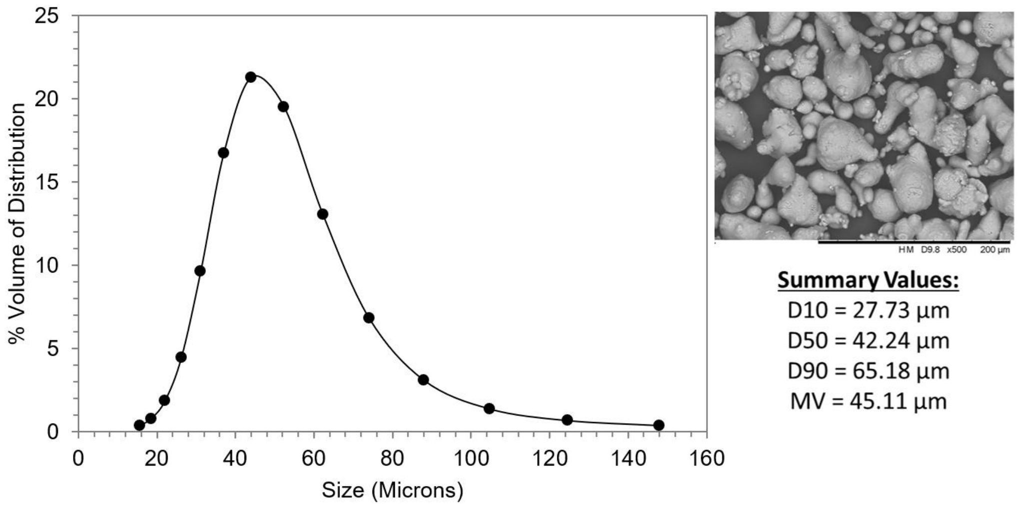

Figure 3-2. Powder particle size distribution and morphology.

Table 3-2. Powder chemical composition.

Element	Mass (%)
Aluminium, Al	Balance
Silicone, Si	9.00 to 11.00
Magnesium, Mg	0.25 to 0.45
Iron, Fe	<0.25
Oxygen, O	<0.20
Titanium, Ti	<0.15
Zinc, Zn	<0.10
Manganese, Mn	<0.10
Nickel, Ni	<0.05
Copper, Cu	<0.05
Lead, Pb	<0.02
Tin, Sn	<0.02

To vary the physical properties of the manufactured samples for testing, the energy density was varied by adjusting the laser power, P (W), exposure time, t (ms), and point distance, d_P (µm) applied to the powder bed. A total of 10 samples were manufactured with varying energy densities, as outlined in Table 3-3. Samples were manufactured in two orientations, Orientation A and Orientation B, as shown in Figure 3-3. The samples' ID in orientation A were given in ascending order according to the energy density, where Sample 1 was printed with the lowest energy density, in contrast to Sample 8, which had the maximum energy density.

Table 3-3. Tested sample manufacturing parameters and resulting energy densities.

Sample No.	**Laser Power, P (W)**	**Exposure time, t (μs)**	**Point Distance, d_p(μm)**	**Hatch Spacing, d_h(μm)**	**Layer Height, d_t (μm)**	**Energy Density, E_d (J/mm^3)**	**Orientatio n**	**Comment**
1	350	25	80	30	80	45.57	A	
2	250	40	90	30	80	46.29	A	
3	350	20	60	30	80	48.61	A	Lack of Fusion
4	350	30	90	30	80	48.61	A	
5	350	40	110	30	80	53.03	A	
6	350	40	100	30	80	58.33	A	
7	350	40	90	30	80	64.8	A	
8	350	40	80	30	80	72.9	A	
9	350	20	60	30	80	48.61	B	
10	350	40	90	30	80	64.81	B	

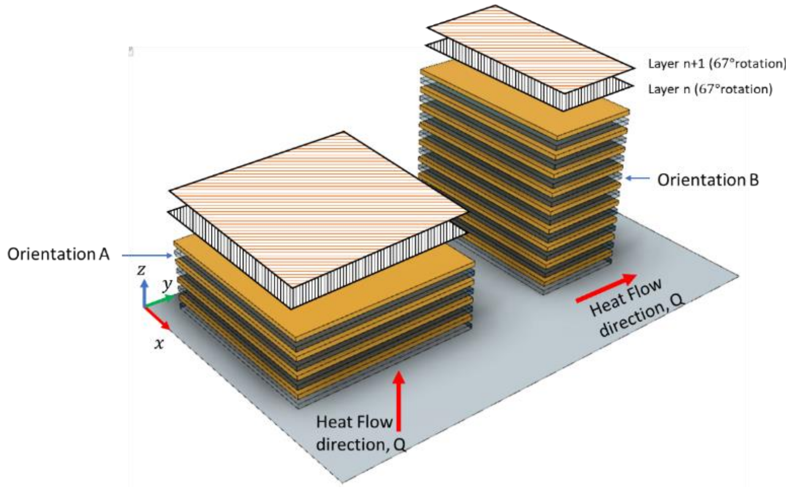

Figure 3-3. Two different print orientations to measure the thermal conductivity in both directions: (a) in-plane, (b) through-plane.

It should be noted that Sample 3 was not manufactured due to the lack of fusion during the build process, resulting in the sample being canceled mid-build. This lack of fusion was due to the large cross-section being melted in Orientation A and the short exposure time resulting in the layer not being fully fused to the previous layer. However, Sample 9, which had the same energy density and parameters, did build successfully due to the smaller cross-section of Orientation B compared to the cross-section of Orientation A samples.

3.2.2 Experimental Measurement of Effective Thermal Conductivity

The effective thermal conductivity of the samples is measured using the apparatus developed in [17], which is modified implantation of the guard hot plate method detailed in ASTM C177 [18]. Figure 3-4 depicts a schematic outlining the main components of this apparatus, along with the instrumentation and control layout. The input thermal power is provided electrically through four cartridge heaters embedded into the primary heating block, which is consequently transferred through the sample to the primary cooling block. To achieve the isothermal conditions within each block and ensure that no heat leaks from the primary heating block to the ambient, the primary blocks are surrounded by a secondary guard block.

Upon achieving the isothermal conditions, the thermal resistance of the sample is calculated as given by:

$$R_{meas} = \frac{(T_a - T_b)}{Q} \tag{3.2}$$

where $(T_a - T_b)$ is the measured temperature gradient within the sample and Q is the input power measured electrically ($Q = IV$). The temperature gradient through the sample is measured using two well-calibrated RTDs (1PT100KN1510) placed 15 mm apart through the sample thickness, as shown in Figure 3-4. Thus, the effective thermal conductivity is determined by simplifying (3.2) as:

$$k_{sample} = \frac{L}{A\left[\frac{(T_a - T_b)}{Q}\right]} \tag{3.3}$$

where L is the distance between the RTDs, and A is the sample cross-sectional area perpendicular to the heat flow.

All blocks are machined from copper, where the cross-sectional area of both primary blocks is 40 mm x 40 mm. The input power to the secondary heating block is independently tuned until its temperature is identical to the primary block. The tested sample is sandwiched between the primary heating and cooling blocks under high pressure of 0.3 MPa with using a clamping mechanism. A load cell (KAF-S, AST, Dresden, Germany) is used to measure the clamping pressure. The whole stack is wrapped with mineral wool insulation with thermal conductivity of 0.032 W/mK to further minimize ambient heat loss or sample bypass.

The temperature of each block was measured at three locations using Omega RTDs (1PT100KN1510), denoted by black circles in Figure 3-4, to ensure the isothermal conditions between the primary and secondary blocks at both sides of the apparatus: the hot side and the cold side. Each RTD is 1 mm in diameter and 15 mm in length. All RTDs are calibrated in an isothermal chamber, a reference RTD (Fluke PRT Model: 5606). Additional details regarding the experimental facility, instrumentation, and control layout are provided in [17], and Chapter 2.

Prior to testing, a drop of mineral oil is applied to the sample surfaces to minimize the contact resistance. Each sample is measured three times to ensure the results repeatability is within the apparatus uncertainty. All the samples are tested at input power to the primary heating block of 40 W to create a reasonable temperature across the sample that can be accurately measured.

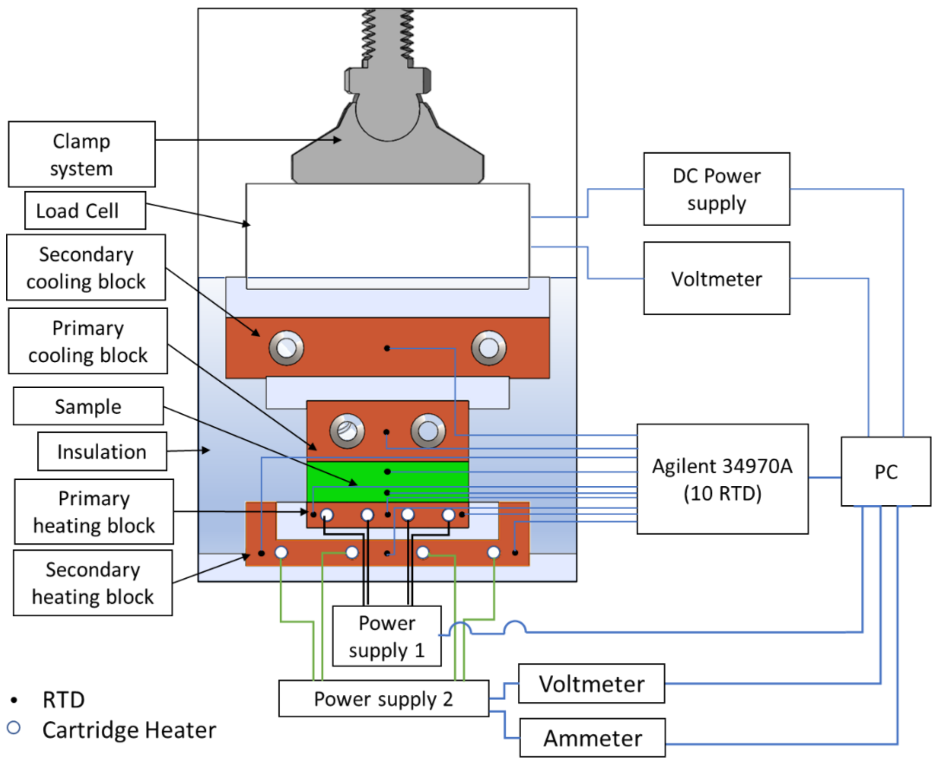

Figure 3-4. Schematic of the used thermal conductivity apparatus along with the instrumentation layout.

3.2.3 Density and Microstructure Characterization

The sample density was determined by micro-sectioning the density cubes built using the energy densities corresponding to the test samples shown in Table 3-3.

Samples were potted in epoxy resin and ground and polished to reveal a cross-section of these density cubes. These polished cross-sections were then imaged using a Keyence digital microscope at a magnification of 500x. This allows for the internal pores to be identified and quantified in terms of size, shape, and number of pores. The analysis of the internal pores is completed using ImageJ image analysis software [19]. This process of the image analysis of the internal porosity is shown in Figure 3-5.

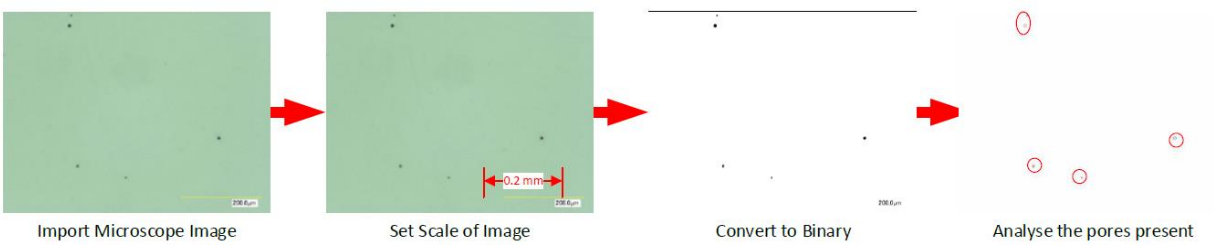

Figure 3-5.Sample image analysis process for density measurement.

The microstructure as-built samples were revealed using an etchant comprising of five parts de-ionized water (H_2O), four parts nitric acid (HNO_3), and one-part hydrofluoric acid (HF). This was applied to the polished micro-section of the samples for 10 seconds to reveal the microstructure of the samples in the build direction, i.e., the z-direction, as shown in Figure 3-3. The resulting microstructure was captured using optical microscopy at a magnification of 200x. The width of the laser tracks can then be measured for the varying laser parameters outlined in Table 3-3.

3.2.4 Chemical Composition

The bulk chemical composition of the as build parts was confirmed using optical emission spectroscopy (OES). In this method, a sample of the as-built AlSi10Mg material is subjected to high energy, whereby an electrical charge is applied to the surface of the metal sample, which vaporizes a small quantity of the surface. The discharged vapors create a distinct chemical signature which is then analyzed to determine the elemental breakdown of the sample. The chemical composition from two of the samples, listed in Table 3-3, was determined by OES. Sample 9 and 10 were testes as they had the highest and lowest energy density applied to them during manufacture. Prior to testing, the samples were prepared by grinding the surface using a silicone-free abrasive pad to smooth the sample surface.

3.3 Results and Discussion

3.3.1 Sample Density Measurements

Figure 3-6 depicts the internal porosity present in the samples manufactured. The samples and corresponding images are identified as per the Sample ID listed in Table 3-3 above. The black regions shown in the cross-sectional images are the internal pores present within the manufactured parts. The porosity is dependant on the applied energy densities and chosen laser processing parameters.

It is clear from the microscopic images that there is porosity present within all the manufactured samples; however, the size, shape, and distribution of these pores vary depending on the energy density applied in the LPBF process. The samples' density is plotted against the energy density in Figure 3-7. Here, the sample density is represented as a percentage of the theoretical density of a sample containing no internal porosity (i.e., a 100% dense sample).

Figure 3-7 shows a change in the density of the samples due to the difference in the input energy densities; however, this change is minor for most samples. Sample 1 does show the lowest density. This sample was processed using the lowest energy density of 45.57 J/mm^3. As evident from the cross-section image of the sample shown in Figure 3-6, the porosity of this sample would appear to conform that the low energy density applied has created a part with a significant lack of fusion in the melting process. Sample 1 had a low exposure time of 25 μs and a default point distance of 80 μm; these result in a lack of melting and, therefore, the fusion between adjacent exposure points resulting in the low-density components and the porosity shown in Figure 3-6.

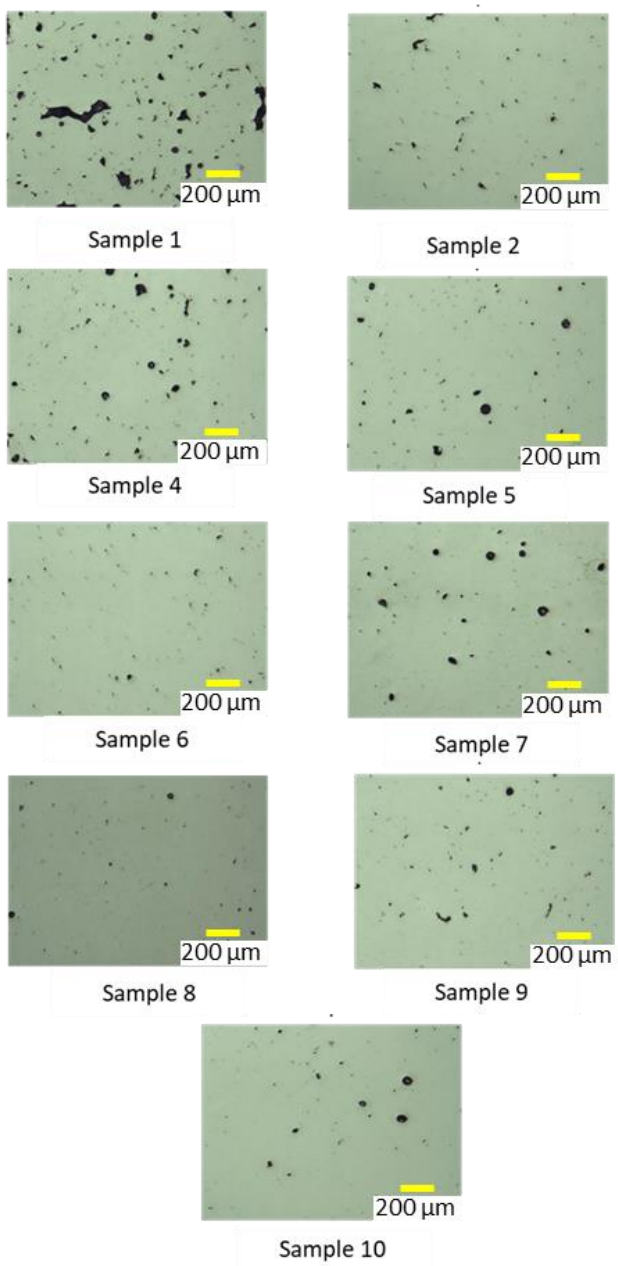

Figure 3-6. Optical microscopy (x100 magnification) of Internal porosity in the manufactured samples.

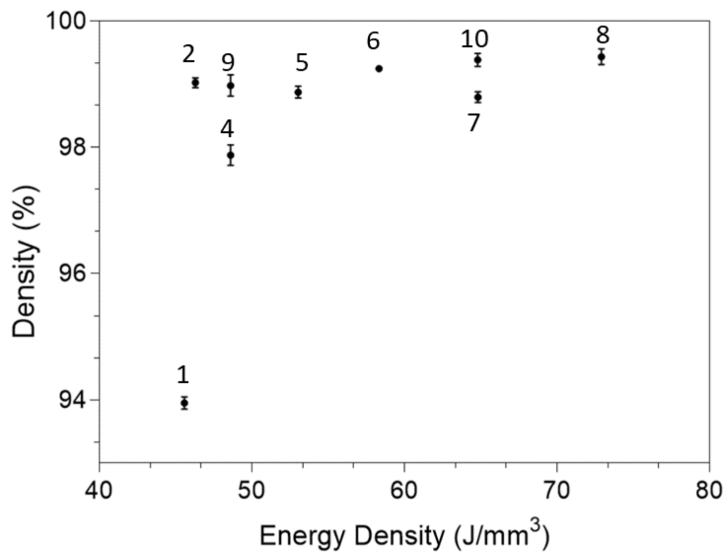

Figure 3-7. Manufactured relative part density with applied energy density.

3.3.2 Microstructure Analysis and Characterization

Altering the laser processing parameters and changing the energy density applied to the manufactured samples has been shown above to affect the porosity of the samples; however, this change in parameters also affects the microstructure of the samples. In particular, the geometry of the laser melt pools and tracks will vary. Figure 3-8 and Figure 3-9 show the microstructure after etchant has been applied for 10 seconds to the polished cross-section in the horizontal and vertical directions, respectively. The contours of the melt pool can be clearly seen in both figures, allowing for the width and depth of the tracks to be measured. The widths and depths of the melt tracks were measured using ImageJ image analysis software at five locations, and an average and standard deviation were calculated, as shown in Figure 3-10a.

The melt pools have a semicircular profile for most of the samples, which is a common feature of metals fabricated via SLM due to the high rates of cooling and solidification of the laser-scanned zones. However, the melt pools diverged from being semicircular shape for few samples, especially for Sample 1, which exhibited an elongated parabolic profile shape. The semicircular shape occurrence resulted from the pool melt melting conditions belonging to the so-called "conduction mode" known in laser welding, similar to what was found by [20] and predicted analytically by Eagar and Tsai model [21]. The difference in the melt pool profile for Sample 1 is not believed to be linked to the keyhole instability due to insufficiently supplied energy density, which was the minimum for this sample. If the associated profile with the melt pool in Sample 1 stemmed from the keyhole instability, then all the samples should demonstrate the same effect, which was not seen in Figure 3-9. This is reflected in the measured width and depth of the melt pool shown in Figure 3-10a, which were relatively high for Sample 1. A similar profile was seen by Karimi et al. [22] for printing with Alloy 718 for short exposure time and small pointwise distance, which is the same scenario for this sample. However, no specific reasons were reported for this phenomenon, which will be discussed later in this section.

The melt pool width showed a monotonic increase with energy density except for the first two samples, while there was no clear trend for the pool depth. This can be understood by investigating each input parameter separately, as shown in Figure 3-10b to Figure 3-10d. Each of these graphs indicates the parameter in interest while keeping all other parameters constant. The melt pool size was more sensitive to the pointwise distance than other parameters and exhibited a decreasing trend for both width and depth. The laser power showed almost no effect on both the melt pool depth and width, which contradicts the findings in [23], [24]. However, these studies were either experimenting with a single laser track or numerically modeling it at constant thermal conductivity, which may not be practically valid for a successive buildup of layers.

It can be concluded that pool width is mainly controlled only by the exposure time and the pointwise distance, as shown in Figure 3-10b and Figure 3-10c. It was observed that reducing the former or increasing the latter increases the pool width. Also, the pool depth cannot be considered a function of the laser power only without addressing the material bulk thermal conductivity being printed, which is a function of the number of pores and distribution.

These findings can explain why the melt pool profile change to an elongated parabolic profile for Sample 1. Comparing Sample 1 to Sample 8 in Figure 3-10a indicates that the pool width is higher for Sample 8 due to having a higher exposure time for the same power and pointwise distance. This shows that the laser power initially diffused in the vertical direction, and when the time is sufficient, it started to dissipate in the lateral direction forming the semicircular pattern. Or that means that heat resistance in the vertical direction was lower than the horizontal direction in Sample 1, which is believed to be directly linked to the higher density of pores. In terms of the pool height, it was expected to be similar due to supplying the same laser power; however, Sample 8 showed a smaller value. This is also connected to the lower void density in Sample 8, which increased its thermal diffusivity, facilitating the heat loss by conduction to the layers below, which in turn, reduced the effective power per unit volume of the pool melt and consequently decreased the resulting height. In other words, the melt pool boundaries are being established because of the heat diffusion mechanism, leading to a semicircular shape when having approximately equiaxial energy dispersion through the sample. One last remarkable feature is that the inherent nature of successive layer buildup present in the SLM process sometimes induces the merging of melt pools dissolving the boundaries in which the newly deposited layers overlapped and obfuscated the preceding layers.

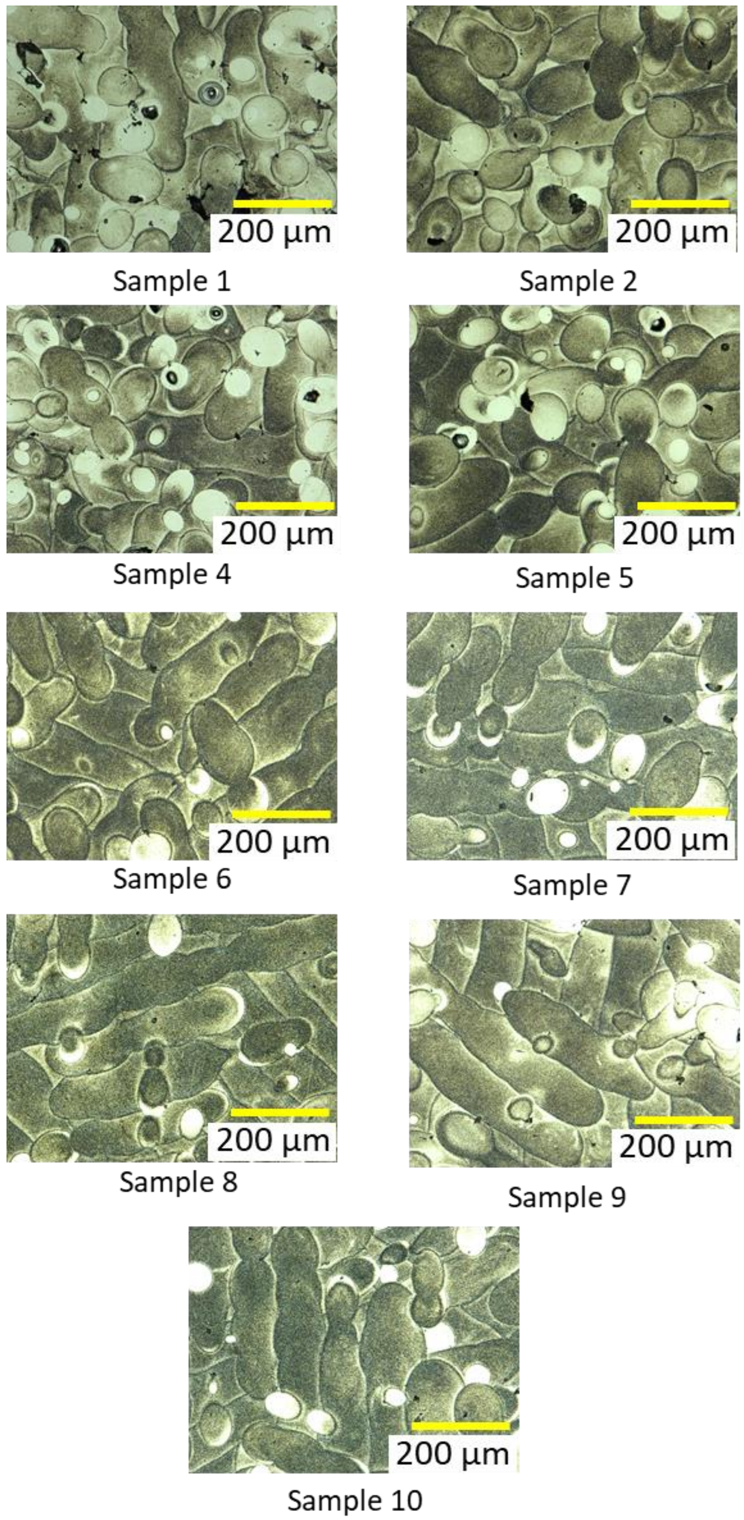

Figure 3-8. Optical microscopy (x500 magnification) images of the laser melt pools of the manufactured samples.

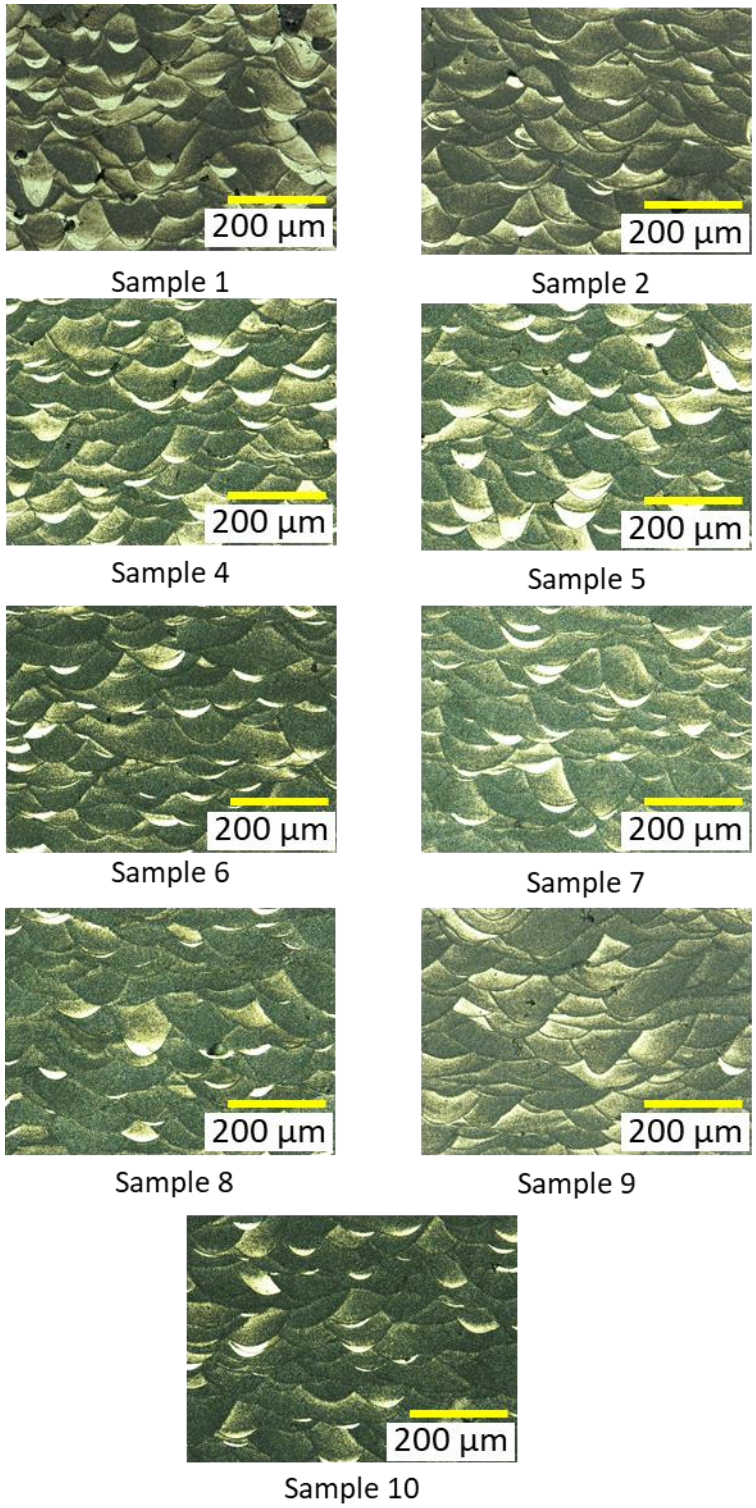

Figure 3-9. Microstructure of manufactured samples in the *z*-direction.

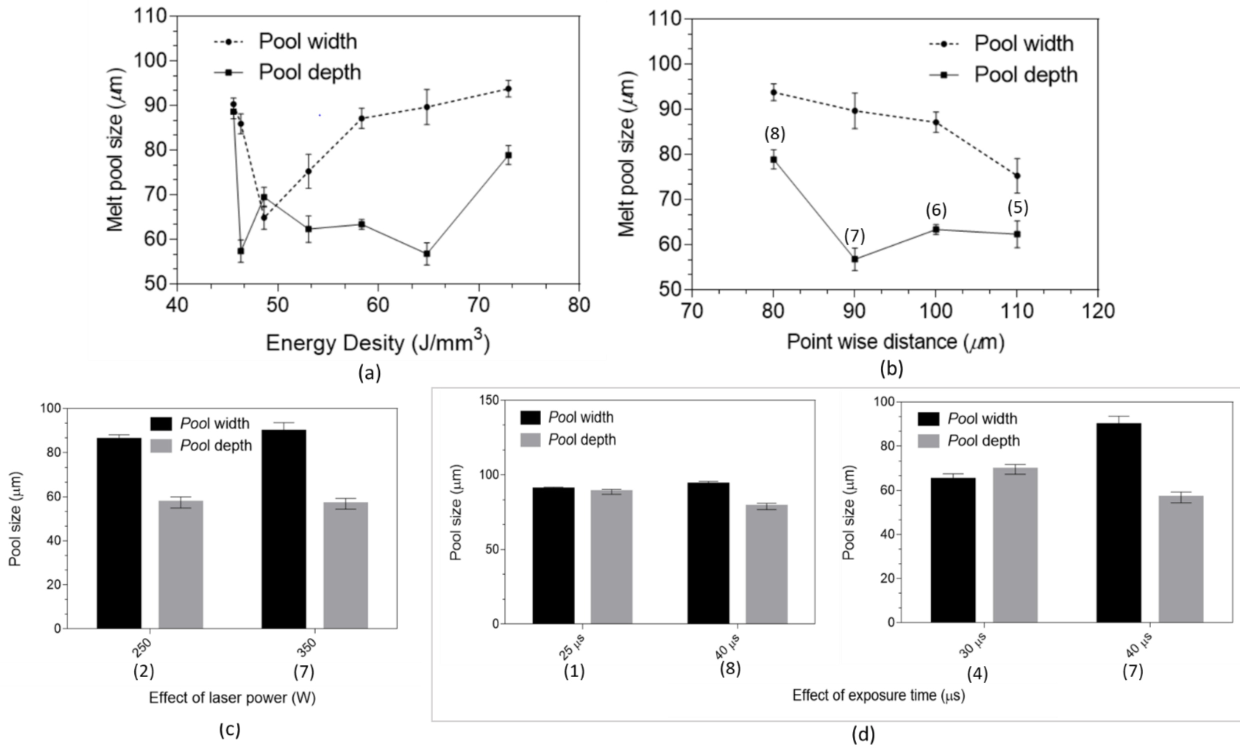

Figure 3-10. Effect of process parameters on the measured melt pool width and depth: (a) energy density, (b) pointwise distance, (c) laser power, (d) exposure time. The number given in round brackets represents the sample ID.

3.3.3 Sample Chemical Composition

The chemical composition experiment was performed for two of the as-built AlSi10Mg samples: 9 and 10, to ensure the quality of the inert environment. We conjecture that the presence of any residual oxygen may induce oxidation, which can significantly affect the thermal conductivity. The following results are from the OES analysis of the as-built AlSi10Mg Samples 9 and 10. The OES analysis confirms that the change in the energy density through adjusting the applied energy density had no effect on the chemical composition of the material manufactured in this study. The chemical composition for both Samples 9 and 10 is shown in Table 3-4 as well as the material specification composition as previously outlined in Table 3-2. The resulting compositions remain within the limits of the manufacture's material data sheet specifications for AlSi10Mg. This result shows that there are now negligible additions of elements in the samples as a result of the varying processing parameters, which considered not to have a significant effect on the thermal conductivity of the material.

Table 3-4. OES results of the composition of Samples 9 and 10.

Element	Material Data Sheet		Sample 9	Sample 10
	Mass %		Mass %	Mass %
Aluminium, Al	Balance		88.95	89.08
Silicone, Si	9.00 to 11.00		10.5	10.04
Magnesium, Mg	0.25 to 0.45		0.304	0.3
Iron, Fe	<0.25		0.167	0.161
Titanium, Ti	<0.15		0.0106	0.0105
Zinc, Zn	<0.10		0.0013	0.0015
Manganese, Mn	<0.10		0.0031	0.003
Nickel, Ni	<0.05		0.004	0.0035
Copper, Cu	<0.05		0.0029	0.0028
Lead, Pb	<0.02		0.0005	0.0005
Tin, Sn	<0.02		0.0017	0.0016

3.3.4 Thermal Conductivity

Figure 3-11 shows the thermal conductivity and the relative density variation with the energy density and the printing speed for Orientation A (all samples except 9 and 10). There is no clear trend between the energy density or the printing speed and the measured thermal conductivity. Also, thermal conductivity does not appear to follow the same trend as the relative density. The relative density increased initially and then stayed almost unchanged beyond an energy density, E_d, of 50 J/mm^3. A similar initial abrupt change was seen in the thermal conductivity; however, no correlation was observed between the density and the thermal conductivity between energy densities of 48 J/mm^3 and 53 J/mm^3. Here thermal conductivity increases despite having a minimal change in the relative density. This indicates that, while the relative density might influence the thermal conductivity for low energy densities, the void fraction is not the only parameter that dictates thermal conductivity at higher energy densities.

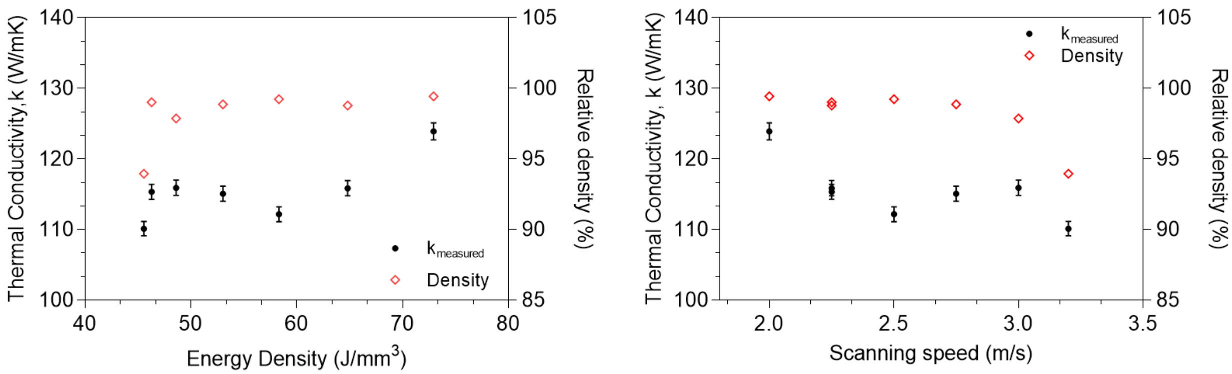

Figure 3-11. The measured thermal as a function of (a) energy density and (b) scanning speed.

Figure 3-12 depicts each input effect of printing parameters on the thermal conductivity separately rather than grouping all as one variable, i.e., energy density. Generally, the maximum difference in thermal conductivity resulting from changing the process parameters was found to be almost 22%, by comparing Sample 9 to Sample 8.

The anisotropic nature of thermal conductivity was examined by comparing Samples 4 to 9 and Samples 7 to 10, that were manufactured at the same energy densities. Generally, Orientation B exhibited lower thermal conductivity, k_{yy}, compared to Orientation A, k_{zz}, although the relative density difference between the samples with the same energy density is not substantial. The build orientation B decreased the thermal conductivity by almost 12.9 % and 7.7 % at energy densities of 48.61 J/mm^3 and 64.81 J/mm^3, respectively. This observation agrees with the previous work of [15]. This was attributed in [15] to the presence of a connected network of Si cellular structure stemming from the rapid solidification experienced by the melt pool in the manufacturing process.

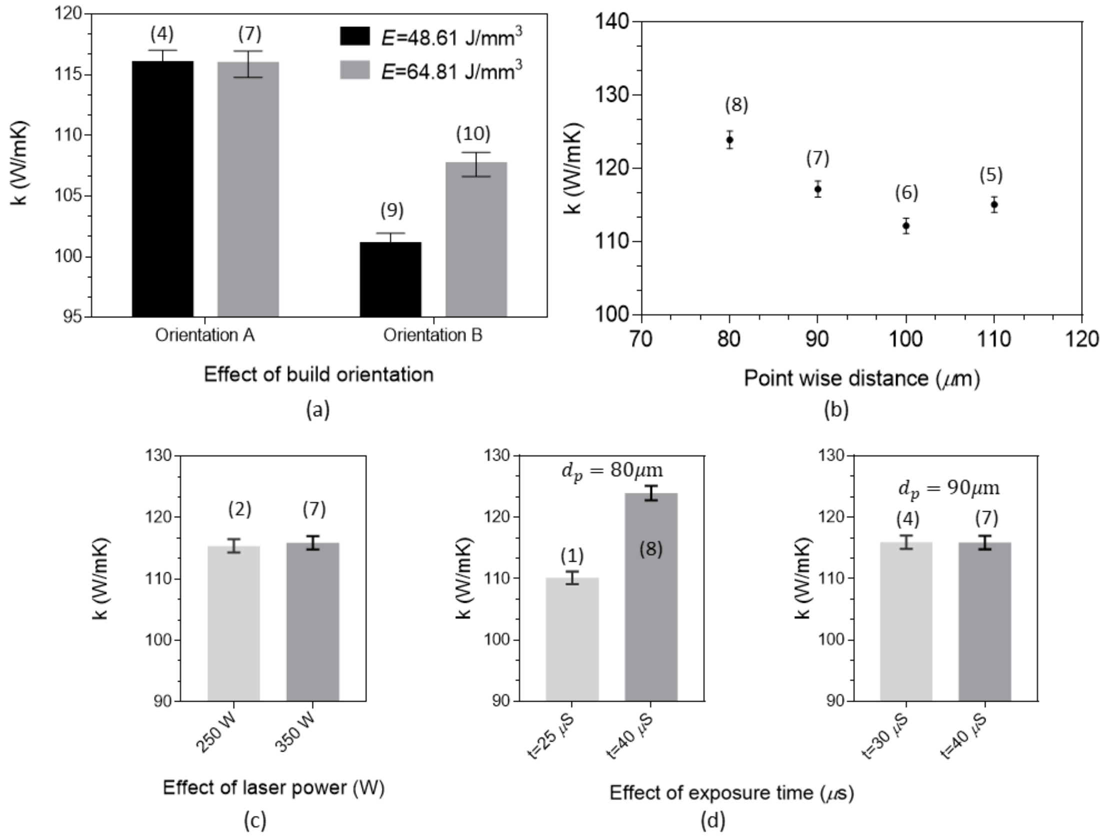

Figure 3-12. The measured thermal conductivity changes with the process parameters: (a) build orientation, (b) pointwise distance, (c) laser power, and (d) exposure time. The number given in round brackets represents the sample ID.

As indicated, the increasing linear trend seen in Figure 3-11a at energy densities higher than 55 J/mm^3 is because of the pointwise distance effect shown in Figure 3-12b, which also contributed dominantly to changing the pool size in Figure 3-10b. Decreasing the pointwise distance increased the thermal conductivity by almost 10.5% when comparing Sample 6 to Sample 8, except for Sample 5, which is discussed later in this section. However, no significant difference in the thermal conductivity was observed with the laser power change as shown in Figure 3-12c, which also conforms with the behaviour for melt pool discussed before in Figure 3-10c.

Two interesting remarks can be deduced from the analogy between the process parameters influence on the melt pool size in Section 3.3.2 and their effect on thermal conductivity here in this section: First, the energy density neither reflects the thermal behavior of SLM 3D-printed parts nor the physics associated with the melt pool. This can be confirmed by comparing samples 3 and 4, which were printed with the same energy density of 48.61 J/mm^3 but with a different set of parameter combinations; nevertheless, the printing of Sample 3 was not successful, as highlighted initially in Section 3.2.1. This complies with the finding reported by Bertoli et al. [25], who investigated the shape of a single track of 316L SS with different sets of process parameters at the same energy density. They found a variation in the deposited pool height at the same energy density, which supports the unreliability of this number to capture the physics of the melt pool. Second, it is hypothesized here that another structure-driven parameter should be considered with the relative density while analyzing the thermal conductivity results, especially for samples with an energy density higher than 50 J/mm^3, which did not follow the relative density variation curve.

Typically, the thermal conductivity of metal is a consequence of two parts: electronic and vibrational. The former is associated with electrons and holes carrying the thermal energy, while the latter is associated with the phonons, i.e., thermal vibrations, passing through the lattice. As a result, the presence of voids influences both parts of the thermal conductivity. Moreover, any disruption in the lattice structure can result in scattering of the phonons, which directly affects the thermal conductivity negatively. For this reason, it was shown that the nanocrystalline materials suffer from low thermal conductivity, as discussed in [26]. Grain boundaries can be viewed as obstacles in the heat transfer path. Therefore, the smaller the grain size, the more distraction to the phonons, and the lower the resulting thermal conductivity compared to a corresponding single crystal material. We conjecture that the same phenomenon is associated with melt pool zones boundaries, shown in Figure 3-9. These boundaries can cause scattering to the phonons and yield a reduction in the effective thermal conductivity. It was revealed that the melt pool boundaries become less distinct [15] and sometimes completely dissolve [27] upon thermal treatment. However, this observation was not considered while analyzing the thermal conductivity improvement, and the main contribution was attributed to Si cellular structure breakdown. We conjecture that the melt pool boundaries and the relative density are the main reasons for the thermal conductivity change. That is why agreement exists between the effect of the process parameters on the melt pool size in Section 3.3.2 and their impact on the thermal conductivity in this section.

To account for the influence of melt pool boundaries, we propose a new structure-based parameter to better embody this behaviour, named here the number of melt pool boundaries per unit length of the heat flow direction, (n). This number is defined as how many times the heat flow path is intersected by the melt pool boundaries and voids. It is calculated by drawing equispaced lines of 50 µm spacing throughout the microstructure imajes and then counting the number of intersecting points on each line. Then, the average number is recorded for all the lines drawn, and the standard deviation is used to predict the associated uncertainty, as shown in Figure 3-13 and Figure 3-14. Having a high number of melt pool boundaries per unit length can deteriorate thermal conductivity and vice versa. This number was normalized and plotted against the energy density along with the normalized relative density and the normalized thermal conductivity, as shown in Figure 3-14. Correlating between this factor and the relative density gives better insight into the thermal conductivity change trends. For example, Sample 1 achieved the lowest thermal conductivity due to experiencing the minimum density and the highest number of melt pool boundaries per unit length of the heat flow direction. Conversely, Sample 8 had a density very close to Samples 2 and 6, yet possessed the lowest number of melt pool boundaries per unit length of the heat flow direction, thus contributing to its higher thermal conductivity. It is believed that having a high number of melt pool boundaries per unit length for Sample 1 originated from having a higher fraction of voids and wider melt zone, as highlighted in Section 3.3.2. By comparing Samples 5, 6, and 7, all had almost the same relative density; still, the thermal conductivity of Sample 6 was lower because of the high number of melt pool boundaries per unit length.

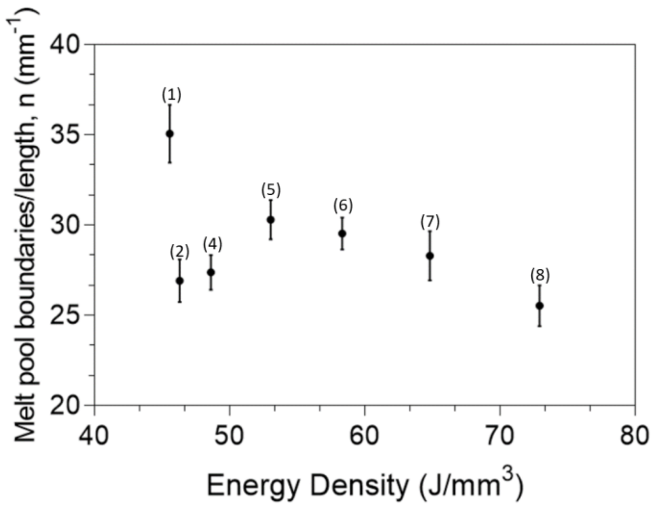

Figure 3-13. The measured melt pool boundaries per unit length of the heat flow direction with the energy density.

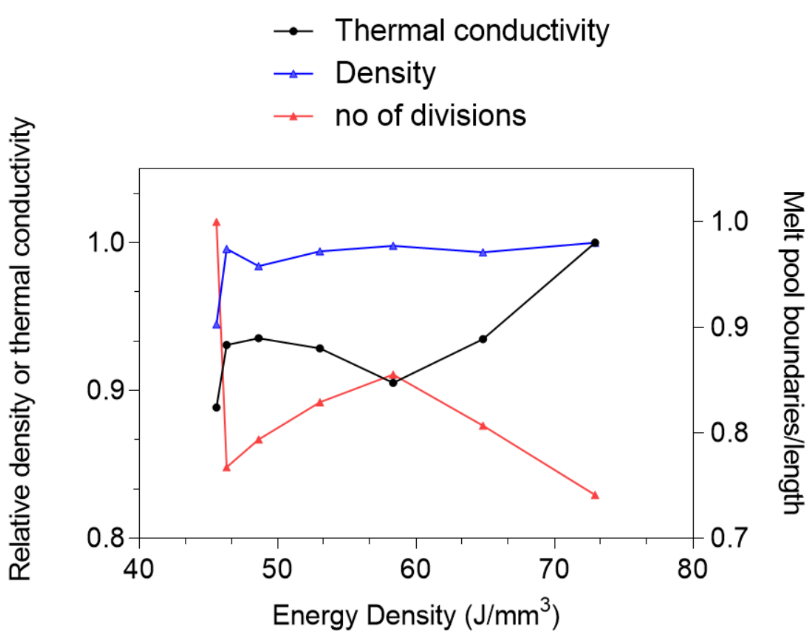

Figure 3-14. Normalized melt pool boundaries per unit length, relative density, and thermal conductivity variation with the energy density.

3.4 Summary & Conclusions

In this work, the effective thermal conductivity of 3D-printed AlSi10Mg alloys fabricated using SLM was characterized experimentally. The impact of the process parameters such as laser power, exposure time, pointwise distance, and build orientation was investigated. Generally, it was shown that changing these parameters can alter the resulting thermal conductivity by up to 22%. The key specific findings can be summarized as follows:

- Firstly, both the thermal conductivity or the melt pool size width was more dominantly influenced by the pointwise distance compared to other processing parameters. Secondly, the laser power exhibited the lowest effect on both the thermal conductivity and the melt pool size. Lastly, the exposure time impact was a function of the pointwise distance value, which again signifies the pointwise distance effect.
- The anisotropic nature in thermal conductivity was examined by changing the sample build orientation, which was found to alter the thermal conductivity significantly, reaching up to 12.9 % at an energy density of 48.61 J/mm^3.
- The thermal conductivity change was attributed to the relative density at energy densities lower than 48 J/mm^3; however, the heat distraction by the melt pool boundaries was the root cause at high energy densities.
- The melt pool boundaries and the microstructure evolution associated with the process parameters variation were quantified by defining a new parameter based on the number of melt pool boundaries per unit length of the heat flow direction. This parameter represents the number of disruptions experienced in the heat flow path because of intersecting the melt pool boundaries, which showed a good correlation with the thermal conductivity

behaviour at high energy densities at which the relative density showed no trend. Therefore, as a conclusion, thermal conductivity is a dependent of the interplay between the relative density and the number of melt pool boundaries per unit length of the heat flow direction.

3.5 References

[1] C. Luo, J. Qiu, Y. Yan, J. Yang, C. Uher, and X. Tang, “Finite element analysis of temperature and stress fields during the selective laser melting process of thermoelectric SnTe,” J. Mater. Process. Technol., vol. 261, no. June, pp. 74–85, 2018, doi: 10.1016/j.jmatprotec.2018.06.001.

[2] Z. Chen et al., “Thermal dynamic behavior during selective laser melting of K418 superalloy: numerical simulation and experimental verification,” Appl. Phys. A Mater. Sci. Process., vol. 124, no. 4, pp. 1–16, 2018, doi: 10.1007/s00339-018-1737-8.

[3] R. Andreotta, L. Ladani, and W. Brindley, “Finite element simulation of laser additive melting and solidification of Inconel 718 with experimentally tested thermal properties,” Finite Elem. Anal. Des., vol. 135, pp. 36–43, Nov. 2017, doi: 10.1016/j.finel.2017.07.002.

[4] A. H. Maamoun, Y. F. Xue, M. A. Elbestawi, and S. C. Veldhuis, “Effect of selective laser melting process parameters on the quality of al alloy parts: Powder characterization, density, surface roughness, and dimensional accuracy,” Materials (Basel)., vol. 11, no. 12, 2018, doi: 10.3390/ma11122343.

[5] A. Boschetto, L. Bottini, and F. Veniali, “Roughness modeling of AlSi10Mg parts fabricated by selective laser melting,” J. Mater. Process. Technol., vol. 241, pp. 154–163, 2017, doi: 10.1016/j.jmatprotec.2016.11.013.

[6] K. Kempen, L. Thijs, J. Van Humbeeck, and J. P. Kruth, “Processing AlSi10Mg by selective laser melting: Parameter optimisation and material characterisation,” Mater. Sci. Technol. (United Kingdom), vol. 31, no. 8, pp. 917–923, 2015, doi: 10.1179/1743284714Y.0000000702.

[7] N. T. Aboulkhair, N. M. Everitt, I. Ashcroft, and C. Tuck, “Reducing porosity in AlSi10Mg parts processed by selective laser melting,” Addit. Manuf., vol. 1, no. November, pp. 77–86, 2014, doi: 10.1016/j.addma.2014.08.001.

[8] Q. Han and Y. Jiao, “Effect of heat treatment and laser surface remelting on AlSi10Mg alloy fabricated by selective laser melting,” Int. J. Adv. Manuf. …, 2019, [Online]. Available: https://link.springer.com/article/10.1007/s00170-018-03272-y.

[9] M. S. I. N. Kamariah, W. S. W. Harun, N. Z. Khalil, F. Ahmad, M. H. Ismail, and S. Sharif, "Effect of heat treatment on mechanical properties and microstructure of selective laser melting 316L stainless steel," IOP Conf. Ser. Mater. Sci. Eng., vol. 257, no. 1, 2017, doi: 10.1088/1757-899X/257/1/012021.

[10] Y. Wang and J. Shi, "Effect of hot isostatic pressing on nanoparticles reinforced AlSi10Mg produced by selective laser melting," Mater. Sci. Eng. A, vol. 788, no. May, p. 139570, 2020, doi: 10.1016/j.msea.2020.139570.

[11] T. Hirata, T. Kimura, and T. Nakamoto, "Effects of hot isostatic pressing and internal porosity on the performance of selective laser melted AlSi10Mg alloys," Mater. Sci. Eng. A, vol. 772, no. June 2019, p. 138713, 2020, doi: 10.1016/j.msea.2019.138713.

[12] EOS GmbH-Electro Optical Systems, "Material Data Sheet: EOS Aluminium AlSi10Mg," pp. 1–5, 2014, [Online]. Available: http://gpiprototype.com/images/PDF/EOS_Aluminium_AlSi10Mg_en.pdf.

[13] P. Yang, L. A. Deibler, D. R. Bradley, D. K. Stefan, and ..., "Microstructure evolution and thermal properties of an additively manufactured, solution treatable AlSi10Mg part," J. Mater. …, 2018, [Online]. Available: https://www.cambridge.org/core/journals/journal-of-materials-research/article/microstructure-evolution-and-thermal-properties-of-an-additively-manufactured-solution-treatable-alsi10mg-part/AF458C0D633BADE92338BB906BED10AE.

[14] E. Strumza, O. Yeheskel, and S. Hayun, "The effect of texture on the anisotropy of thermophysical properties of additively manufactured AlSi10Mg," Additive Manufacturing. Elsevier, 2019, [Online]. Available: https://www.sciencedirect.com/science/article/pii/S2214860419301800.

[15] R. R. J. Sélo, S. Catchpole-Smith, I. Maskery, I. Ashcroft, and C. Tuck, "On the thermal conductivity of AlSi10Mg and lattice structures made by laser powder bed fusion," Addit. Manuf., vol. 34, no. March, p. 101214, 2020, doi: 10.1016/j.addma.2020.101214.

[16] C. Silbernagel, I. Ashcroft, P. Dickens, and M. Galea, "Electrical resistivity of additively manufactured AlSi10Mg for use in electric motors," Additive Manufacturing. Elsevier, 2018, [Online]. Available: https://www.sciencedirect.com/science/article/pii/S2214860418300769.

[17] A. Elkholy, M. Rouby, and R. Kempers, "Characterization of the anisotropic thermal conductivity of additively manufactured components by fused filament fabrication," Prog. Addit. Manuf., vol. 4, no. 4, pp. 497–515, 2019, doi: 10.1007/s40964-019-00098-2.

[18] ASTM C177, "Standard Test Method for Steady-State Heat Flux Measurements and Thermal Transmission Properties by Means of the Guarded-Hot-Plate," ASTM Int., pp. 1–23, 2013, doi: 10.1520/C0177-13.2.

[19] M. D. Abràmoff, P. J. Magalhães, and S. J. Ram, "Image processing with imageJ," Biophotonics Int., vol. 11, no. 7, pp. 36–41, 2004, doi: 10.1117/1.3589100.

[20] W. E. King et al., "Observation of keyhole-mode laser melting in laser powder-bed fusion additive manufacturing," J. Mater. Process. Technol., vol. 214, no. 12, pp. 2915–2925, 2014, doi: 10.1016/j.jmatprotec.2014.06.005.

[21] T. W. Eagar and N. S. Tsai, "Temperature Fields Produced By Traveling Distributed Heat Sources.," Weld. J. (Miami, Fla), vol. 62, no. 12, pp. 346–355, 1983.

[22] P. Karimi, T. Raza, J. Andersson, and L. E. Svensson, "Influence of laser exposure time and point distance on 75-μm-thick layer of selective laser melted Alloy 718," Int. J. Adv. Manuf. Technol., vol. 94, no. 5–8, pp. 2199–2207, 2018, doi: 10.1007/s00170-017-1019-1.

[23] Y. Li and D. Gu, "Parametric analysis of thermal behavior during selective laser melting additive manufacturing of aluminum alloy powder," Mater. Des., vol. 63, pp. 856–867, 2014, doi: 10.1016/j.matdes.2014.07.006.

[24] Y. Du, X. You, F. Qiao, L. Guo, and Z. Liu, "A model for predicting the temperature field during selective laser melting," Results Phys., vol. 12, no. November 2018, pp. 52–60, 2019, doi: 10.1016/j.rinp.2018.11.031.

[25] U. Scipioni Bertoli, A. J. Wolfer, M. J. Matthews, J. P. R. Delplanque, and J. M. Schoenung, "On the limitations of Volumetric Energy Density as a design parameter for Selective Laser Melting," Mater. Des., vol. 113, pp. 331–340, 2017, doi: 10.1016/j.matdes.2016.10.037.

[26] H. Dong, B. Wen, and R. Melnik, "Relative importance of grain boundaries and size effects in thermal conductivity of nanocrystalline materials," Sci. Rep., vol. 4, p. 7037, 2014, doi: 10.1038/srep07037.

[27] P. Yang, M. A. Rodriguez, L. A. Deibler, and ..., "Effect of thermal annealing on microstructure evolution and mechanical behavior of an additive manufactured AlSi10Mg part," J. Mater. …, 2018, [Online]. Available: https://www.cambridge.org/core/journals/journal-of-materials-research/article/effect-of-thermal-annealing-on-microstructure-evolution-and-mechanical-behavior-of-an-additive-manufactured-alsi10mg-part/5DCDF31075608013C1A95679C34FB31E.

Chapter 4 Pool Boiling Heat Transfer Enhancement Using 3D-Printed Fixtures Manufactured by FFF[3]

In this chapter, Fused Filament Fabrication (FFF) is utilized to produce low-cost, porous polymer fixtures designed to alter bubble dynamics and improve the pool boiling heat transfer characteristics from flat copper surfaces. The fixtures examined here consist of a uniform pattern of square cells. An open-source fused filament fabrication 3D printer was used to manufacture the fixtures from PLA, and they were attached mechanically to the boiling surface. The wickability of the printed porous samples was investigated using the rate-of-rise method, which shows that printing build orientation can affect their capillary pressure. The boiling experiments were performed under saturated conditions using deionized water as the working fluid at a pressure of 1 atm. The fixture's geometrical parameters, such as the unit cell size, the pitch, and the fixture height, were examined for their impact on the pool boiling curve.

4.1 Introduction & Background

Recent advances in microelectronic technologies and the ever-growing tendency toward miniaturization require more effective cooling methods ever to fulfill the high heat flux demands of these applications. Nucleate pool boiling is a promising solution for these challenges due to the associated high heat transfer coefficient and the almost constant temperature of the working fluid. It has therefore been implemented in many applications, including thermosyphons, nuclear reactors, and immersion cooling systems. For most boiling applications, it is desirable to have a

[3] This chapter has been published as a peer-reviewed journal paper titled "Enhancement of Pool Boiling Heat Transfer Using 3D-printed Polymer Fixture" in *Experimental Thermal and Fluid Science journal*.

high heat transfer coefficient (HTC) and a high critical heat flux (CHF) and, to this end, there have been numerous studies that attempt to increase these metrics in various ways. These enhancement techniques can be broadly classified into three categories: generation of a disturbance near the surface, modification of the changing working fluid, or alteration of the heating surface.

Creating a disturbance near the surface during ebullition improves the HTC by facilitating bubble detachment and increasing bubble departure frequency. It also helps to defer the CHF by delaying the horizontal coalescence of the vapour bubbles. This disturbance can be actively triggered by the use of ultrasonic vibration [1], electrohydrodynamics [2], or by employing a passive rotor just above the surface [3]. Although boiling heat transfer phenomena primarily depend on the boiling surface characteristics, the employment of nanofluids has shown a dramatic increase in the CHF [4]. You et al. [4] performed saturated pool boiling experiments with different concentrations of alumina (Al_2O_3) nanoparticles suspended in distilled water at a pressure of 2.89 psi. It was found that the CHF was improved by 200% compared with pure water. However, they indicated that the HTC in the nucleation zone was not affected. This was attributed to the surface tension increase [4] and nanoparticle deposition on the heater [5] during the boiling process.

The passive surface modification approach has garnered attention in many recent studies, especially with the growing evolvement of the manufacturing techniques. Surface modification has been extensively studied and implemented to create several macrostructures such as fins [6], re-entrant cavities [7], dimples [8], and tunnels [9]. Also, it has been examined using nanostructure topologies employing different manufacturing techniques, such as powder heat sintering, spraying, meshing, soldering, and brazing, as reviewed Kim et al. [10]. However, the stability of these nanostructures is still an issue and can be solved using different methodologies, including high-temperature annealing [11]. The reader is referred to two recent review papers that summarize how these surface modifications are fabricated and their influence on the pool boiling heat transfer rate [12], [13]. Generally, the primary function of micro- or macro-structured surfaces is to provide separate pathways for liquid and vapour near the CHF which serve to impede the early stages of dry-out and decrease wall superheat. In other words, they create capillary action for replenishing liquid in order to be able to supply the nucleation sites, even at high heat fluxes. On the other hand, the nanostructures improve HTC by increasing the heat transfer area and providing additional active nucleation cavities.

The adoption of a porous structure for the enhancement of pool boiling heat transfer has been extensively investigated in the literature from different aspects: manufacturing methods, the associated underlying mechanism, and modeling. Different methods were utilized to create either a uniform thin porous layer coating on the boiling surface or a modulated porous layer coating. Jun et al. [14] studied the effect of the porous layer thickness and the sintered particle diameter on both the CHF and HTC for water at atmospheric pressure. They achieved around twice the CHF and an eight-fold increase in HTC compared with the bare surface. It was shown that increasing the particle size had a positive effect on both the HTC and the CHF. In the literature, a uniform layer of porous coating has been implemented and investigated using various fabrication techniques such as vapour blasting [15], cold spray [16], applying a mixture of copper powder, [17] electrodeposition [18], and powder sintering [19]. Ha and Graham [19] revealed that the formation and the growth of the vapour layer inside the porous structure represent the major limitation that impedes the further enhancement of the CHF and may degrade the HTC at high heat fluxes. They examined the influence of the inclusion of vapour escape channels, either in the porous coating itself or in the solid surface underneath the coating, to facilitate the bubbles' escape and prevent vapour layer growth. Using these channels, they enhanced the CHF and the HTC by approximately 265%–347% and 307%–426%, respectively, compared with the flat surface.

Liter and Kaviany [20] suggested another modification for the porous coating by constructing a modulated wick porous structure composed of conical stacks of sintered copper particles. This resulted in an approximately threefold improvement of the CHF compared with the plain surface. A review of the manufacturing methods used for creating porous structures for pool boiling is available in [21].

The employment of hierarchical surface structures that combine nano, micro, and macro topologies is an effective method to achieve further enhancement of the pool boiling heat transfer rate in both nucleate boiling and CHF regions. Gheitaghy et al. [11] carried out a comparative experimental pool boiling study on three copper surfaces: one with mesochannels, the second with a porous nano-structure coating, and the third with a combination of both. It was demonstrated that a CHF of 170 W/cm^2 was achieved by using the porous mesochannel, which represents a 210% improvement over the plain surface. Moreover, the HTC reached 23.5 W/cm^{2}K, which corresponds to a 390% enhancement compared with the plain surface. A similar effort was exerted by Rioux et al. [22]; however, the major difference is the method used to manufacture the nano-, micro-, and macrostructures.

Another approach that also falls under porous surface modification is the attachment of porous fixtures to the plain unmodified boiling surface. Kim at al. [23] attached a single-layered metallic wire mesh fixture to improve the CHF for water at 1 atm. The metallic fixture was etched through an electrochemical process to create nano-/micro-sized pores through its internal structure in order to sustain the replenishing liquid to the heated surface, which mitigated the dry-out zone expansion and enhanced the CHF by approximately 84% compared with the plain one. Also, Mori and Okuyama [24] tested the influence of attaching a commercially available exhaust honeycomb porous filter on the boiling heat transfer rate for DI water at atmospheric conditions [24] and also in the presence of a nanofluid in another study [25]. It was found that the CHF reached 2.5 MW/m^2, which represents about 2.5 times that of the bare surface.

This chapter proposes the usage of a commercially accessible, low-cost thermoplastic 3D printing additive manufacturing method to create a customizable, low-conductivity, porous wick material that can be easily attached to the boiling surface to help regulate the liquid and vapour phases.

4.2 Fixture Fabrication and Wickability Measurement

4.2.1 Fixture Design and Preparation

Fused filament fabrication (FFF) is arguably the most popular 3D printing technology owing to the low-cost, accessible hardware, the wide array of filament feedstock materials, and a large, open-source development community. The FFF process relies on melting a thermoplastic filament through a hot nozzle that moves in the *x*–*y* plane and deposits the plastic on a platform that moves relative to the nozzle in the *z*-direction. The movement of both the nozzle and the platform are controlled using G-code generated by slicing software responsible for dividing the CAD model into printable layers.

The polymer fixture configuration used in the present study is shown in Figure 4-1. The fixtures consist of an array of square cavities separated by 0.5 mm thick walls. The design principle of the fixture is to provide replenishing pathways for the liquid to reach the dried-out spots, which may occur at higher heat fluxes. As shown in Figure 4-1, this fixture design has three geometrical parameters: the unit cell size, s, the pitch, p, and the fixture height, H. Also, the traces of the printed roads in the sliced fixture walls are shown in Figure 4-1. The unit cell size and the fixture height were varied according to Table 4-1, while the pitch was considered a dependent variable. The parameter A_w in Table 4-1 is the contact area between the fixture and the boiling surface, while n is the number of the fixture cells or channels. The outer dimensions of the fixture were held at 15 mm x 15mm to match the copper boiling surface dimensions. The fixtures were fabricated using an Ultimaker 2 3D printer using a 100% infill of PLA filament. Other printing process variables were set using an open-source slicing software (Cura 3.5.1), according to Table 4-2. The thermophysical properties of the 3D-printed polymer fixtures are given in Table 4-3.

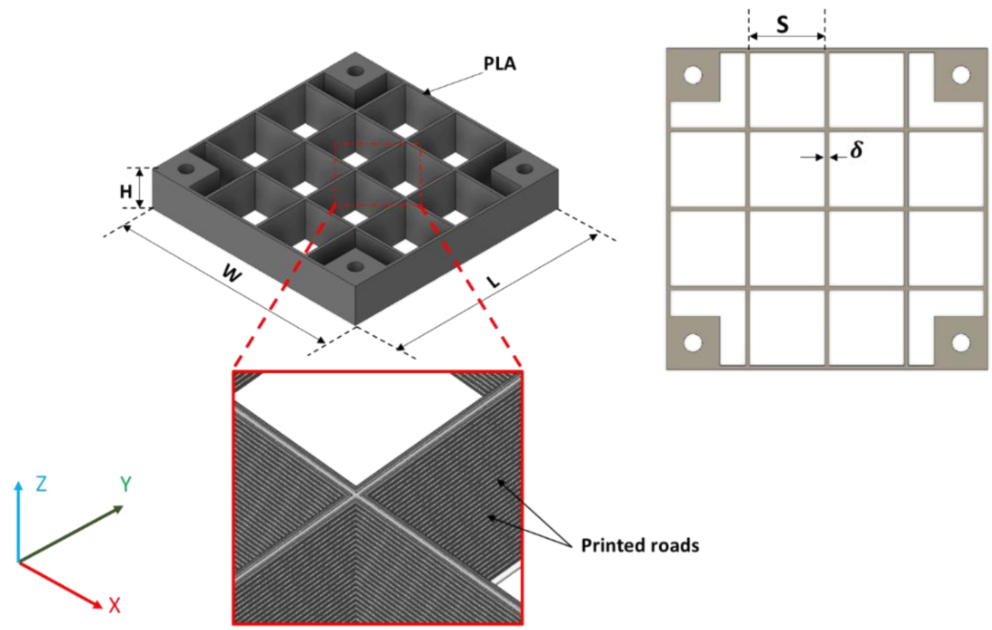

Figure 4-1: Fixture geometrical parameters.

Table 4-1. Fixtures' geometrical parameter codes.

Fixture	Height, *H* (mm)	Cell size, *S* (mm)	δ (mm)	No. of cells or channels, n	Wetted area, A_w (mm^2)
A	2	6.7	0.5	4	58.18
B	4	6.7	0.5	4	58.18
C	6	6.7	0.5	4	58.18
D	2	4.3	0.5	9	71.8
E	2	1.9	0.5	36	99.7

Table 4-2. Parameters used to print the samples.

Parameter	Value
Layer height	0.1 mm
Raster width	0.4 mm
Infill %	100 %
Nozzle temperature, T_N	200 °C
Platform temperature, T_b	60 °C
Speed, v	60 mm/s

Table 4-3. PLA thermophysical properties.

Density, ρ (kg/m^3) [26]	**Thermal conductivity, k (W/mK) [27]**	**Thermal Capacity, C (J/kgK) [28]**	**Melting Temperature (^{O}C) [26]**
1100-1211	0.1–0.2	1800	150

The fixtures have four holes which can be easily fixed to the copper boiling surface using plastic screws. The top surface of the boiling chip was prepared using two successive steps of first polishing with silica carbide emery paper (1000/3000), followed by 600 grit sandpaper. Finally, it was rinsed using isopropanol to remove any oxidation residuals or contamination.

4.2.2 Fixture Wickability and Wettability Measurements

As a thermal process, the FFF printing technique creates internal voids and pores in the manufactured components, even at 100% infill, which has a substantial effect on the mechanical and thermal properties [29]. Many investigations have employed the Taguchi method, and design of experiment (DOE) approaches to address the effect of the printing process variables on the generated porosity and, hence, on the mechanical strength of the printed components [30]. In some studies, researchers sought to decrease the resulting porosity to enhance the components' mechanical properties [29]. In the current study, we take advantage of the pores and voids generated during printing, adopting them as capillaries, to create a wicking material to supply liquid to the dry spots at the CHF.

The performance of the wick can be measured using two parameters: the capillary pressure and the permeability [31]. The former embodies the driving force of replenishing liquid flow through the wick material, while the latter controls the pressure drop or the resistance that it may encounter. The wickability of the polymer fixture is characterized here using the rate-of-rise test, during which the sample is vertically dipped in ethanol, which starts to rise through the wick; this method has been been well established through the literature and commonly utilized in several studies [31]–[33]. The results of this experiment will be used to justify the pool boiling results in Section 4.4.

As discussed before, the printing parameters can change the material porosity and hence the wickability performance as well; therefore, three samples with a dimension of 30 mm x 150 mm x 1 mm were printed in different build orientations, as shown in Figure 4-2a. This will help in understanding the polymer fixture wicking capability in all directions. Sample I represents the wicking capability of the porous material along the printing roads, while Samples II and III represent the perpendicular directions for two different configurations. Also, a microscopic photo for the printed sample is shown in Figure 4-2b to show the capillaries created by the printing process and highlight the road disconnection problem that may exist in the printed part, which was revealed in an earlier study [27].

Figure 4-3 depicts the capillary rate-of-rise facility, which was performed as described in [31]. The 3D-printed samples were held vertically using a laboratory holder and immersed in the ethanol reservoir. The liquid level rise was detected over time using a FLIR Thermal camera (Model A6751sc). The ethanol liquid level in the reservoir was assumed to be constant throughout the testing time because the absorbed amount was too small. During the ethanol rise, the capillary pressure was balanced with a pressure drop and gravity as given by the following equation:

$$\Delta P_{cap} = \frac{\mu\varepsilon}{K} h \frac{dh}{dt} + \rho g h \tag{4.1}$$

where $\Delta P_{c,max}$ is the maximum capillary pressure, and h is the ethanol height. K and ε are the sample's permeability and porosity. This equation can be rearranged and written in the form given by Eq. (4.2), which can be used to obtain the capillary pressure and the parameter, $\frac{K}{\varepsilon}$, by setting $x = \frac{1}{h}$ and $y = \frac{dh}{dt}$, according to Eq. (4.3).

$$\left(\Delta P_{cap} \cdot K\right) \cdot \frac{1}{h} - \rho g K = \mu\varepsilon \frac{dh}{dt} \tag{4.2}$$

$$y = \frac{\Delta P_{cap} \cdot K}{\mu\varepsilon} \cdot x - \frac{\rho g K}{\mu\varepsilon} \tag{4.3}$$

$\Delta P_{c,max}$ can be utilized to derive the sample effective radius as given in Eq. (4.4).

$$\Delta P_{c,max} = \frac{2\sigma}{r_{eff}} \tag{4.4}$$

where σ is the surface tension of the working fluid, while r_{eff} is the effective capillary radius of the 3D-printed wick sample.

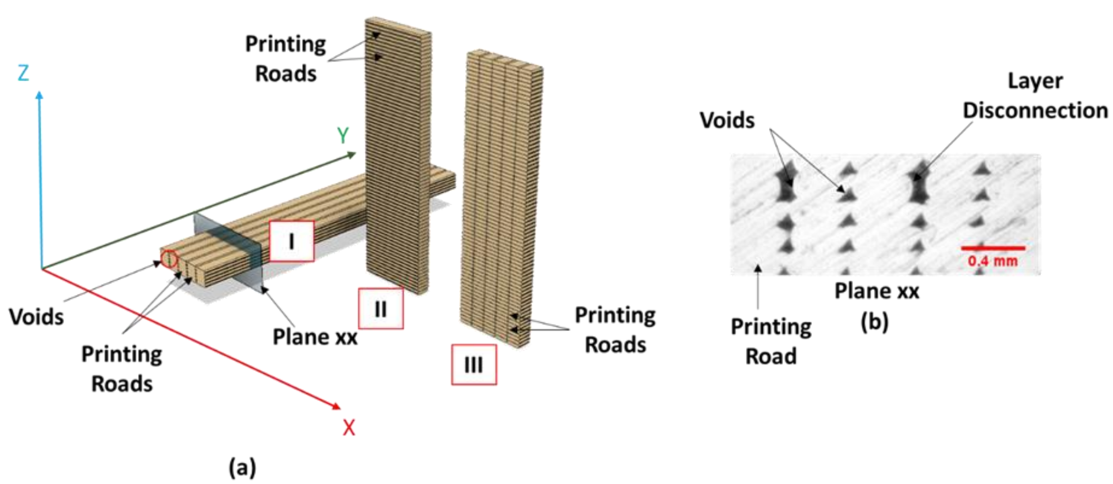

Figure 4-2: (a) The printed samples for the wickability measurement, (b) microscopic photo of the printed sample at plane *xx*.

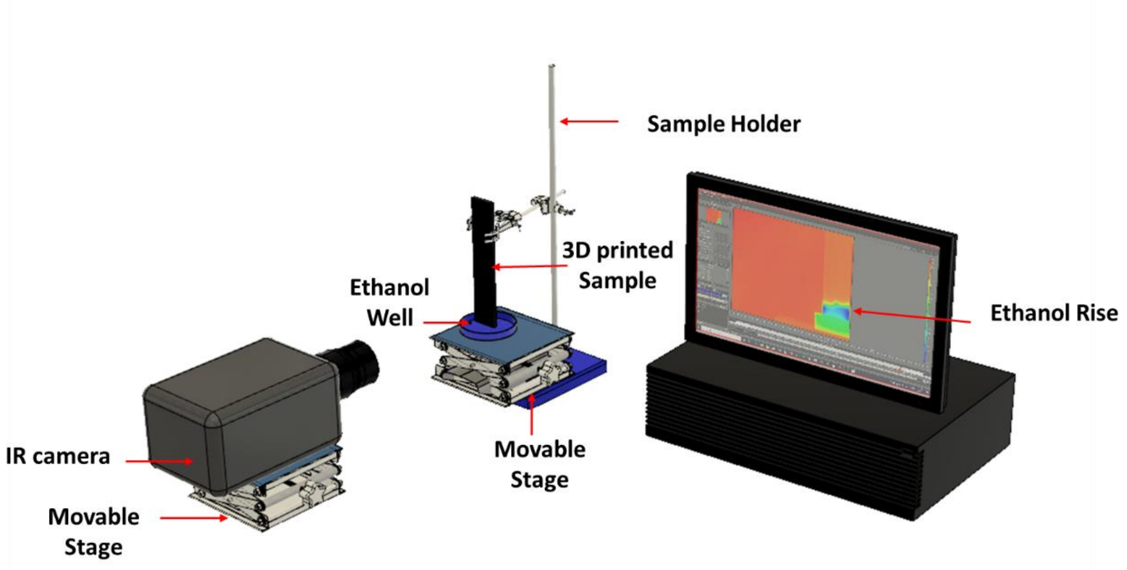

Figure 4-3: The rate-of-rise capillary experiment for the wickability measurement of the printed sample.

Figure 4-4 depicts a comparison between the rate of ethanol rise for all samples. As can be seen, Sample I achieved the best capillary performance as expected because the fluid can easily flow along the printed road's direction through the continuous pores in the sample, shown previously in in Figure 4-2b. Although the other two specimens do not have a connected pores network, the ethanol could rise perpendicular to the printing roads, which can be attributed to the periodic capillary rise process induced by the valve effect, which is explained in [34]. Figure 4-5 illustrates the IR images for the three samples at a time t=40 s. This figure indicates the fast rise of the ethanol through Sample I compared with the other samples and also shows that the ethanol interface is not homogeneous throughout the sample, which pertains to the road disconnection problem that may occur during printing, as highlighted in Figure 4-2a.

Although the printing process parameters can be easily controlled through the slicing software, a few random parameters, such as the homogeneity of the filament material and the environment temperature, can still play a factor in the temperature distribution throughout the sample. This may affect the material flow through the nozzle or the adhesion between the printing roads, resulting in the road disconnection artifact. The capillary results were used to predict the sample's permeability and the effective bore radius, as listed in Table 4-4. The sample porosity was measured experimentally in an earlier study [27] and was found to be 11.7 % according to the used printing parameters given in to Table 4-2.

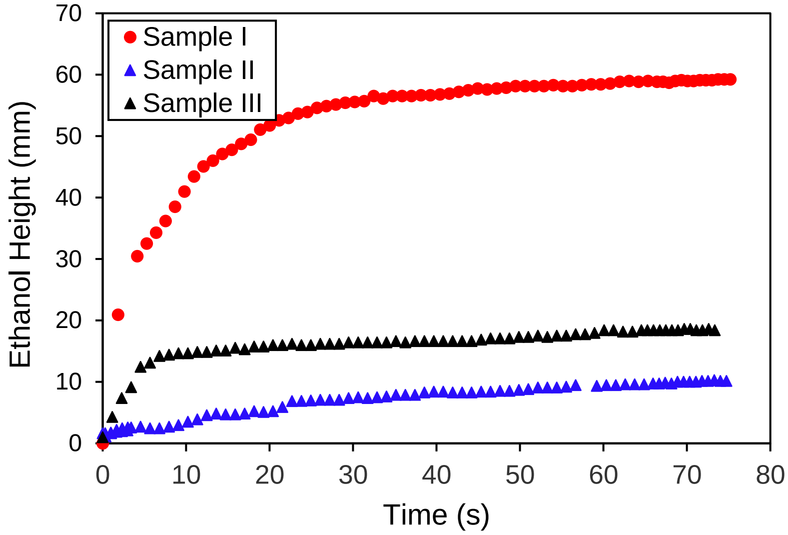

Figure 4-4: The measured capillary rise of ethanol for the 3D-printed sample at different build directions.

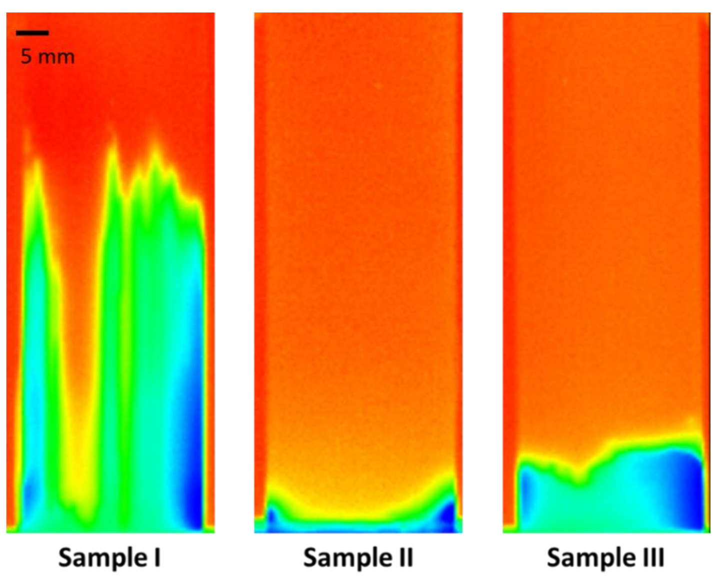

Figure 4-5: Thermal imaging for the ethanol rise at time t=40 s.

Table 4-4. The measured permeability and the effective pore radius for the 3D-printed samples.

Sample	Permeability, K (m^2)	Effective Pore Radius, r_{eff} (mm)
I	5.4 x 10^{-11}	0.095
II	8.7 x 10^{-12}	0.60
III	2.85 x 10^{-10}	0.39

Besides the measurement of the wickability performance of the samples, as explained before, their surfaces were characterized through the wettability and surface roughness measurements. The static contact angle was measured for the three samples using KRUS device (model DSA100E). Sample I was utilized to capture the contact angle along the printing roads, where the camera was situated perpendicular to the roads, whereas Sample II was used to view the contact angle from the other direction, where the camera is parallel to the printing roads. Sample II achieved the maximum contact angle of 82.7°±5°, followed by Sample III with a value of 59.72 ±6° and finally Sample I with a contact angle of 34.5 ±6°. It is noticeable that the contact angle normal to the printing roads, Sample I, is lower compared to the parallel, Sample II, because the bubble is spread along the cavities between the roads under the capillary action. The surface roughness of the 3D samples was experimented without any polishing step (as printed) using a profilometer (Bruker ContourGT-K). Each sample was measured at five different locations to determine an average representative value. The roughness values were found 2.88 µm, 2.47 µm, and 14.89 µm for Sample I, Sample II, Sample III, respectively. The uncertainty in these values was estimated to be less than 11%. It is indicated that the surface roughness for sample I and II are very close because it represents the resulted protrusions between the printing roads.

4.3 Experimental Apparatus and Methodology

4.3.1 Pool Boiling Apparatus

A schematic of the pool boiling test facility employed in this study is shown in Figure 4-6. The boiling surface was manufactured from oxygen-free copper (k=390 W/mK) and had a surface area of 15 mm x 15 mm exposed to the working fluid. The integrated heating block has four cartridge heaters (200 W each) to generate the required heat flow into the pool. The heated block was wrapped with a silica aerogel insulation (k=0.014 W/mK) to minimize heat loss. The power was transferred axially through the heating block, which had area contraction to 15 mm x 15 mm, intensifying the heat flux through the boiling surface. The input power to the heating block was controlled using a DC power supply (Aim-TTi CPX400D) and quantified as the electrical power. The heat loss was estimated numerically using an ANSYS steady-state thermal module. The problem was formulated based on inputting the convection heat transfer coefficient on the boiling surface in the range 50 kW/m^2K, while having all other boundaries exposed to free convection with a heat transfer coefficient of 10 W/m^2K. Heat loss through the insulation was found to be less than 5%. The polymer fixture was attached mechanically to the boiling surface, as shown in Figure 4-6b. The wall surface temperature was acquired by measuring the heating block temperature 2 mm away from the surface, along with the measured heat flux, as given by Eq. (4.7) and explained in Section 4.3.2.

The boiling chamber was manufactured from acrylic with dimensions of 15 cm x 15 cm x 15 cm, which allowed visualization of bubbles dynamically over the boiling surface. Two auxiliary immersion heaters of 150 W were inserted in the boiling chamber to control the thermodynamic state of the working fluid and account for heat loss from the chamber body.

The condensation system consisted mainly of a copper coil heat exchanger situated above the free surface of the working fluid level to recycle the resulting vapour back to the boiling chamber by circulating chilled cooling water at 5 $^{\circ}$C. The chamber was vented to the atmosphere through a small opening near the top to ensure that the experiments were carried out at atmospheric pressure. Three thermocouples were employed to measure the surface temperature (Eq. (4.7), the saturation temperature of the working fluid temperature, and the maximum temperature of the cartridge heaters. All the thermocouple readings were acquired using an Agilent 34970A data acquisition unit every 10 s. The input power was measured electrically using the power supply voltmeter and ammeter. The power supply, cooling water chiller, and the data acquisition were connected to the PC and were controlled and monitored using a MATLAB script. The photos were acquired at 240 fps using a Sony DEF-1709-802 camera module.

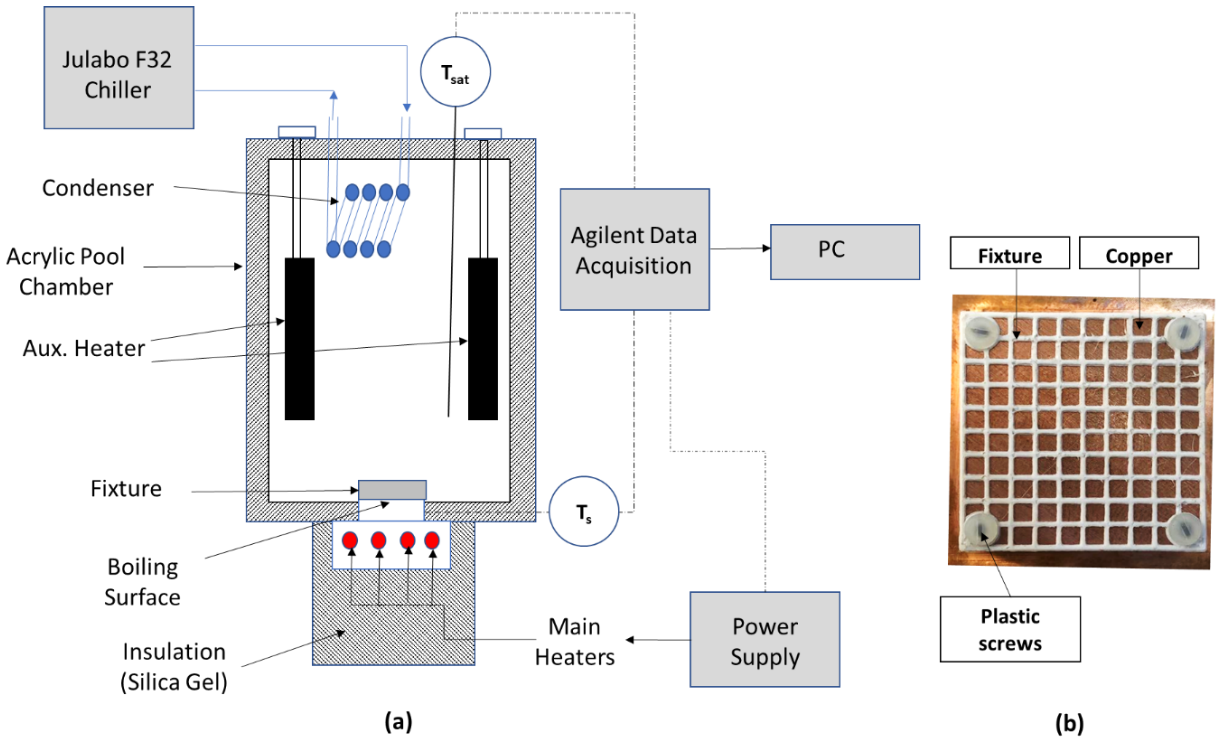

Figure 4-6: (a) Pool boiling heat transfer apparatus, (b) 3D-printed fixture attached to the surface.

4.3.2 Testing Procedure

Before each run, the deionized water was heated to saturation conditions using the auxiliary heaters incorporated in the boiling chamber, and an additional heating time of approximately 20 min was included to reduce any non-condensable gases dissolved in the water. The input power was increased by 10 W/cm^2 and the system allowed to come to steady state until reaching the CHF. The CHF was identified when the surface temperature encountered an abrupt temperature rise. At CHF the power supply to the heaters was turned off when the surface temperature reached 180 ˚C to guarantee safe operation of the heaters. Steady-state conditions were verified at each heat flux when the surface temperature change was not more than 0.1 ˚C over 100 seconds. The heat flux was measured as

$$q'' = \frac{V\ I}{A} \tag{4.5}$$

where, V is the voltage imposed across the heaters, I is the current draw, and A is the boiling surface area. The boiling heat transfer coefficient is then calculated as

$$h = \frac{q''}{T_s - T_{sat}} \tag{4.6}$$

where T_{sat} is the working fluid saturation temperature, and T_s is the surface temperature given by

$$T_s = T_m - \frac{q''\ \Delta z}{k} \tag{4.7}$$

where T_m is the measured temperature at distance $\Delta z = 2\ mm$ from the boiling surface and k is the thermal conductivity of the copper heating block.

4.3.3 Uncertainty Analysis

The uncertainties for all measured quantities are listed in Table 4-5.

Table 4-5. Uncertainties in the measured variables.

Parameter	Uncertainty
Boiling surface area, A	1 x 10^{-5} (m^2)
Thermocouples	0.5 K
Voltage	0.1% of reading ± 2 digits
Current	0.3% of reading ± 2 digits

The error propagation method of [35] was used to estimate the resulting uncertainty in the calculated quantities. This method applied to the heat transfer coefficient is given by

$$U_h = \sqrt{\begin{gathered}\left(\frac{\partial h}{\partial V} U_V\right)^2 + \left(\frac{\partial h}{\partial I} U_I\right)^2 + \\ \left(\frac{\partial h}{\partial T_s} U_{T_s}\right)^2 + \left(\frac{\partial h}{\partial T_{sat}} U_{T_{sat}}\right)^2 + \left(\frac{\partial h}{\partial A} U_A\right)^2\end{gathered}} \tag{4.8}$$

where U_i is the uncertainty of quantity i. Generally, the maximum uncertainties in the input power, the heat transfer coefficient, and the heat flux were found to be less than 3%, 13% and 5%, respectively.

4.4 Results and Discussion

4.4.1 Baseline Results for a Bare Surface

The apparatus was validated by performing some initial baseline tests using the bare copper surface and comparing the results to studies from the literature [11], [24], [36], [37] as depicted in Figure 4-7. Overall, the agreement is reasonable. The discrepancy between the results can be attributed to different parameters, such as the heater size, surface roughness, contact angle, and surface aging.

The repeatability of the current setup was characterized by carrying out two tests for the bare surface and good repeatability was demonstrated, as shown in Figure 4-7.

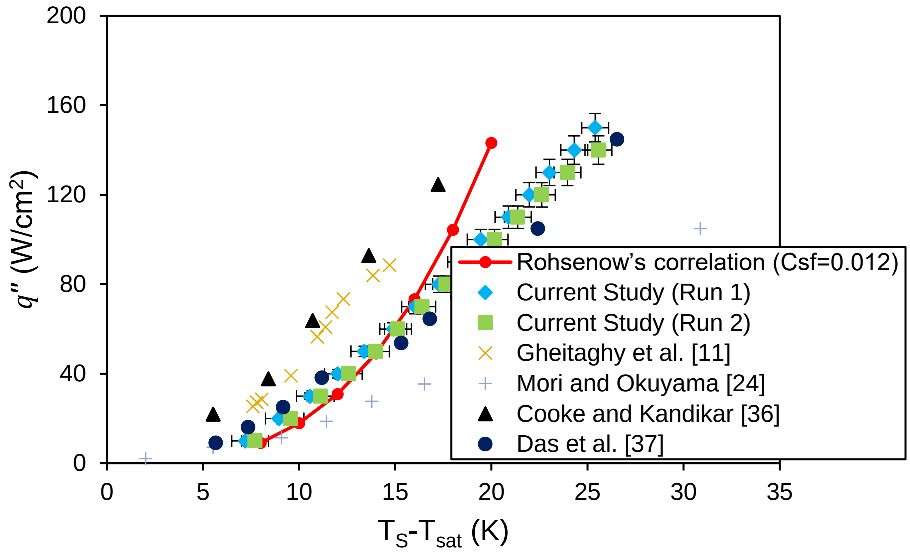

Figure 4-7**:** Validation of the current study for bare copper with studies from the literature [11], [24], [36], [37].

4.4.2 Working Principle of the Fixtures

Decreasing the heater size increases the CHF by delaying the horizontal coalescence of the vapour bubbles and increasing the liquid supply from the heater surface edges, which has been demonstrated by [38].The boiling fixture in the present study has the same effect by dividing the heating area into small areas that work as individual heaters until coalescence happens above the fixture.

Photos of the transient bubble dynamics for Fixture D at a low heat flux of 10 W/cm^2 are shown in Figure 4-8. The bubble dynamics are represented schematically in Figure 4-9 for different heat fluxes. Figure 4-8 shows the two-phase flow from two different views; however, they are not synchronized. The bubbles initiate at the interface between the surface and the fixture. These corners seem to work as small cavities capable of trapping the vapour and initiating the bubbles. The bubbles were directed toward the centre of the unit cells due to the associated momentum force, F_m, emerging from phase change from liquid to vapour, as shown in Figure 4-9. As the bubbles grow, they may coalesce before detaching from the surface, as shown in Figure 4-8. At high heat fluxes, a large bubble occupies each unit cell and merges with bubbles from the other cells, until it covers the whole fixture with a vapour film and causes the CHF, as shown in Figure 4-9.

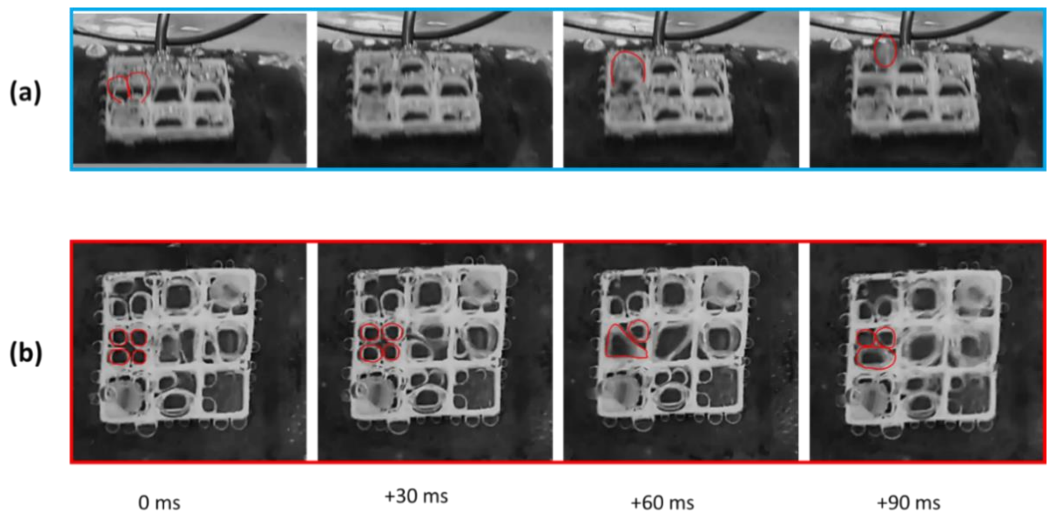

Figure 4-8**:** Bubble nucleation through Fixture D at a heat flux of 10 W/cm^2: (a) oblique view, (b) top view.

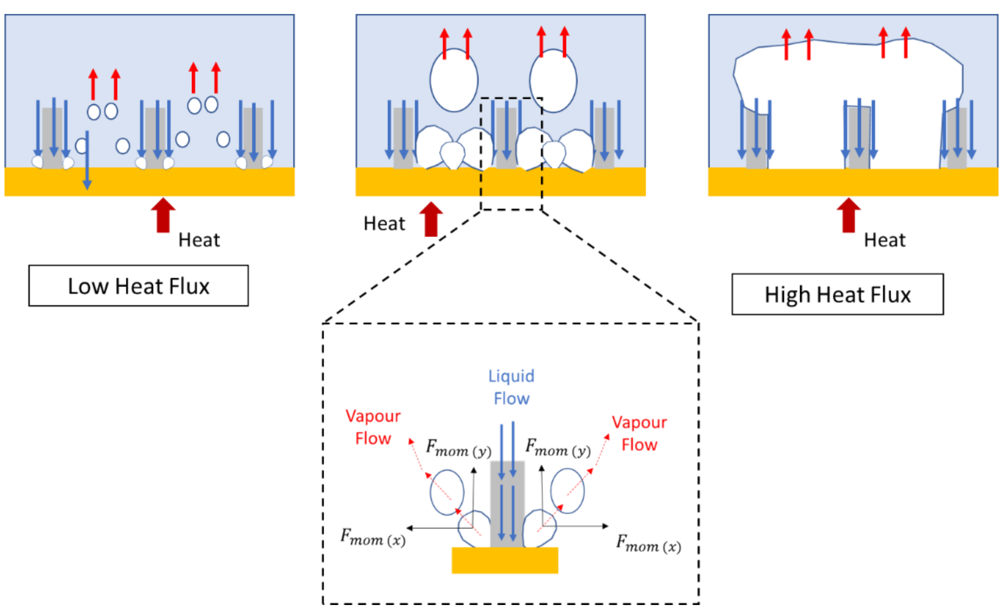

Figure 4-9**:** Schematic of bubble nucleation and coalescence with increasing heat flux.

The fixture walls remain wet and supply the bare area of the boiling surface, which can be explained using the thermal analysis in Figure 4-10. The thermal resistance of the 3D-printed fixture is relatively large due to the low conductivity of PLA which causes the heat to preferentially flow through the uncovered area of the surface and triggers the bubbles' initiation mechanism. So, no bubbles are generated from the polymer fixture walls, keeping it wetted with the liquid phase. The resistance, R_{con}, shown in Figure 4-10a, is a result of the imperfect attachment that may exist between the fixture and the boiling surface.

In essence, the main function of the fixture can be summarized in three points. First, it makes the heat preferentially transfer to the bare area of the copper, hence creating a thermal gradient along the boiling surface, increasing the temperature locally at the uncovered area of the boiling surface, initiating the bubbles early, even at low heat fluxes. Second, it divides the boiling surface into small heaters and delays the bubbles' horizontal coalescence such that this happens outside the fixture, hence increasing the CHF. Third, it separates the liquid and vapour phases as well as provides a wick structure that can facilitate liquid wicking to the heating surface. The phase separation happens under the influence of the momentum force (shown in Figure 4-9) induced by the fin effect explained in [39], which makes the bubbles be directed away from the fixture walls.

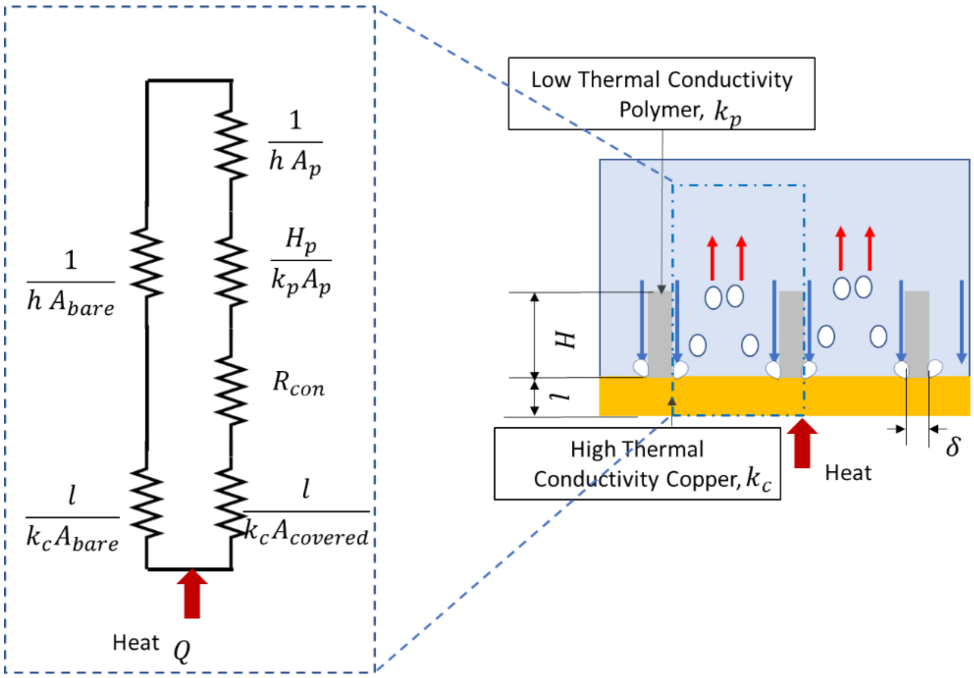

(a)

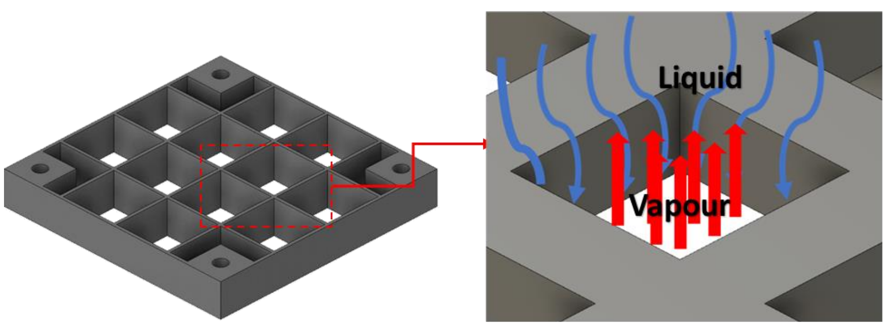

(b)

Figure 4-10**:** (a) thermal circuit of the copper-polymer combination (b) liquid and vapour paths.

4.4.3 Effect of the Fixture Unit Cell Size

As established in the previous section, the bubbles nucleate at the polymer–copper interface and coalesce following the fixture pattern. Therefore, by changing the geometrical variables of the fixture, we were able to control the nucleation sites, especially at low heat flux. The effect of unit cell size is shown in Figure 4-11 and Figure 4-12. Decreasing the cell size enhanced the heat transfer coefficient in the nucleation zone; however, it had an adverse effect on the CHF. This can be explained with the help of the flow visualization photos for different cell sizes at the same fixture height of 2 mm, as depicted in Figure 4-13. These photos suggest that the cell size dictates the bubbles' size over the heating surface. For instance, the small cell size, Fixture E in Figure 4-13a (iii), imposed a smaller bubble size compared with other cases, which we conjecture has a direct effect on the bubble departure diameter frequency. We hypothesize that small cell size fixtures decrease the bubble departure diameter and increase the frequency, which enhances the heat transfer coefficient at low heat fluxes. Moreover, small-sized unit cells impose more corners over the boiling surface and generate more bubbles at a lower wall superheat. However, at high heat fluxes, the contribution of the small unit cell fixture becomes detrimental because a relatively moderate percentage of the boiling area is covered with a low-conductivity material, as discussed previously. The heat transfer coefficient reached a maximum of 7.7 W/cm^{2}K for Fixture E at a heat flux of 120 W/cm^2, which represents a 45% improvement over the bare surface. However, The HTC enhancement hit its maximum at a heat flux of 10 W/cm^2 and was about 81% for the same fixture.

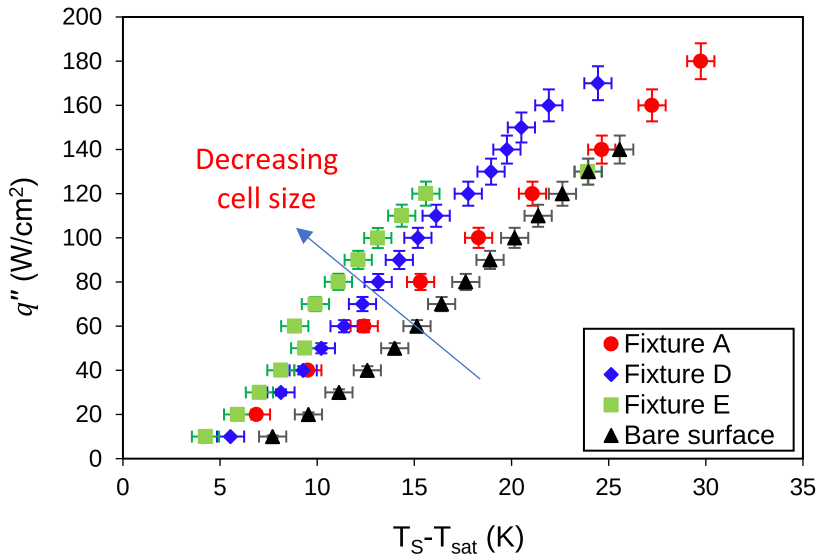

(a)

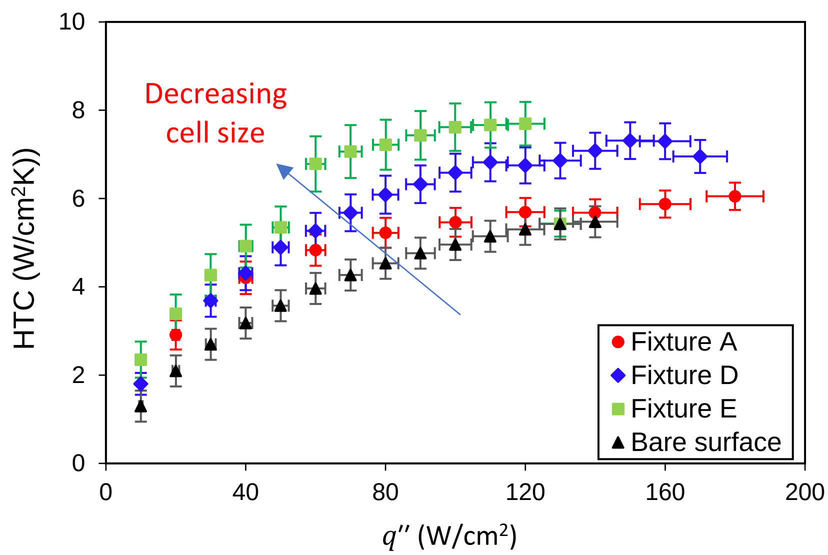

(b)

Figure 4-11**:** The effect of the fixture unit cell size on (a) boiling curve, (b) heat transfer coefficient (HTC).

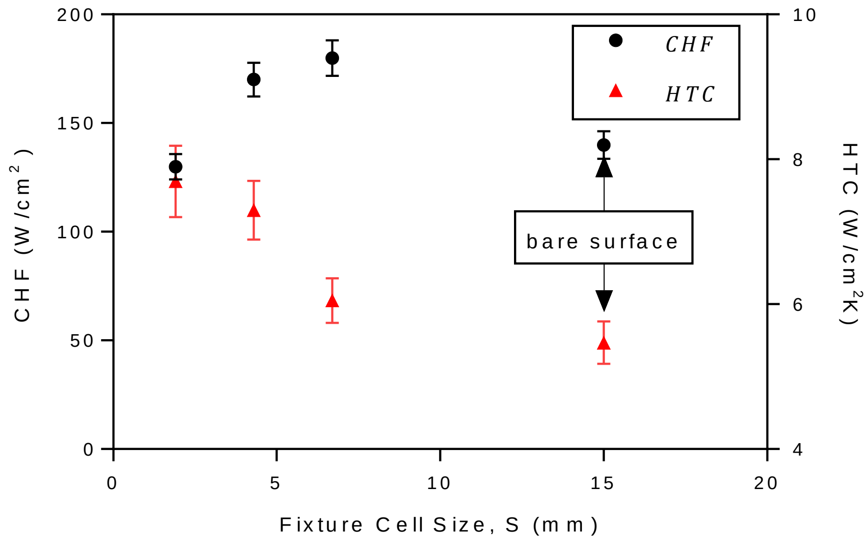

Figure 4-12**:** The effect of the fixture unit cell size on the maximum HTC and the CHF.

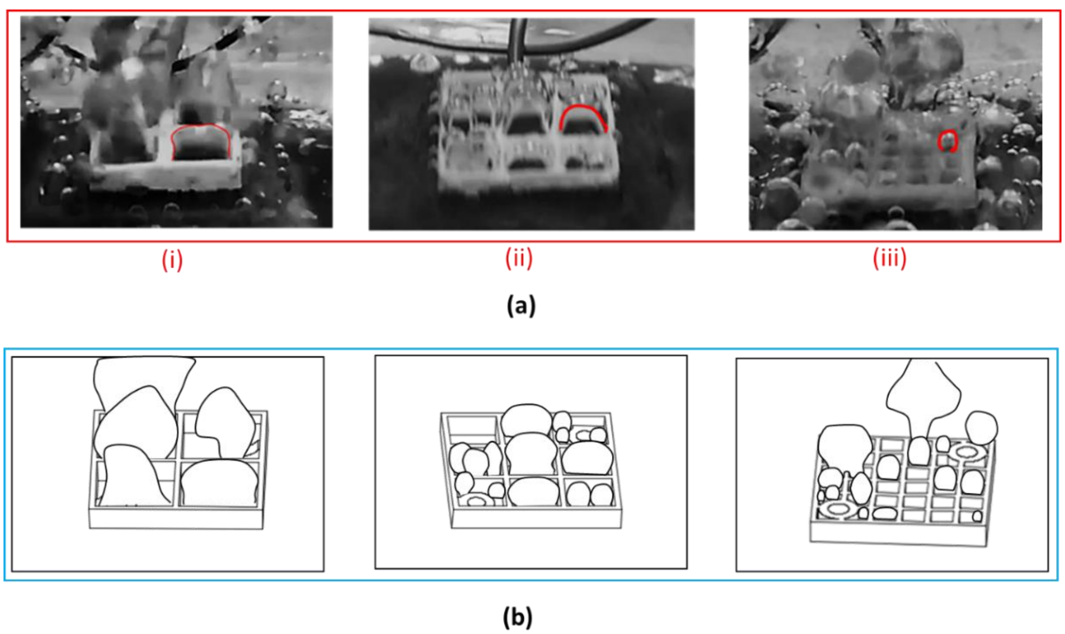

Figure 4-13: (a) Photos of bubble dynamics for different fixtures, with different cell sizes at a fixture height of 2 mm at heat flux of 10 W/cm^2: (i) Fixture A, *S*= 6.7 mm, (ii) Fixture D, S= 4.3 mm, (iii) Fixture E, *S*= 1.9 mm; (b) A schematic of the bubbles' behaviour at different fixture cell sizes.

4.4.4 Effect of Fixture Height

The effect of fixture wall height was investigated at the largest unit cell with a width of 6.7 mm. The influence of fixture wall height on the boiling curve and the heat transfer coefficient is shown in Figure 4-14 and Figure 4-15. Here, all the fixtures achieved a higher heat transfer coefficient at low heat fluxes compared with the bare surface. However, increasing the fixture height deteriorated the heat transfer coefficient at low and high heat fluxes, and also decreased the CHF compared with the smallest fixture height (*Fixture A*). The maximum improvement of the CHF occurred at the smallest height of 2 mm, which represents a 29% improvement in CHF compared with the bare surface. Increasing the fixture height delayed the coalescence of the bubbles to further downstream in the pool at low heat fluxes. Note the difference between Figure 4-16 and Figure 4-17, which shows that the coalescence was delayed so as to happen further downstream and there was an increase in the time during which the bubbles escape and dissipate their stored energy, which resulted in a lower heat transfer coefficient.

The fixture delayed the formation of the large mushroom bubble outside of the fixture at the CHF, as discussed previously. However, large fixture heights cause high friction losses for the vapour phase, especially at high heat fluxes and mitigate the effect of the convection currents happening outside the surface, hence decreasing the CHF.

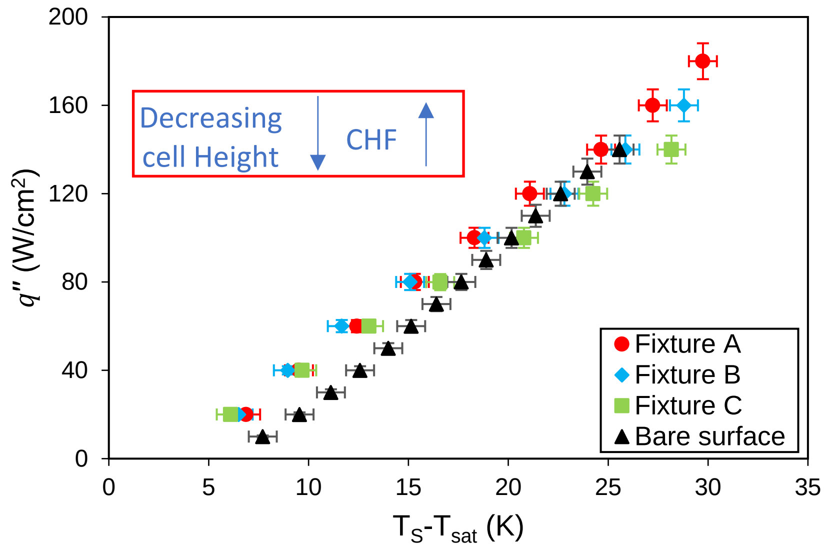

(a)

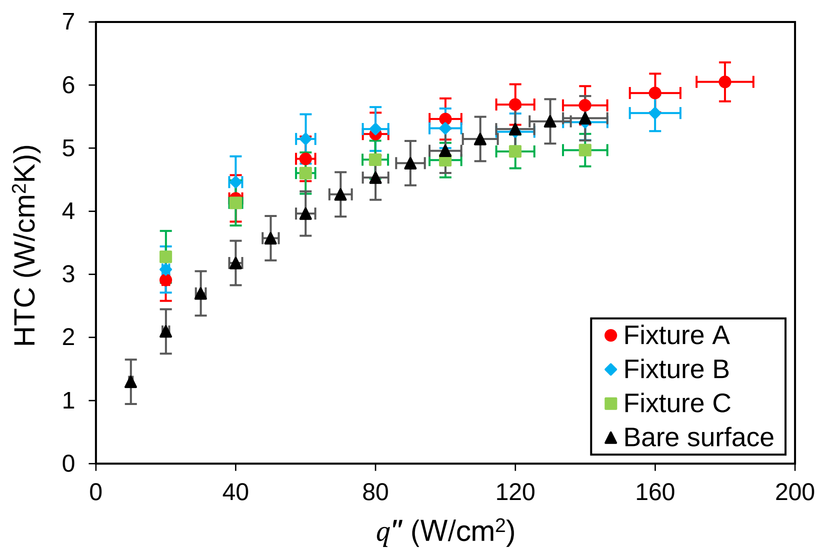

(b)

Figure 4-14**:** The effect of the fixture height, (a) boiling curve, (b) heat transfer coefficient.

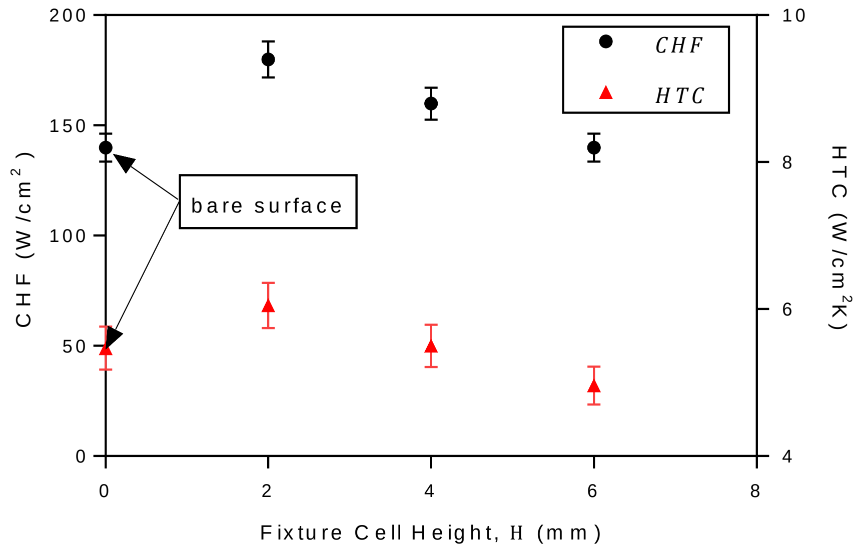

Figure 4-15**:** The effect of the fixture height on the maximum HTC and the CHF.

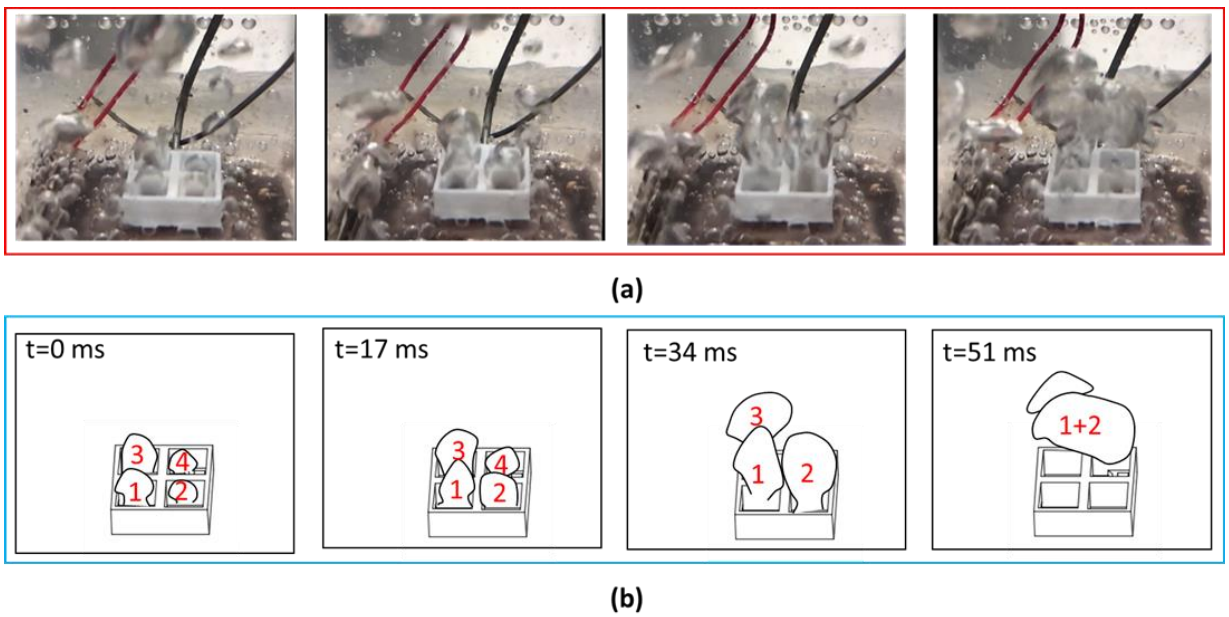

Figure 4-16**:** (a) Photos of bubble dynamics for a unit cell with a size of 6.7 mm at a heat flux of 10 W/cm^2 for Fixture B, *H*= 4 mm; (b) A schematic showing the behaviour of the bubble for Fixture B, *H*= 4 mm.

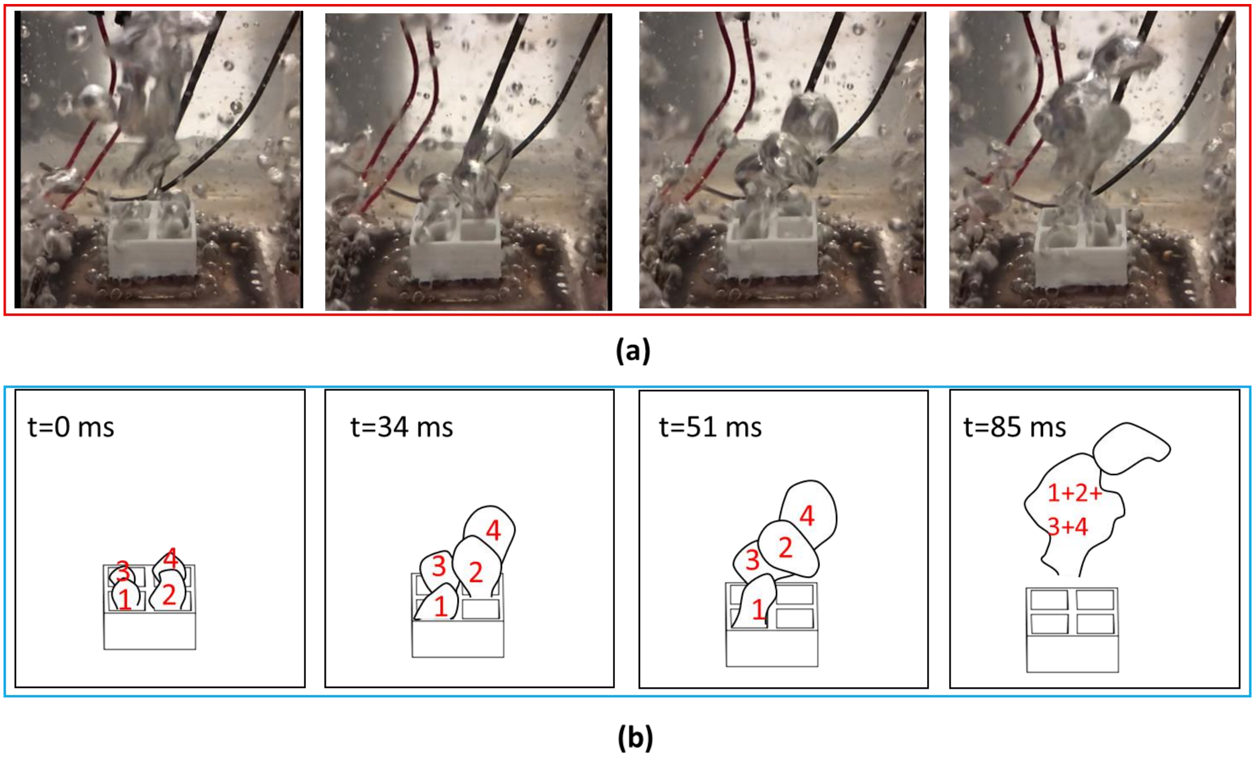

Figure 4-17**:** (a) Photos of bubble dynamics for a unit cell size of 6.7 mm at a heat flux of 10 W/cm^2 for Fixture C, *H*= 6 mm; (b) A schematic showing the behaviour of the bubble for Fixture C, *H*= 6 mm.

The effect of the fixture height on the vapour pressure drop through the fixture channels and also on the wickability of the fixture itself can be explained by the application of the viscous-capillary limit CHF model, which was employed in [19] for a porous material, and also in [24] for a porous honeycomb. This model depends on the assumption that the CHF is triggered when the pressure drop encountered by the liquid–vapour path reached the maximum capillary limit of the wick material. The liquid–vapour flow path through the fixture is shown in Figure 4-18a.

$$\Delta p_{c,max} = \Delta p_l + \Delta p_v + \Delta p_a \tag{4.9}$$

where, Δp_l, and Δp_v are the frictional pressure drop for the liquid and the vapour phases, respectively, while Δp_a is the accretional pressure drop originated from the phase change.

This model postulates that near the CHF the fixture walls are only occupied by the water phase, and no dry-out happens below or inside the fixture, while the fixture channels are filled with the vapour phase. For more details about this model, the reader is referred to the work carried out by [24]. By using the Darcy equation for the frictional pressure drop for both phases, Eq. (4.9) can be written as follows:

$$\Delta p_{c,max} = \frac{\mu_l Q_{max} H_p}{K A_W \rho_l h_{fg}} + \frac{32\mu_v H_p Q_{max}}{\rho_v n S^4 h_{fg}} + \frac{\rho_v}{2}\left(\frac{Q_{max}}{(\rho_v n S^2) h_{fg}}\right)^2 \tag{4.10}$$

where μ_l, μ_v, ρ_l and ρ_v are the liquid viscosity, the vapour viscosity, the liquid density, and the vapour density, respectively, while h_{fg} is the latent heat of vaporization. A_W, n, S and H_p are the contact area, number of cells or channels, cell size, and the height of the fixture, respectively, as given in Table 4-1. K and $\Delta p_{c,max}$ are the permeability and maximum capillary pressure, which are considered to be the key factors for any wick or porous material [31], and were measured experimentally as described in Section 4.2.2. Q_{max} is the maximum heat transfer rate. Equation (4.10) is a simple quadratic function, which can be solved to predict the CHF as follows:

$$q_{CHF} = \frac{Q_{max}}{A} = \frac{-B + \sqrt{B^2 + 4C\left(2\sigma / r_{eff}\right)}}{2AC} \tag{4.11}$$

where A and B are given as follows:

$$B = \frac{\mu_l H_p}{K A_W \rho_l h_{fg}} + \frac{32\mu_v H_p}{\rho_v n S^4 h_{fg}}, \quad C = \frac{\rho_v}{2}\left(\frac{1}{\left(\rho_v n S^2 h_{fg}\right)}\right)^2 \tag{4.12}$$

Figure 4-18 shows the effect of the fixture height on the CHF and compares it with the viscous–capillary model given by Eq. (4.10). The permeability and capillary pressure for Sample II from Table 4-4 were utilized to predict the CHF using the model because the wicking liquid is transported to the boiling surface through the fixture, perpendicular to printing roads. See Figure 4-1 for the traces of the printed road in the sliced printed fixture. Although the rate-of-rise for other samples is higher, as shown in Figure 4-4, it was tricky to print the fixtures in such a way that the printing roads were perpendicular to xy plane in Figure 4-1. An attempt was made to print the fixtures with support material in the same build direction as in Sample I in Figure 4-2; however, the resulting fixture was very weak because the fixture wall thickness and height was small. Future work could determine the best printing parameters, perhaps using a smaller nozzle and an easy-to-remove support. It is indicated that the model predicted well the falling trend of the CHF with the increase in fixture height. The fixture height increase expanded the liquid–vapour path, shown in Figure 4-18a and, hence, increased the resulting frictional pressure drop for both phases, as given by Eq. (4.10). It is worth mentioning that the predicted values have an error and are higher when compared with the experimental results, especially at large fixture heights. This pertains to the model assumption that the dry-out will not happen near the fixture wall; however, it is probable this will occur because the polymer has a very low thermal conductivity compared with the copper boiling surface, as highlighted in Section 4.4.2.

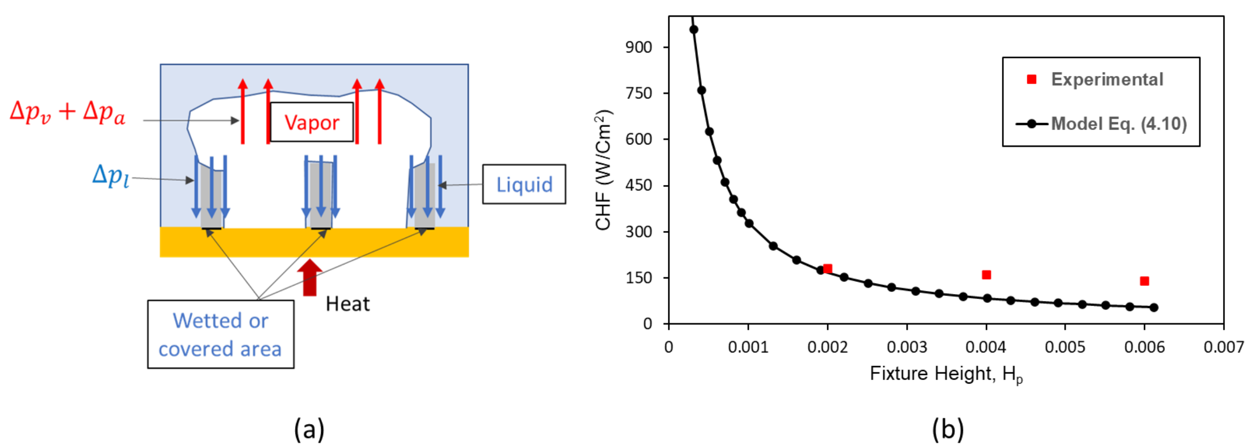

Figure 4-18**:** a) the liquid–vapour path used for the CHF viscous-capillary model, b) comparison between the CHF model and the experimental results for the fixture height effect.

4.4.5 Comparison with Relevant Studies from The Literature

The results for the current fixture were compared with other experimental work for fixtures from the literature, as shown in Figure 4-19. It is indicated that the current fixture achieved lower wall superheat—hence, better HTC—compared with the honeycomb fixture [24] and metallic wire fixture [23]. However, the honeycomb fixture achieved the maximum CHF. The main advantage of the current fixture comes from the employment of a commercially accessible low-cost thermoplastic 3D-printing method to fabricate a low conductive porous customizable wick material. For instance, the metallic wire mesh used in [23] needed an initial electrochemical etching process to generate internal nano- or micropores inside. The geometric optimization for the honeycomb fixture carried out by [24] was not possible because this fixture is an off-the-shelf porous plate that was originally used as an air filter. Moreover, the FFF manufacturing method can be potentially optimized to tailor the wick porous material parameters, such as porosity, permeability, and the effective pore radius through changing the printing parameters.

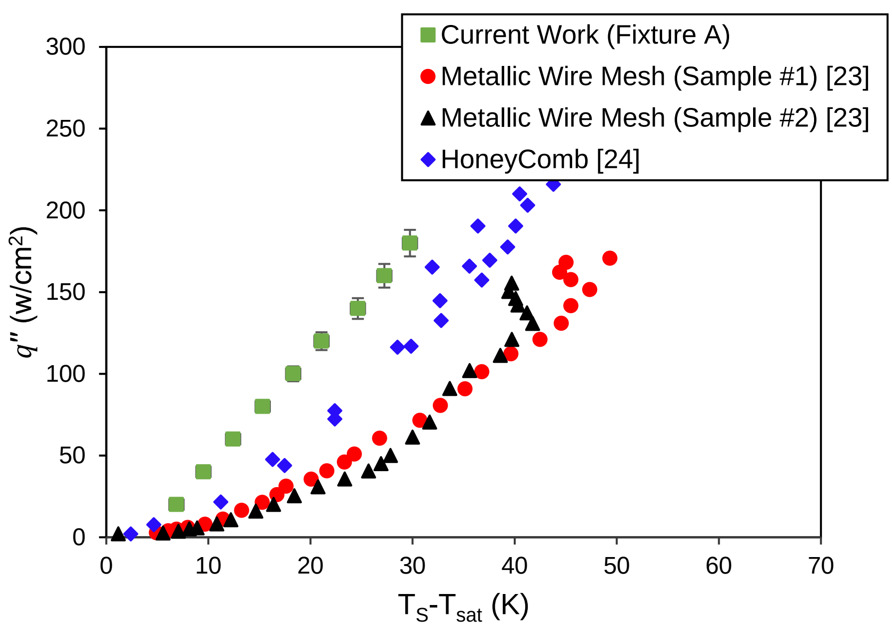

Figure 4-19: Comparison between the current study and few studies from the literature.

4.5 Summary and Outlook

In the current chapter, we investigated the capability of using low-cost additive manufacturing FFF to fabricate a low conductive wick for enhancing the CHF and HTC. The wickability performance of the printed parts was investigated through the rate-of-rise method. A series of saturated pool boiling experiments of deionized water were performed for copper surfaces with 3D-printed porous polymer fixtures at 1 atm. Two geometrical parameters of the fixture were examined: the fixture height and the unit cell size. The main findings are summarized in the following points:

- The FFF additive manufacturing created internal voids and pores through the fabricated fixture, which work as capillaries capable of wicking the liquid. The wickability performance of the 3D-printed structure depends on the process variables and the build orientation in particular.
- The capillary pressure along the direction of the printing road was higher compared with the other directions due to the existence of a continuous pores network.
- Decreasing the fixture cell size at the same height of 2 mm showed a superior heat transfer coefficient, which reached up to an 81% increase compared with the plain surface.
- Increasing the fixture height at the same cell size of 6.7 mm degraded the CHF. A small fixture height achieved a 20% augmentation in CHF as compared with plain surfaces.
- The viscous-capillary model predicted well the trend of changing the fixture height on the CHF and showed that increasing the fixture height increased the frictional pressure drop through the fixture cells for the vapour phase and also for the liquid flow through the fixture pores.

4.6 References

[1] H.-Y. Kim, Y. G. Kim, and B. H. Kang, "Enhancement of natural convection and pool boiling heat transfer via ultrasonic vibration," in ASME 2003 Heat Transfer Summer Conference, 2003, pp. 295–302.

[2] M. Sheikhbahai, M. Nasr Esfahany, and N. Etesami, "Experimental investigation of pool boiling of Fe3O4/ethylene glycol-water nanofluid in electric field," Int. J. Therm. Sci., vol. 62, pp. 149–153, 2012, doi: 10.1016/j.ijthermalsci.2011.10.004.

[3] A. Suriyawong, S. Saisorn, and S. Wongwises, "Pool boiling heat transfer enhancement of distilled water with passive rotating blades installed above the heating surface," Exp. Therm. Fluid Sci., vol. 87, pp. 109–116, 2017, doi: 10.1016/j.expthermflusci.2017.04.025.

[4] S. M. You, J. H. Kim, and K. H. Kim, "Effect of nanoparticles on critical heat flux of water in pool boiling heat transfer," Appl. Phys. Lett., vol. 83, no. 16, pp. 3374–3376, 2003, doi: 10.1063/1.1619206.

[5] H. Kim, H. S. Ahn, and M. H. Kim, "On the Mechanism of Pool Boiling Critical Heat Flux Enhancement in Nanofluids," J. Heat Transfer, vol. 132, no. 6, p. 061501, 2010, doi: 10.1115/1.4000746.

[6] M. A. Chan, C. R. Yap, and K. C. Ng, "Pool Boiling Heat Transfer of Water on Finned Surfaces at Near Vacuum Pressures," J. Heat Transf., vol. 132, no. 3, pp. 1–6, 2010, doi: 10.1115/1.4000054.

[7] Y. Sun, G. Chen, S. Zhang, Y. Tang, J. Zeng, and W. Yuan, "Pool boiling performance and bubble dynamics on microgrooved surfaces with reentrant cavities," Appl. Therm. Eng., vol. 125, pp. 432–442, 2017, doi: 10.1016/j.applthermaleng.2017.07.044.

[8] A. Suszko and M. S. El-Genk, "Bubbles Transient Growth in Saturation Boiling of PF-5060 Dielectric Liquid on Dimpled Cu Surfaces," J. Therm. Sci. Eng. Appl., vol. 8, no. 2, p. 021016, 2016, doi: 10.1115/1.4032367.

[9] T. Halon, B. Zajaczkowski, S. Michaie, R. Rulliere, and J. Bonjour, "Experimental study of low pressure pool boiling of water from narrow tunnel surfaces," Int. J. Therm. Sci., vol. 121, pp. 348–357, 2017, doi: 10.1016/j.ijthermalsci.2017.07.028.

[10] D. E. Kim, D. I. Yu, D. W. Jerng, M. H. Kim, and H. S. Ahn, "Review of boiling heat transfer enhancement on micro/nanostructured surfaces," Exp. Therm. Fluid Sci., vol. 66, pp. 173–196, 2015, doi: 10.1016/j.expthermflusci.2015.03.023.

[11] A. M. Gheitaghy, H. Saffari, and M. Mohebbi, "Investigation pool boiling heat transfer in U-shaped mesochannel with electrodeposited porous coating," Exp. Therm. Fluid Sci., vol. 76, pp. 87–97, 2016, doi: 10.1016/j.expthermflusci.2016.03.011.

[12] G. Liang and I. Mudawar, “Review of pool boiling enhancement by surface modification,” Int. J. Heat Mass Transf., vol. 128, pp. 892–933, 2019, doi: 10.1016/j.ijheatmasstransfer.2018.09.026.

[13] L. Lin and M. A. Kedzierski, “Review of low-GWP refrigerant pool boiling heat transfer on enhanced surfaces,” Int. J. Heat Mass Transf., vol. 131, pp. 1279–1303, 2019, doi: 10.1016/j.ijheatmasstransfer.2018.11.142.

[14] S. Jun, J. Kim, D. Son, H. Y. Kim, and S. M. You, “Enhancement of Pool Boiling Heat Transfer in Water Using Sintered Copper Microporous Coatings,” Nucl. Eng. Technol., vol. 48, no. 4, pp. 932–940, 2016, doi: 10.1016/j.net.2016.02.018.

[15] T. M. Anderson and I. Mudawar, “Microelectronic cooling by enhanced pool boiling of a dielectric fluorocarbon liquid,” J. Heat Transfer, vol. 111, no. 3, pp. 752–759, 1989, doi: 10.1115/1.3250747.

[16] R. J. MacNamara, T. L. Lupton, R. Lupoi, and A. J. Robinson, “Enhanced nucleate pool boiling on copper-diamond textured surfaces,” Appl. Therm. Eng., vol. 162, no. December 2018, p. 114145, 2019, doi: 10.1016/j.applthermaleng.2019.114145.

[17] J. Y. Chang and S. M. You, “Enhanced boiling heat transfer from micro-porous surfaces: Effects of a coating composition and method,” Int. J. Heat Mass Transf., vol. 40, no. 18, pp. 4449–4460, 1997, doi: 10.1016/S0017-9310(97)00057-4.

[18] C. M. Patil, K. S. V. Santhanam, and S. G. Kandlikar, “Development of a two-step electrodeposition process for enhancing pool boiling,” Int. J. Heat Mass Transf., vol. 79, pp. 989–1001, 2014, doi: 10.1016/j.ijheatmasstransfer.2014.08.062.

[19] M. Ha and S. Graham, “Pool boiling characteristics and critical heat flux mechanisms of microporous surfaces and enhancement through structural modification,” Appl. Phys. Lett., vol. 111, no. 9, 2017, doi: 10.1063/1.4999158.

[20] S. G. Liter and M. Kaviany, “Pool-boiling CHF enhancement by modulated porous-layer coating: Theory and experiment,” Int. J. Heat Mass Transf., vol. 44, no. 22, pp. 4287–4311, 2001, doi: 10.1016/S0017-9310(01)00084-9.

[21] C. M. Patil and S. G. Kandlikar, “Review of the manufacturing techniques for porous surfaces used in enhanced pool boiling,” Heat Transf. Eng., vol. 35, no. 10, pp. 887–902, 2014, doi: 10.1080/01457632.2014.862141.

[22] R. P. Rioux, E. C. Nolan, and C. H. Li, “A systematic study of pool boiling heat transfer on structured porous surfaces: From nanoscale through microscale to macroscale,” AIP Adv., vol. 4, no. 11, 2014, doi: 10.1063/1.4902343.

[23] H. Kim, Y. Park, H. Kim, C. Lee, D. W. Jerng, and D. E. Kim, “Critical heat flux enhancement by single-layered metal wire mesh with micro and nano-sized pore structures,” Int. J. Heat Mass Transf., vol. 115, pp. 439–449, 2017, doi: 10.1016/j.ijheatmasstransfer.2017.08.066.

[24] S. Mori and K. Okuyama, “International Journal of Multiphase Flow Enhancement of the critical heat flux in saturated pool boiling using honeycomb porous media,” Int. J. Multiph. Flow, vol. 35, no. 10, pp. 946–951, 2009, doi: 10.1016/j.ijmultiphaseflow.2009.05.003.

[25] S. Mori, S. Mt Aznam, R. Yanagisawa, and K. Okuyama, “CHF enhancement by honeycomb porous plate in saturated pool boiling of nanofluid,” J. Nucl. Sci. Technol., vol. 53, no. 7, pp. 1028–1035, 2016, doi: 10.1080/00223131.2015.1087353.

[26] L. Trhlíková, O. Zmeskal, P. Psencik, and P. Florian, “Study of the thermal properties of filaments for 3D printing,” AIP Conf. Proc., vol. 1752, no. 2016, 2016, doi: 10.1063/1.4955258.

[27] A. Elkholy, M. Rouby, and R. Kempers, “Characterization of the anisotropic thermal conductivity of additively manufactured components by fused filament fabrication,” Prog. Addit. Manuf., vol. 4, no. 4, pp. 497–515, 2019, doi: 10.1007/s40964-019-00098-2.

[28] “Polylactic Acid (PLA, Polylactide) :: MakeItFrom.com.” https://www.makeitfrom.com/material-properties/Polylactic-Acid-PLA-Polylactide (accessed Jan. 01, 2020).

[29] X. Wang, L. Zhao, J. Y. H. Fuh, and H. P. Lee, “Effect of porosity on mechanical properties of 3D printed polymers: Experiments and micromechanical modeling based on X-ray computed tomography analysis,” Polymers (Basel)., vol. 11, no. 7, 2019, doi: 10.3390/polym11071154.

[30] K. G. J. Christiyan, U. Chandrasekhar, and K. Venkateswarlu, “A study on the influence of process parameters on the Mechanical Properties of 3D printed ABS composite,” IOP Conf. Ser. Mater. Sci. Eng., vol. 114, p. 012109, 2016, doi: 10.1088/1757-899X/114/1/012109.

[31] D. Deng, Y. Tang, G. Huang, L. Lu, and D. Yuan, “Characterization of capillary performance of composite wicks for two-phase heat transfer devices,” Int. J. Heat Mass Transf., vol. 56, no. 1–2, pp. 283–293, 2013, doi: 10.1016/j.ijheatmasstransfer.2012.09.002.

[32] Y. Tang, D. Deng, G. Huang, Z. Wan, and L. Lu, “Effect of fabrication parameters on capillary performance of composite wicks for two-phase heat transfer devices,” Energy Convers. Manag., vol. 66, pp. 66–76, 2013, doi: 10.1016/j.enconman.2012.09.027.

[33] S. Zhang et al., “Experimental study on the capillary performance of aluminum micro-grooved wicks with reentrant cavity array,” Int. J. Heat Mass Transf., vol. 139, pp. 917–927, 2019, doi: 10.1016/j.ijheatmasstransfer.2019.05.091.

[34] J. Zeng, L. Lin, Y. Tang, Y. Sun, and W. Yuan, “Fabrication and capillary characterization of micro-grooved wicks with reentrant cavity array,” Int. J. Heat Mass Transf., vol. 104, no. January, pp. 918–929, 2017, doi: 10.1016/j.ijheatmasstransfer.2016.09.007.

[35] S. J. Kline, “Describing uncertainty in single sample experiments,” Mech. Eng., vol. 75, pp. 3–8, 1953.

[36] D. Cooke and S. G. Kandlikar, “Effect of open microchannel geometry on pool boiling enhancement,” Int. J. Heat Mass Transf., vol. 55, no. 4, pp. 1004–1013, 2012, doi: 10.1016/j.ijheatmasstransfer.2011.10.010.

[37] A. K. Das, P. K. Das, and P. Saha, "Nucleate boiling of water from plain and structured surfaces," Exp. Therm. Fluid Sci., vol. 31, no. 8, pp. 967–977, 2007, doi: 10.1016/j.expthermflusci.2006.10.006.

[38] S. M. Kwark, M. Amaya, R. Kumar, G. Moreno, and S. M. You, "Effects of pressure, orientation, and heater size on pool boiling of water with nanocoated heaters," Int. J. Heat Mass Transf., vol. 53, no. 23–24, pp. 5199–5208, 2010, doi: 10.1016/j.ijheatmasstransfer.2010.07.040.

[39] S. G. Kandlikar, "Controlling bubble motion over heated surface through evaporation momentum force to enhance pool boiling heat transfer," Appl. Phys. Lett., vol. 102, no. 5, 2013, doi: 10.1063/1.4791682.

Chapter 5 A High-precision Experimental Facility for the Characterization of Pool Boiling Heat Transfer

In chapter 4, a proof-of-concept study was first conducted to investigate the enhancement of the boiling heat transfer coefficient through the attachment of polymer fixture to the conventional bare copper surface, which has been published and presented in the HEFAT2019 conference [1] and extended in a journal paper [2]. This study was implemented using a rudimentary boiling facility developed to prove the concept and establish a deep understanding of the pool boiling testing challenges. In this chapter, a world-class pool boiling apparatus was designed to allow for simultaneous flow visualization and characterization of the heat transfer coefficient (HTC) and the critical heat flux (CHF) for various material and refrigerant combinations. This apparatus incorporates many key features, such as the ability to swap the surface and also the capability to test different orientations of the surface. Consequently, this chapter is divided into two main parts. On one side, The first part details the main components of the new boiling apparatus. This apparatus was subsequently used to predict the measurement repeatability by investigating the effect of the surface oxidation and contamination on the pool boiling performance for bare copper surfaces. On the other side, the second part presents a new 3D structure fabricated from Al alloy via the SLM technique to enhance and control the pool boiling heat transfer rate.

5.1 Boiling facility

Over the last few decades, two-phase flow heat dissipation systems have been widely applied in several industries, such as power electronics, refrigeration, and chemical processing. Nucleate boiling offers the ability to transfer the heat efficiently for large distances owing to its HTC.

The experimental method for obtaining the boiling curve is commonly implemented using two approaches: either electrically powering a flat plain surface, representing a part of the bottom surface of the fluid pool, or powering a submerged immersion ribbon heater and measuring the resulting surface temperature. While the thermodynamic state of the working fluid is controlled through some auxiliary heaters either immersed in the pool or wrapped around the fluid vessel. The former approach is more popular and better for the visualization of bubble dynamics. However, the surface size needs to be carefully selected to be considered as an infinite heater [3,4]. Several key issues are associated with the pool boiling experimentation using this approach pertaining to the accuracy of the temperature measurement, heat loss minimization, measurement repeatability, etc. Most of these issues are described in this section.

Accurate prediction of the pool boiling curve pertains to the accuracy of the heat flux and surface temperature measurements, which was poorly implemented in some studies in the literature. For instance, these studies, such as in [5–8], quantified the input power electrically, neglecting the heat loss. Moreover, although all studies mentioned the uncertainties in the thermocouple's temperature readings, some did not predict the wall superheat's uncertainty at the boiling surface.

The repeatability of the measured HTC and CHF is one of the experimental challenges with pool boiling heat transfer research, demonstrated by comparing several studies available in the literature for a bare copper surface in Table 5-1and Figure 5-1. Here there exists a large discrepancy between the data, even with the same heater size. This is attributed to the variation in several parameters, such as the contact angle, surface roughness, and aging. On the other hand, having a different heater size and shape (circular/rectangular) can significantly influence the CHF, as highlighted by [3,4]. The CHF tends to increase with the heater size decrease due to the enhanced replenishing liquid supply at the heater sides. Although many studies showed a drastic improvement of both HTC and the CHF, it is hard to justify and compare their results due to neglecting the infinite conditions. To achieve the infinite conditions, the heater's characteristic dimensionless length should be larger than 20, as described in [3,4]. The heater's dimensionless size is defined as the ratio between the heater length and the capillary length of the working fluid.

Another issue that only a few previous studies touches is the induced convection current by the rising bubbles above a finite heater size. This secondary flow was seen by Borishanski to have a considerable effect on the CHF. This issue was investigated by Lienhard et al. [9], who introduced a new convection parameter in the popular Zuber correlation for predicting the peak heat flux. It is believed that this issue is highly pronounced when having a small ratio of the pool diameter to the main boiling surface. Consequently, the pool size should be large enough to mitigate this effect.

This chapter addresses these challenges and introduces the development and calibration of a high-accuracy pool boiling apparatus with a relatively large boiling surface area is detailed. This apparatus is unique primarily because it involves quantifying the input power thermally by measuring the axial temperature gradient through a well-calibrated meter bar, not only at the horizontal direction (surface angle, $\beta = 0$) but also for a wide range of angles up to 90 degrees, with large visualization field of view. This is done by rotating the whole rig employing a swing mechanism as explained later in this section.

Table 5-1. Bare surface conditions for several studies from the literature.

Study	**CHF (W/cm^2)**	**Heater geometry: *D or l* (mm)**	**Contact angle, θ°**	**Roughness, Ra, µm**
Yang et al. 2010 [10]	165	Rec. (12)	-	-
Kwark et al. 2010 [7]	101	Rec. (10)	-	-
Rioux et al. 2014[11]	123.23	Circ. (12.7)	73.26	0.0681
	157.87		53.73	0.288
Xu and Zhao 2015[12]	119	Rec. (25)	-	-
Shi et al. 2015 [13]	150	Rec. (10)	-	-
Rahman et al. 2015 [14]	116	Rec. (10)	-	-
Jaikumar and Kandlikar 2016 [15]	128	Rec. (10)	-	
Amir et al. 2016 [16]	87	Circ. (21)	70	0.2
Kim et al. 2016 [17]	76-160	Rec. (10)	55-85	0.041-2.3
Sun et al. 2017 [18]	121	Rec. (10)	-	-
Chen et al. 2019 [19]		Circ. (12.7)	-	-
Mac et al. 2019 [20]	115.9	Rec. (15)	84	0.25

Figure 5-2 shows a detailed view of the boiling facility used in the present investigation. It consists of three main parts: the boiling vessel, the input power module, and the vapor recovery unit. The boiling vessel comprises two flanged stainless-steel cylindrical pipes, sandwiching a chemical-resistant Viton gasket for sealing requirements. The upper pipe has a diameter of 8 in (202.7 mm) and a length of 18 in (450 mm) and includes four 4-inch (100 mm) sight glass ports for visualization purposes. The lower pipe is 6 in (152 mm) in diameter and encloses the heating system, whose top flange houses a 30 mm x 30 mm copper chip at its center, which serves as the boiling surface. Two compact PID-controlled 1 kW secondary immersion heaters with a nominal diameter of 5/8 inches (15.8 mm) and a heating length of 4 7/8 inches (123.8 mm) were used to maintain the thermodynamic state of the working fluid and overcome heat losses from the vessel body to the ambient.

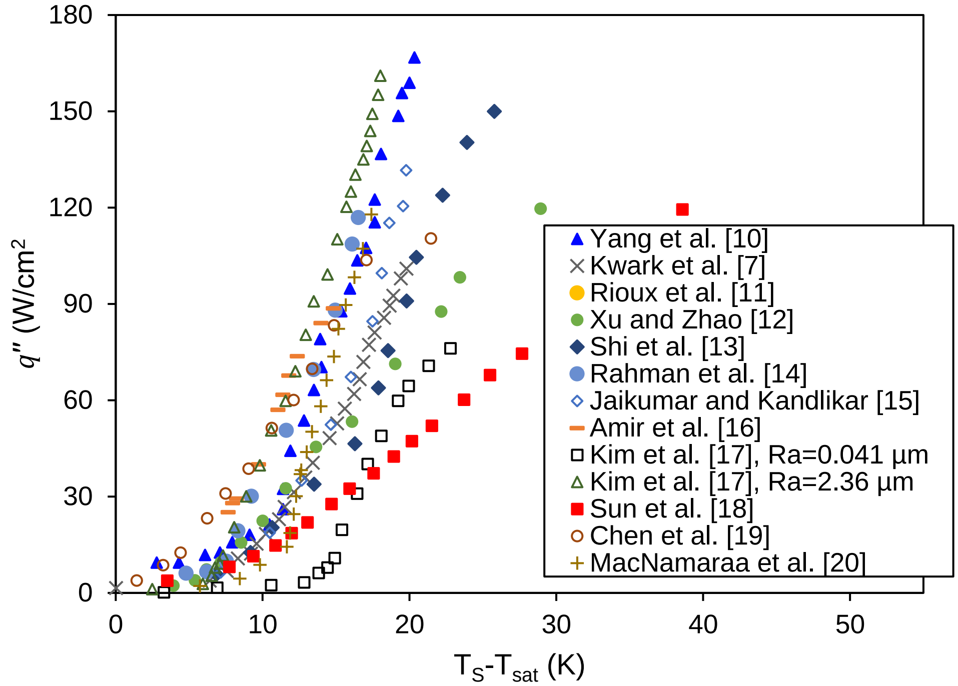

Figure 5-1. Comparison between some studies from the literature for the bare surface.

The area ratio of the pool to the boiling surface was designed to be larger than 30 to mitigate the effect of the convection currents induced by the auxiliary heaters. The boiling chamber is closed by a stainless-steel lid from the top, sealed by another Viton gasket, and clamped against the boiling vessel through eight ¾ inch stainless steel bolts.

The heating element assembly, shown in Figure 5-3, comprises seven main components: the boiling test section, sealing gaskets, PEEK base plate, the heating elements block, the meter bar support, insulation, and the enclosure. The heating block was machined from oxygen-free copper with thermal conductivity of 390 W/mK and divided into three sections: the power source section, the contraction section, and the metering section. The power source section is 55 mm x 50 mm x 47 mm and includes fourteen cartridge heaters. Each heater is rated for 500 W, with a diameter of 3/8 in (9.525 mm) and length of 2 in (50 mm) and fabricated from Inconel material with a maximum working temperature of 1400 °F (760 °C). The contraction section is designed to intensify the heat flux going to the meter bar and ultimately to the boiling surface.

The metering section (meter bar) is 40 mm in length and includes four holes of 0.5 mm in diameter 6 mm apart to incorporate K-type thermocouples to measure the thermal gradient, and hence calculating the heat flux flowing to the boiling surface. The boiling chip has a pocket 1.5 mm deep to facilitate its attachment to the meter bar. This stack was tightly clamped using two end flanges of the lower pipe. The effect of contact resistance was lessened by incorporating a silicone grease (Omega 201), with thermal conductivity around 2.3 W/mK. All the heating part components were wrapped with alumina-silicate ceramic insulation, with a maximum working temperature of 2010 °F (1098 °C), to minimize the heat losses and ensure the linearity of the temperature gradient.

The condensation system consisted of a helical-type coil, with a diameter of ¼ in (6.35 mm), situated above the free surface of the working fluid level to recycle the vapor back to the boiling chamber by circulating chilled cooling water at 20 ^{o}C. The pressure inside the chamber is maintained at atmospheric pressure by changing the water flow at each heat flux, along with a solenoid valve connected to a vacuum pump (Vacuubrand MZ 2C NT +2AK). The solenoid valve was set to open when the pressure exceeded 1.01 bar. The pressure inside the tank was monitored remotely, using Gems transducer (Model 2200BG6F002233DA) and visually using a Winters PEM gauge pressure (Model PEM154). The resulting fluctuations were approximately ±0.5 kPa. All sensors and valves were incorporated into the top lid through NPT Swagelok fittings.

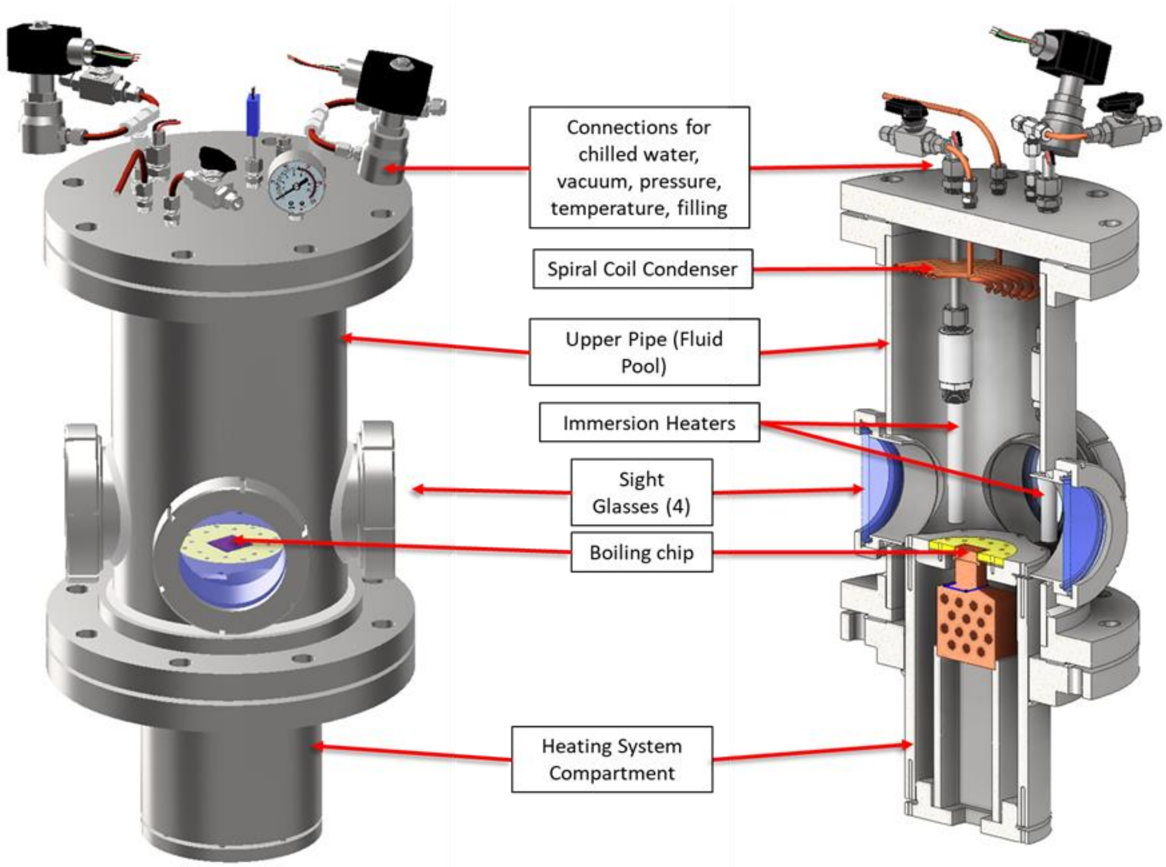

Figure 5-2. Overview of the experimental apparatus.

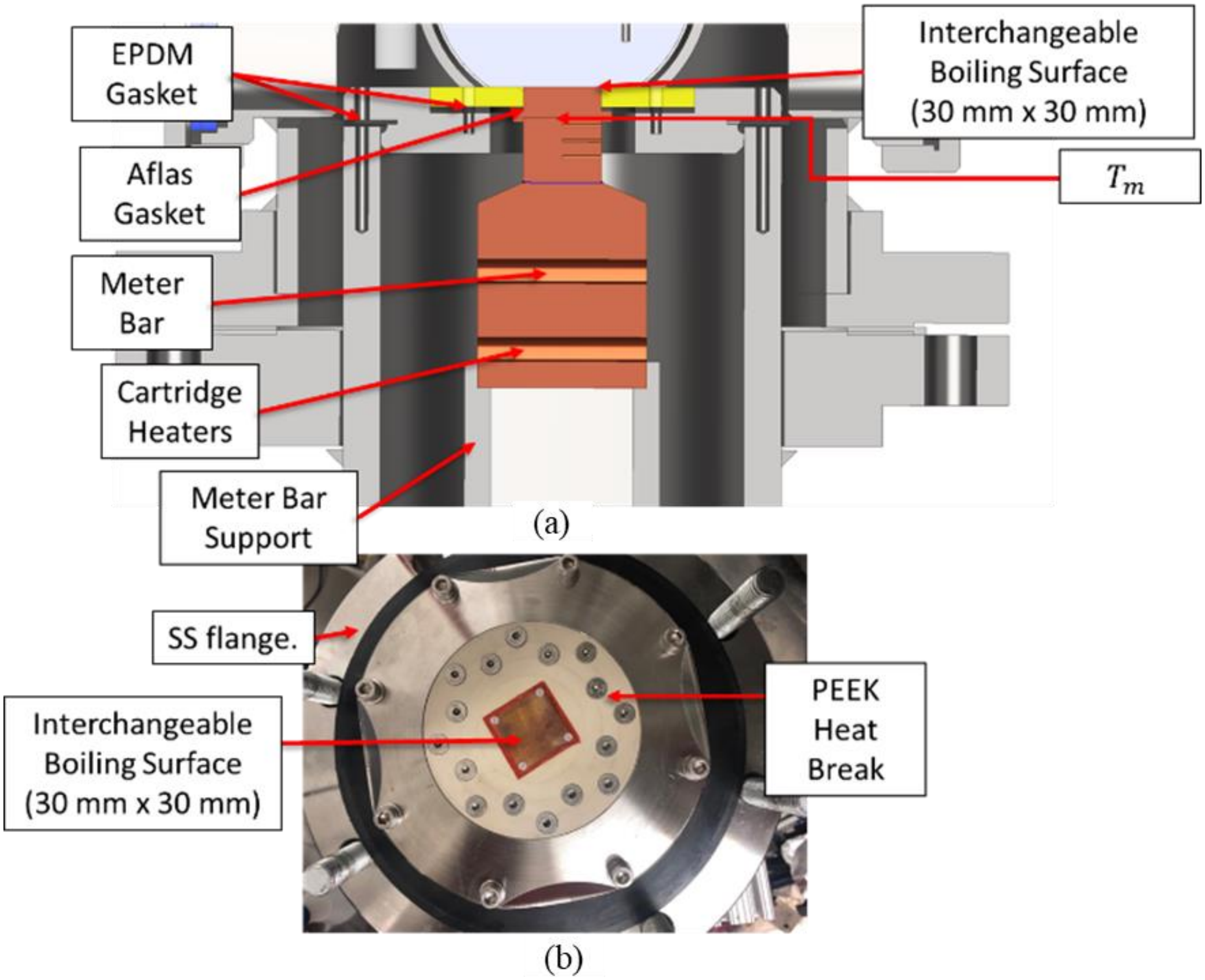

Figure 5-3. Detailed views of the input power system (a) Section view, (b) plan view.

The boiling facility is hanged, freely to rotate, on an aluminum frame, through a swing mechanism, as shown in Figure 5-4. The mechanism consists of two stainless steel clamps, holding the boiling vessel and permits the rotation using two ball bearings of 50 mm in diameter. To eliminate the heat loss through the stainless-steel clamps, two thermal brakes manufactured from Garolite (G10) are sandwiched between them and the boiling vessel. Our novel swing mechanism aided in testing the boiling surface at different angles and easing the working fluid unloading process.

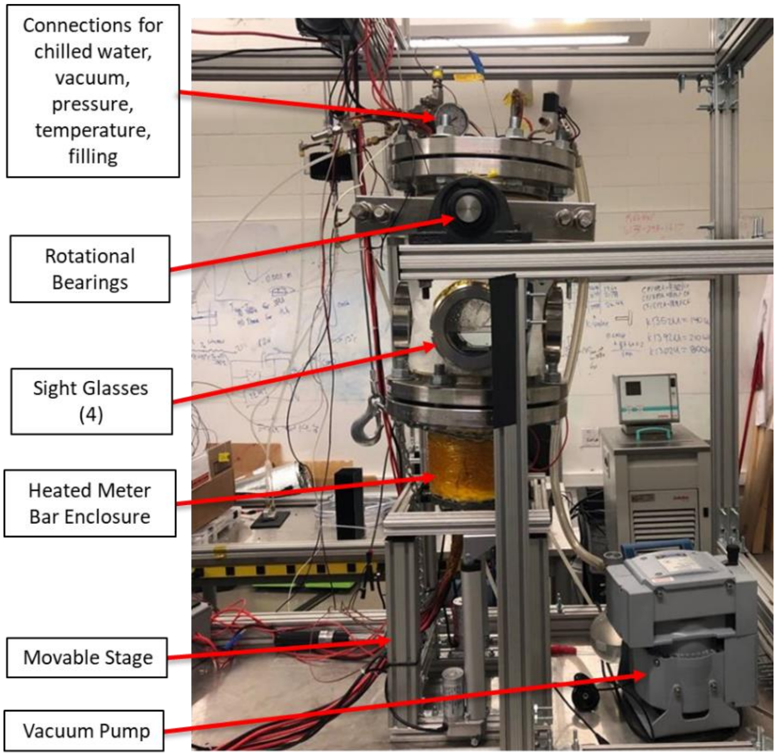

(a)

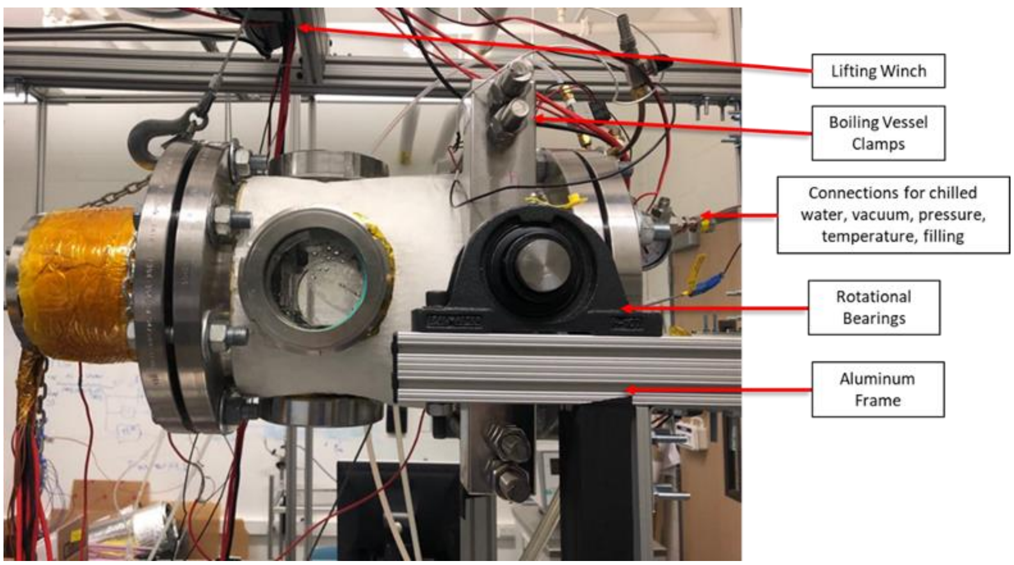

(b)

Figure 5-4. Photos of the experimental apparatus with the heating surface in the (a) horizontal position, (b) vertical positional.

5.1.1 Data Acquisition

An Agilent 34970A data acquisition was used to acquire the thermocouples temperatures and the pool pressure using a 34901A multiplexer card. A 34907A card was used to control the solenoid valves through its output DC channels. The input power to the cartridge heaters was provided through two DC power supplies (Aim-TTi CPX400D). The water saturation temperature was predicted using the measured pressure. A MATLAB script was written to collect the measured parameters, control the input power, and the solenoid valves.

5.1.2 Experimental Procedure

Prior to running the tests, the fluid pool was examined for leakage for a few hours with the help of a vacuum pump (Vacuubrand MZ 2C NT +2AK). Once the sealing was assured, the DI water was allowed to flow from a small tank to the boiling vessel under the pressure difference. To mitigate the non-condensable gases effect, the water was continuously boiled for 1.5 hours with a frequent release of the air through the solenoid valve until reaching the saturation temperature.

For testing purposes, the input power was incremented by 5 W/cm^2 at low heat fluxes, below 15 W/cm^2, and above 70 W/cm^2 until reaching the CHF. At the nucleation regime of moderate heat fluxes, the power was increased by increments of 10 W/cm^2. The temperatures were recorded at the quasi-steady state conditions at each power level. The steady-state condition was recognized when the max slope of all temperatures averaged over 18 minutes reached a value below 0.003 K/s. Each heat flux takes around 25 minutes to attain steady-state conditions. The complete boiling curve measurement takes approximately 5 hours. The CHF was determined when observing an abrupt increase of the surface temperature (around 5 °C increase between two successive readings). To maintain the safe operation of the test facility at the CHF, the cartridge heaters are switched off, and simultaneously, the pressure inside the vessel is increased using an air pressure line connected to the tank through another controlled solenoid valve. The rapid increase of pressure forces the liquid to wet the surface, which yields to a rapid decrease of the meter bar temperature, ensuring safe temperature for the Aflas gasket.

5.1.3 Data Reduction & Uncertainty Analysis

Drawing the pool boiling curve requires the measurement of the heat flux, wall superheat, and the heat transfer coefficient, which can be predicted using the following equations:

$$\mathrm{q}'' = -k\frac{dT}{dx} \tag{5.1}$$

where, k is meter bar thermal conductivity, and dT/dx is the generated temperature gradient inside the bar.

$$h = \frac{q''}{T_s - T_{sat}} \tag{5.2}$$

where $T_s - T_{sat}$ is the wall superheat. The heater surface temperature is detected using the measured heat flux along with another thermocouple, T_m, located 10.3 mm away from the surface, as shown in Figure 5-3a, and can be given by:

$$T_s = T_m - \frac{q''\,\Delta z}{k} \tag{5.3}$$

Table 5-2 shows the uncertainty for each input parameter. The thermocouples were calibrated against each other using from 30 ℃ to 300 ℃, which resulted in a maximum temperature uncertainty of 0.2 ℃.

Table 5-2.Uncertainties in the input variables.

Parameter	Uncertainty
Boiling surface area, A	8 x 10^{-7} (m^2)
Thermocouples, T	0.2 ℃
Copper thermal conductivity	±2% of the nominal value
Thermocouple position, Δx	±5% of the hole diameter

The uncertainties in measuring the heat flux and HTC were determined using the error propagation such as in [21]. This technique applied to HTC as follows:

$$U_h = \sqrt{\left(\frac{\partial h}{\partial q''} U_{q''}\right)^2 + \left(\frac{\partial h}{\partial T_s} U_{T_s}\right)^2 + \left(\frac{\partial h}{\partial T_{sat}} U_{T_{sat}}\right)^2} \tag{5.4}$$

where U_i is the uncertainty for the quantity i. The uncertainty in the temperature gradient, dT/dx, through the meter bar was calculated using the method proposed by Kempers [22]. It depends on assuming a window for each temperature measurement, bounded by the temperature and position uncertainties, through which the point can exist. This is followed by employing the Monte Carlo approach, assuming random, normally-distributed values for each thermocouple temperature measurement and position within its respective window. Then, finding all the possible linear trend lines for the temperature profile, whose slopes follow a normal distribution. This distribution can be used to get the temperature uncertainty using the standard deviation, σ, for a confidence level of 95%.

Figure 5-5 shows the predicted uncertainties in the heat flux and the heat transfer coefficient. The uncertainty at low heat fluxes is relatively high at approximately 17% for both parameters. Beyond heat flux of 10 W/cm^2 however, uncertainty in the measured HTC is reduced approximately to 6%.

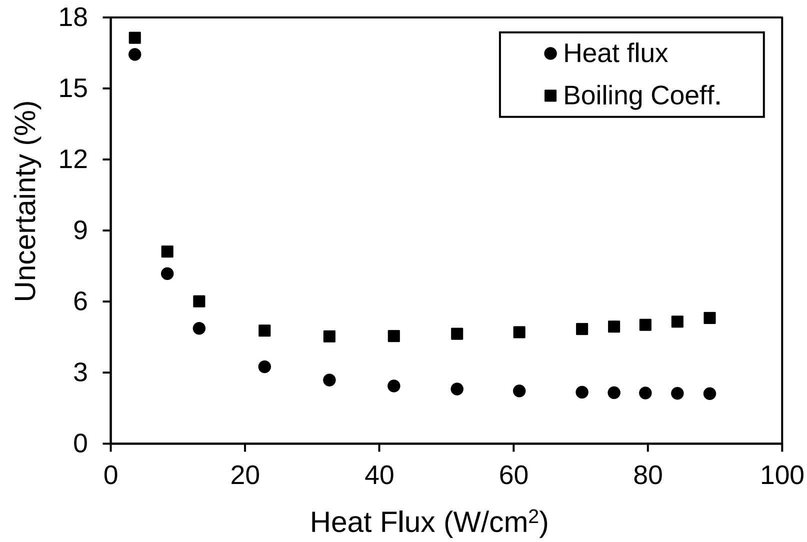

Figure 5-5. The predicted uncertainty for the heat flux and HTC.

5.2 Investigation of Surface Aging

Surface aging happens due to oxidation and contamination that the surface may encounter during boiling experiments. Sinha-Ray [9] showed how the copper surface color became greenish after boiling in water due to the oxidation. Therefore, some researchers pre-boiled their surfaces for a few hours before running the experiments to age surfaces. However, aging effects on pool boiling performance and the repeatability of the results have not been investigated in detail.

In this context, this section investigates the pool boiling heat transfer enhancement gained by surface contamination and oxidation and these effects on the repeatability of the boiling performance.

5.2.1 Samples Preparation

Two copper surfaces (C110) were prepared in the same manner according to the polishing sequence given by Table 5-3. The surfaces were then rinsed by isopropanol and finally using warm DI water. Two aging approaches were investigated. The first approach is to boil on the fresh surface for only one run and leaving it for a few days without running for aging purposes. This is followed by continuous testing of the boiling surface for several runs, which the case of Surface *I*. The second approach is to keep boiling on the surface, starting from the first day for several runs, which is the case of Surface *II*. It is worth mentioning that the pool water was changed prior to each run. Figure 5-6 shows a comparison between the surface morphology before and after the last boiling for Surface *I*. Boiling left many spots through the oxidized layer, which we believe are the nucleation sites. The surface roughness was measured for both surfaces before and after boiling at nine different locations using a profilometer (Bruker Contour GT-K). For fresh surfaces, the roughness was found to be 0.337 ± 0.044 µm, and 0.354 ± 0.81 µm for Surface *I*, and Surface *II*, respectively. The aging increased the surface roughness for both surfaces by approximately 15 %.

Table 5-3. Polishing procedure.

	Sandpaper	**Time (min)**	**Direction**
Step 1	800	2	Unidirectional
Step 2	1000	2	All directions
Step 3	1200-4000	10	All directions
Step 4	1000	70 strokes	Unidirectional

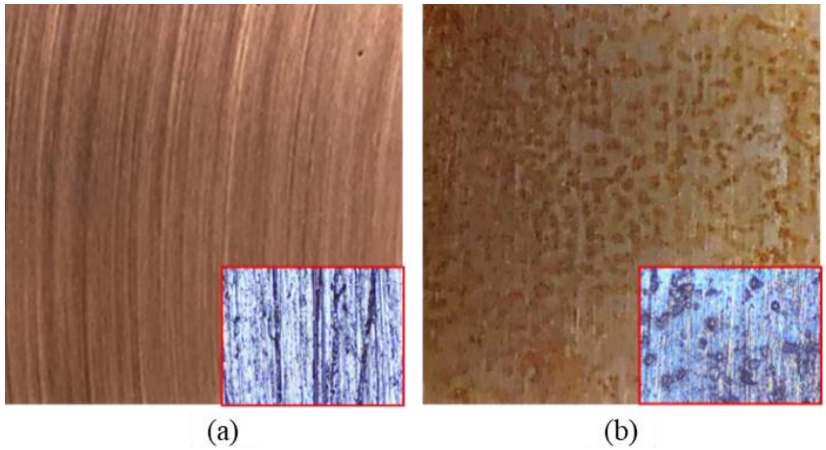

Figure 5-6. Microscopic photos at 10x and real images of the boiling ship surface (a) before boiling, (b) after boiling (run 7).

5.2.2 Measurement Repeatability

Figure 5-7 and Figure 5-8 show the effect of surface aging on the pool boiling performance for both surfaces. For both surfaces, the pool boiling curve moves to the left under the influence of aging. Therefore, for the same heat flux, the aged surfaces achieved lower wall superheat, and hence high HTC. The enhancement ratio of the HTC reached up to 22% at heat flux 51 W/cm^2 for Surface *I*, and 19% at a heat flux of 42 W/cm^2 for Surface *II* compared to the fresh surface (Run 1). This is attributed to surface contamination and oxidation, as expected and explained in the previous section. This is also evidenced by the surface roughness increase during the boiling experiments.

Although the surface aging showed around 20% enhancement of the HTC, it almost did not significantly affect the CHF. In conclusion, to obtain a repeatable result within 5% for the same copper surface, 25 hours of continuous pre-boiling is required before the testing, as shown in Figure 5-9. This figure represents the aging effect on the wall superheat at two heat flux levels for Surface I. Each 5 hours represents a separate run, that was done in a different day. This is a very important result for producing pool boiling results in a repeatable way for the same surface, especially when examining the improvement gained by the attachment of surface fixtures, such as [2,23–25]. Without aging the surface, it is difficult to justify if the enhancement is resulted from the fixture attachment or surface contamination, particularly when changes are relatively small compared to the baseline bare surfaces.

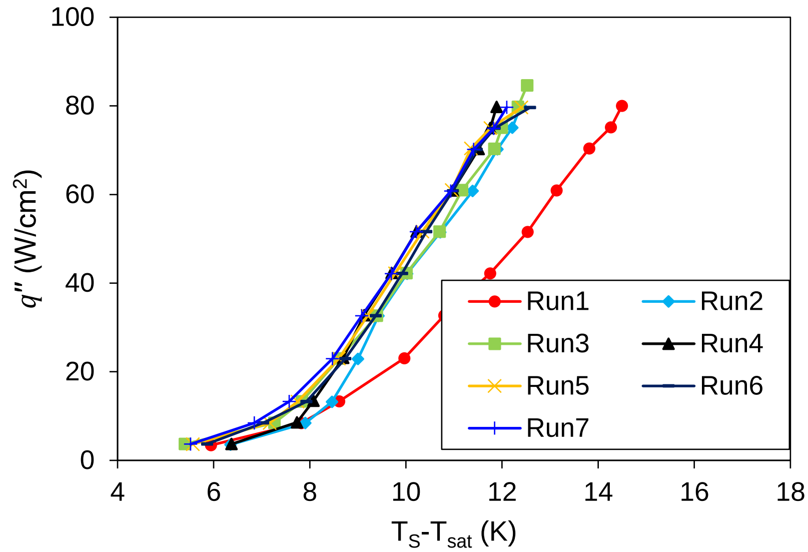

Figure 5-7. The effect of aging on the pool boiling curve for Surface *I*.

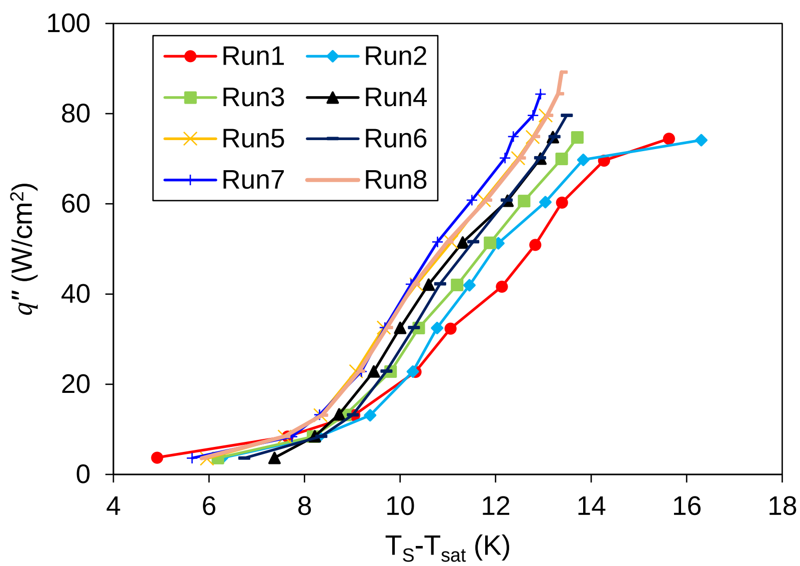

Figure 5-8. The effect of aging on the pool boiling curve for Surface *II*.

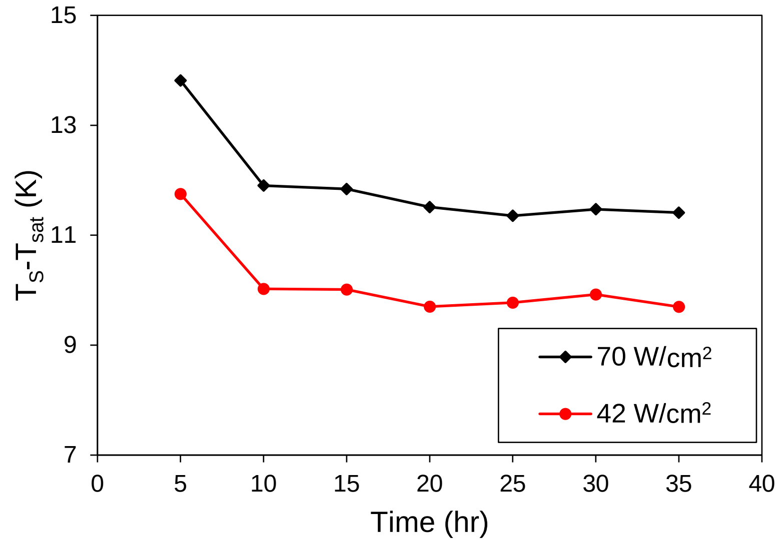

Figure 5-9. The aging effect for Surface *I* at two heat flux levels.

The repeatability issue resulting from the aging effect can be overcome by polishing the surface consistently and testing it for the same number of hours. This is shown in Figure 5-10 and Figure 5-11. Comparing surface with different aging periods can pronounce the repeatability issue, as shown in Figure 5-12. This factor, along with roughness and the contact angle, represent the critical reasons behind the large discrepancy between the experimental literature results highlighted in Figure 5-1.

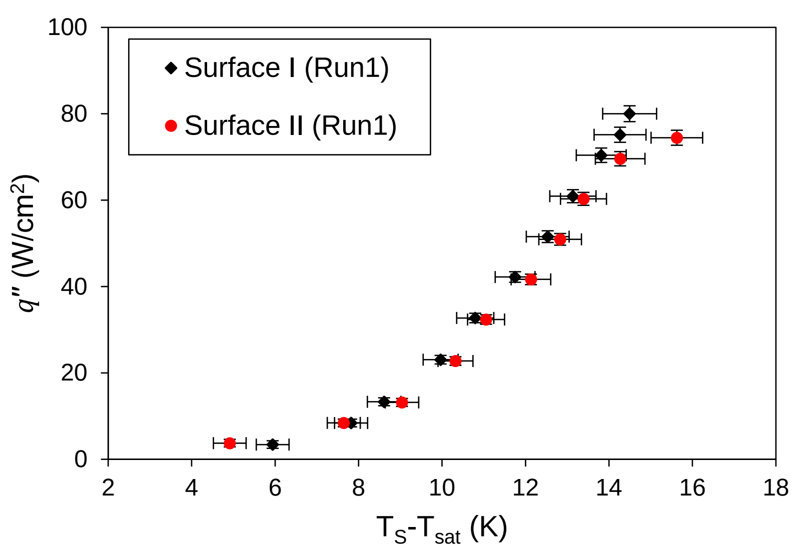

Figure 5-10. Comparison between both surfaces for Run 1.

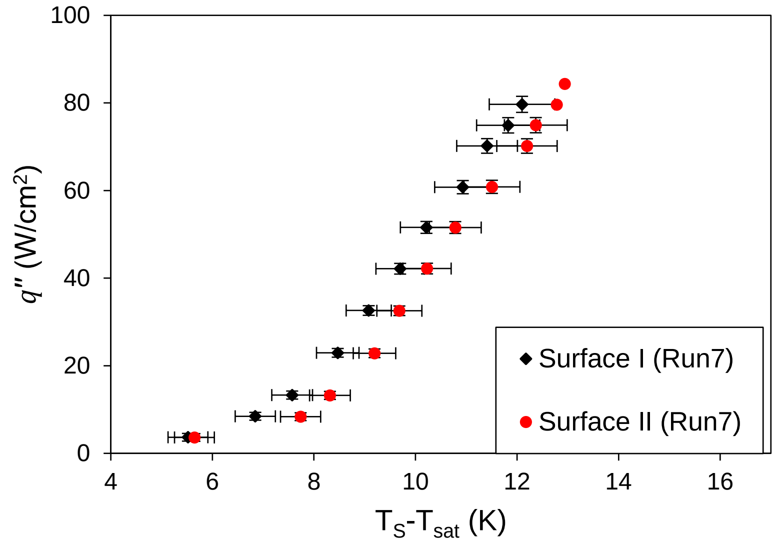

Figure 5-11. Comparison between both surfaces for Run 7.

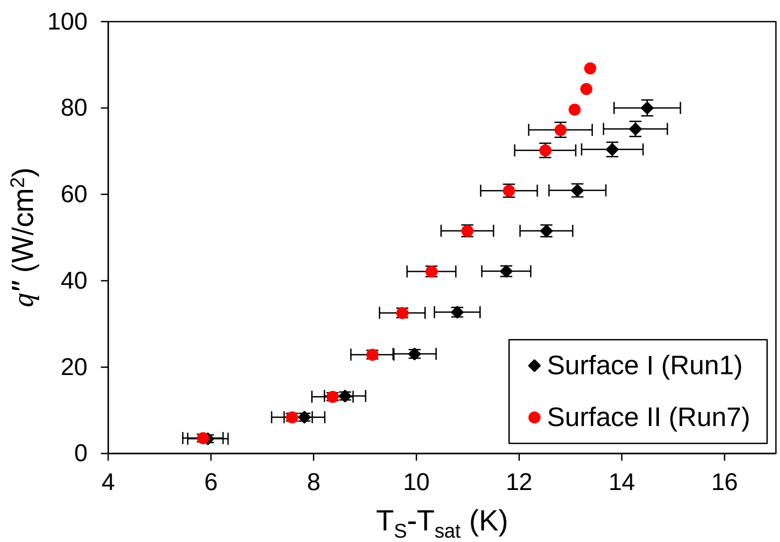

Figure 5-12. Comparison between both surfaces at different runs.

5.3 Enhancement of Pool Boiling Performance Using SLM Structures

Extensive work was exerted to promote the HTC and CHF, either using passive or active techniques. Passive enhancement methods such as surface modification have garnered attention recently due to their capability to enhance the HTC and the CHF to high levels, reaching up to 200-600% compared to the bare surface [26–28], without the requirement for external power. However, some of these techniques offer relatively low enhancement percentages (frequently less than 100%) for either the HTC or CHF [6,29–31]. For instance, Saeidi et al. [6] tested the effect of surface copper aluminizing and found the CHF enhancement can reach up to 37% for water compared to the unmodified surface.

The main principle of such methods is to help create multiscale surface topologies to enhance the HTC by augmenting the heat transfer surface area and nucleation site density. As well as construct wicking capillaries to separate the flow phases, assisting the replenishing liquid in wetting the surface at high heat fluxes, hence improving the CHF. Most of these methods were reviewed by [28,32].

This section proposes using the selective laser melting (SLM) additive manufacturing technique to build 3D spherical re-entrant cavities that cannot be fabricated using conventional machining. SLM was recently used in very few studies to enhance the heat transfer rate by pool boiling. For example, Hayes et al. printed a conical hollow shaped structure to separate the liquid and vapor pathways using the SLM technique [33]. This structure directs the phases through two holes built at the cone surface's upper and bottom sides. The vapor flow is directed to the conical upper holes and the liquid to the side holes if the conical hole size is larger than the bubble departure diameter and vice versa. They concluded that using multiple conical modules with incorporated microchannels enhanced the CHF and HTC further up to two times and four times, respectively, compared to the bare aluminum surface. Ho et al. [34] employed SLM to fabricate innately micro-fin and micro-cavity substrates from AlSi10Mg powder. Their heat transfer characteristics were examined using FC-72 at the atmospheric conditions. They compared these substrates to a plain Al-6061 revealing an enhancement in HTC by 70% and 76% for CHF. Wong et al. [35] utilized the selective laser melting to 3D print an octet-truss lattice array, representing an organized porous structure. The lattice array aided in the HTC increase by 2.81 times to the bare surface using FC-72 as working fluid under atmospheric conditions. This was attributed to the additional nucleation sites, surface area, and capability of the matrix to facilitate the liquid suction through its capillaries. Zhang et al. [5] implemented the SLM method's scan line spacing scheme to precisely change the process printing variable and construct a fine grid made from stainless steel. They achieved 303 W/cm^2 for the 1.1 mm grid width sample, which is three times higher than the bare surface's CHF value, which was resulted from the grid ‘‘partition effect” that delayed the Helmholtz instability and the coalescence of the dry spots at high heat fluxes.

Several studies have accepted Re-entrant cavities to be capable of trapping vapor and providing stable bubble nucleation sites, even at lower wall superheat. Table 5-4 summarizes most of the studies that implemented the re-entrant in the literature using conventional machining techniques. Consequently, they have been widely utilized in multiple commercial heat exchangers, such as Turbo-B tubes, Thermoexcle-E tubes, and Gewa-T tubes [36–38], etc. However, these studies investigated 2D shaped re-entrant channels (grooves), not cavities. Therefore, we aim to examine the performance of 3D spherical re-entrant cavities fabricated from Al alloy via the SLM technique.

Table 5-4. Re-entrant cavities literature review.

Study	(Cylindrical /Planar)	Studied configuration	Manufacturing Method
Nakayama 1980 [39]	Planar	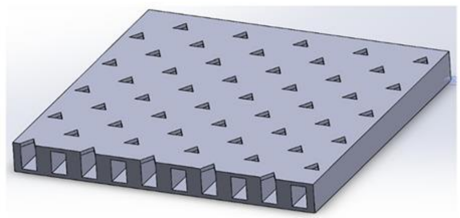	Machining
Stephan and Mitrovic 1981 [40]	Cylindrical	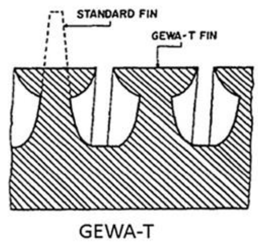	Fins winding with spiral.
Ma et al. 1986 [41]	-	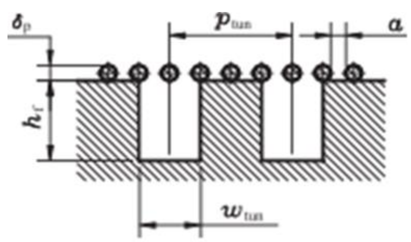	Parallel rectangular grooves of cross section covered with sintered screen.
Chien and Webb 1998 [42]	Cylindrical		Integral-fin was wrapped with pierced copper foil.
Das et al. 2009 [43]	Planar	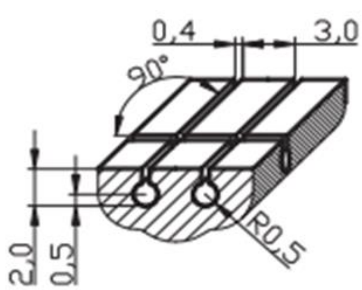	Wire-Electro Discharge Machining

Table 5.4 Continue. Re-entrant cavities literature review.

Study	(Cylindrical /Planar)	Studied configuration	Manufacturing Method
Zhang et al. 2016 [44]	Planar	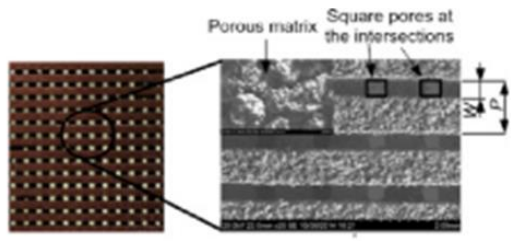	Ploughing/Extrusion (P/E) method
Deng et al. 2016 [45]	Planar	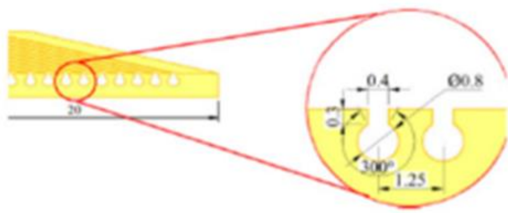	Machining / Solid-state sintering of copper powder
Sun et al. 2017 [46]	Planar		Orthogonal P/E method on pure copper substrates
Hao et al. 2017 [47]	Planar	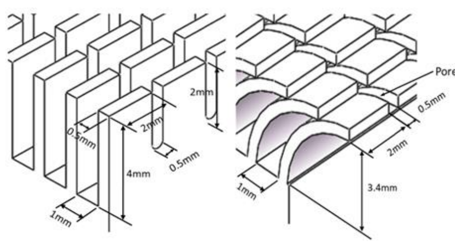	Shape memory alloy (SMA)

5.3.1 Boiling Samples Preparation

Two boiling samples were examined: one bare surface and another surface with embedded 3D spherical re-entrant cavities. The proposed design and geometrical parameters of the boiling sample with re-entrant cavities are shown in Figure 5-13 and Table 5-5.

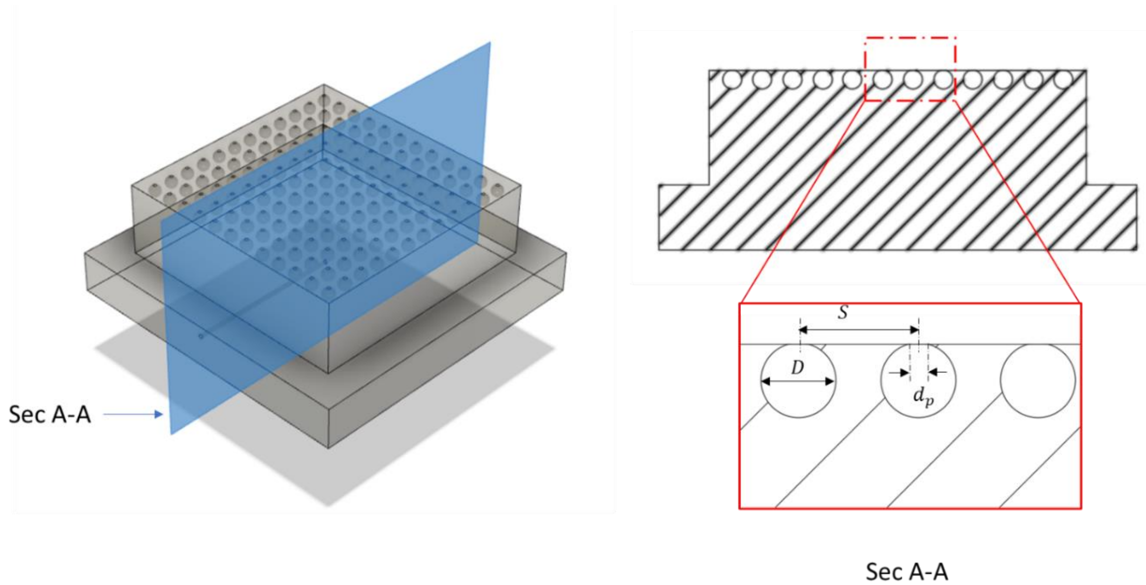

Figure 5-13. The proposed structure fabricated by SLM.

Table 5-5. Proposed re-entrant cavities geometry.

Pore diameter, D	Cavity diameter, d_p	Spacing, S	No. of cavities, n
1.5 mm	0.4 mm	2.4 mm	12 x 12

The SLM EOS M 290 (EOS GmbH, Munich, Germany) facility at Additive Metal Manufacturing (AMM) company for metal 3D printing in Concord, Canada, was utilized to build the boiling surfaces used in the current section. The printing parameters details and material are similar to what has been used in chapter three for building the thermal conductivity samples except with a different layer height of 20 µm, laser spot diameter of 80 µm, and power of 400 W. The thermal conductivity of the current samples was measured employing the same approach used in chapter three. It was found to be 125 W/m K. Figure 5-14 depicts some microscopic images of the 3D printed surface captured with a Leica MZ10 F stereomicroscope (Leica Microsystems GmbH, Wetzlar, Germany). In contrast, Figure 5-15 shows a bunch of cavities taken with a Bruker-micro-

CT (model: SKYSCAN 1272). These figures depict the cavities' pores are not circular and have a small variation in their diameters, which pertains to the adherence of some half-sintered particles at the pores' contour, which is an inherent property of the SLM method. However, this artifact is not intense for the cavity's inner surface due to having a larger diameter of 1.5 mm, which is very close to a sphere as designed, as shown in Figure 5-15b. A closer inspection of the cavities' inner surface shows that this property caused a high roughness. Similar behavior is observed for the boiling sample top surface, which is believed to act as nucleation sites, even for the bares sample without re-entrant cavities.

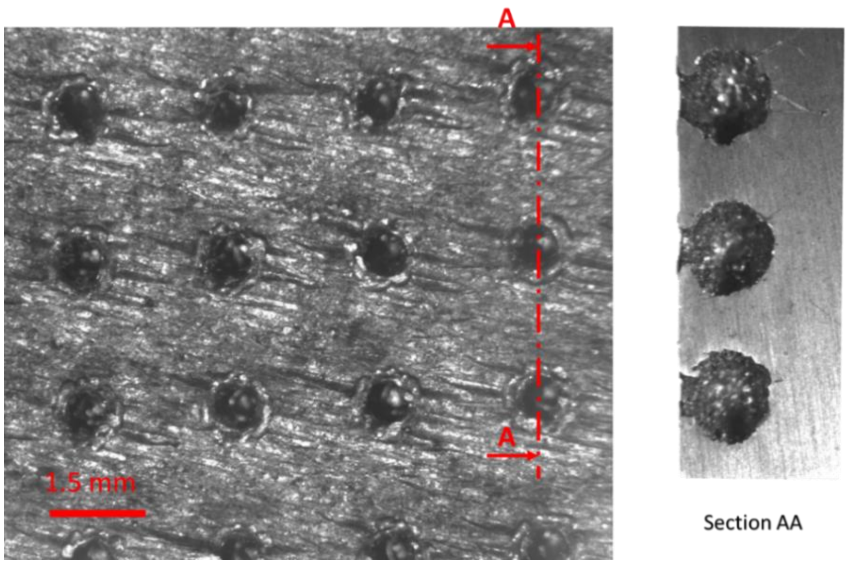

Figure 5-14. Microscopic photos for the boiling sample with re-entrant cavities.

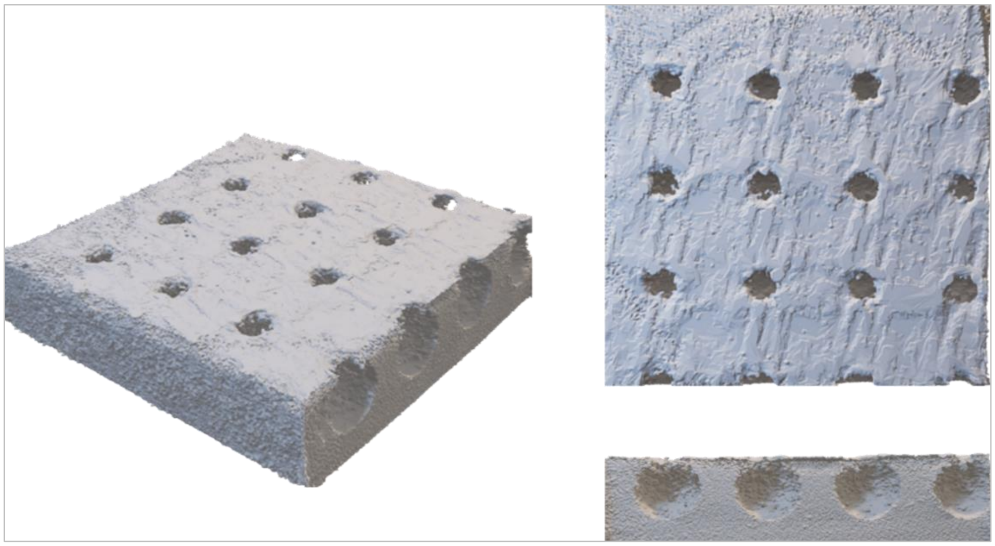

(a)

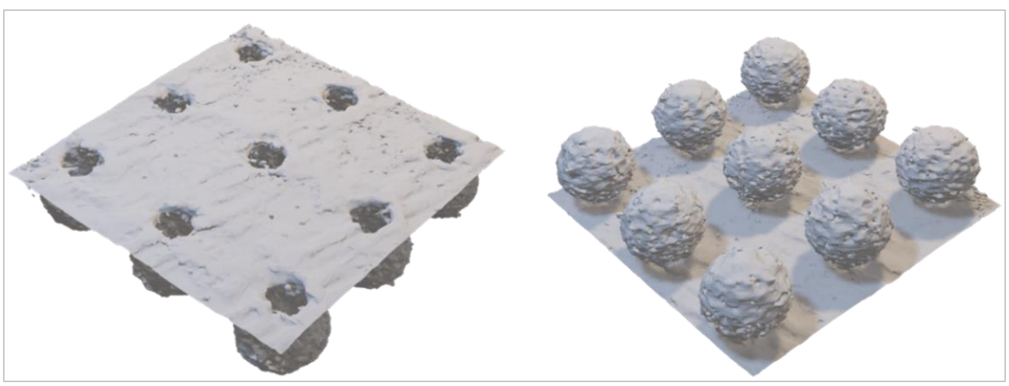

(b)

Figure 5-15. Three dimensional for a part of the boiling sample with re-entrant cavities reconstructed from μCT images: (a) top surface (b) the inner surface of the spherical cavities.

5.3.2 Results

Figure 5-16 shows the pool boiling curves for both printed surfaces: the solid bare surface and the structured surfaces with re-entrant cavities. Both surfaces were examined with saturated water at a pressure of 1 atm for heat fluxes ranges from 2 to 100 W/cm^2. It is apparent that the onset of nucleate boiling (ONB) for the surface with re-entrant cavities happened at a much smaller wall superheat (1.7 °C) compared to the solid bare surface (6.8 °C), evident by the slope change of the boiling curve. This is attributed to the presence of the re-entrant cavities, which could easily trap the vapor at lower wall superheat. Increasing the heat flux beyond the ONB shifted the pool boiling curve to the left for the surface with re-entrant cavities compared to the bare surface, indicating the enhancement of the heat transfer coefficient and suggesting the increase of the nucleation site density. However, at high heat fluxes, the boiling curve for the surface with re-entrant cavities tended to approach the boiling curve for the solid counterpart until intercrossing it at a heat flux of 85 W/cm^2 and then achieving worse performance till the end of the examined range of the heat fluxes. This can be highlighted in Figure 5-17, which indicates a rapid increase of the HTC until hitting a maximum of 14 W/cm^2 k at a heat flux of 75.5 W/cm^2 for the surface with re-entrant cavities. Conversely, the bare surface monotonic increasing trend for the entire range examined. The enhancement percentage at the maximum HTC was found to be 27.5 %; however, the maximum enhancement ratio happened at a lower heat flux of 3.5 W/cm^2 and was observed to be 285% compared to the bare surface.

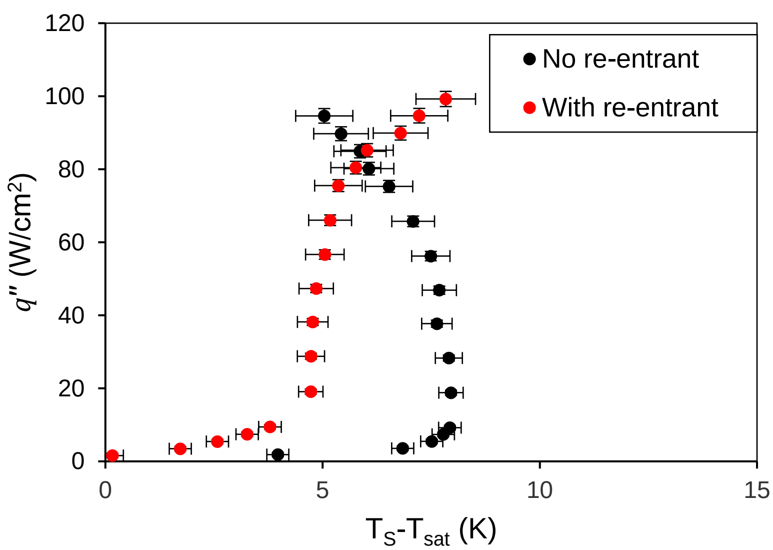

Figure 5-16. Comparison of the pool boiling curve between the 3D printed bare surface and the 3D printed with re-entrant cavities.

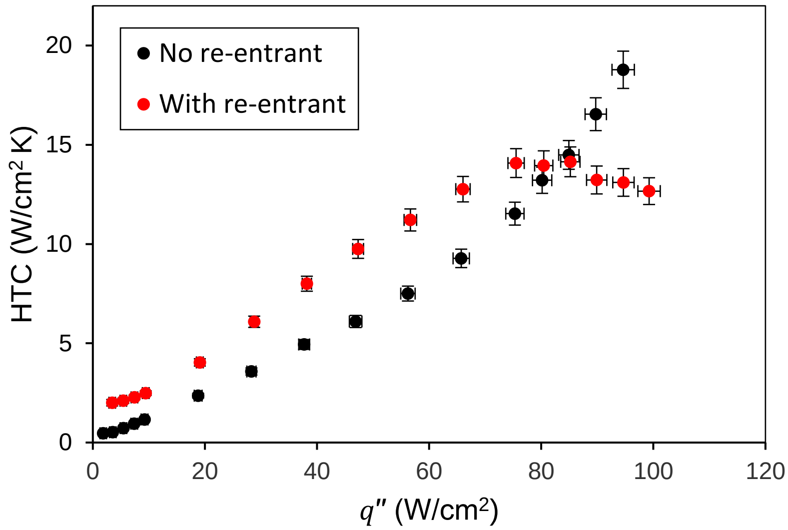

Figure 5-17. Comparison of the boiling HTC between the 3D printed bare surface and the 3D printed with re-entrant cavities.

Figure 5-18 shows the bubble growth for the bare solid 3D-printed surface at low heat flux (q''=3.56 W/cm^2), while Figure 5-19 shows the bubble growth behaviour for the boing surface with re-entrant cavities at an approximately equivalent heat flux of 3.45 W/cm^2. Compared to the solid bare surface, the re-entrant cavities structured surface showed an increased nucleation site with organized patterns and roughly equal sized-bubbles. The bare surface had only a few nucleation sites at this heat flux, resulting from the tiny pores created between adjacent particles during the SLM manufacturing process. Figure 5-18 shows that the bare solid surface promoted two distinct behaviors for successive bubble formation and growth. By comparing the two bubbles denoted by the red and blue arrows in these figures, we can see that bubble 1 started to nucleate and form at time t=60 ms, and then grew faster by the coalescence with the adjacent bubble until being expulsed to the fluid pool at t=90 ms. On the other hand, bubble 2 showed a prolonged growth rate without interaction or coalescence with other bubbles, which started at t=90 ms until reaching the proper size and the needed buoyancy force at t=220 ms to detach from the surface.

Consequently, it can be concluded that the bare surface could promote low and high-frequency bubbles depending on the distribution of the active nucleation sites across the surface.

In contrast, the coalescence was the dominant mechanism for the bubble growth for the surface with re-entrant cavities, as indicated by bubbles 1 and 2 in Figure 5-19. This facilitated the increase of the bubbles' departure frequency. Higher frequency and the nucleation site density increase yielded a notable enhancement of the HTC compared to the bare surface, as explained previously in Figure 5-17. This coalescence behaviour was more organized and improved in the case of the structured surface with re-entrant cavities, even at moderate heat fluxes, as depicted in Figure 5-21compared to Figure 5-20. These figures show the formation of a bunch of mushroom bubbles for both surfaces. However, their sizes were approximately equal and more organized for the surface with re-entrant cavities, which we think enhanced the coalescence between them and increase the departure frequency resulting in improving the heat dissipation rate by pool boiling. However, the performance degradation at high heat fluxes for the re-entrant cavities (Figure 5-16) can be analyzed using Figure 5-22 and Figure 5-23, which compares both surfaces at different heat fluxes. As mentioned above, the structured re-entrant cavities surface promoted a better organized equal-sized bubbles pattern at all heat fluxes. Nonetheless, having bigger large mushroom bubbles at a heat flux of 94 W/cm^2 can slowdown the replenishing liquid influx to the surface, which may increase the wall superheat in such cases and deteriorate the HTC. It is worth mentioning that the bare solid surface achieved a negative slope of the boiling curve at heat flux larger than 56 W/cm^2. This behaviour was seen for some literature enhancement methods, such as [48–52]. This was analyzed by Jaikumar and Kandlikar [53] to be as a result of (1) Macroconvection heat transfer mechanism induced by the vapor and liquid phase separation or (2) the activation of secondary nucleation sites at high heat fluxes. It is believed that the bare solid 3D printed surface tested in the current work may depend on the latter claim due. This interesting feature will be further investigated in a future study by comparing a machined Al 6061 sample to the 3D printed sample tested here. This study would also involve other surfaces with re-entrant cavities of different geometrical parameters. These samples are already manufactured and will be tested soon in the near future.

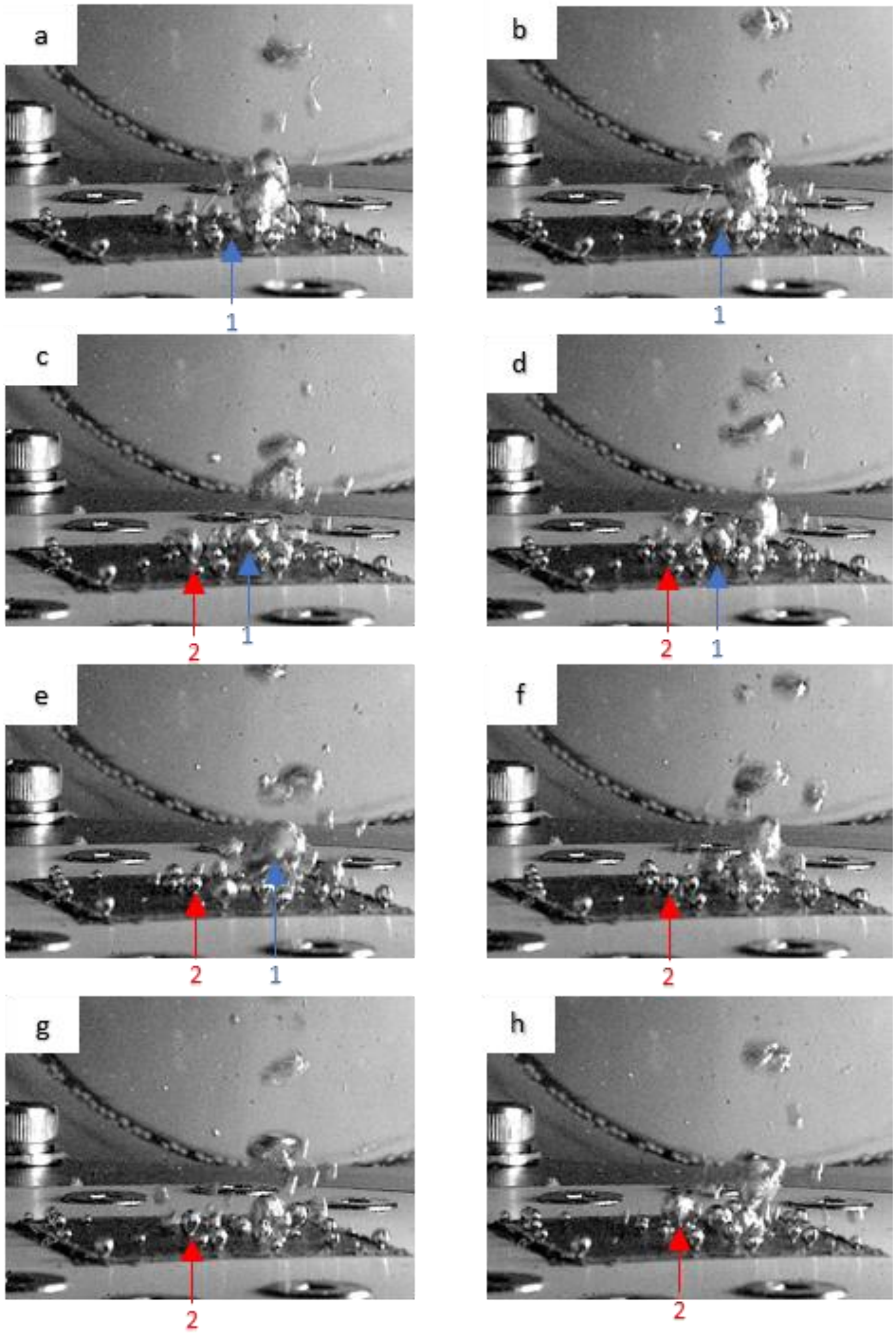

Figure 5-18. Successive bubble growth for the bare surface at heat flux of q''=3.56 W/cm^2 at different times: (a) 0 ms, (b) 60 ms, (c) 70 ms, (d) 90 ms, (e) 120 ms, (f) 150 ms, (g) 190 ms, (h) 220 ms.

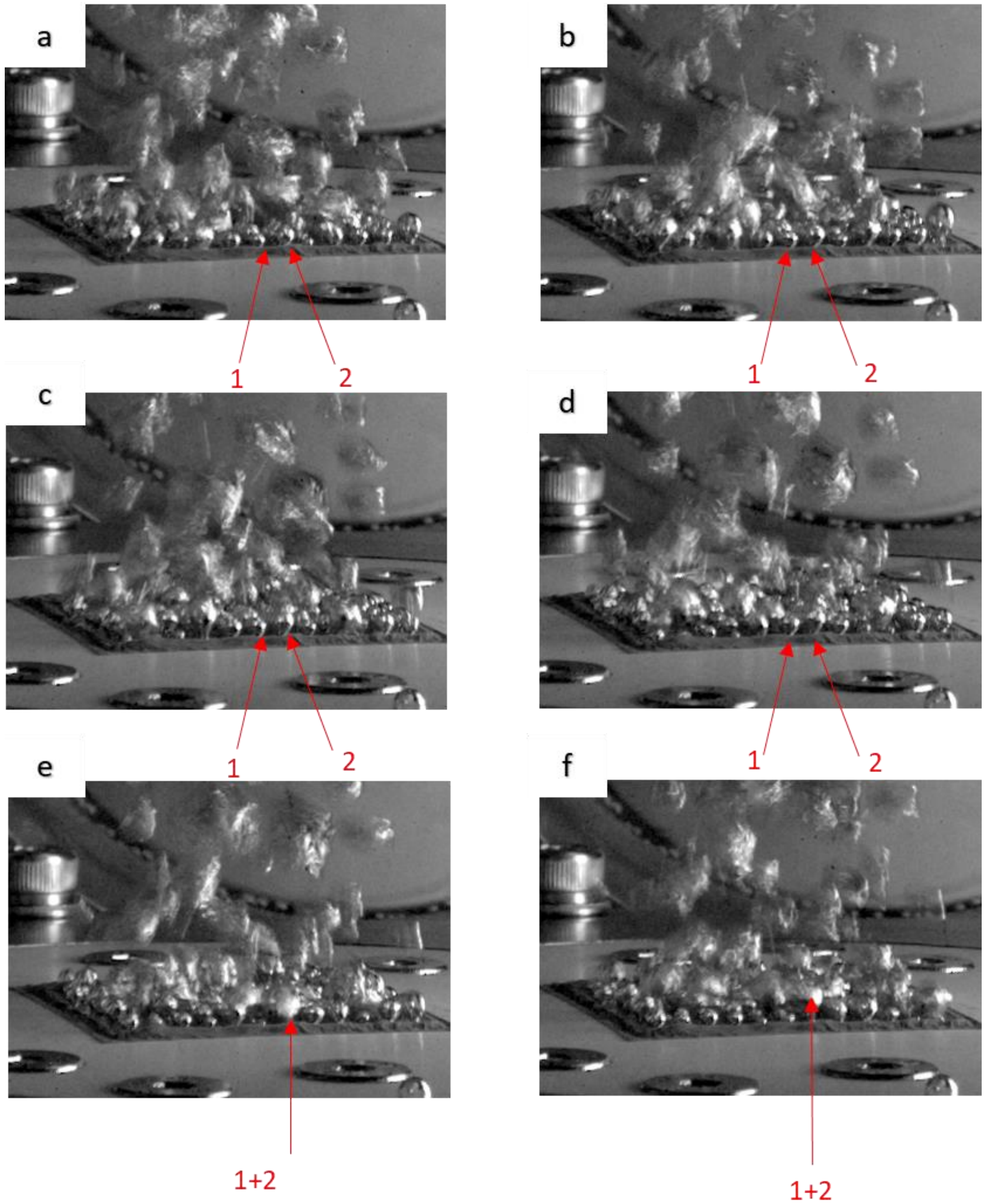

Figure 5-19. Successive bubble growth for the surface with re-entrant cavities at heat flux q'' of 3.45 W/cm^2 at different times: (a) 0 ms, (b) 20 ms, (c) 30 ms, (d) 40 ms, (e) 50 ms, (f) 60 ms.

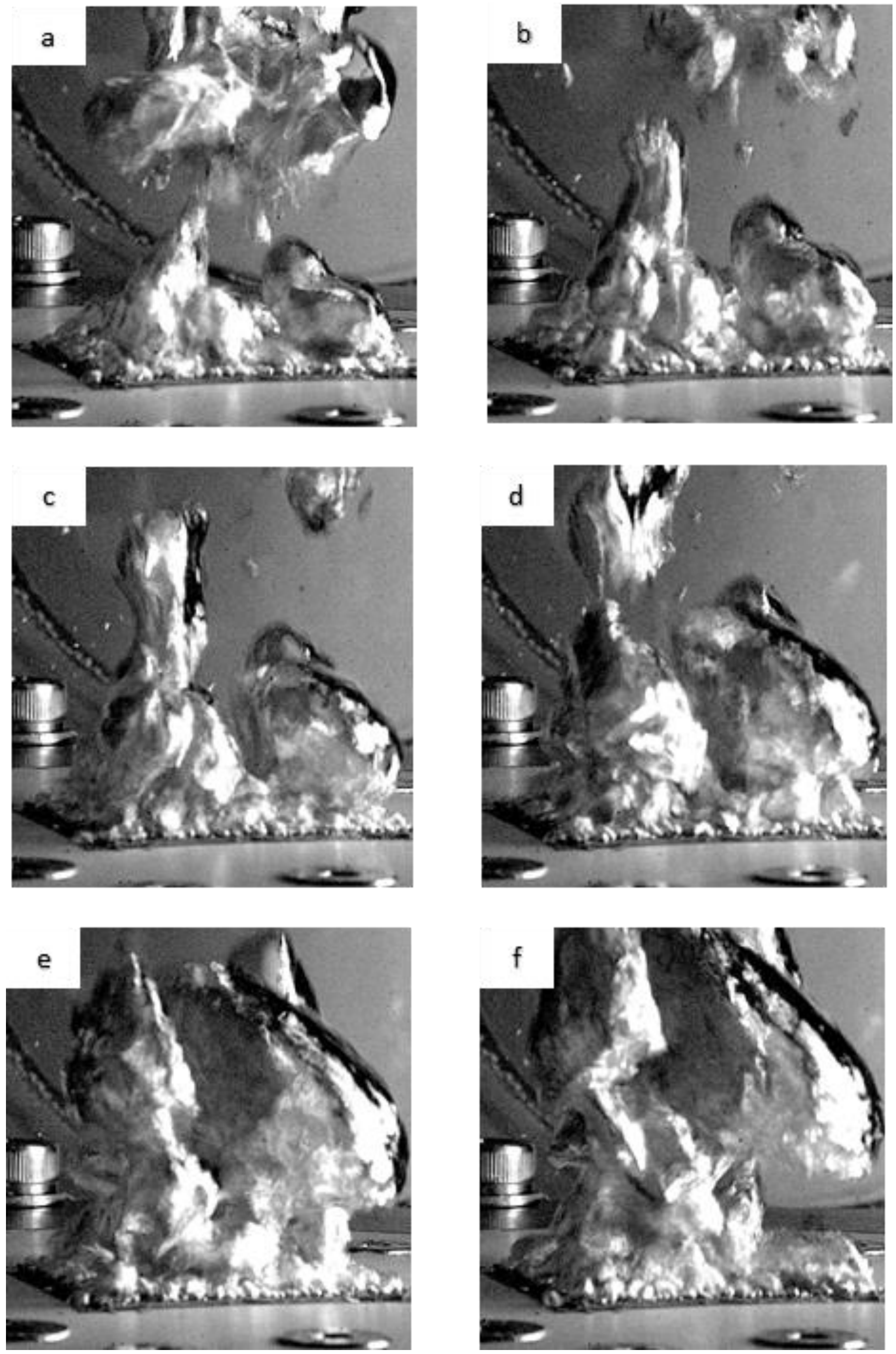

Figure 5-20. Successive bubble growth for the bare surface at a heat flux of q''=46.88 W/cm^2 for different times: (a) 0 ms, (b) 10 ms, (c) 20 ms, (d) 30 ms, (e) 50 ms, (f) 60 ms.

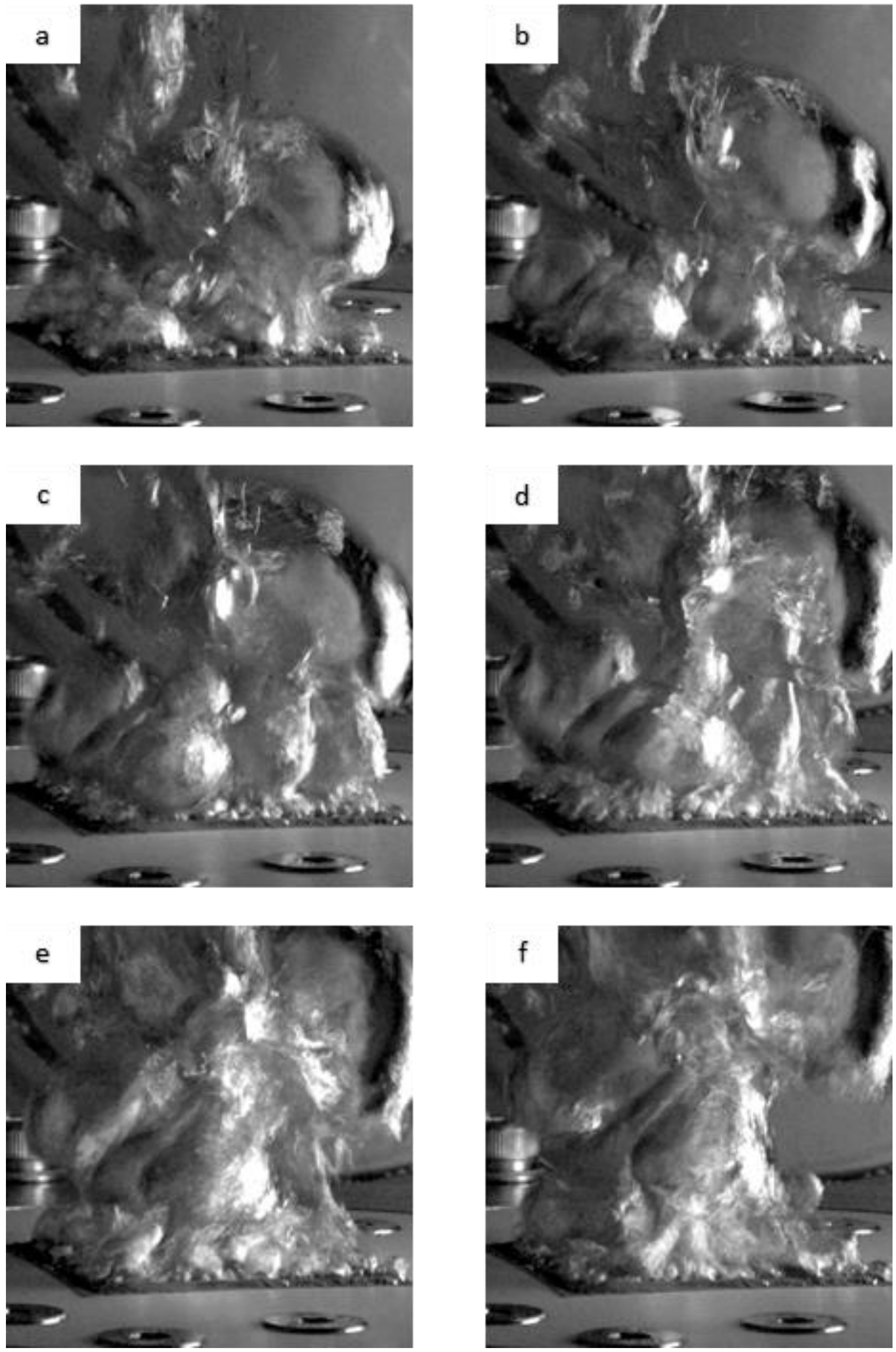

Figure 5-21. Successive bubble growth for the surface with re-entrant cavities at heat flux of q''=47.32 W/cm^2 for different times: (a) 0 ms, (b) 10 ms, (c) 20 ms, (d) 30 ms, (e) 40 ms, (f) 50 ms.

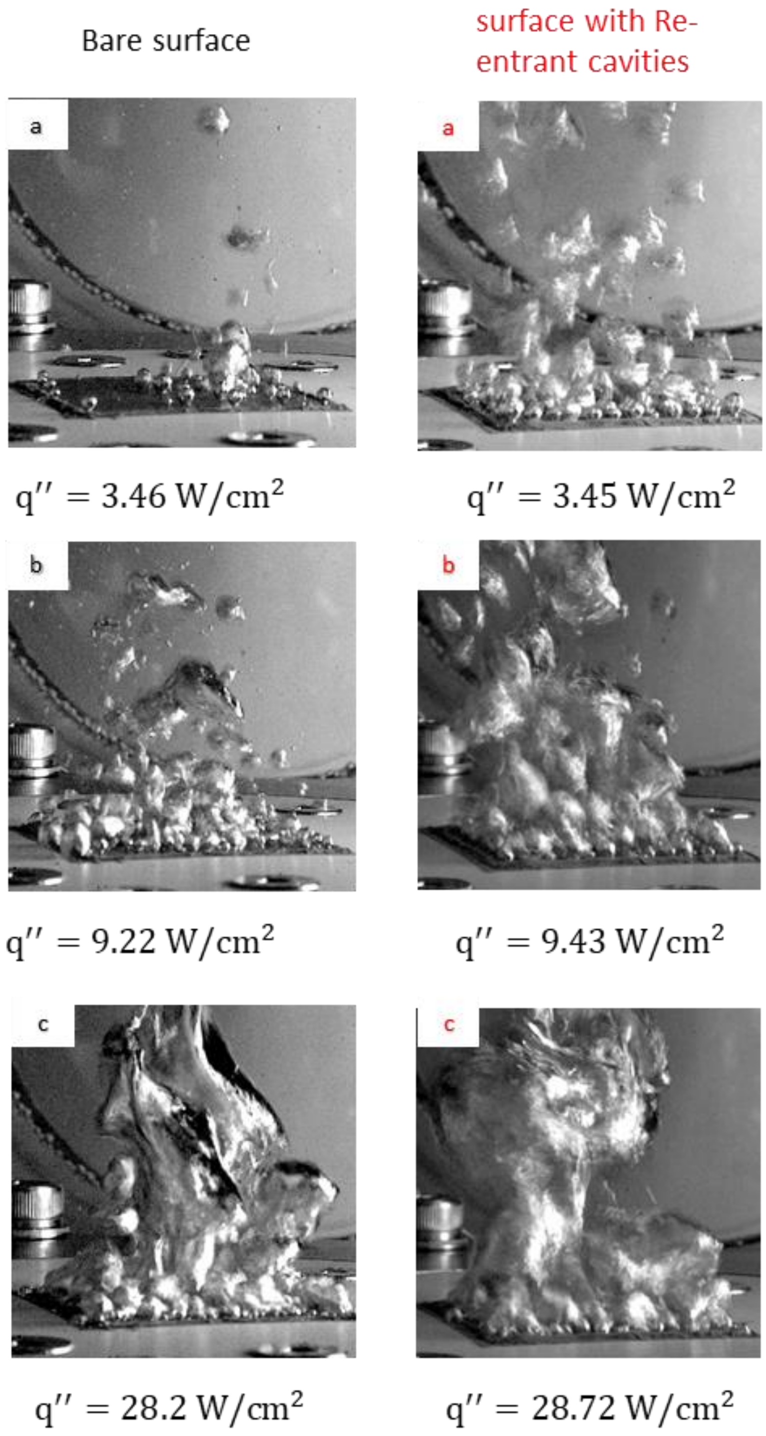

Figure 5-22. Boiling visualization comparison between both surfaces at low heat fluxes.

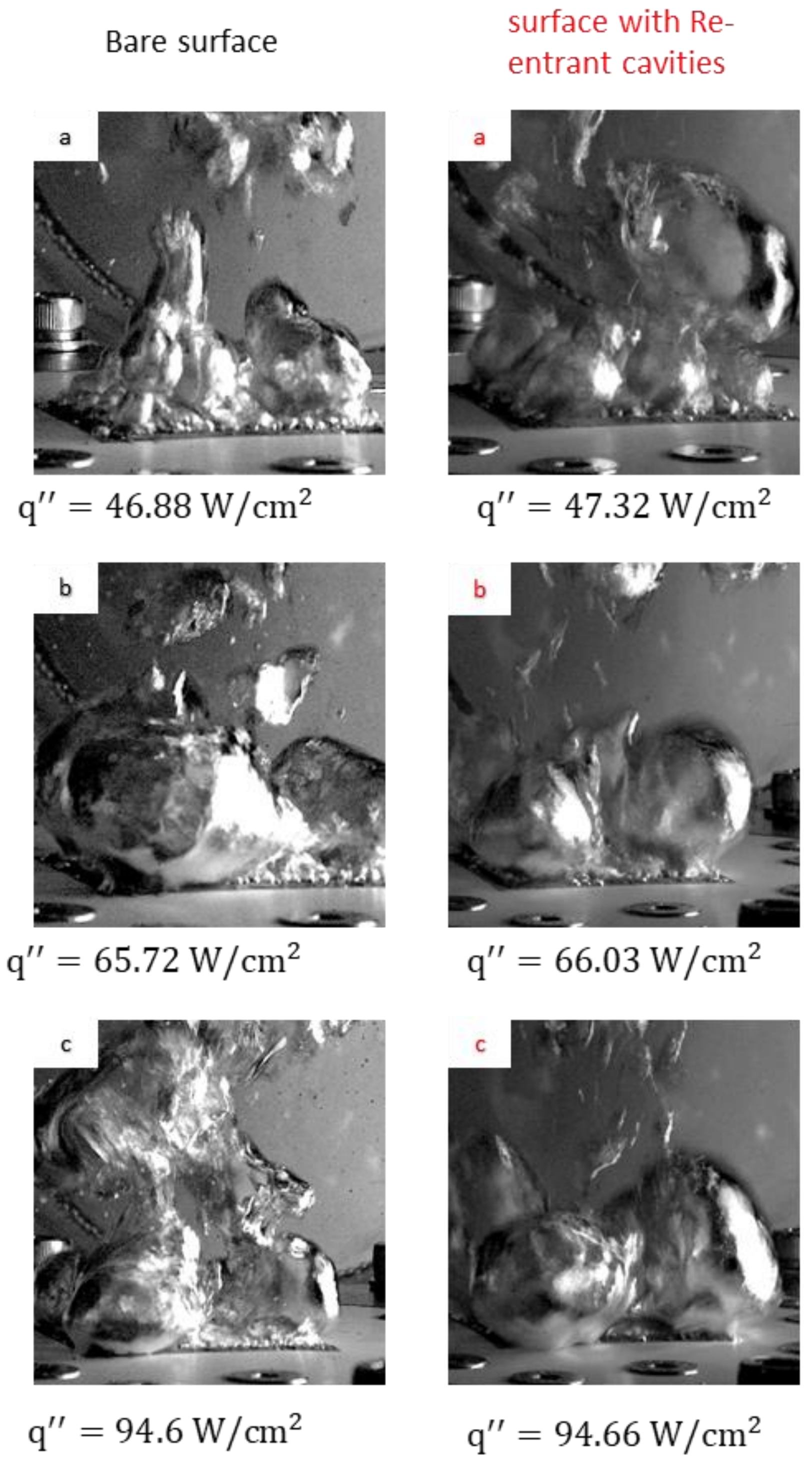

Figure 5-23. Boiling visualization comparison between both surfaces at high heat fluxes.

5.4 Summary & Conclusions

In the first part of the chapter, a high-accuracy boiling apparatus with a large boiling surface of 30 mm x 30 mm was calibrated and commissioned to investigate the effect of surface aging on the repeatability of boiling heat transfer. It was concluded that at least 25 hours of continuous boiling are needed to get repeatable results for the same surface, which was deemed enough for the surface to be entirely aged. However, to get consistent, reproducible results between different surfaces, the aging period and approach should be the same. Comparison between surfaces, with different aging times even with relatively similar roughness and contact angle, pronounced the repeatability problem.

The second part of the chapter introduced a novel SLM manufactured structure to enhance the HTC. This structure consists of a uniform pattern of 3D spherical re-entrant cavities with a pore diameter of 0.4 mm, cavity diameter of 1.5 mm, and spacing of 2.4 mm. All the experiments were performed with water at the saturated conditions at a pressure of 1 atm. The preliminary results demonstrated that the surface with re-entrant cavities had a significant effect on the HTC, which reached up to 285% of improvement at low heat fluxes compared to the bare solid. This is referred to the re-entrant cavities' capability to initiate an organized uniform pattern of bubbles across the boiling surface at low heat flux.

5.5 References

[1] A. Elkholy, R. Kempers, Enhancement of Pool Boiling Heat Transfer using 3D-Printed Polymer Fixtures, in: 14th Int. Conf. Heat Transf. Fluid Mech. Thermodyn., 2019: p. 6.

[2] A. Elkholy, R. Kempers, Enhancement of pool boiling heat transfer using 3D-printed polymer fixtures, Exp. Therm. Fluid Sci. 114 (2020) 110056. https://doi.org/10.1016/j.expthermflusci.2020.110056.

[3] S. Mt Aznam, S. Mori, A. Ogoshi, K. Okuyama, CHF enhancement of a large heated surface by a honeycomb porous plate and a gridded metal structure in a saturated pool boiling of nanofluid, Int. J. Heat Mass Transf. 115 (2017) 969–980. https://doi.org/10.1016/j.ijheatmasstransfer.2017.07.089.

[4] H. Lienhard, Peak Pool Boiling Heat -Flux Measurements, J. Heat Transfer. (1973) 477–482.

[5] C. Zhang, L. Zhang, H. Xu, P. Li, B. Qian, Performance of pool boiling with 3D grid structure manufactured by selective laser melting technique, Int. J. Heat Mass Transf. 128 (2019) 570–580. https://doi.org/10.1016/j.ijheatmasstransfer.2018.09.021.

[6] D. Saeidi, A.A. Alemrajabi, N. Saeidi, Experimental study of pool boiling characteristic of an aluminized copper surface, Int. J. Heat Mass Transf. 85 (2015) 239–246. https://doi.org/10.1016/j.ijheatmasstransfer.2015.01.110.

[7] S.M. Kwark, G. Moreno, R. Kumar, H. Moon, S.M. You, Nanocoating characterization in pool boiling heat transfer of pure water, Int. J. Heat Mass Transf. 53 (2010) 4579–4587. https://doi.org/10.1016/j.ijheatmasstransfer.2010.06.035.

[8] J.S. Kim, A. Girard, S. Jun, J. Lee, S.M. You, Effect of surface roughness on pool boiling heat transfer of water on hydrophobic surfaces, Int. J. Heat Mass Transf. 118 (2018) 802–811. https://doi.org/10.1016/j.ijheatmasstransfer.2017.10.124.

[9] M. Engineering, An Induced-Confection Effect Upon, (2016) 1–5.

[10] Y. Yang, X. Ji, J. Xu, Pool boiling heat transfer on copper foam covers with water as working fluid, Int. J. Therm. Sci. 49 (2010) 1227–1237. https://doi.org/10.1016/j.ijthermalsci.2010.01.013.

[11] R.P. Rioux, E.C. Nolan, C.H. Li, A systematic study of pool boiling heat transfer on structured porous surfaces: From nanoscale through microscale to macroscale, AIP Adv. 4 (2014). https://doi.org/10.1063/1.4902343.

[12] Z.G. Xu, C.Y. Zhao, Experimental study on pool boiling heat transfer in gradient metal foams, Int. J. Heat Mass Transf. 85 (2015) 824–829. https://doi.org/10.1016/j.ijheatmasstransfer.2015.02.017.

[13] B. Shi, Y.-B. Wang, K. Chen, Pool boiling heat transfer enhancement with copper nanowire arrays, Appl. Therm. Eng. 75 (2015) 115–121. https://doi.org/10.1016/j.applthermaleng.2014.09.040.

[14] M. Mahamudur Rahman, J. Pollack, M. Mccarthy, Increasing Boiling Heat Transfer using Low Conductivity Materials, Sci. Rep. 5 (2015) 12–14. https://doi.org/10.1038/srep13145.

[15] A. Jaikumar, S.G. Kandlikar, Enhanced pool boiling heat transfer mechanisms for selectively sintered open microchannels, Int. J. Heat Mass Transf. 88 (2015) 652–661. https://doi.org/10.1016/j.ijheatmasstransfer.2015.04.100.

[16] A.M. Gheitaghy, H. Saffari, M. Mohebbi, Investigation pool boiling heat transfer in U-shaped mesochannel with electrodeposited porous coating, Exp. Therm. Fluid Sci. 76 (2016) 87–97. https://doi.org/10.1016/j.expthermflusci.2016.03.011.

[17] J. Kim, S. Jun, R. Laksnarain, S.M. You, Effect of surface roughness on pool boiling heat transfer at a heated surface having moderate wettability, Int. J. Heat Mass Transf. 101 (2016) 992–1002. https://doi.org/10.1016/j.ijheatmasstransfer.2016.05.067.

[18] Y. Sun, G. Chen, S. Zhang, Y. Tang, J. Zeng, W. Yuan, Pool boiling performance and bubble dynamics on microgrooved surfaces with reentrant cavities, Appl. Therm. Eng. 125 (2017) 432–442. https://doi.org/10.1016/j.applthermaleng.2017.07.044.

[19] G. Chen, C.H. Li, Combined effects of liquid wicking and hydrodynamic instability on pool boiling critical heat flux by two-tier copper structures of nanowires and microgrooves, Int. J. Heat Mass Transf. 129 (2019) 1222–1231. https://doi.org/10.1016/j.ijheatmasstransfer.2018.10.002.

[20] R.J. MacNamara, T.L. Lupton, R. Lupoi, A.J. Robinson, Enhanced nucleate pool boiling on copper-diamond textured surfaces, Appl. Therm. Eng. 162 (2019). https://doi.org/10.1016/j.applthermaleng.2019.114145.

[21] S.J. Kline, Describing uncertainty in single sample experiments, Mech. Eng. 75 (1953) 3–8.

[22] R. Kempers, P. Kolodner, A. Lyons, A.J. Robinson, A high-precision apparatus for the characterization of thermal interface materials, Rev. Sci. Instrum. 80 (2009). https://doi.org/10.1063/1.3193715.

[23] S. Mori, K. Okuyama, International Journal of Multiphase Flow Enhancement of the critical heat flux in saturated pool boiling using honeycomb porous media, Int. J. Multiph. Flow. 35 (2009) 946–951. https://doi.org/10.1016/j.ijmultiphaseflow.2009.05.003.

[24] H. Kim, Y. Park, H. Kim, C. Lee, D.W. Jerng, D.E. Kim, Critical heat flux enhancement by single-layered metal wire mesh with micro and nano-sized pore structures, Int. J. Heat Mass Transf. 115 (2017) 439–449. https://doi.org/10.1016/j.ijheatmasstransfer.2017.08.066.

[25] R. Pastuszko, Pool boiling heat transfer on micro-fins with wire mesh – Experiments and heat flux prediction, Int. J. Therm. Sci. 125 (2018) 197–209. https://doi.org/10.1016/j.ijthermalsci.2017.11.019.

[26] P.J. Berenson, Experiments on pool-boiling heat transfer, Int. J. Heat Mass Transf. 5 (1962) 985–999. https://doi.org/10.1016/0017-9310(62)90079-0.

[27] M.M. Rahman, E. Ölçeroılu, M. McCarthy, Scalable Nanomanufacturing of Virus-templated Coatings for Enhanced Boiling, Adv. Mater. Interfaces. 1 (2014) 1–6. https://doi.org/10.1002/admi.201300107.

[28] G. Liang, I. Mudawar, Review of pool boiling enhancement by surface modification, Int. J. Heat Mass Transf. 128 (2019) 892–933. https://doi.org/10.1016/j.ijheatmasstransfer.2018.09.026.

[29] E.J.T. Pialago, O.K. Kwon, C.W. Park, Nucleate boiling heat transfer of R134a on cold sprayed CNT-Cu composite coatings, Appl. Therm. Eng. 56 (2013) 112–119. https://doi.org/10.1016/j.applthermaleng.2013.03.046.

[30] S. Das, S.D. Kumar, S. Bhowmik, Enhancement of nucleate pool boiling heat transfer on silicon oxide thin film surface, Procedia Eng. 90 (2014) 530–537. https://doi.org/10.1016/j.proeng.2014.11.768.

[31] S. Das, D.S. Kumar, S. Bhaumik, Experimental study of nucleate pool boiling heat transfer of water on silicon oxide nanoparticle coated copper heating surface, Appl. Therm. Eng. 96 (2016) 555–567. https://doi.org/10.1016/j.applthermaleng.2015.11.117.

[32] K.C. Leong, J.Y. Ho, K.K. Wong, A critical review of pool and flow boiling heat transfer of dielectric fluids on enhanced surfaces, Appl. Therm. Eng. 112 (2017) 999–1019. https://doi.org/10.1016/j.applthermaleng.2016.10.138.

[33] A. Hayes, P.A. Raghupathi, T.S. Emery, S.G. Kandlikar, Regulating Flow of Vapor to Enhance Pool Boiling, Appl. Therm. Eng. (2018). https://doi.org/10.1016/j.applthermaleng.2018.12.091.

[34] J.Y. Ho, K.K. Wong, K.C. Leong, Saturated pool boiling of FC-72 from enhanced surfaces produced by Selective Laser Melting, Int. J. Heat Mass Transf. 99 (2016) 107–121. https://doi.org/10.1016/j.ijheatmasstransfer.2016.03.073.

[35] K.K. Wong, K.C. Leong, Saturated pool boiling enhancement using porous lattice structures produced by Selective Laser Melting, Int. J. Heat Mass Transf. 121 (2018) 46–63. https://doi.org/10.1016/j.ijheatmasstransfer.2017.12.148.

[36] P.J. Marto, L.V.J. Lepere, Pool boiling heat transfer from enhanced surfaces to dielectric fluids, J. Heat Transfer. 104 (1982) 292–299. https://doi.org/10.1115/1.3245086.

[37] L.H. Chien, R.L. Webb, Visualization of pool boiling on enhanced surfaces, Exp. Therm. Fluid Sci. 16 (1998) 332–341. https://doi.org/10.1016/S0894-1777(97)10032-2.

[38] A.E. Bergles, 1995 Max Jakob Memorial Award Lecture Heat Transfer Enhancement — The Encouragement and Accommodation of High Heat Fluxes, J. Heat Transfer. 119 (1997) 8–19.

[39] W. Nakayama, T. Daikoku, H. Kuwahara, T. Nakajima, Dynamic model of enhanced boiling heat transfer on porous surfaces: Part II: Analytical modeling, J. Heat Transfer. 102 (1980) 451–456. https://doi.org/10.1115/1.3244321.

[40] K. Stephan, J. Mitrovic, Heat Transfer in Natural Convective Boiling of Refrigerants and Refrigerant--Oil Mixtures in Bundles of T-shaped Finned Tubes, Am. Soc. Mech. Eng. (1981) 131–146.

[41] T. Ma, X. Liu, J. Wu, H. Li, Effects of geometrical shapes and parameters of reentrant grooves on nucleate pool boiling heat transfer from porous surfaces, in: Int. Heat Transf. Conf. Digit. Libr., Begel House Inc., 1986.

[42] L.H. Chien, R.L. Webb, A parametric study of nucleate boiling on structured surfaces part II: Effect of pore diameter and pore pitch, Am. Soc. Mech. Eng. Heat Transf. Div. HTD. 326 (1996) 137–143.

[43] A.K. Das, P.K. Das, P. Saha, Performance of different structured surfaces in nucleate pool boiling, Appl. Therm. Eng. 29 (2009) 3643–3653. https://doi.org/10.1016/j.applthermaleng.2009.06.020.

[44] S. Zhang, Y. Tang, J. Zeng, W. Yuan, J. Chen, C. Chen, Pool boiling heat transfer enhancement by porous interconnected microchannel nets at different liquid subcooling, Appl. Therm. Eng. 93 (2016) 1135–1144. https://doi.org/10.1016/j.applthermaleng.2015.10.044.

[45] D. Deng, W. Wan, J. Feng, Q. Huang, Y. Qin, Y. Xie, Comparative experimental study on pool boiling performance of porous coating and solid structures with reentrant channels, Appl. Therm. Eng. 107 (2016) 420–430. https://doi.org/10.1016/j.applthermaleng.2016.06.172.

[46] Y. Sun, G. Chen, S. Zhang, Y. Tang, J. Zeng, W. Yuan, Pool boiling performance and bubble dynamics on microgrooved surfaces with reentrant cavities, Appl. Therm. Eng. 125 (2017) 432–442. https://doi.org/10.1016/j.applthermaleng.2017.07.044.

[47] W. Hao, T. Wang, Y. yan Jiang, C. Guo, C. hong Guo, Pool boiling heat transfer on deformable structures made of shape-memory-alloys, Int. J. Heat Mass Transf. 112 (2017) 236–247. https://doi.org/10.1016/j.ijheatmasstransfer.2017.04.113.

[48] A. Jaikumar, S.G. Kandlikar, Ultra-high pool boiling performance and effect of channel width with selectively coated open microchannels, Int. J. Heat Mass Transf. 95 (2016) 795–805. https://doi.org/10.1016/j.ijheatmasstransfer.2015.12.061.

[49] A. Jaikumar, S.G. Kandlikar, Enhanced pool boiling heat transfer mechanisms for selectively sintered open microchannels, Int. J. Heat Mass Transf. 88 (2015) 652–661. https://doi.org/10.1016/j.ijheatmasstransfer.2015.04.100.

[50] C.M. Patil, S.G. Kandlikar, Pool boiling enhancement through microporous coatings selectively electrodeposited on fin tops of open microchannels, Int. J. Heat Mass Transf. 79 (2014) 816–828. https://doi.org/10.1016/j.ijheatmasstransfer.2014.08.063.

[51] C. Kruse, A. Tsubaki, C. Zuhlke, T. Anderson, D. Alexander, G. Gogos, S. Ndao, Secondary pool boiling effects, Appl. Phys. Lett. 108 (2016). https://doi.org/10.1063/1.4941081.

[52] A. Jaikumar, S.G. Kandlikar, Pool boiling enhancement through bubble induced convective liquid flow in feeder microchannels, Appl. Phys. Lett. 108 (2016). https://doi.org/10.1063/1.4941032.

[53] A. Jaikumar, S.G. Kandlikar, Pool boiling inversion through bubble induced macroconvection, Appl. Phys. Lett. 110 (2017). https://doi.org/10.1063/1.4977557.

Chapter 6 Investigation of the Thermal Performance of Geyser Boiling in a Small Diameter Two-Phase Loop Thermosyphon[4]

This chapter investigates the geyser boiling phenomenon (GBP) occurring in a passively cooled, two-phase loop thermosyphon. The influence of the heating load, working fluid, fill ratio, and the evaporator surface design on thermosyphon thermal performance and the associated instabilities were studied. These parameters were examined for different fluid and machined evaporator configurations. The fast Fourier transform, and the standard deviation of the evaporator temperature and the system pressure were employed together with flow regime visualization to characterize and quantify the GBP intensity and frequency. This study represents the initial baseline study towards achieving the last objective, which aims to investigate the thermal performance enhancement of the two-phase loop thermosyphon (TPLT) using SLM evaporators.

6.1 Introduction & Background

The last decade has witnessed immense progress in microelectronics and telecommunication technologies, leading to further miniaturization of electronic components and higher power densities. These applications demand compact, robust, reliable and effective cooling methods. Two-phase thermosyphons represent one of the most promising methods owing to their simple construction and no requirement for external driving power. Thermosyphons have been widely utilized in applications ranging from the cooling of data centers [1], [2], power electronics [3]–[6], heat recovery systems [7], and solar energy systems [8], [9].

---

[4] This chapter has been published as a peer-reviewed journal paper titled “Experimental Investigation of Geyser Boiling in a Small Diameter Two-Phase Loop Thermosyphon” in *Experimental Thermal and Fluid Science*.

Typically, thermosyphons are wickless, gravity-driven closed loops with excellent heat transfer capability arising from the high heat transfer coefficients of the boiling and condensation processes of the working fluid. Thermosyphons can be found into two types: the reflux type or the loop one. For the reflux type, the evaporate and condenser are connected through one adiabatic tube, where the liquid and vapor phase are flowing countercurrent to each other, which promotes flow instabilities at high heat fluxes. This can be avoided in the two-phase loop thermosyphon (TPLT), which encompasses four components: the evaporator, the riser, the condenser, and the downcomer. The heat absorbed by the evaporator promotes the liquid ebullition and its conversion into vapor. The vapor flows upward through the riser to the condenser, where it condenses and releases its latent heat. The condensed liquid returns to the evaporator through the downcomer under the influence of gravity to complete the cycle. This signifies the requirement of positioning the condenser above the evaporator. The working fluid circulates naturally within the thermosyphon because of the buoyancy force produced by the density difference between the downcomer and the riser.

Many factors affect the TPLT performance, such as the fill ratio, defined as the volume ratio of the fluid relative to the total volume, [10], [11], fluid type [12], pipe size [13], and the presence of non-condensable gas [14]. Recent reviews for thermosyphons and heat pipes that further address the working principles, operational limits, and modeling are available in [15], [16].

Although thermosyphons have exceptional heat transport ability, they can experience operational instabilities, particularly the geyser boiling phenomenon (GBP), which can occur in both reflux and looped thermosyphons [17], [18]. The GBP mostly occurs in small-diameter thermosyphons at low heat fluxes and high fill ratios, and is attributed to the rapid expansion of the vapor in the evaporator where the bubbles coalesce and grow to fill the pipe, forming a large

Taylor vapor bubble in the riser, which traps a liquid slug above. The liquid slug is propelled upward to the condenser until the vapor–liquid interface abruptly shatters because of bubble collapse. As a result of heat rejection at the condenser or by mixing with the sub-cooled liquid, the Taylor bubble is suppressed, and gravity drives the condensed liquid back to the evaporator to repeat the process. This intermittent behavior induces pressure and temperature fluctuations accompanied by vibrations and noticeable sounds, which Negishi and Sawada recognized as water hammer [19].

The onset of GBP-induced vibrations can be a stimulus for weakening the welding points, creating leakage problems, and reducing the device lifetime, particularly when the thermosyphon is working in dynamic environments, such as in moving vehicles and aircraft, which should therefore be avoided. In this context, the present chapter is devoted to investigating the influence of evaporator surface structure on the GBP for a small-diameter TPLT.

Griffith [20] was the first to experimentally elucidate the transport mechanism of the GBP in a two-phase reflux thermosyphon. Boure et al. [21] reviewed all types of instabilities, mechanisms, and causes that may exist in two-phase flows. Negislii and Sawada [19] investigated the performance of a closed two-phase thermosyphon under variable fill ratios and inclination angles for water and ethanol. They concluded that the fill ratio must be between 25–60% for water, whereas it should be 40–75% for ethanol to avoid the GBP. In the same way, many researchers [22]–[26] investigated the effect of many other parameters on the GBP for the reflux thermosyphon, such as the inclination angle, condenser cooling rate, the coolant temperature, the pressure, the evaporator length, aspect ratio, and the tube diameter.

Niro and Beretta [27] developed a correlation to distinguish between the main boiling regimes: intermittent boiling, GBP, and fully developed boiling. They suggested that the transition between the regimes depends on the time ratio between the waiting time for the bubble to nucleate and the essential time for the bubbles to grow. For instance, if the nucleation waiting time is dominant, it is recognized as intermittent boiling. Smith et al. [17] characterized the boiling regimes in the reflux type thermosyphon into four regimes—churn, bubbly, geyser, and slug/plug—based on the confinement number and the vapor generation rate. Pabón et al. [28] revealed that the controlling parameter for geysering to occur depends on the height difference between the nucleation sites and the liquid free surface. If the height difference is small, the resulting pressure surge that originates from geysering will be small because less energy is stored in the bubble and vice versa.

Kujawska et al. [29] examined the effect of the addition of nanoparticles and/or chemical stabilizers to the base fluid on the GBP for the reflux thermosyphon. They showed that both the nanoparticles and chemical stabilizers influenced the GBP, and together these (base fluid, nanoparticles, and the stabilizer) could suppress the GBP completely.

Jouhara et al. [30] was the first study to numerically model the geysering flow using the conventional Lee model for a closed two-phase thermosyphon with water and R134a as the working fluids, and compared it with the visualization results. However, rapid growth of the Taylor bubble was not accurately captured, which was further studied by [31]; they improved the conventional Lee model without neglecting the essential superheat to initiate the nucleation at the heated walls, which showed good agreement with the transient visualization results.

Fewer studies have addressed the GBP in loop thermosyphons. Garrity et al. [32], [33] proposed a methodology which anticipates the inception of the instability using the derivative of the evaporator pressure drop with respect to the mass flux through the thermosyphon. They reasoned that the fluctuations were triggered when the derivative of the pressure drop-flow rate function is negative. Khodabandeh and Furberg [13] investigated the corresponding instabilities for high and low heat fluxes for copper nano- and micro-porous evaporator surfaces in a water-cooled TPLT using R134a as the working fluid. It was shown that these enhanced surfaces lowered the oscillation intensity compared with a smooth evaporator. Chang et al. [34] categorized the instabilities that LTPT may encounter into either low heat flux instabilities or high heat flux instabilities. Low heat flux instabilities are characterized by the existence of a Taylor bubble and having a substantial waiting time, which stimulates a larger amplitude of evaporator temperature oscillation. However, the high heat flux instability is agitated by a spectrum of smaller bubbles with a shorter waiting time. Tecchio et al. [35], [36] developed TPLT, for cooling aircraft power electronics which consisted of one shared evaporator and two condensers with water as the working fluid. They investigated the GPB at different fill ratios for multiple combinations of free convection and forced convection at the condensers. They also measured accelerations induced by the geysering instability by attaching an accelerometer at one of the evaporator faces. They found that the acceleration is sensitive to the condensers' thermal resistance ratio.

Liu et al. [18], [37] examined the effect of fill ratio on geysering in TPLT with R134a as the working fluid. They quantified GBP intensity by employing the power spectral density and the standard deviation for the pressure wave fluctuations. They found that the initiating heater power which triggered geysering instabilities decreased by increasing the fill ratio. They further visualized the flow patterns at the evaporator outlet and observed the flow regime change in a periodic cycle from single phase bubbly flow to churn flow.

Overall, the effect of the geometrical and operational parameters on the geysering phenomenon for two-phase reflux thermosyphons was studied extensively. Relatively few studies have addressed GBP in TPLT and most of these have focused primarily on understanding the geysering mechanism itself. Therefore, the current chapter examines the influence of changing the evaporator surface geometrical parameters, in conjunction with the operational parameters (fill ratio and the working fluid), on the thermal performance and the GBP for TPLT.

6.2 Experimental Setup & Methodology

The loop thermosyphon apparatus used in the present study is shown schematically in Figure 6-1and in the photographs in Figure 6-2. This thermosyphon consists of an aluminum, side-heated evaporator connected to a naturally aspirated aluminum condenser located 1150 mm above the evaporator using flexible transparent nylon tubing for the riser and a downcomer to facilitate two-phase flow visualization. The riser has 9.5 mm (3/8 inch) outer diameter tubing with an inner diameter of 7.5 mm (0.295 inches) while the downcomer has a 6.35 mm (1/4 inch) outer diameter with an inner diameter of 4.8 mm (0.19 inches). All tube fittings are Swagelok fittings.

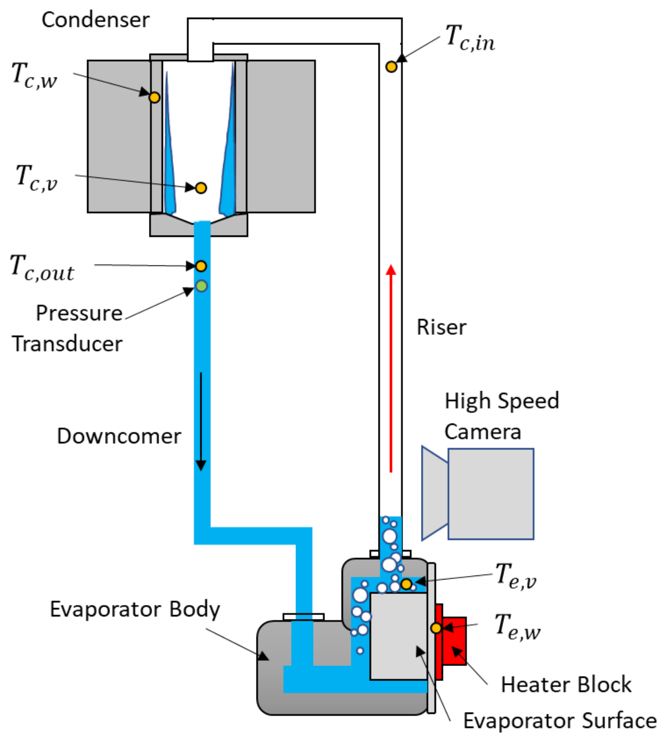

Figure 6-1: Schematic of loop thermosyphon apparatus and instrumentation.

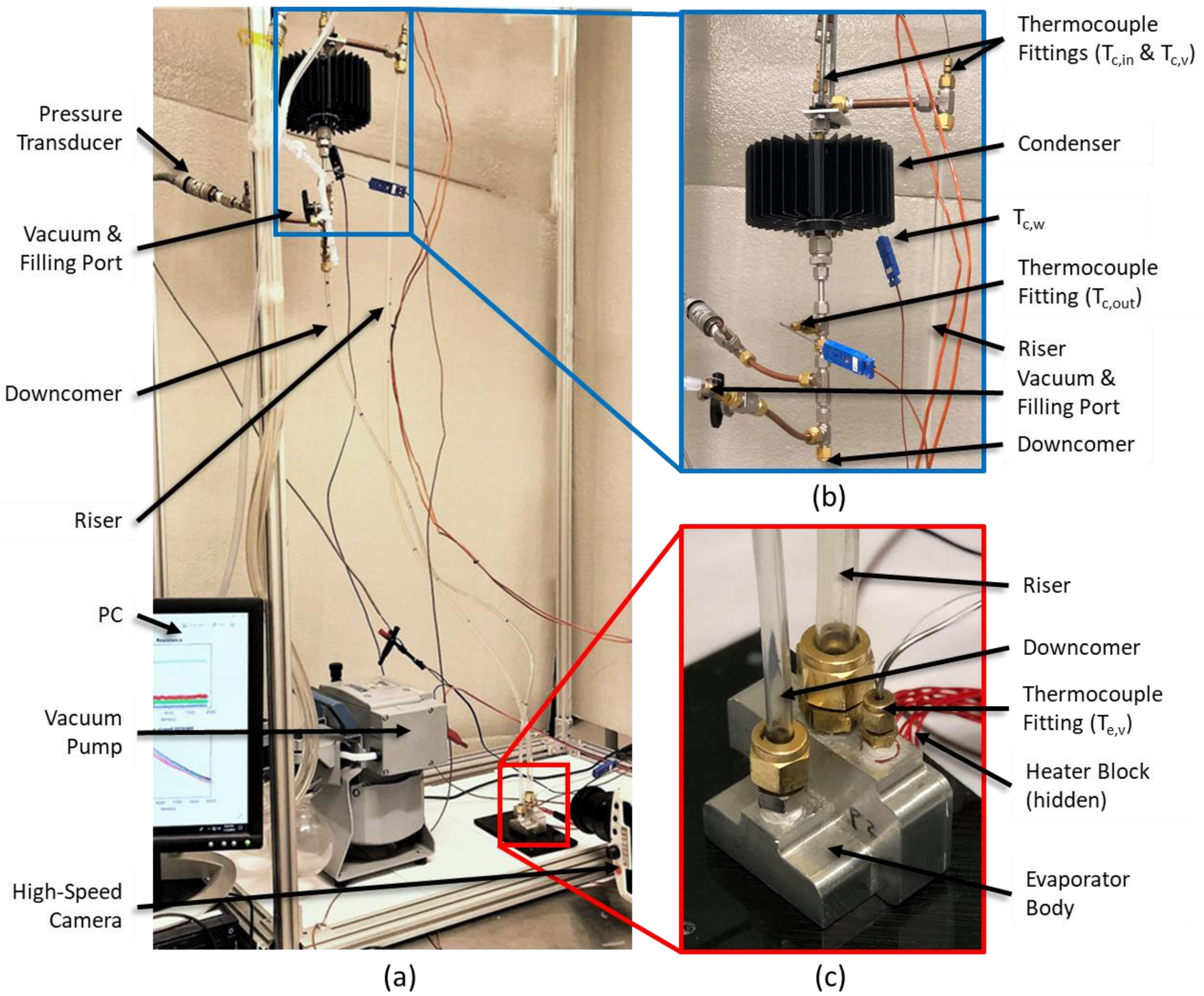

Figure 6-2: (a) Overview of experimental apparatus, (b) closeup of condenser section, (c) closeup of the evaporator section.

6.2.1 Condenser Section

A detailed view of the natural convection condenser is shown in Figure 6-3. It consists of a radial finned heat sink (TitanTurbo HS-5430-0537, Lamina Lighting Inc.) like that used in [38]. The heat sink was drilled and tapped to accommodate the inlet flow and a thermocouple inserted into the vapor space through a T-fitting. The bottom end of the heat sink was closed with a tapered cap (shown in Figure 6-3b) to form a closed chamber. The vapor condenses on the inner diameter of this chamber and the heat is conducted out to the fins where it is dissipated to the ambient air by natural convection. The condensate flows downward through the tapered cap to the downcomer to return to the evaporator.

The condenser is instrumented with 1.59 mm (1/16 inch) diameter, T-type thermocouples just before the inlet, in the center of the condensation chamber, just after the condenser at the top of the downcomer and embedded into the base of one of the fins. These correspond to $T_{c,in}$, $T_{c,v}$, $T_{c,out}$, and $T_{c,w}$ in Figure 6-1 and Figure 6-2b, respectively. An additional T-type thermocouple measures ambient air temperature, T_{amb}.

A pressure transducer (Gems 2200BG6F002233DA) is connected to the downcomer using a T-fitting just below the condenser to monitor system pressure as indicated in Figure 6-1 and Figure 6-2b. A vacuum and filling port is located just below the pressure transducer which uses another T-fitting as shown in Figure 6-2b.

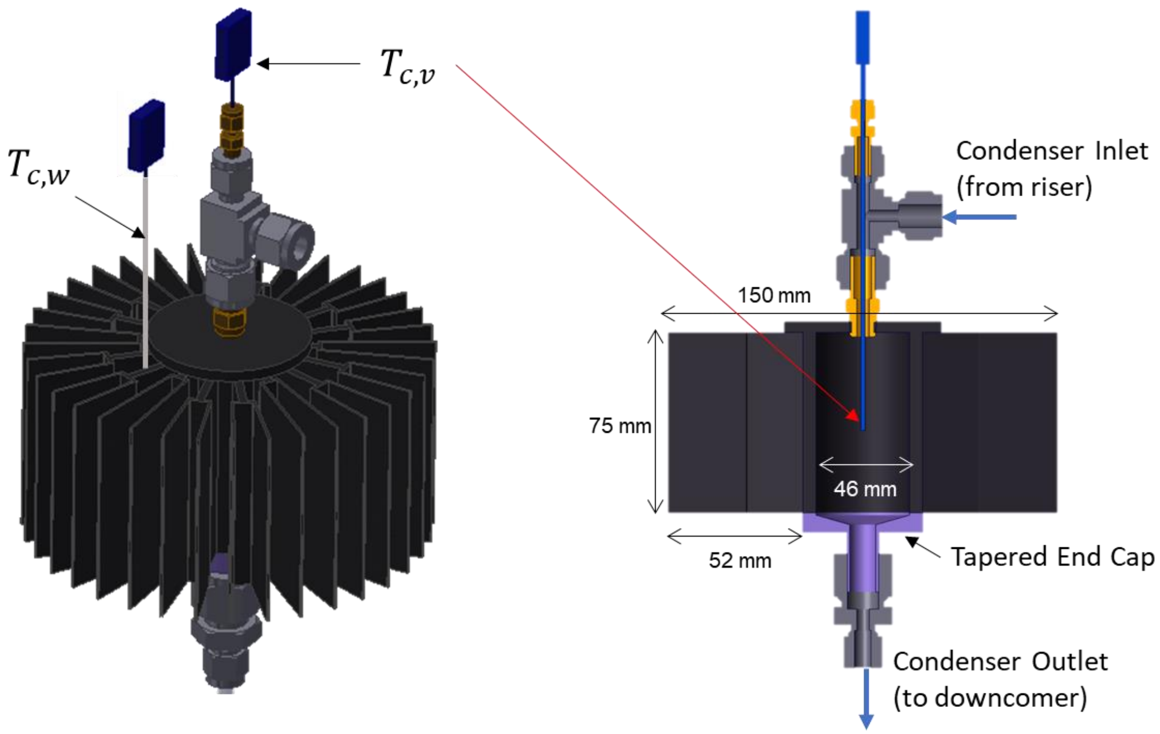

(a) (b)

Figure 6-3: Radially finned natural convection condenser.

6.2.2 Evaporator Section

Detailed exploded views of the evaporator section are shown in Figure 6-4a and a cross-section illustrating the flow path is shown in Figure 6-4b. Each evaporator is comprised of an evaporator body and the evaporator surface. The evaporator body contains and directs the flow of working fluid and connects the evaporator section to the downcomer and riser. Liquid flowing downward from the condenser enters through the inlet and flows horizontally along the bottom channel to feed the heated evaporator surface. Each evaporator surface is bolted to a corresponding evaporator body using a series of M3 screws to form a closed evaporator section where the flow is ducted through the evaporator surface structures (which are detailed below) without bypass. This joint was sealed using a silicone adhesive.

Each evaporator is instrumented with a 1.59 mm (1/16 inch) diameter T-type thermocouple inserted through a fitting just above the evaporator surface ($T_{e,v}$ as shown in Figure 6-1 and Figure 6-4a). A 0.5 mm (0.02 inch) diameter T-type thermocouple was inserted into a groove machined into the back of the evaporator surfaces to monitor evaporator wall temperature ($T_{e,w}$). Heat is applied to the evaporator surface using a copper heater block as shown in Figure 6-4 with a contact patch of 21.5 mm x 49 mm. The heater block contains six cartridge heaters (Sun Electric Heater) with a diameter of 3.1 mm (1/8 in) and length of 12.5 mm (1/2 in). The input power was controlled using DC power supply (Aim TTi, CPX400D) and quantified by measuring the imposed voltage and the resulting current. The copper heater block was bolted to the evaporator surface with two M3 screws and a small amount of thermal paste (ARCTIC, MX-4) to help minimize thermal contact resistance.

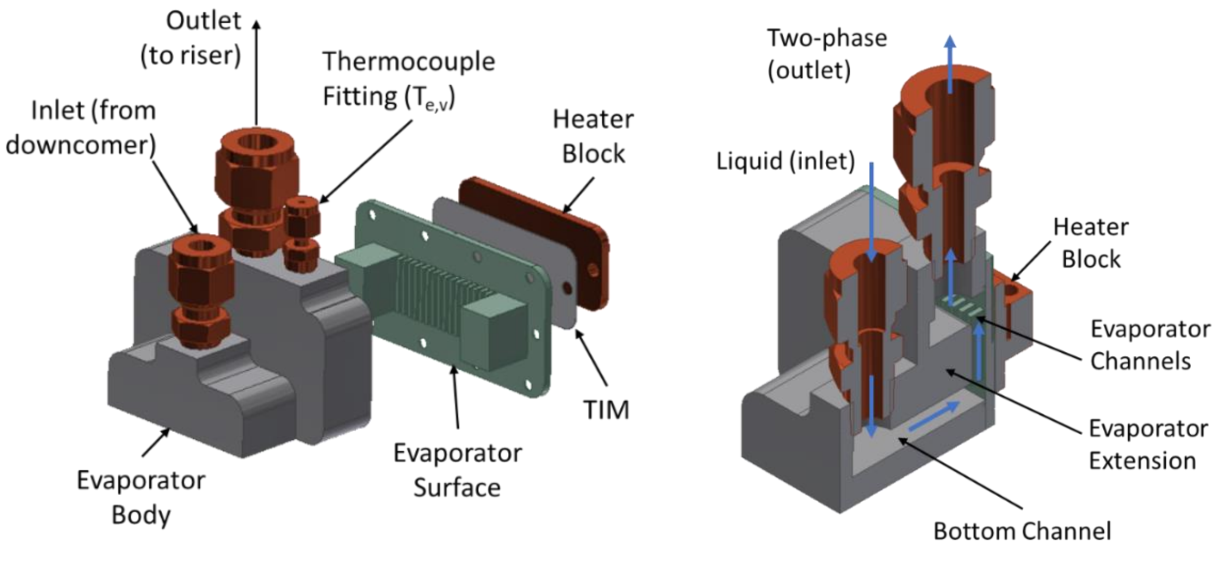

(a) (b)

Figure 6-4 (a) Exploded view of the evaporator, (b) cross-section view of evaporator highlighting flow path.

6.2.3 Evaporator Designs & Working Fluids

The geyser phenomenon was examined for three evaporator designs with different hydraulic channel diameters, as depicted in Figure 6-5. The first design, D1, consists of a staggered array of vertical holes with 3 mm diameters spaced 6 mm apart (Figure 6-5a). The other two designs (shown in Figure 6-5b and c) consist of an array of vertical fins with heights of 3 mm and 1.5 mm, and fin spacings of 1 mm and 0.5 mm, which are denoted D2 and D3, respectively. The geometries of the evaporator designs are summarized Table 6-1.

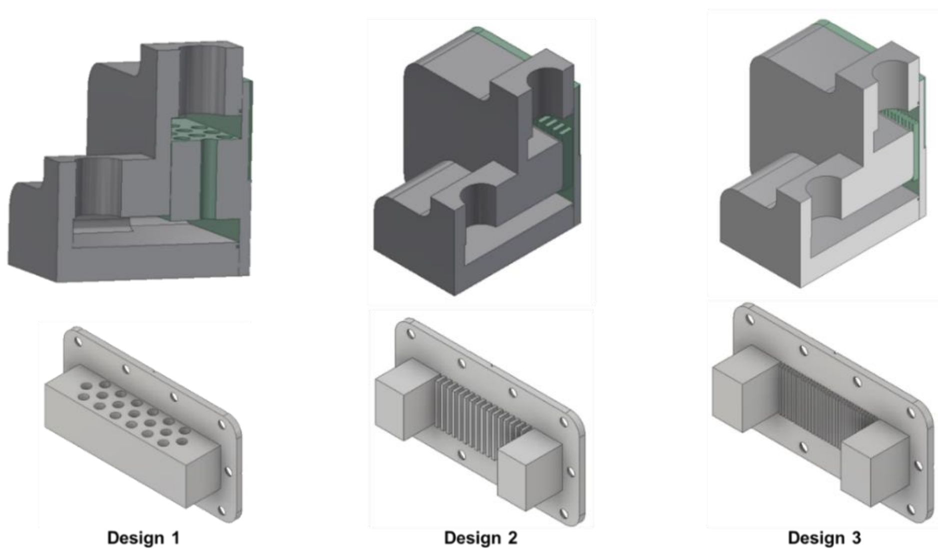

(a) (b) (c)

Figure 6-5: Different evaporator designs: (a) holes, (b) ducted long fins, (c) ducted small fins.

Table 6-1. Geometrical characteristics for each evaporator.

Evaporator Design	Boiling Surface Area (mm^2)	Channel Hydraulic Diameter (mm)
Holes (D1)	2507	3
Ducted long fins (D2)	1582	1.5
Ducted small fins (D3)	1575	0.75

Two working fluids with different vapor pressures were examined (deionized water and ethanol) to examine the effect of evaporator structure for different bubble dynamics. Both fluids are transparent, to facilitate visualization of the flow behavior, non-toxic, and have a high figure of merit (FOM). Table 6-2 shows the thermophysical properties for each fluid at atmospheric pressure.

Table 6-2. Thermophysical properties for each fluid at atmospheric pressure (1 bar).

Fluid	T_{sat} (°C)	ρ_l (kg/m^3)	ρ_v (kg/m^3)	μ_l (kg/mS)	σ (mN/m)	h_{fg} (kJ/kg)	FOM [17]
DI Water	100	957.9	0.5978	0.282×10^{-3}	59	2257	6925
Ethanol	78.37	757	1.4	0.4×10^{-3}	17	960	1574

Here, the objective was to understand how the geometry of these structures, in conjunction with the working fluid, influence evaporator confinement on the geysering phenomenon and the thermal performance of the loop. The effective bubble size is a result of the force interaction between surface tension and the buoyancy which can be represented as a function of the capillary length given by

$$\lambda_c = \sqrt{\frac{\sigma}{(\rho_l - \rho_v)g}} \tag{6.1}$$

where, ρ_l and ρ_v are the liquid and vapor densities while σ is the surface tension. The significance of the bubble size relative to the channel size can be represented by the confinement number which is the ratio of the capillary length to the channel diameter, given by

$$\mathrm{Co} = \frac{\lambda_c}{D} = \frac{1}{D}\sqrt{\frac{\sigma}{(\rho_l - \rho_v)g}} \tag{6.2}$$

where, D, is the inner diameter of the riser or the channel diameter.

A high confinement number, $\mathrm{Co} = 1$, represents microscale flow, whereas when it is minimal, $\mathrm{Co} \ll 1$, the boiling is considered pool boiling because the pipe is large relative to the bubble size. The flow is considered confined when the confinement number is between 0.3 and 0.4 [17]. The confinement number was calculated for each set of combinations of the evaporator fluid type based on the riser diameter and the evaporator hydraulic diameter, as given by Table 6-3.

In addition, four different fill ratios were examined for each set of combinations: 11%, 17%, 28%, and 38%. The fill ratio was calculated here, based on the volumetric ratio between the working fluid in the loop and the total volume. The total volume was measured accurately by evacuating the loop and letting water flow into the loop from a graduated tank and measuring the withdrawn volume.

Table 6-3. The confinement number and the capillary length for each combination between the fluid and the evaporator.

Combination	**Capillary Length, λ_c (mm)**	**The Ratio of Capillary Length to Channel Hydraulic Diameter**	**Confinement Number, Co, Based on the Riser Diameter**
Holes (D1)-Deionised Water	2.5	0.83	0.33
Holes (D1)-Ethanol	1.5	0.5	0.2
Ducted Long Fins (D2)-Deionised Water	2.5	1.67	0.33
Ducted Long Fins (D2)- Ethanol	1.5	1	0.2
Ducted Small Fins (D3)-Deionised Water	2.5	3.3	0.33
Ducted Small Fins (D3)- Ethanol	1.5	2	0.2

6.2.4 Instrumentation & Data Acquisition

The temperature distribution throughout the thermosyphon was measured using the seven T-type thermocouples in the condenser and evaporator sections as discussed above and summarized as yellow circles in Figure 6-2.

Flow visualization in the riser was performed using a high-speed camera, (Phantom v1612), equipped with Nikon lens (IF Aspherical MACRO (1:2) Ø72) to image the two-phase flow regimes at the evaporator exit at a frequency of 100 fps. Simultaneous measurements of the temperatures, pressure, and heater voltage were acquired every 0.15 seconds using an Agilent 34970A data acquisition unit, while the heater current was measured using the power supply's internal ammeter.

6.2.5 Experimental Procedure

Prior to charging the loop with the working fluid, the loop was rinsed with the working fluid and then evacuated to low pressure. Leakage tests were performed by evacuating the loop to approximately 0.07 bar using a vacuum pump (Vacuubrand MZ 2C NT +2AK) and monitoring the pressure 3–4 hours. Once it was established that the loop was not leaking, the working fluid was degassed externally to remove any dissolved non-condensable gases. The required quantity of working fluid was then supplied to the empty loop through the filling port and drawn in by the vacuum. During testing, the power was increased in increments of 20 W and the temperatures were monitored until they were at steady-state (or quasi-steady, depending on the tests) which typically took 40 minutes per step. The steady or quasi-steady data were recorded at each increment.

6.2.6 Data Reduction & Uncertainty Analysis

The thermal performance of the thermosyphon was quantified by its overall thermal resistance, R_t, and given by the following equation:

$$R_t = \frac{T_{e,w} - T_{amb}}{Q} \tag{6.3}$$

where $T_{e,w}$ is the evaporator wall temperature and T_{amb} is the ambient air temperature. This overall thermal resistance represents the sum of four component resistances: the evaporator resistance, the riser resistance, the condensation resistance, and the convection resistance given by:

$$R_e = \frac{T_{e,w} - T_{e,v}}{Q} \tag{6.4}$$

$$R_{riser} = \frac{T_{e,v} - T_{c,v}}{Q} \tag{6.5}$$

$$R_c = \frac{T_{c,v} - T_{C,w}}{Q} \tag{6.6}$$

$$R_{conv} = \frac{T_{C,w} - T_{amb}}{Q} \tag{6.7}$$

where $T_{e,v}$, $T_{c,v}$, $T_{c,w}$ are the temperatures of the evaporator vapor, condenser vapor, condenser wall respectively (shown in Figure 6-1–Figure 6-4). Q is the input power at the evaporator and can be calculated as:

$$Q = VI - Q_{loss} \tag{6.8}$$

where V is the applied voltage and I is the current into the heater, and Q_{loss} is the heat loss from the evaporator by convection and radiation to the ambient. Q_{loss} was estimated by evacuating the thermosyphon and tuning the power until reaching an equivalent evaporator temperature when the thermosyphon was in operation (typically less than 5%).

The GBP frequency was measured by employing the fast Fourier transform method for the pressure signal. The intensity of the GBP events was calculated using the standard deviation for the system pressure and the evaporator temperature signals. The uncertainties for all measured quantities are given in Table 6-4.

Table 6-4. The uncertainty for each input parameter.

Parameter	Uncertainty	
Temperature	± 0.1 °C	
Voltage	Range	± (% of reading + % of range)
	10 V 100 V	0.0035 + 0.0005 0.0045 + 0.0006
Current	0.3% of reading ± 2 digits	
Pressure	0.25% FS (FS=45 PSIG)	

The resultant uncertainty in calculating the thermal resistances was estimated by the error propagation method by Kline and McClintock [39] and is given by

$$U_R = \sqrt{\left(\frac{\partial R}{\partial V} U_V\right)^2 + \left(\frac{\partial R}{\partial I} U_I\right)^2 + \left(\frac{\partial R}{\partial T_1} T_1\right)^2 + \left(\frac{\partial R}{\partial T_2} T_2\right)^2} \tag{6.9}$$

where U_i is the uncertainty of quantity i.

6.3 Results & Discussion

An overview of thermosyphon thermal performance, along with the simultaneous photos captured using the high-speed camera, is presented and discussed first to establish the mechanisms and factors contributing to the GBP. The GBP is then further examined in the following sub-sections in the context of changing the geometrical and operational parameters of the thermosyphon loop.

6.3.1 Geyser Boiling Mechanism

Figure 6-6 illustrates the instantaneous pressure and temperature history under quasi-steady conditions for evaporator D1 at different heating loads when working with water at a moderate fill

ratio of 28%. Geyser boiling was observed as evidenced by the pressure and temperature fluctuations, particularly at low powers. The pressure fluctuation frequency, f_p, increased linearly with the imposed load, as demonstrated in Figure 6-7. In contrast, the standard deviation, SD_T, of the temperature fluctuation decreased until achieving a constant value of 0.14 ºC at an input power of 120 W, which is about one order of magnitude lower than that observed at low powers. From a thermal performance standpoint, Figure 6-8 demonstrates the influence of the input power on the thermal resistance of each component of the thermosyphon. The convection resistance is nearly constant and dominates regardless of the heating load due to the relatively small heat transfer coefficients associated with natural convection; however, a slight decrease R_{conv} is observed at higher temperatures, partly due to improved natural convection and the radiative component.
The condensation resistance is relatively small for all powers due the high heat transfer coefficient associated with film condensation, the relatively large internal surface area of the condenser, and the high conductivity of the aluminum heat sink.

The riser resistance decreases with increasing heat load, as shown in Figure 6-8. Here, the riser resistance is defined by the temperature difference between the evaporator and the condenser, and consequently by the pressure drop through the riser. Although increasing the heat flux tends to increase the pressure drop through the riser (due to higher flowrates), its rate of increase per heat flux (*dP/dQ*) decreases, which results in decreasing the riser resistance with the heat flux. The two-phase pressure drop through the riser is a function of different parameters such as the liquid viscosity, the quality, and the vapor velocity. Increasing the heat flux changes the contribution of each of these parameters in the resultant pressure drop. For example, increasing the heat flux increases the pressure, hence decreasing the liquid viscosity, however, it increases the vapor velocity.

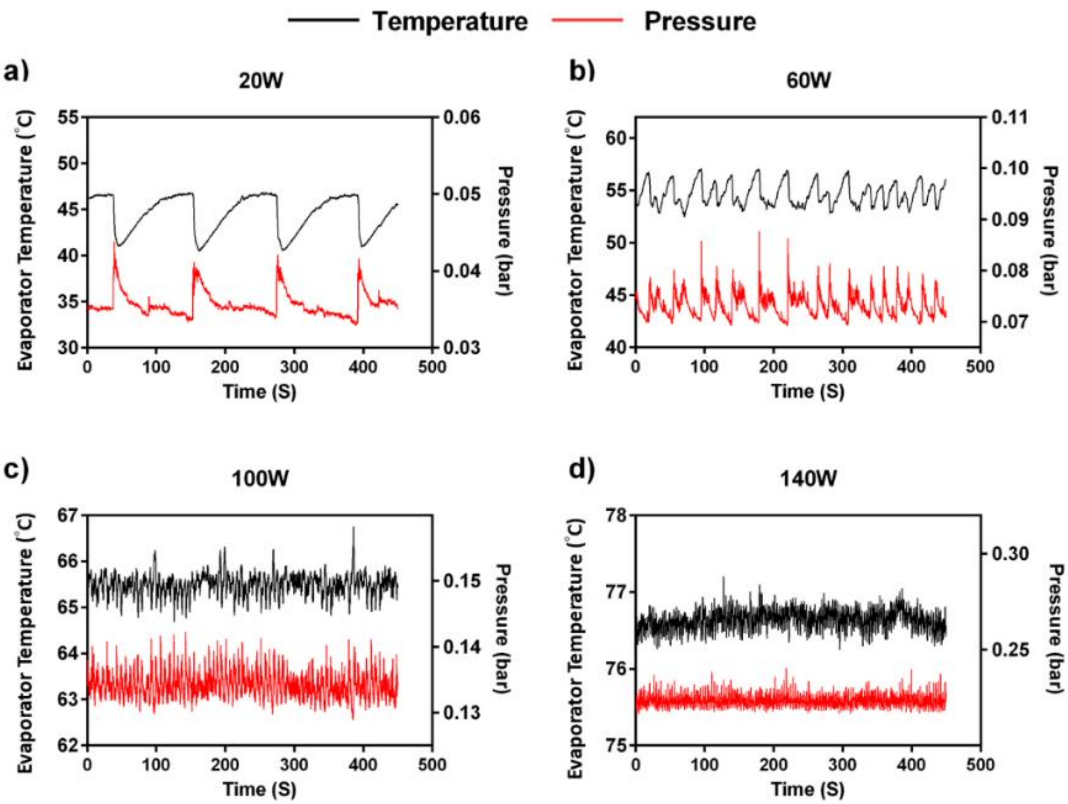

Figure 6-6: The evaporator temperature and the system pressure for evaporator Design 1 with water as the working fluid at fill ratio of 28% for different loads: (a) 20 W, (b) 60 W, (c) 100 W, (d) 140 W.

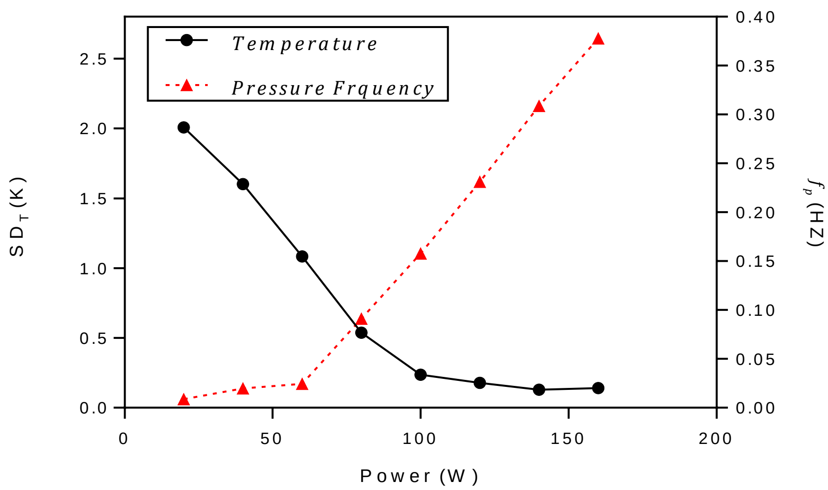

Figure 6-7: The effect of increasing the input power on the pressure fluctuation frequency and the evaporator temperature fluctuation for the evaporator of Design 1 with water as the working fluid at fill ratio of 28%.

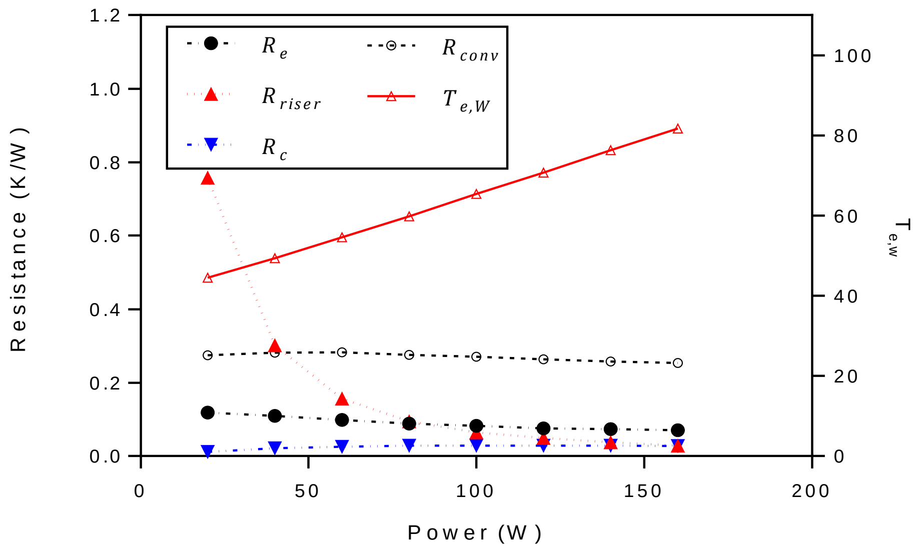

Figure 6-8: The effect of increasing the input power on the thermal resistance of each side of the thermosyphon for the evaporator of Design 1 with water as the working fluid at a fill ratio of 28%.

To identify the mechanisms contributing to the GBP, a single geyser event is shown in Figure 6-9 which represents a complete cycle of how the system pressure and evaporator temperature change during quasi-steady operation. This case examines evaporator D1, with water at fill ratio of 28% for an input power of 20 W (corresponding to a region from Figure 6-6a). Corresponding images of the two-phase flow in the riser (above the evaporator outlet) and downcomer are shown at key times in Figure 6-9c.

The pressure graph can be divided into two regions: first, the decreasing region until 152 s followed by sharp upsurge and another gradual reduction in the second region from 157.35 s until the cycle ends. The inverse of this trend happens in the evaporator temperature (Figure 6-9b).

The first region starts as a liquid phase with no apparent movement of the liquid, which can be considered to be pool boiling because the evaporator temperature does not reach the critical superheat for the bubbles to nucleate. Therefore, the heat transfer rate is characterized only by natural convection mode.

At t=97.65 s, a few bubbles are seen to approach and later coalesce, forming a larger bubble at t=98.1 s. However, the size of the bubble is observed to decrease which may be due to condensation occurring as the bubble advects into the liquid column in the riser. As such, the boiling regime is bubbly with pulsating tiny movements of the liquid column, which explains corresponding small-scale pressure and temperature fluctuations.

At t=98.7 s, the bubbles formed a relatively large Taylor bubble, denoted by a red line, which trapped a liquid slug and propelled it upward to the condenser. Here, we conjecture that the buoyancy force was not sufficient to overcome the weight of the liquid column, limiting circulation; this effect is more pronounced in cases with high fill ratio. Consecutive Taylor bubbles are formed, and each bubble traps a liquid slug above each other, which can be viewed as a slug–plug flow. Nevertheless, these Taylor bubbles either deform, and the liquid slug returns to the evaporator, as shown in t=98.96 to 98.99 s, or decrease in size and lift upwards, forming the slug–plug flow shown from t=100.2 to 100.23 s.

The pressure reading starting from the beginning of the cycle until this stage plateaus, which at the same time is accompanied by the presence of a large, stagnant vapor bubble in the downcomer above the evaporator inlet. Again, we suspect this bubble does not flow upward because its buoyancy is resisted by the weight and the capillary action of the liquid in the downcomer, which has a smaller diameter to the riser.

At t=112.8 s, the pressure starts to decrease slightly and, simultaneously, the liquid–vapor interface in the downcomer begins to change. We conjecture that this is due to a reduction in evaporation rate as the bubbles flowing through the riser take longer to reach the liquid-free surface, which has risen over time. Consequently, the vapor bubble in the downcomer begins to move, as shown, from t=112.8 to115.95 s. The pressure decline also helps the growth of bubbles through the riser, increasing the buoyancy, which in turns initiates the flow which starts circulating accompanied by a sharp rise in the pressure from t=157.62 to 157.88 s.

The flow circulation causes the evaporator to flood with subcooled liquid, causing a decrease in temperature, as shown in Figure 6-9b. While the fluid is circulating, it tends to entrain some bubbles into the downcomer, which is the reason for having a large vapor bubble through the downcomer to begin with.

In the second region, there is no flow, and the heat transfer again becomes a single-phase natural convection, t=163.2 s. Thus, no bubbles exist due to the low temperature of the evaporator. During the waiting time while the bubbles nucleate, the pressure gradually decreases as a result of the low evaporation rate compared with the vapor condensation occurring in the condenser.

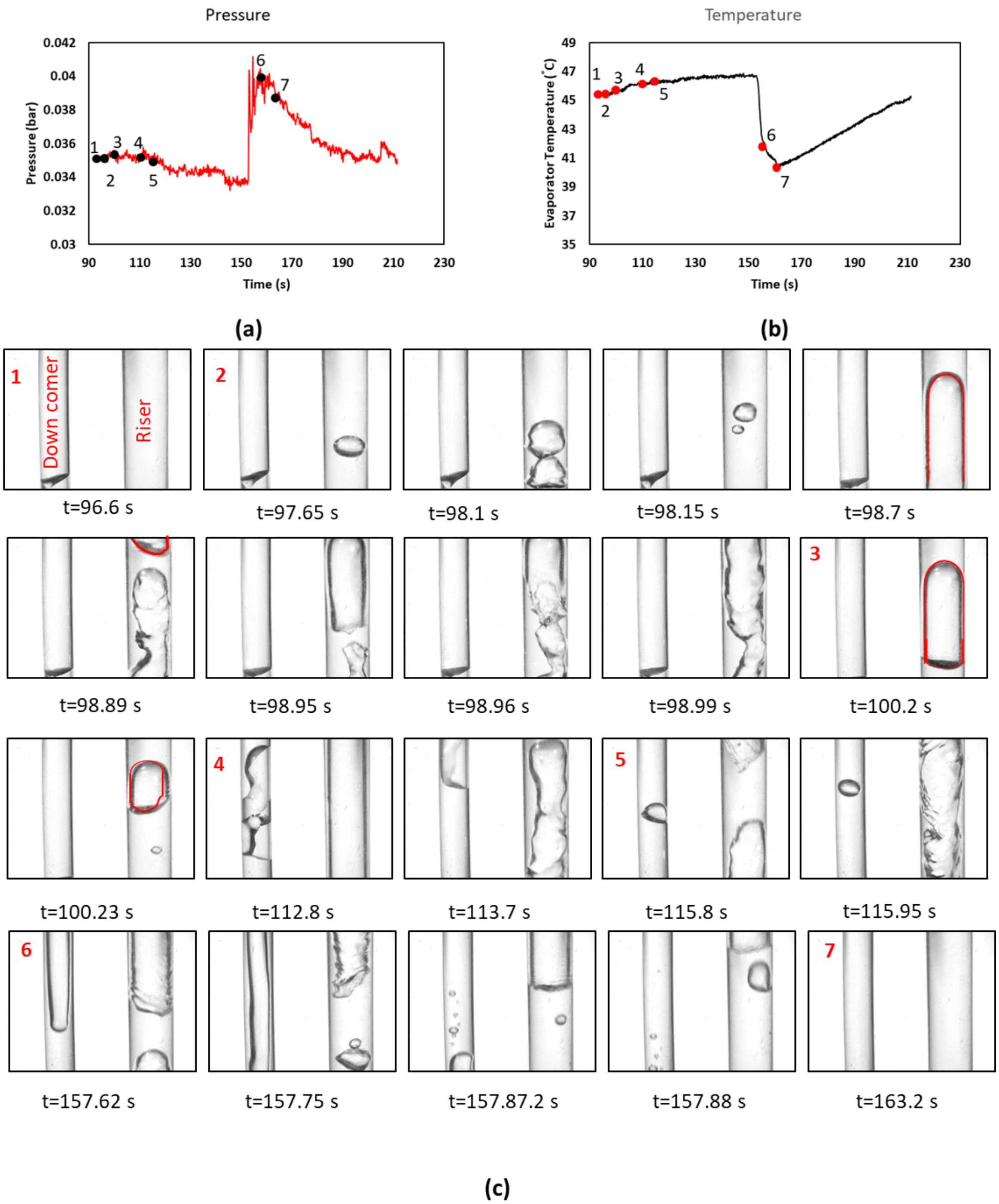

Figure 6-9: The effect of geyser boiling on: (a) pressure, (b) evaporator temperature, (c) flow visualization with water as the working fluid at fill ratio of 28% for heating load of 20 W.

6.3.2 Effect of Working Fluid

The working fluid can significantly influence thermosyphon thermal performance through its influence on bubble dynamics in the evaporator and the hydraulic performance of the loop. The effect of working fluid was investigated here by comparing water and ethanol in the thermal–hydraulic performance of the looped thermosyphon.

Figure 6-10 shows a comparison between the thermal resistance of the thermosyphon charged with water and ethanol as a function of heat transfer rate for evaporator D1, at a moderate fill ratio of 28%. Ethanol achieved superior performance compared with water for all heating loads with 39% lower thermal resistance than water at an input heater power of 20 W. Although ethanol had a better performance at low heat fluxes, both fluids achieved the same performance at high powers. At low heat fluxes, the riser resistance was dominant as described in detail in Section 6.3.3, and it was higher for water. As for high heat fluxes, the riser resistance is lessened, making the convection resistance dominates, which was the same for both fluids. The reason for the riser resistance decrease with the heat flux increase, is related to the pressure drop through the riser, which was discussed previously in 6.3.1. Also, this figure shows a comparison between the thermal performance of the investigated thermosyphon in the current work with different studies from the literature for naturally aspirated loop thermosyphon [40]–[43]. As can be seen, all data showed the same falling trend of the thermosyphon overall resistance with increasing power. However, the average value of each is different due to the difference in the geometrical values or operational parameters, such as the design of the evaporator and the condenser, the height difference between them, the fluid type, and the fill ratio. The effect of the working fluid was studied by Cataldo and Thome [43], as shown in this figure, and also by [12]. Both concluded that high-pressure fluid is better from the thermal point of view, which agrees with the current finding.

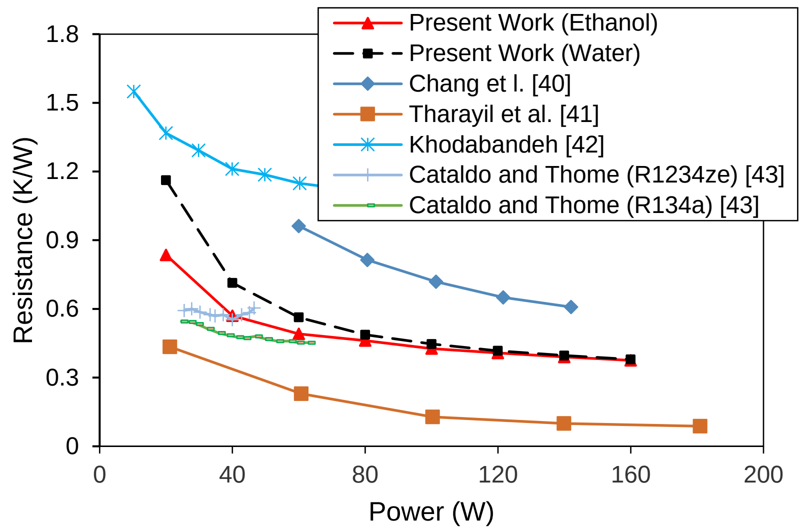

Figure 6-10: Comparison between water and ethanol in terms of the total resistance for the evaporator of Design 1 at the same fill ratio of 28% for different loads compared to different studies from the literature [40]–[43].

Regarding the geysering and performance instabilities, Figure 6-11 shows a comparison between both fluids at the same fill ratio of 28% for evaporator D1 in terms of the fluctuation intensity and frequency. The pressure fluctuation intensity and its frequency were higher for ethanol compared with water, while it is the opposite for the evaporator temperature fluctuation intensity. This is attributed to the fact that ethanol is a higher-pressure fluid which induces smaller bubble sizes and activates more nucleation sites. This is because of ethanol's smaller confinement number (Table 6-3) and evidenced by the flow visualization photos in Figure 6-12. The decrease of the bubble departure diameter increases bubble frequency, which results in lower surface temperature fluctuations and higher-pressure frequencies (Figure 6-11b and c).

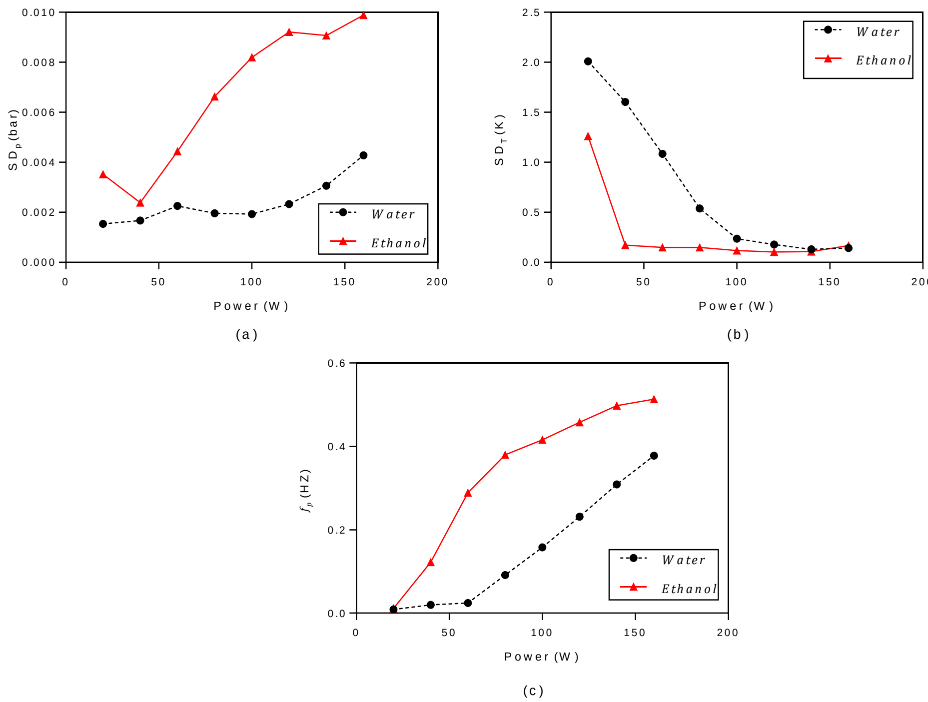

Figure 6-11: Comparison between water and ethanol evaporator D1 at a fill ratio of 28% in terms of: (a) the standard deviation of the pressure fluctuation, SD_P; (b) the standard deviation of the evaporator temperature fluctuation, SD_T; (c) the pressure fluctuation frequency, f_P.

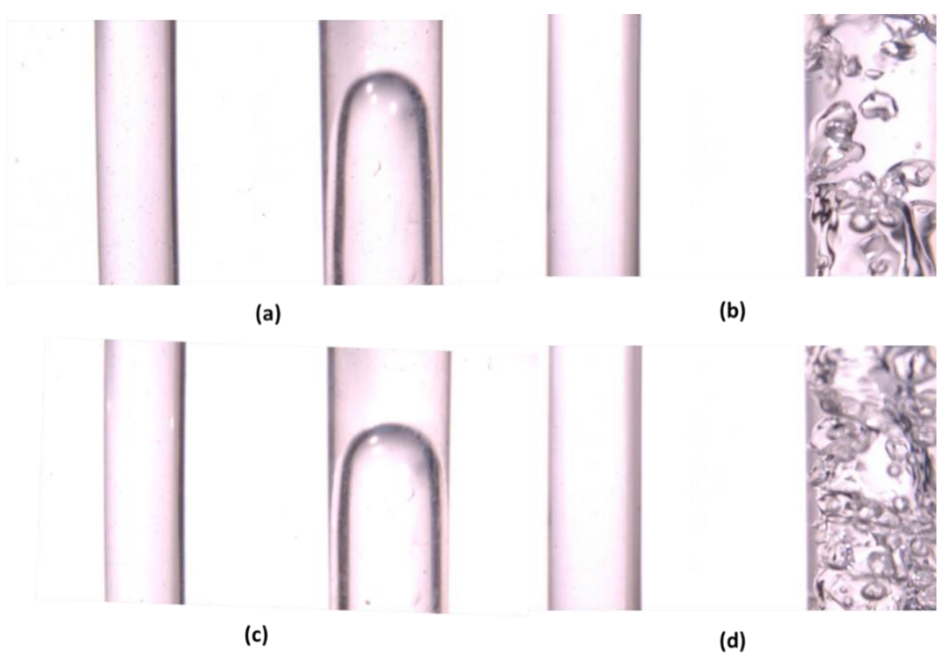

Figure 6-12: Comparison between water and ethanol at different input heater power: (a) water at 20 W, (b) ethanol at 20 W, (c) water at 140 W, (d) ethanol at 140 W.

6.3.3 Effect of Fill Ratio

Previous research has shown that the fill ratio alters the liquid column above the heating source, which has a direct effect on the GBP in the reflux thermosyphon [28] and also in the TPLT [37]. Consequently, the influence of increasing fill ratio on the evaporator temperature and the system pressure for the evaporator D1 is shown in. Figure 6-13. The pressure measured at the outlet of the condenser (shown in Figure 6-2a) was highest at the lowest fill ratio (Figure 6-13) and higher than the saturation pressure corresponding to $T_{c,v}$, which suggests that the liquid was subcooled. The degree of subcooling decreased by increasing the fill ratio at low heating loads, which supports the contention that the mass flow rate increases with the fill ratio, which was also observed in [43].

The effect of fill ratio on the thermosyphon thermal resistance as a function of heat transport rate is shown in Figure 6-14. The thermal resistance decreases by reducing the fill ratio until achieving approximately the same value at high heating load, which was also found by [40], [41], as shown in this figure. However, Tharayil et al. [41] found that decreasing the fill ratio below 30% causes the performance deterioration.

The reason for the performance enhancement with the fill ratio decrease can be understood by comparing the resistance for each side of thermosyphon for each case at two power levels—20 W and 120 W—as shown in Figure 6-15. The riser resistance is the dominant resistance at low power; however, its contribution is lessened at higher powers. The riser resistance is related to the pressure drop across the riser, which can be estimated by comparing the saturation pressure at the evaporator and condenser. It was found that the pressure drop through the riser at low heating loads increases with increasing the fill ratio at a given heat flux. This can be attributed to change in the vapor quality through the riser or the mass flow rate through the cycle.

Another interesting observation from Figure 6-14, is the decrease of thermal resistance by increasing the heater power except for the lowest fill ratio. Increasing the heat transfer at the same fill ratio decreases the pressure drop rate per heat flux (*dP/dQ*) across the riser, which in turn decreases the riser resistance and the overall resistance as discussed previously in Section 6.3.1. However, in the case of the lowest fill ratio, the evaporator resistance begins to increase again from 80 W until reaching the CHF at a power of 120 W. The thermal resistance increase at high heat fluxes in this case pertains to the intermittent dry-out of the evaporator.

In terms of the thermal instability, Figure 6-16 shows the effect of fill ratio on the instabilities' evaluation parameters. Generally, increasing the fill-ratio intensifies the temperature and pressure fluctuation amplitudes. For high fill-ratios, the temperature fluctuations were damped by increasing the heating load, which is contrary to [18], which demonstrated that geysering is more likely to happen at moderate heat fluxes for high fill ratios. This indicates the existence of another parameter that affects the GBP, which was not studied in [18], which we propose is the evaporator geometry and is discussed in the next section. The combination of all the parameters together—heating load, fill ratio, evaporator design, and fluid type—contributes to GBP in a different way. In the case of the lowest fill ratio of 11%, the fluctuation intensity increases with the heating load due to the intermittent dry-out and flooding of the evaporator, as highlighted earlier in this section. Although increasing fill ratio yielded an increase in fluctuation amplitude of pressure and temperature, the maximum pressure frequency occurred at a moderate fill ratio of 28%.

We conjecture that the pressure fluctuation frequency results not only from bubble generation, but also the flow rate through the loop because the pressure was measured at the condenser outlet. We think that the mass flow rate increased with fill ratio increase at low heating loads as discussed earlier; however, it is different for each heat flux. The fill ratio, along with the heat flux, can alter the vapor quality across the evaporator, which has a direct effect on the density of the two-phase flow through the riser, its pressure drop and flow resistance, and the resultant friction force. Also, the vapor quality affects the driving force and originates from the density difference between the riser and the downcomer. The balance between these two forces at each combination between the heat flux and the fill ratio dictates the mass flow rate through the loop.

From a practical standpoint, these results show that lower fill ratios result in lower thermal resistance and serve to improve the thermal–hydraulic stability of the thermosyphon. However, the evaporator is more liable to experience dry-out at lower powers at low fill ratios.

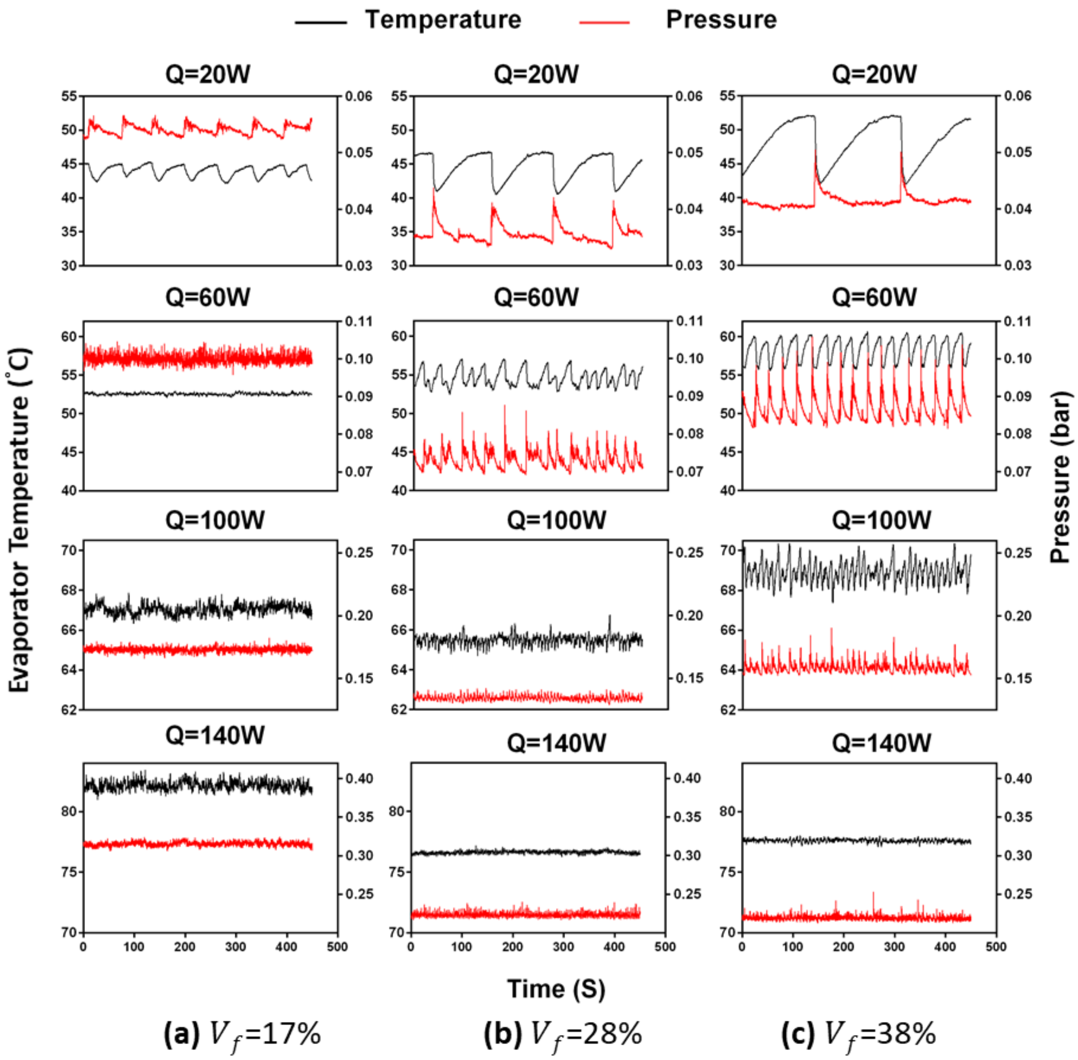

Figure 6-13: The evaporator temperature and the system pressure for evaporator D1 with water as the working fluid at different fill ratios and heating loads.

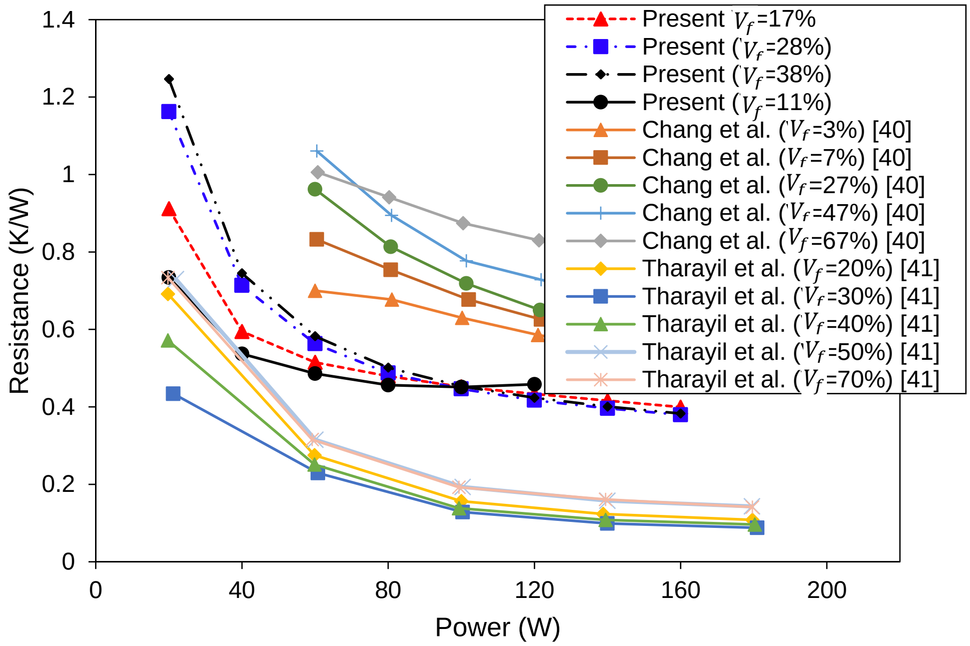

Figure 6-14: The effect of increasing the fill ratio on the total thermal resistance of the thermosyphon for evaporator D1 with water as the working fluid for different heating loads compared to different studies from the literature [40], [41].

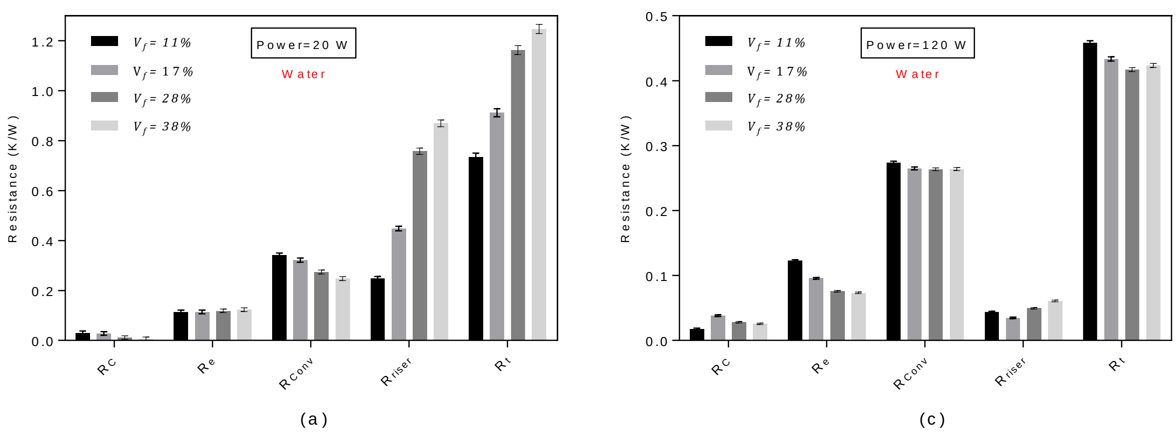

Figure 6-15: The effect of increasing the fill ratio on each side of the thermosyphon at two different powers: a) 20 W b) 120 W.

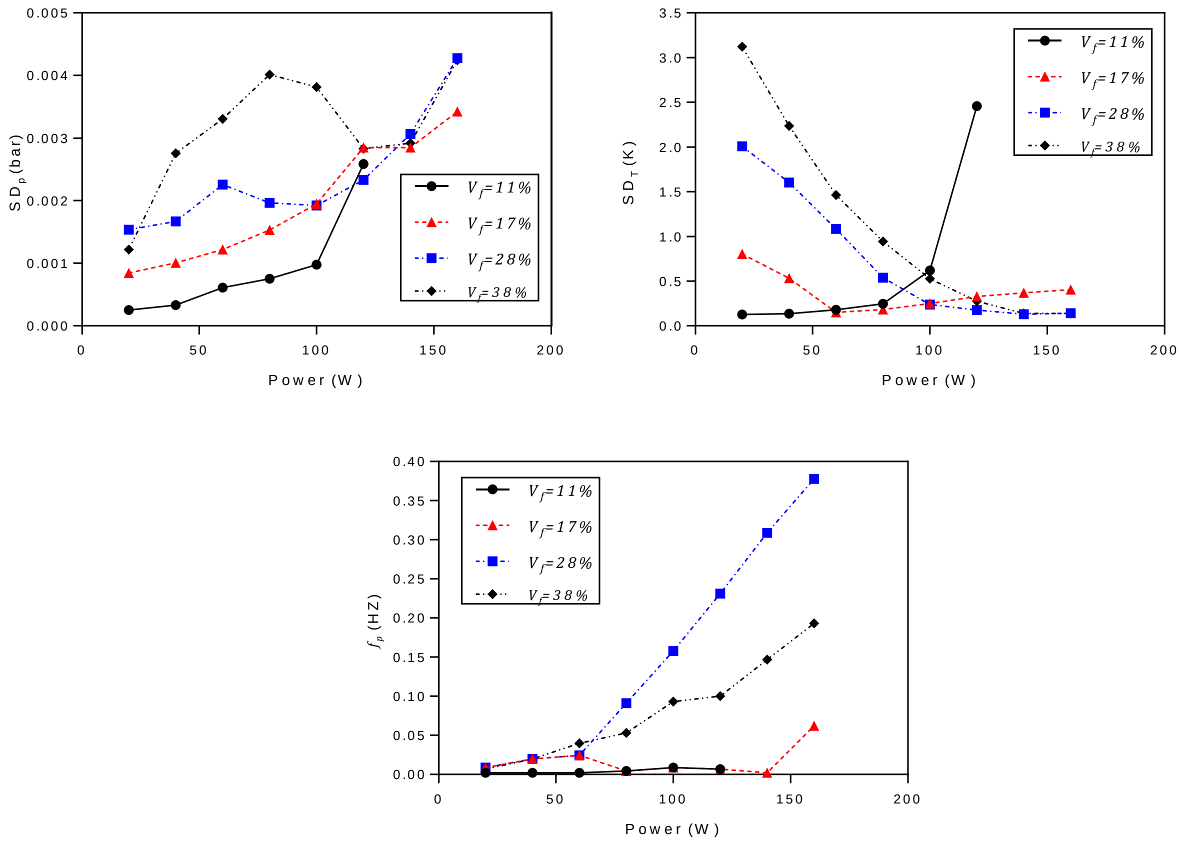

Figure 6-16: The effect of increasing the fill ratio on the performance instabilities for evaporator D1 with water as the working fluid in terms of: (a) the pressure fluctuation standard deviation, SD_P; (b) the temperature fluctuation standard deviation, SD_T; (c) the pressure fluctuation frequency, f_P.

6.3.4 Effect of Evaporator Design

The evaporator design affects the fluid quality at the evaporator outlet, which in turn changes the hydraulic performance and the mass flow rate through the cycle. The combination of the fluid thermophysical properties, the fill-ratio and the evaporator geometrical parameters (hydraulic diameter and heat transfer area) controls the thermal and hydraulic performance of the cycle. To examine this effect, three different evaporator designs were tested.

The effect of the evaporator design on the total resistance was compared for each design for both fluids at different fill ratios, as depicted in Figure 6-17. It was found that evaporator design had little effect on the total resistance of the thermosyphon and any difference is diminished by increasing the fill ratio, especially for water. This can be understood by examining how the evaporator design influences each resistance of the loop at a fill ratio of 17% for two heating loads—20W and 120 W—as shown in Figure 6-18. At low powers, the total resistance is dominated by the riser resistance for both fluids. However, at the higher powers, the riser resistance becomes very small and the effect of evaporator resistance becomes more pronounced and becomes a more dominant resistance. Consequently, it can be concluded that evaporator design change not only affects its resistance but also influences the riser resistance.

Regarding the boiling instabilities, Figure 6-19 and Figure 6-20 show the instability results with respect to evaporator design for water and ethanol. A high fill ratio of 28% was chosen to present these results because the GBP effect is intensified by increasing the fill ratio shown above. In contrast to the small effect of the evaporator design on the thermal resistance at high fill ratio (Figure 6-17), here the GBP is significantly affected by the evaporator design. Practically, this reinforces the idea that the geysering phenomena should be taken into consideration along with thermal resistance, to design an efficient robust thermosyphon; particularly for applications where minimal temperature excursions are permitted. Evaporator D3, which had the smallest hydraulic diameter, showed intense pressure and temperature fluctuations when working with water, while the other evaporators exhibited lower instabilities. Also, the pressure frequency experienced a substantial increase in evaporator D1 at a power of 100 W. We speculate this is where the flow transitions from the gravity-dominant regime into the friction regime [44], where the flow rate tends to hit a maximum. For ethanol, evaporators D2 and D3 experienced similar low-pressure fluctuation intensity and frequency; however, evaporator D3 showed higher temperature instabilities. Therefore, the evaporator that has a hydraulic diameter close to the fluid capillary length (Table 6-3) achieved better stability.

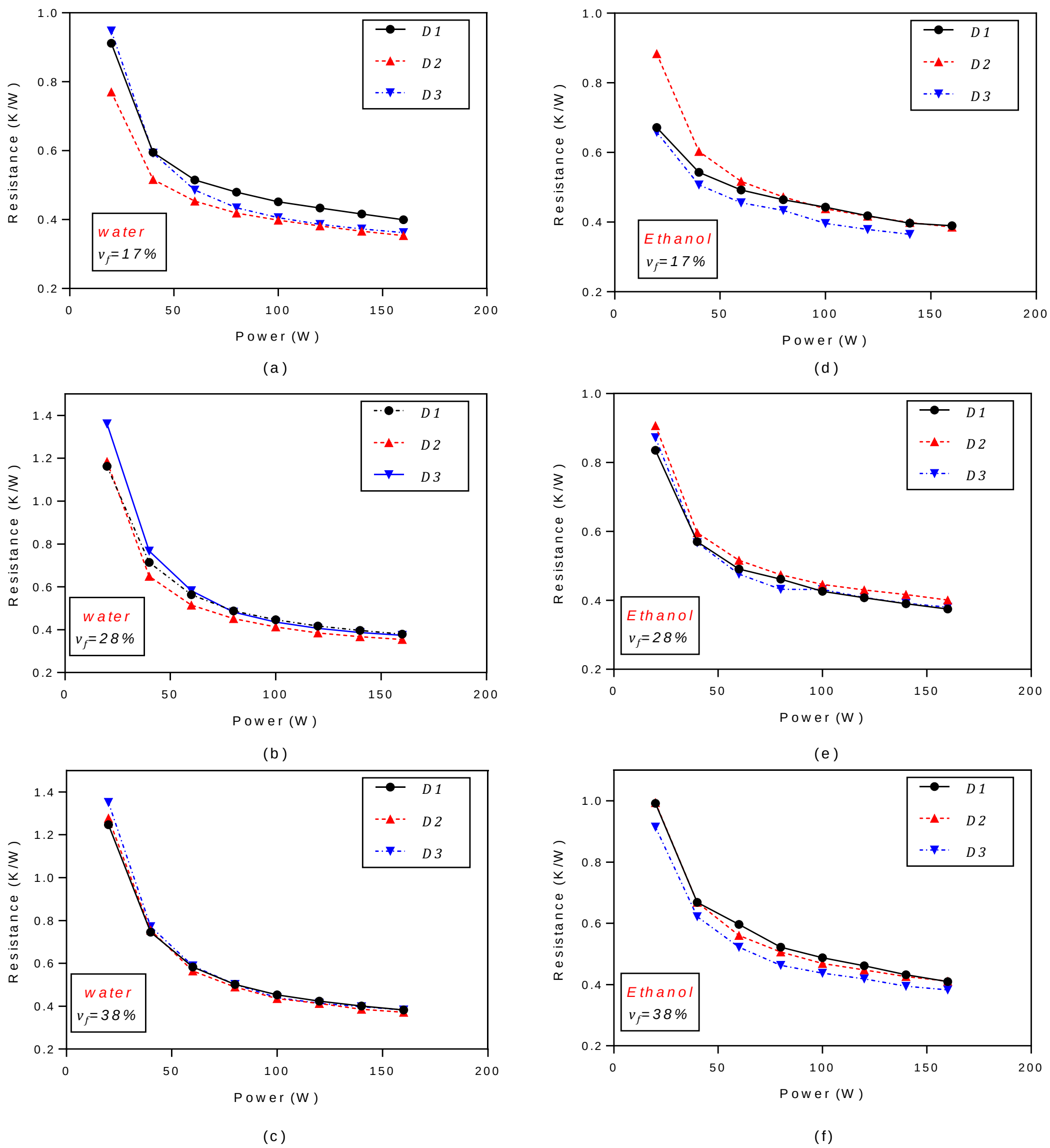

Figure 6-17: The effect of evaporator design on the total thermal resistance of the thermosyphon for both working fluids at different fill ratios. (a) water at $V_f = 17\%$, (b) water at $V_f = 28\%$, (c) water at $V_f = 38\%$, (d) ethanol at $V_f = 17\%$, (e) ethanol at $V_f = 28\%$, (f) ethanol at $V_f = 38\%$.

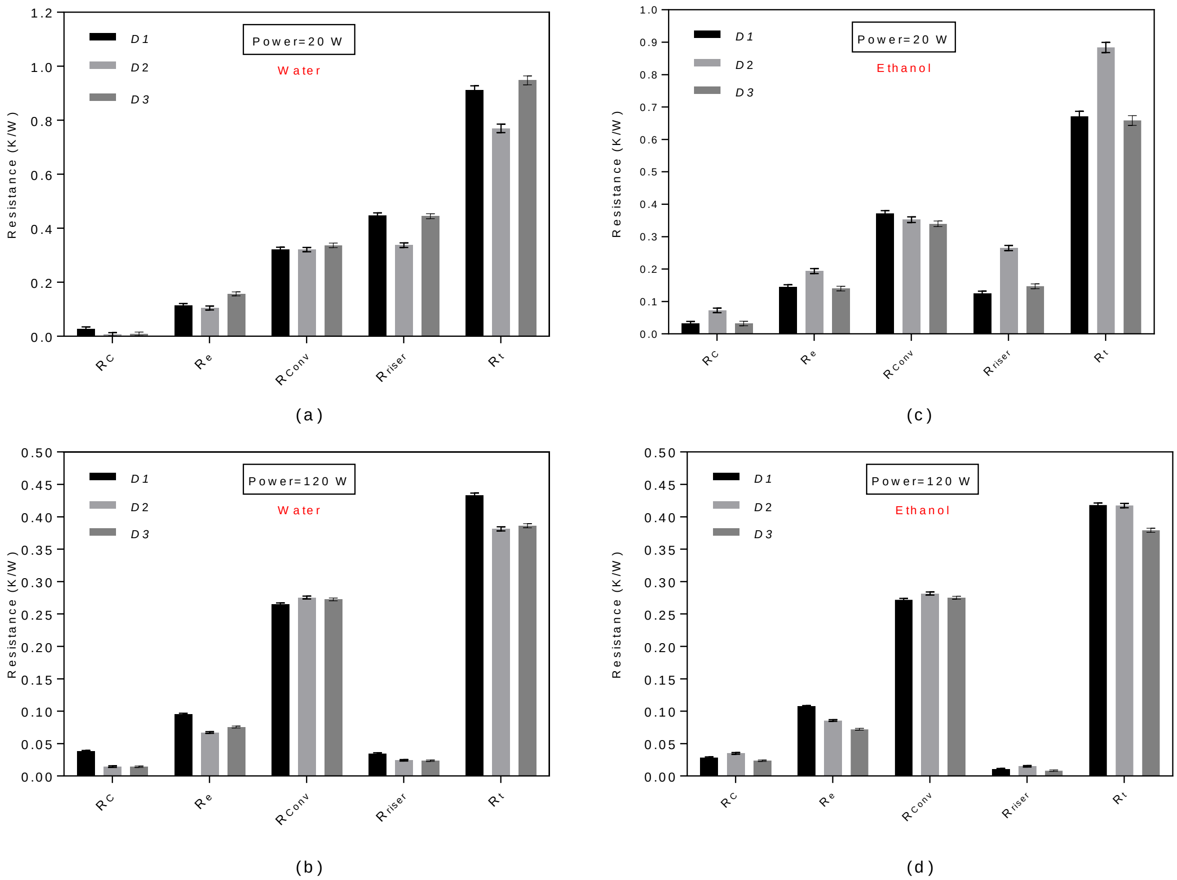

Figure 6-18: The effect of evaporator design on each resistance of the thermosyphon for both working fluids with fill ratio of 17% at different heating loads: (a) water at heating load of 20 W, (b) water at heating load of 120 W, (c) ethanol at heating load of 20 W, (d) ethanol at heating load of 120 W.

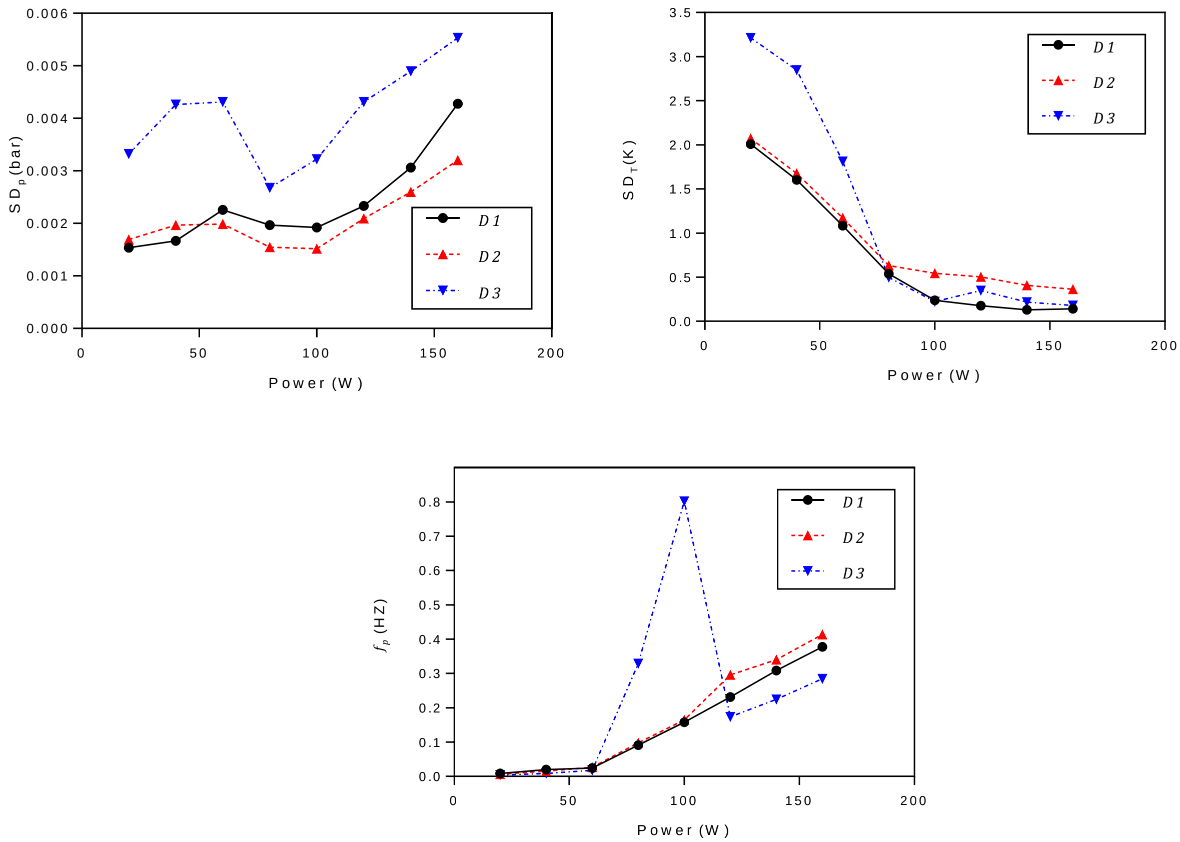

Figure 6-19: The effect of the evaporator design on the performance instabilities with water as the working fluid at fill ratio of 28% in terms of (a) the pressure fluctuation standard deviation; (b) the temperature fluctuation standard deviation, SD_T; (c) the pressure fluctuation frequency, f_P.

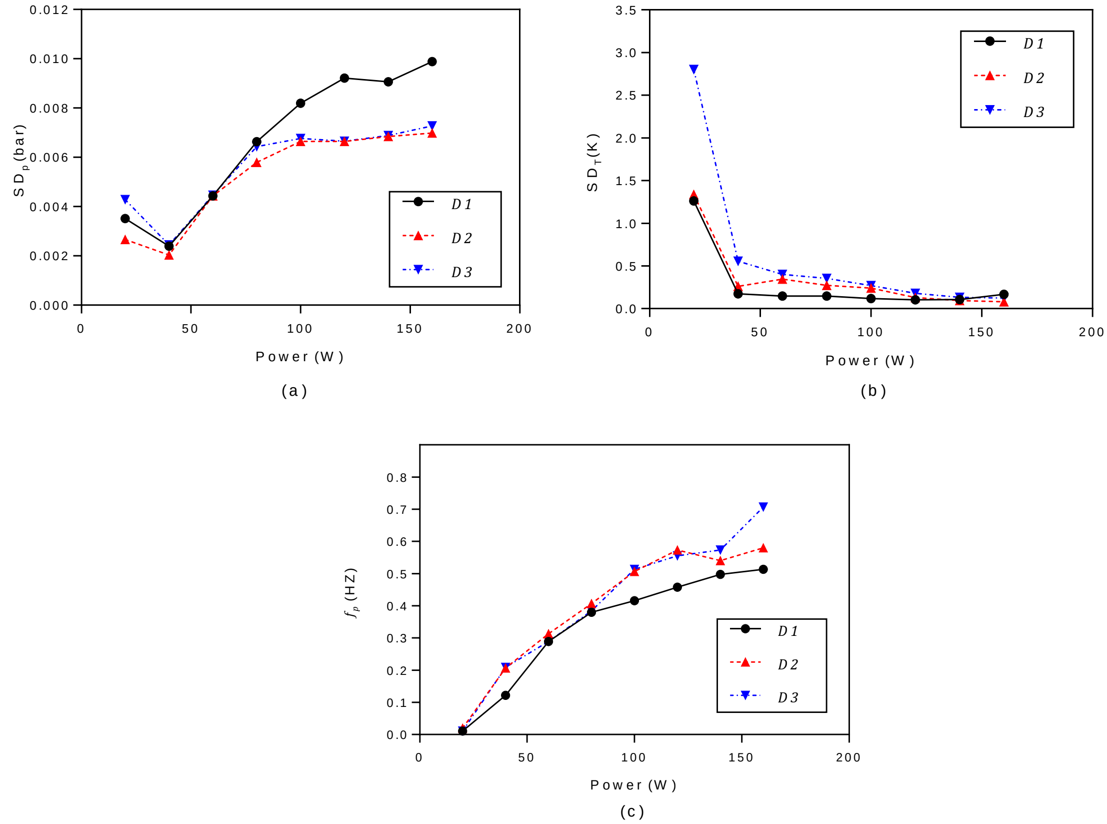

Figure 6-20: The effect of the evaporator design on the performance instabilities with ethanol in terms of: (a) the pressure fluctuation standard deviation, SD_p; (b) the temperature fluctuation standard deviation, SD_T; (c) the pressure fluctuation frequency, f_p.

6.4 Summary & Conclusions

The geysering boiling phenomenon was experimentally studied in two-phase loop thermosyphons for two working fluids, three fill-ratios, and three evaporator geometries. The instabilities caused by the geysering phenomenon were characterized using the fast Fourier transform method and the standard deviation for the temperature and pressure signals. The main outcomes can be summarized as follows:

- Increasing the heat flux at the same fill ratio and the same evaporator design decreased the thermosyphon overall resistance and mitigated the GBP temperature fluctuations. The heat flux increase reduced the resulting pressure drop per heat flux (*dP/dQ*) through the riser, and hence decreased the riser resistance, making the saturation temperatures of both condenser and evaporator approach each other.

- The thermosyphon using ethanol achieved lower thermal resistance, especially at lower powers, and had lower evaporator temperature fluctuations compared with water. This is due to having lower surface tension, which activates more nucleation sites, decreasing the bubble departure diameter, which in turn enhances the bubble departure frequency and the heat dissipation rate of the evaporator. Nevertheless, the pressure fluctuation amplitude was larger for ethanol, which may affect the thermosyphon; this may have practical implications.

- Increasing the fill ratio from 17% to 38% intensified the standard deviation of the temperature and pressure instabilities and lowered thermosyphon thermal resistance. However, it increased maximum heat transport capacity due to delaying the onset of early dry-out of the evaporator. In contrast, working below a fill ratio of 17% not only instigated early dry-out and limited the loop capacity, but also induced other types of instabilities related to the intermittent dry-out and flooding of the evaporator close to failure.

- The evaporator geometry design had minimal influence on the overall thermal resistance of the thermosyphon at high fill ratios, particularly for water. However, it does influence the corresponding thermal–hydraulic stabilities considerably. Evaporators D1 and D2 achieved more stable temperatures and pressures for water, while D2 and D3 were more stable for the ethanol thermosyphon.

6.5 References

[1] H. Zhang, Z. Shi, K. Liu, S. Shao, T. Jin, and C. Tian, "Experimental and numerical investigation on a CO2loop thermosyphon for free cooling of data centers," Appl. Therm. Eng., vol. 111, pp. 1083–1090, 2017, doi: 10.1016/j.applthermaleng.2016.10.029.

[2] H. Zhang, S. Shao, C. Tian, and K. Zhang, "A review on thermosyphon and its integrated system with vapor compression for free cooling of data centers," Renew. Sustain. Energy Rev., vol. 81, no. November 2016, pp. 789–798, 2018, doi: 10.1016/j.rser.2017.08.011.

[3] C. L. Ong, N. Lamaison, J. B. Marcinichen, and J. R. Thome, "Two-phase mini-thermosyphon electronics cooling, Part 1: Experimental investigation," Proc. 15th Intersoc. Conf. Therm. Thermomechanical Phenom. Electron. Syst. ITherm 2016, pp. 574–581, 2016, doi: 10.1109/ITHERM.2016.7517599.

[4] V. G. Pastukhov and Y. F. Maydanik, "Active coolers based on copper-water LHPs for desktop PC," Appl. Therm. Eng., vol. 29, no. 14–15, pp. 3140–3143, 2009, doi: 10.1016/j.applthermaleng.2009.04.016.

[5] M. K. Na, J. S. Jeon, H. Y. Kwak, and S. S. Nam, "Experimental study on closed-loop two-phase thermosyphon devices for cooling MCMs," Heat Transf. Eng., vol. 22, no. 2, pp. 29–39, 2001, doi: 10.1080/014576301462236.

[6] A. Elkholy and R. Kempers, "A COMPACT INTEGRATED THERMOSYPHON HEAT SINK FOR POWER ELECTRONICS COOLING," in Proceedings of the ASME 2019 International Mechanical Engineering Congress and Exposition IMECE2019, 2019, pp. 1–9.

[7] H. I. Abu-Mulaweh, "Design and performance of a thermosiphon heat recovery system," Appl. Therm. Eng., vol. 26, no. 5–6, pp. 471–477, 2006, doi: 10.1016/j.applthermaleng.2005.08.003.

[8] T. Zhang, G. Pei, Q. Zhu, and J. Ji, "Investigation on the Optimum Volume-Filling Ratio of a Loop Thermosyphon Solar Water-Heating System," J. Sol. Energy Eng., vol. 138, no. 4, p. 041006, 2016, doi: 10.1115/1.4033403.

[9] C. Huang, W. K. Lin, and S. R. Wang, "Two-Phase Closed-Loop Thermosyphon Solar Water Heater with Porous Wick Structure: Performance and Start-Up Time," Arab. J. Sci. Eng., vol. 42, no. 11, pp. 4885–4894, 2017, doi: 10.1007/s13369-017-2660-6.

[10] Z. Tong, X. H. Liu, Z. Li, and Y. Jiang, "Experimental study on the effect of fill ratio on an R744 two-phase thermosyphon loop," Appl. Therm. Eng., vol. 99, pp. 302–312, 2016, doi: 10.1016/j.applthermaleng.2016.01.065.

[11] K. Kiran Kumar and M. Ram Gopal, “Experimental studies on CO2based single and two-phase natural circulation loops,” Appl. Therm. Eng., vol. 31, no. 16, pp. 3437–3443, 2011, doi: 10.1016/j.applthermaleng.2011.06.029.

[12] B. Palm and R. Khodabandeh, “Choosing Working Fluid for Two-Phase Thermosyphon Systems for Cooling of Electronics,” J. Electron. Packag., vol. 125, no. 2, p. 276, 2003, doi: 10.1115/1.1571570.

[13] R. Khodabandeh and R. Furberg, “Heat transfer, flow regime and instability of a nano- and micro-porous structure evaporator in a two-phase thermosyphon loop,” Int. J. Therm. Sci., vol. 49, no. 7, pp. 1183–1192, 2010, doi: 10.1016/j.ijthermalsci.2010.01.016.

[14] H. Toyoda and Y. Kondo, “Effect of Non-Condensable Gas Leakage on Long Term Cooling Performance of Loop Thermosyphon,” J. Electron. Cool. Therm. Control, vol. 03, no. 04, pp. 131–135, 2013, doi: 10.4236/jectc.2013.34014.

[15] A. Franco and S. Filippeschi, “Closed loop two-phase thermosyphon of small dimensions: A review of the experimental results,” Microgravity Sci. Technol., vol. 24, no. 3, pp. 165–179, 2012, doi: 10.1007/s12217-011-9281-6.

[16] D. Jafari, A. Franco, S. Filippeschi, and P. Di Marco, “Two-phase closed thermosyphons: A review of studies and solar applications,” Renew. Sustain. Energy Rev., vol. 53, pp. 575–593, Jan. 2016, doi: 10.1016/j.rser.2015.09.002.

[17] K. Smith, A. J. Robinson, and R. Kempers, “Confinement and vapour production rate influences in closed two-phase reflux thermosyphons Part B: Heat transfer,” Int. J. Heat Mass Transf., vol. 120, pp. 1241–1254, 2018, doi: 10.1016/j.ijheatmasstransfer.2017.12.046.

[18] Y. Liu, Z. Li, Y. Li, S. Kim, and Y. Jiang, “Experimental investigation of geyser boiling in a two-phase closed loop thermosyphon with high filling ratios,” Int. J. Heat Mass Transf., vol. 127, pp. 857–869, 2018, doi: 10.1016/j.ijheatmasstransfer.2018.07.018.

[19] K. Negislii and T. Sawada, “HEAT TRANSFER PERFORMANCE OF AN INCLINED TWO-PHASE CLOSED THERMOSYPHON,” Int. J. Heat Mass Transf., vol. 26, no. 8, pp. 1207–1213, 1983, doi: 10.1016/S0017-9310(83)80175-6.

[20] P. Griffith, “geysering in liquid-filled lines,” ASME Pap. 62-HT-39, 1962.

[21] J. A. Boure, A. E. Bergles, and L. S. Tong, “Review of Two-Phase Flow Instability,” Nucl. Eng. Des., vol. 25, pp. 165–192, 1973, doi: Doi: 10.1016/0029-5493(73)90043-5.

[22] M. R. S. Emami, S. H. Noie, M. Khoshnoodi, M. T. H. Mosavian, and A. Kianifar, “Investigation of geyser boiling phenomenon in a two-phase closed thermosyphon,” Heat Transf. Eng., vol. 30, no. 5, pp. 408–415, 2009, doi: 10.1080/01457630802414979.

[23] H. Imura, K. Sasaguchi, H. Kozai, and S. Numata, “Critical heat flux in a closed two-phase thermosyphon,” Int. J. Heat Mass Transf., vol. 26, no. 8, pp. 1181–1188, Aug. 1983, doi: 10.1016/S0017-9310(83)80172-0.

[24] C. Casarosa, E. Latrofa, and A. Shelginski, “The geyser effect in a two-phase thermosyphon,” Int. J. Heat Mass Transf., vol. 26, no. 6, pp. 933–941, 1983, doi: 10.1016/S0017-9310(83)80117-3.

[25] T. F. Lin, W. T. Lin, Y. L. Tsay, J. C. Wu, and R. J. Shyu, “Experimental investigation of geyser boiling in an annular two-phase closed thermosyphon,” Int. J. Heat Mass Transf., vol. 38, no. 2, pp. 295–307, 1995, doi: 10.1016/0017-9310(95)90019-5.

[26] I. Khazaee, R. Hosseini, and S. H. Noie, “Experimental investigation of effective parameters and correlation of geyser boiling in a two-phase closed thermosyphon,” Appl. Therm. Eng., vol. 30, no. 5, pp. 406–412, 2010, doi: 10.1016/j.applthermaleng.2009.09.012.

[27] A. Niro and G. P. Beretta, “Boiling regimes in a closed two-phase thermosyphon,” Int. J. Heat Mass Transf., vol. 33, no. 10, pp. 2099–2110, 1990.

[28] N. Y. Londoño Pabón, J. P. Florez Mera, G. Serafin Couto Vieira, and M. Barbosa Henriques Mantelli, “Visualization and experimental analysis of Geyser boiling phenomena in two-phase thermosyphons,” Int. J. Heat Mass Transf., vol. 141, pp. 876–890, 2019, doi: 10.1016/j.ijheatmasstransfer.2019.06.052.

[29] A. Kujawska, B. Zajaczkowski, L. M. Wilde, and M. H. Buschmann, “Geyser boiling in a thermosyphon with nanofluids and surfactant solution,” Int. J. Therm. Sci., vol. 139, no. January, pp. 195–216, 2019, doi: 10.1016/j.ijthermalsci.2019.02.001.

[30] H. Jouhara, B. Fadhl, and L. C. Wrobel, “Three-dimensional CFD simulation of geyser boiling in a two-phase closed thermosyphon,” Int. J. Hydrogen Energy, vol. 41, no. 37, pp. 16463–16476, 2016, doi: 10.1016/j.ijhydene.2016.02.038.

[31] X. Wang, Y. Wang, H. Chen, and Y. Zhu, “International Journal of Heat and Mass Transfer A combined CFD / visualization investigation of heat transfer behaviors during geyser boiling in two-phase closed thermosyphon,” Int. J. Heat Mass Transf., vol. 121, pp. 703–714, 2018, doi: 10.1016/j.ijheatmasstransfer.2018.01.005.

[32] P. T. Garrity, J. F. Klausner, and R. Mei, “Instability phenomena in a two-phase microchannel thermosyphon,” Int. J. Heat Mass Transf., vol. 52, no. 7–8, pp. 1701–1708, 2009, doi: 10.1016/j.ijheatmasstransfer.2008.10.005.

[33] P. T. Garrity, J. F. Klausner, and R. Mei, “A flow boiling microchannel evaporator plate for fuel cell thermal management,” Heat Transf. Eng., vol. 28, no. 10, pp. 877–884, 2007, doi: 10.1080/01457630701378333.

[34] S. W. Chang, D. C. Lo, K. F. Chiang, and C. Y. Lin, “Sub-atmospheric boiling heat transfer and thermal performance of two-phase loop thermosyphon,” Exp. Therm. Fluid Sci., vol. 39, pp. 134–147, 2012.

[35] J. L. G. Oliveira, C. Tecchio, K. V. Paiva, M. B. H. Mantelli, R. Gandolfi, and L. G. S. Ribeiro, “In-flight testing of loop thermosyphons for aircraft cooling,” Appl. Therm. Eng., vol. 98, pp. 144–156, 2016, doi: 10.1016/j.applthermaleng.2015.12.008.

[36] C. Tecchio, J. L. G. Oliveira, K. V. Paiva, M. B. H. Mantelli, R. Galdolfi, and L. G. S. Ribeiro, “Geyser boiling phenomenon in two-phase closed loop-thermosyphons,” Int. J. Heat Mass Transf., vol. 111, pp. 29–40, 2017, doi: 10.1016/j.ijheatmasstransfer.2017.03.092.

[37] Y. Liu, Z. Li, Y. Li, Y. Jiang, and D. Tang, “Heat transfer and instability characteristics of a loop thermosyphon with wide range of filling ratios,” Appl. Therm. Eng., vol. 151, no. January, pp. 262–271, 2019, doi: 10.1016/j.applthermaleng.2019.02.031.

[38] K. Smith, S. Siedel, A. J. Robinson, and R. Kempers, “The effects of bend angle and fill ratio on the performance of a naturally aspirated thermosyphon,” Appl. Therm. Eng., vol. 101, pp. 455–467, 2016, doi: 10.1016/j.applthermaleng.2016.01.024.

[39] S. J. Kline, “Describing uncertainty in single sample experiments,” Mech. Eng. 75 3-8., pp. 1–9, 1954.

[40] C. C. Chang, S. C. Kuo, M. T. Ke, and S. L. Chen, “Two-phase closed-loop thermosyphon for electronic cooling,” Exp. Heat Transf., vol. 23, no. 2, pp. 144–156, 2010, doi: 10.1080/08916150903402807.

[41] T. Tharayil, N. Gitty, L. G. Asirvatham, and S. Wongwises, “Effect of Filling Ratio and Tilt Angle on the Performance of a Mini-Loop Thermosyphon,” J. Therm. Sci. Eng. Appl., vol. 11, no. 6, pp. 1–11, 2019, doi: 10.1115/1.4043464.

[42] R. Khodabandeh, “Thermal performance of a closed advanced two-phase thermosyphon loop for cooling of radio base stations at different operating conditions,” Appl. Therm. Eng., vol. 24, no. 17–18, pp. 2643–2655, 2004, doi: 10.1016/j.applthermaleng.2004.05.006.

[43] F. Cataldo and J. R. Thome, “Experimental Performance of a Completely Passive Thermosyphon Cooling System Rejecting Heat by Natural Convection Using the Working R134a,” vol. 140, no. June, pp. 1–11, 2018, doi: 10.1115/1.4039706.

[44] A. Chehade, H. Louahlia-Gualous, S. Le Masson, and E. Lépinasse, “Experimental investigations and modeling of a loop thermosyphon for cooling with zero electrical consumption,” Appl. Therm. Eng., vol. 87, pp. 559–573, 2015, doi: 10.1016/j.applthermaleng.2015.05.041.

Chapter 7 Experimental Investigation of the Thermal Performance of a Two-Phase Loop Thermosyphon with an Additively Manufactured Evaporator[5]

This chapter investigates the effect of a novel additively manufactured heating surface on the performance of a two-phase loop thermosyphon. The loop consists of a radial finned, air-cooled condenser connected to an aluminum evaporator through nylon tubing for flow visualization purposes. The side-heated evaporator surface consists of mini-channels with a hydraulic diameter of 1.5 mm. Two evaporator surfaces were examined: (1) with smooth conventionally machined aluminum channels and (2) with 3D-printed channels manufactured by selective laser melting (SLM). This loop is the same as the one used previously in chapter 6, but with forced convection condenser and reduced height to decrease the domination of the convection and the riser resistances in the total resistance. The loop thermal performance, and the associated instabilities, were tested at different fill ratios and two different working fluids. The intensity of operational instabilities was captured using the maximum fluctuation amplitude of the evaporator wall temperature. This chapter touches the relevant literature briefly because it is already covered in the previous chapter.

7.1 Introduction & Background

Closed-loop thermosyphons can achieve high heat transfer rates at compact sizes, motivating their application in many fields. Despite their exceptional heat transfer abilities**,** thermosyphons suffer

---

[5] This chapter has been submitted as a peer-reviewed journal paper titled "Experimental Investigation of the Thermal Performance of a Two-Phase Loop Thermosyphon with an Additively Manufactured Evaporator" in *Applied Thermal Engineering*.

from instabilities causing temperature and pressure fluctuations within the system, disturbing the component being cooled and the mechanical integrity of the system [1]–[3].

Geyser boiling phenomenon is an instability stemming from heat inputs being insufficient to maintain continuous boiling in the evaporator [4], [5]. The phenomenon has been described as vapor bubbles formed on the evaporator walls [6] explosively expanding [3] due to the increase in internal pressure and reduction in the hydraulic head [2], pushing the liquid column in the riser upwards at high speeds [7]. The process is repeated once the expelled working fluid returns to the evaporator through the loop. The unstable and intermittent nature of the process results in fluctuations in temperature, pressure, and heat transfer rates [3]. Dry-out of the working fluid is another form of instability resulting from the filling ratio being insufficient to handle the heat load [8]. Under dry-out conditions, mass flow returning from the condenser is not enough to maintain a liquid film layer above the liquid pool [1], [9], and dry spots emerge on the heating surfaces [2]. The phenomenon produces large-amplitude oscillations of evaporator temperature while the evaporator is subjected to constant heat flux [10].

The relationship of design parameters to stability has been the subject of previous works. Tong et al. determined that riser diameters too large for given heat loads could lead to inactive or oscillatory operation states [11]. Evaporator diameter's effect on stability has also been studied with water and ethanol in [12]. Hydraulic diameters closer to the capillary length of working fluids were found to be preferable for stable operation. Ethanol was seen to create high-pressure fluctuations despite its desirable thermal resistance characteristics. Khodabandeh et al. has observed that smaller evaporator channel depths to increased loop operational instabilities [13]. Instabilities appeared at low heat fluxes in the form of intermittent boiling due to insufficient heat load and backflow.

Low filling ratios were found to provide the highest heat transfer rates but were prone to the near dry-out phenomenon [14]. Liu et al. detailed geysering cycles as consisting of single-phase, bubbly, and churn flows; and concluded that geyser occurrence is more likely under high filling ratios and moderate heat flux [15]. The authors further determined that geysering occurs for a wider range of input heat fluxes for moderate filling ratios compared to high filling ratios.

Establishing an understanding of instabilities and developing methods to manage them make up major obstacles before thermosyphons' widespread usage. Vieria et al. eliminated geysering in a loop thermosyphon intended for avionics applications by constructing a wicked internal wall on the flat box evaporator, which increased the density of nucleation sites [16]. Khodabandeh et al. tested an evaporator with nano- and micro-porous structures, which reduced oscillations over the entire input power range while achieving higher heat transfer coefficients pertaining to the increased frequency of nucleation sites [17].

It is seen that the thermal performance and stability of thermosyphons can be improved with evaporator geometry [12], [13] and surface enhancements [16], [17]. Based on these conclusions, structural and surface properties, as well as geometries of heat transfer devices can be tailored for thermosyphon performance. Additive manufacturing methods appear as ideal candidates for producing such tailored parts with intricate structures and geometries out of a broader range of materials.

As discussed above, there is still a need to better categorize and characterize the thermal performance and stability characteristics of loop thermosyphons. Additive manufacturing methods present improvement opportunities for heat transfer devices; however, there has been no study on their effect on thermosyphon operation. In response, this study aims first to improve the understanding of thermosyphon thermal instabilities, and second, to investigate the performance of additively manufactured heating surfaces using different working fluids at various filling ratios.

7.2 Experimental Setup & Methodology

7.2.1 Modified Thermosyphon Loop

This study involves the modification of the loop thermosyphon used in the previous chapter to decrease the riser and the convection resistances, which were found to dominate the loop total thermal resistance. Therefore, here the height difference between the condenser and the evaporator was decreased to 930 mm, and the condenser conditions were changed to forced convection. The data acquisition, geometrical parameters of all loop sections, and control equipment used in the study are similar to the loop used previously, as illustrated in Figure 7-1. For more details and specific information about the size of each section of the loop, please see the previous chapter.

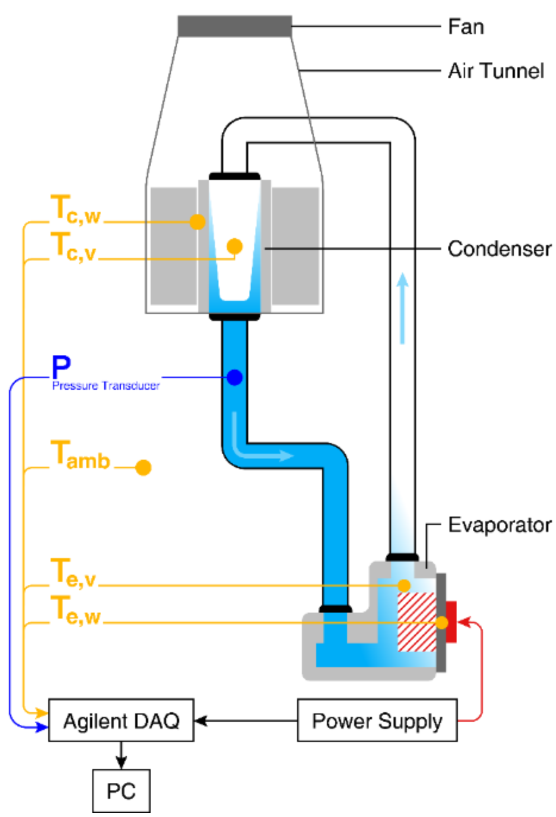

Figure 7-1**:** Experimental setup and instrumentation.

The condenser used is a modified radial finned heat sink (TitanTurbo HS-5430-0537, Lamina Lighting Inc.). It was drilled and tapped at the center to attach a T-fitting in order to incorporate a thermocouple for measuring the fluid flow temperature at the center of the heat sink passage ($T_{c,v}$), as detailed in [12] and shown in Figure 7-2(c). The heat extracted from the flow is conducted through the fins and later dissipated to ambient air by forced convection using a fan located at the top of a plastic enclosure around the condenser assembly. Two thermocouples are employed to measure the fin base surface temperature ($T_{c,w}$) on the heat sink and the ambient temperature (T_{amb}).

The evaporator section design was kept the same, in which the heating surface is a swappable part of enabling testing of different heating surfaces with the same thermosyphon loop, as shown in Figure 7-2(b). Input power is provided electrically through a heated copper block comprised of six cartridge heaters (Sun Electric Heater, Salem, MA) with 3.1 mm (1/8 in) diameter and 12.5 mm (1/2 in) length and attached to the heating surface using two M3 screws. A groove on the back of the heating surface houses a thermocouple measuring the evaporator wall temperature ($T_{e,w}$). Another thermocouple inserted through the evaporator body measures the fluid temperature inside the evaporator ($T_{e,v}$). Supplied power is controlled with the DC power supply (CPX400D, Aim TTi, Cambridgeshire, UK) and quantified using the voltage and current measurements. The evaporator assembly is covered with mineral wool insulation of 0.032 $Wm^{-1}K^{-1}$ to minimize heat loss to the ambient air.

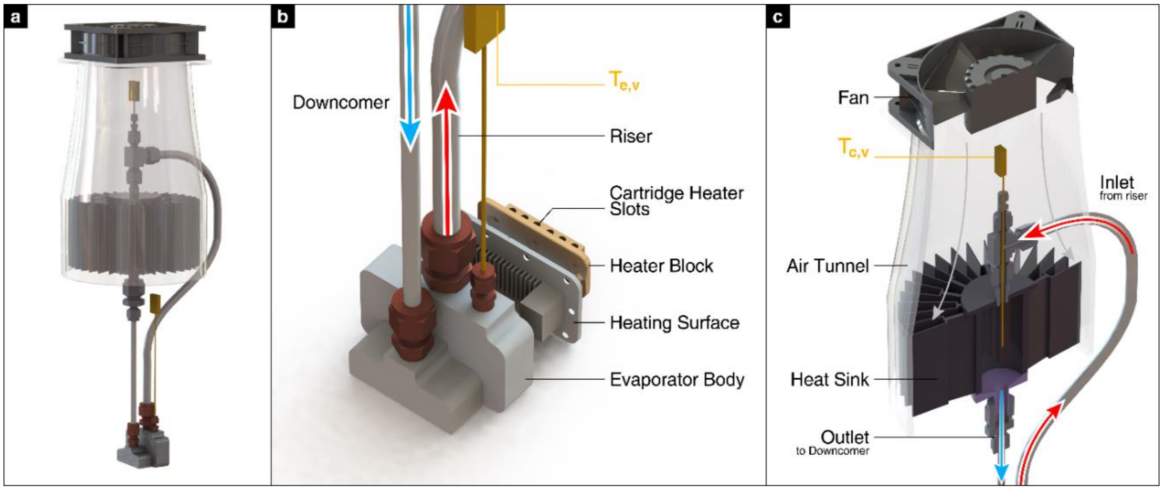

Figure 7-2**:** Experimental setup (a) overall layout (b) evaporator (c) condenser sections.

Experimental Procedure and Data Acquisition

The system was initially tested for leakages by evacuating the loop to a very low pressure using a vacuum pump (MZ 2C NT + 2AK, Vacuubrand, Wertheim, Germany) and monitoring the pressure for several hours. Prior to each run, the loop was rinsed with the working fluid and evacuated to low pressure. Working fluids were degassed outside in a vacuum chamber before charging to the loop to remove dissolved non-condensable gases.

In all experiment runs, the fan was run at the same speed, and heating power was incremented in steps of 20 W until temperatures reached a steady or quasi-steady state in each operation setting. Temperature data from the five T-type thermocouples, pressure data from the transducer, and heater voltage data were acquired simultaneously every 0.15 s using an Agilent 34970A data acquisition unit (Agilent Technologies, Santa Clara, CA). Heater current readings were obtained from the power supply's internal ammeter.

Data Reduction and Uncertainty Analysis

Thermal performance of individual sections of the thermosyphon can be assessed by their thermal resistances, provided in Eq. (7.1): Eq. (7.4).

$$R_e = \frac{T_{e,w} - T_{e,v}}{Q} \tag{7.1}$$

$$R_{riser} = \frac{T_{e,v} - T_{c,v}}{Q} \tag{7.2}$$

$$R_c = \frac{T_{c,w} - T_{c,v}}{Q} \tag{7.3}$$

$$R_{conv} = \frac{T_{c,w} - T_{amb}}{Q} \tag{7.4}$$

where $T_{e,w}$, $T_{e,v}$, $T_{c,v}$, $T_{c,w}$, and T_{amb} are the temperatures of the evaporator wall, evaporator vapor, condenser vapor, condenser wall, and ambient air, respectively; and Q is the evaporator input power, calculated as:

$$Q = VI - Q_{loss} \tag{7.5}$$

where V is the voltage, I is the heater current and Q_{loss} is the heat loss from the evaporator to the ambient air by convection and radiation, determined in the previous study.

The loop's overall thermal resistance can be obtained by adding up all the thermal resistances, resulting in Eq. (7.6).

$$R_t = \frac{T_{e,w} - T_{amb}}{Q} \tag{7.6}$$

Kline and McClintock's error propagation method was used to estimate the resulting uncertainty of thermal resistances with Eq. (7.7).

$$U_R = \sqrt{\left(\frac{\partial R}{\partial V} U_V\right)^2 + \left(\frac{\partial R}{\partial I} U_I\right)^2 + \left(\frac{\partial R}{\partial T_1} U_{T_1}\right)^2 + \left(\frac{\partial R}{\partial T_2} U_{T_2}\right)^2} \tag{7.7}$$

where U_i is the uncertainty of quantity i. The maximum fluctuation amplitudes of the evaporator temperature were used to determine the intensity of geyser events.

7.2.2 Sample Preparation

In this study, one machined and one additively manufactured aluminum heating surfaces were tested for their effect on the geyser boiling phenomenon and the loop's overall thermal performance. The evaporators are visualized in Figure 7-3. Images 2-4 were captured using a Leica MZ10 F stereomicroscope (Leica Microsystems GmbH, Wetzlar, Germany).

Additively manufactured heating surface was produced by Additive Metal Manufacturing (Concord, ON, Canada) using an EOS M 290 (EOS GmbH, Munich, Germany) unit to selectively melt $AlSi_{10}Mg$ powder, whose specifications as per the supplier are provided in Table 7-1. A Yb: YAG laser of 400 W power and 80 μm beam diameter was used at scanning speeds of up to 7.0 m/s to trace cross-sections of the part on the powder bed in layers 20 μm thickness. Traced powders were fused and subsequently solidified. After solidification of each layer, the build plate was lowered, and the powder was redeposited over the layer for tracing of the next cross-section.

Table 7-1: Percent composition of the $AlSi_{10}Mg$ alloy.

Al	**Si**	**Fe**	**Cu**	**Mn**	**Mg**	**Ni**	**Zn**	**Pb**	**Sn**	**Ti**
Balance	9.0-11.0	0.55 max	0.05 max	0.45 max	0.25-0.45	0.05 max	0.10 max	0.05 max	0.05 max	0.15 max

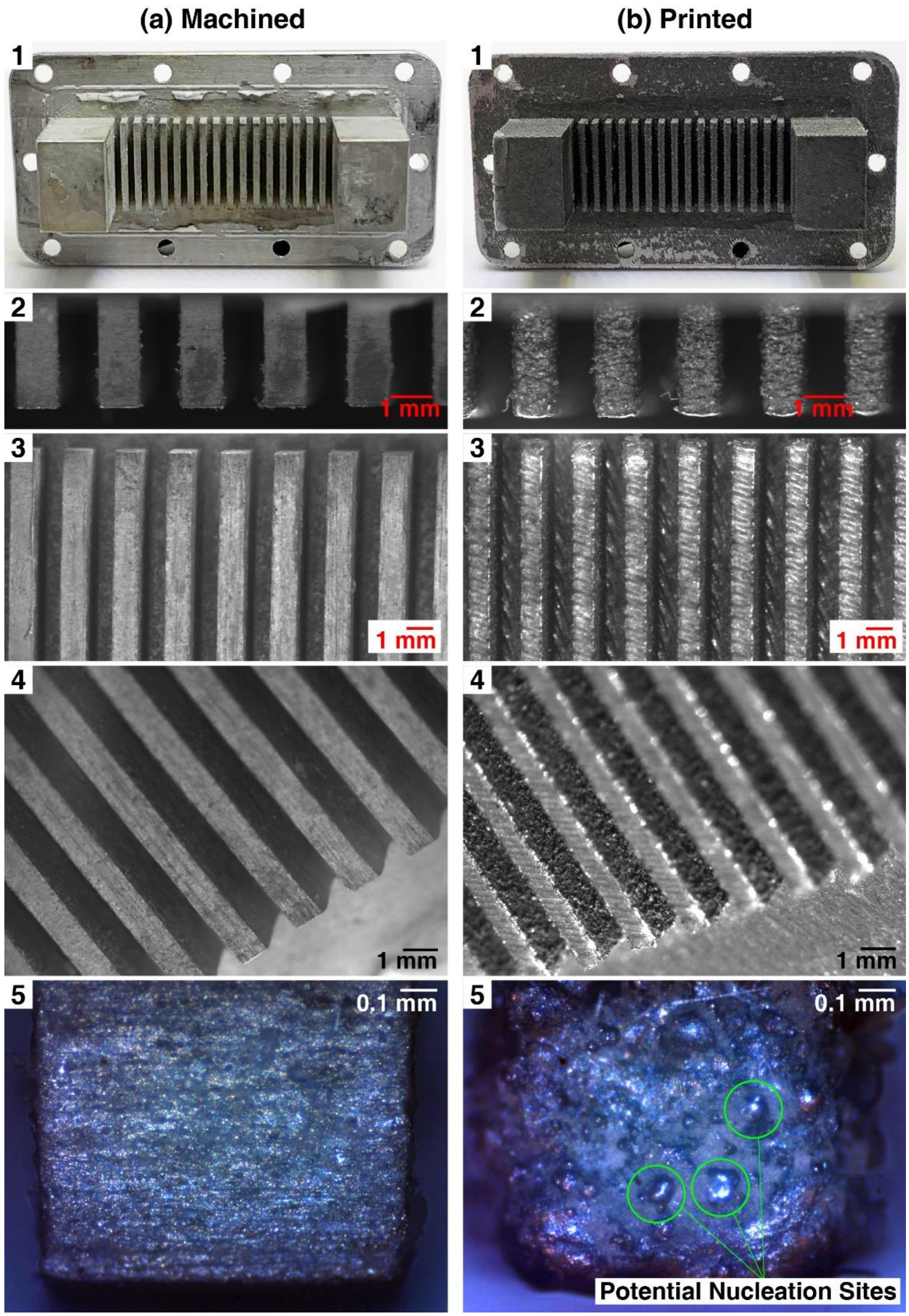

Figure 7-3: Microscope images of the machined and printed evaporators.

7.2.3 Mass Flow Rate Prediction Model

The mass flow rate through the thermosyphon loop can help explain the thermal performance and stability; hence, it is a useful parameter to track its variation with respect to design parameters. Previous works used direct measurement tools such as Coriolis flowmeters [18], as well as indirect methods to calculating mass flow rates based on heat losses in a pre-heated segment of the loop [19] or on pressure drops through the loop [20]. Indirect methods are attractive alternatives to direct ones, as they neither disrupt the flow nor lead to measurement errors.

In this work, mass flow rate estimates were calculated based on pressure drops along the riser. An iterative process illustrated in Figure 7-4 was used to match calculated riser pressure drops (ΔP_{calc}) predicted from the mass flow rate ($\dot{m}$) to the experimental pressure drops (ΔP_{exp}). Experimental pressure drop in the riser was derived as the difference between the evaporator outlet pressure and the condenser outlet pressure (P), neglecting the pressure drop through the condenser as it is shorter and has a larger diameter than the evaporator. The evaporator outlet pressure was assumed to be the saturation pressure that corresponds to the temperature ($T_{e,v}$).

` Pressure drops in the riser were believed to be due to friction and elevation change only, and acceleration-related losses were disregarded as the riser is nearly adiabatic. The working fluid was assumed to be a saturated liquid with negligible subcooling at the evaporator inlet. In each iteration, a different guess for quality at the evaporator outlet (x) was made, and a mass flow rate ($\dot{m}$) based on the measured heat input (Q) was calculated.

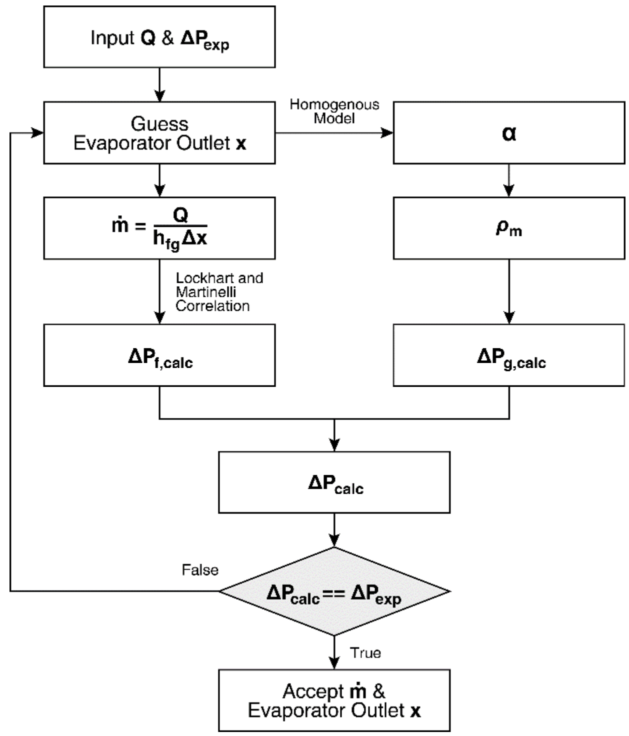

Figure 7-4: Mass flow rate prediction model.

Two-phase frictional pressure drops ($\Delta P_{f,calc}$) corresponding to the calculated mass flow rates were derived from the single-phase pressure drops using the Lockhart and Martinelli correlation, given by Eq. (7.8): Eq. (7.12). Guessed outlet quality (x) was then used in the homogenous model given in Eq. (7.13) to calculate the void fraction (α) of the two-phase mixture in the riser. Assuming the quality stays constant along the riser, the elevation pressure drop ($\Delta P_{g,calc}$) was calculated using Eq. (7.14) and Eq. (7.15), where h is the riser height.

$$\Delta P_{f,two\text{-}phase}=\Delta p_L \Phi_L^2 \tag{7.8}$$

or

$$\Delta P_{f,two\text{-}phase}=\Delta p_v \Phi_v^2 \tag{7.9}$$

$$X=\sqrt{\frac{\Delta P_L}{\Delta P_v}} \tag{7.10}$$

$$\Phi_L{}^2 = 1 + \frac{C}{X} + \frac{1}{X^2} \tag{7.11}$$

$$\Phi_v{}^2 = 1 + CX + X^2 \tag{7.12}$$

$$\frac{1-\alpha}{\alpha} = \frac{1-x}{x} \cdot \frac{\rho_g}{\rho_L} \tag{7.13}$$

$$\rho_m = \alpha \rho_g + (1-\alpha)\rho_L \tag{7.14}$$

$$\Delta P_{g,calc} = \rho_m \, g \, h \tag{7.15}$$

Sum of the frictional and gravitational pressure drops (ΔP_{calc}) was then compared to the measured pressure drop (ΔP_{exp}). Mass flow rate based on the evaporator outlet quality (x) that gives the least difference between the calculated and experimental pressure drops was then assumed to be the correct value for the case.

The predicted mass flow rates are not intended to be used as absolute values considering the assumptions made while developing the current model. However, it can be used to gain insight into the influence of the design parameters on the loop thermal performance and the associated instabilities, as described in Section 7.3.4.2.

7.3 Results & Discussion

An analysis is performed to examine the loop thermal performance and the corresponding instabilities. Three parameters; filling ratio, working fluid, and heating surface, are studied. The results section firstly starts with an overview of the loop performance and stability, highlighting the contribution of each component in the loop; after which variations in the performance factors with respect to the examined parameters are introduced in their respective sections.

7.3.1 Overview of The Loop Thermal Performance and Instabilities

7.3.1.1 Thermal Performance

Figure 7-5 displays the variation of thermal resistances associated with evaporation and condensation of a 30 mL charge of water with respect to increasing input power in the thermosyphon loop equipped with the machined evaporator.

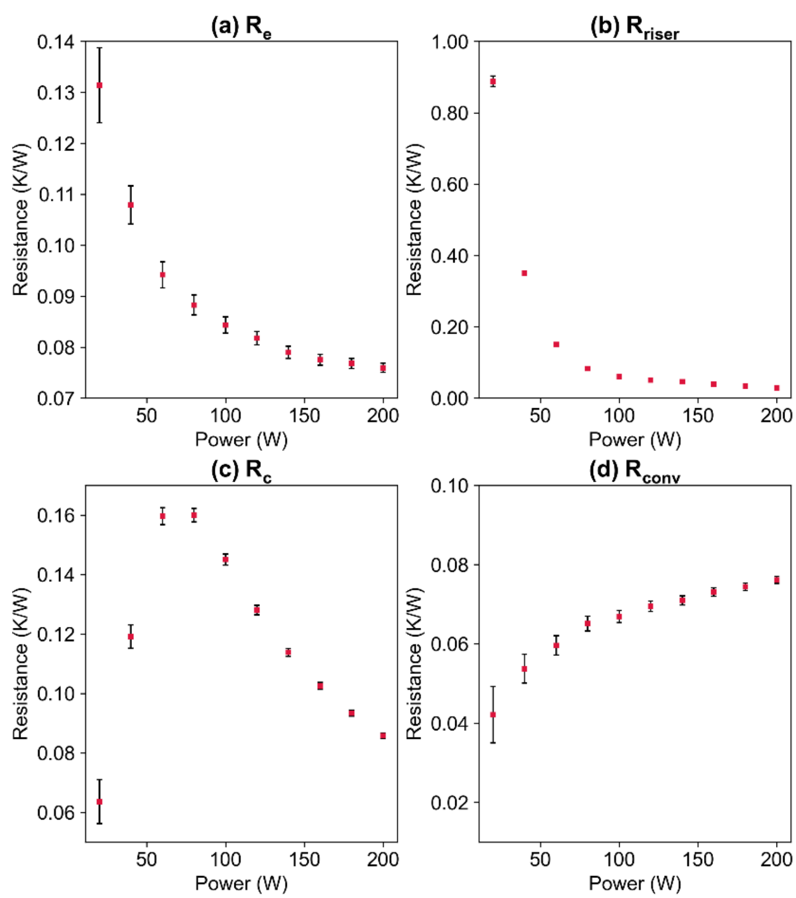

Figure 7-5: Effect of input power on the thermal resistance of (a) evaporator; (b) riser; (c) condenser; (d) forced convection outside condenser during operation with the machined heating surface and a 30 mL charge of water.

Evaporator and riser thermal resistances were observed to decrease drastically with increasing power in the initial portions of the power range tested; and continue decreasing further at a lower rate in the later portions. The overall trend of decreasing resistance with increasing heat flux is attributed to changes in the flow regime. Bubbles generation rate is low at low input heat fluxes, and the rare bubbles are condensed by the mostly sub-cooled and dominantly single-phase liquid column in the riser. Repeated generation and subsequent quenching of bubbles lead to geyser instability. Ineffective and unstable evaporation results in high-temperature differences between the fluid and the heating surface; and, therefore, low heat transfer coefficient and high resistance values. Increased heat inputs start providing sufficient energy to sustain bubbly flow, and both the evaporator and the riser thermal resistances were seen to converge to their minimum values towards the end of the tested range of input power.

Riser thermal resistance is the largest contributor to the total thermal resistance of the system, and its magnitude was seen to drop significantly in the 25-100 W input heat flux range. Further increases to the heat flux do not improve the riser resistance significantly.

Condenser thermal resistance rapidly increased to a maximum value at an input power of 60 W, and subsequently dropped gradually with the input power increase. This can be explained by examining the time variation of condenser resistance, shown in Figure 7-6, which depicts a consistent fluctuation pattern from a minimal value near zero to some positive value.

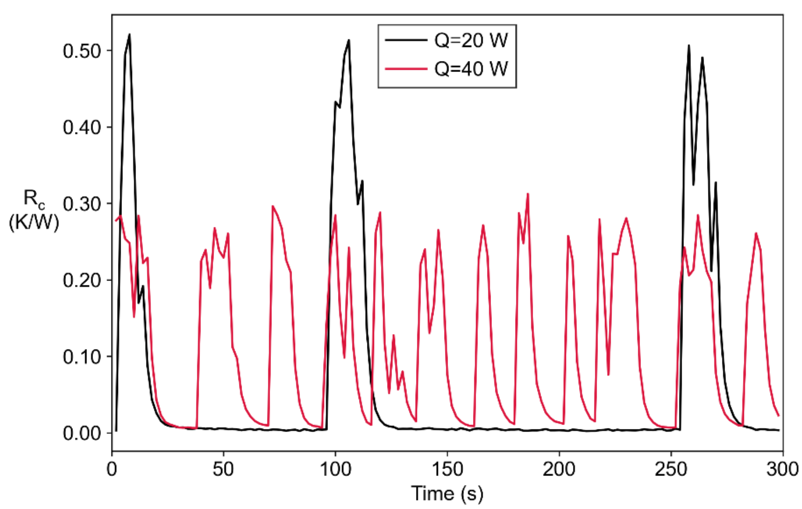

Figure 7-6: Time variation of condenser resistance in (a) 20 W and (b) 40 W input power during operation with the machined heating surface and a 30 mL charge of water.

At low input powers, low vapor generation rates in the evaporator resulted in a delayed and intermittent buildup of buoyancy forces on the liquid column occupying the riser. In each cycle, geysering occurred during these “waiting periods” for the development of enough buoyancy. While the liquid column was waiting to be lifted, vapor left in the rest of the loop was being effectively condensed through the condenser. Condensation of high-quality vapor led to high heat transfer coefficients and low condenser resistances. Once the liquid column was lifted and started circulating, the condenser was passed by a two-phase mixture with low vapor fraction, resulting in decreased heat transfer coefficients and high condenser resistances. This portion of the cycle in operation at 20 W input power is denoted as the “circulation period” in Figure 7-6. Cycles with unstable operation at low input powers can therefore be described as “waiting periods” followed by riser liquid circulations, with low and high condenser resistances, respectively. As input power was increased, evaporation and bubble generation intensified, as evidenced by decreasing evaporator and riser resistances shown in Figure 7-5 (a) and (b). Subsequently, the waiting periods got shorter, leading to more frequent circulation of riser liquid, as can be seen in Figure 7-6 from the increasing frequency of condenser resistance peaks with increasing input power. Higher frequency of two-phase flow passing by the condenser resulted in higher values of time-averaged condenser resistance, as plotted in Figure 7-5 (c) while flow remains unstable.

It was found through visual inspection that a power input of 60 W is the final point at which geysering occurs with 30 mL of water and corresponds to the peak of the resistance curve of Figure 7-5 (c). At 60 W, two-phase flow started circulating through the loop continuously as the input power was enough to sustain bubbly flow without “waiting periods.” After this point, the condenser heat transfer coefficient increased, and the resistance dropped, which we believe is because higher input powers further increase the vapor fraction. A similar peak in the condenser resistance curve was also observed with ethanol at lower power inputs, as discussed further in Section 7.3.4.2. Therefore, we suggest that the condenser resistance curve can be used as a monitor for geyser occurrence. It should be noted that the curve does not provide any indication of geyser intensity.

Figure 7-5 (d) displays convection resistance increasing slightly with increasing input power, which is contrary to expectations. As the fan had a constant speed in all test conditions, the forced convection heat transfer coefficient and the convection resistance are expected to remain constant over the range of input powers tested. This apparent change in resistance is attributed to using the electric power directly as the input thermal energy for resistance calculations without deducting heat losses, which were believed to change slightly over the tested range of power inputs. As a result, the assumed heat load is overestimated to a larger extent at low powers. With losses becoming insignificant relative to total power inputs at high powers, the resistance values showed little change.

7.3.1.2 Stability

Intensity of thermal instabilities was evaluated in terms of the maximum evaporator wall temperature fluctuations, recorded with a sampling period of 0.15 s. Figure 7-7 displays the variation of fluctuation magnitude with respect to input power in operation with 30 mL of water. Amplified fluctuations at the lower end of the input power range are linked to the high intensity of geysering induced instabilities. Heat inputs insufficient to maintain steady bubbly flow led to cycles of bubble generation and condensation, resulting in temperature fluctuations with high frequency and amplitudes. Stability improved, and temperature fluctuations dropped as low as 1.7°C as geysering lost effect with increasing heat input, only to be worsened again towards the higher end of the power range with the emergence of the intermittent dry-out phenomenon. High power inputs brought high evaporation rates, resulting in poor liquid availability and increased evaporator temperatures, especially with low filling ratios. The evaporator temperature fluctuated with the intermittent arrival of condensed liquid from the downcomer. The magnitude of fluctuations grew as the evaporator was heated to higher temperatures with higher power inputs. The temperature fluctuations due to geysering had amplitudes as high as 4.13°C, whereas the maximum fluctuation amplitude due to dry-out was 2.44°C.

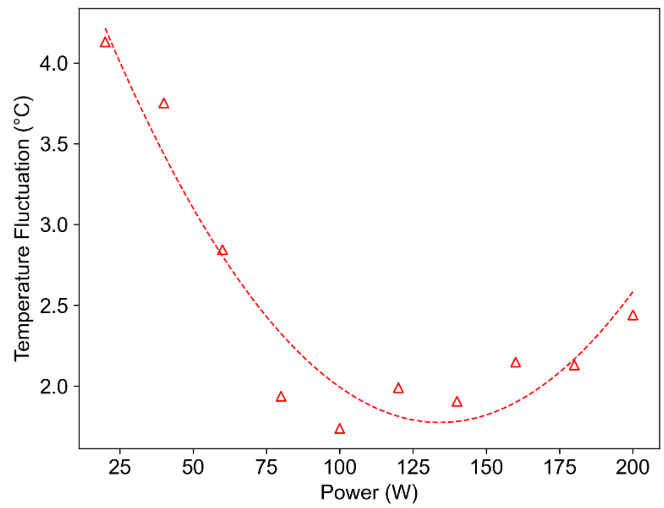

Figure 7-7: Maximum fluctuations in evaporator wall temperature in the quasi-steady state with the machined heating surface and a 30 mL charge of water.

7.3.2 Effect of Fluid Charge

The working fluid charge determines the maximum heat loads, and available volumes in the evaporator and the riser pertain to the occurrence of dry-out and geysering events, respectively. Therefore the fluid charge can directly affect the loop thermal performance and stability, both of which are investigated in this section.

7.3.2.1 Thermal Performance

The total thermal resistance of the loop can be used as a metric to assess the overall thermal performance. Variation of total thermal resistance with input power at different working fluid charges is shown in Figure 7-8. In the initial portion of the input power range, it can be distinctly seen that higher filling ratios lead to higher total thermal resistances. This is due to higher amounts of liquid suppressing bubble generation and evaporation, causing high-temperature differences across ends of the riser. As heat input increased, the charge lost its effect on the total resistance, as can be seen in Figure 7-8 with the data markers of different charges coming closer to one another near the high end of the power range. This can be explained by the riser resistance becoming insignificant compared to other thermal resistances at high input powers regardless of filling ratio. Figure 7-9 compares the magnitudes of thermal resistances at different power inputs with a 30 mL charge of water. As boiling became more effective with higher heat inputs, and the two-phase flow circulated faster; the temperature difference between ends of the riser decreased, and riser thermal resistance lost its dominance in the total resistance. Among the other resistance components, evaporator and convection resistances are independent of filling ratio, further contributing to convergence of overall thermal resistances with different filling ratios.

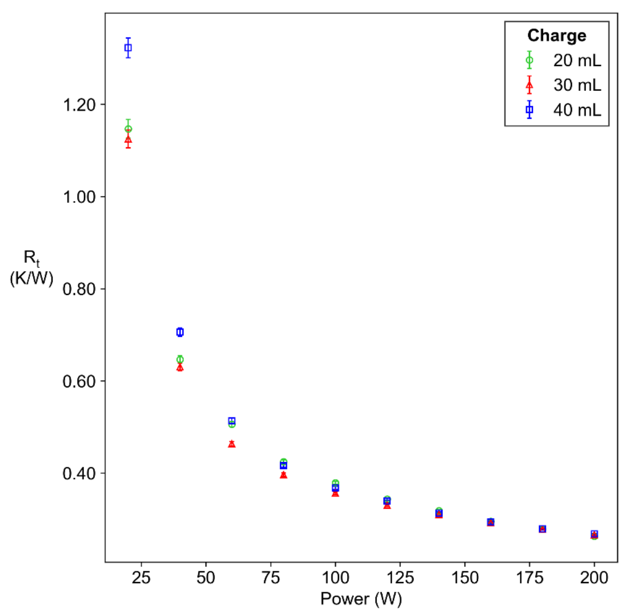

Figure 7-8: Effect of input power on the total thermal resistance of the loop with the machined heating surface using different charges of water.

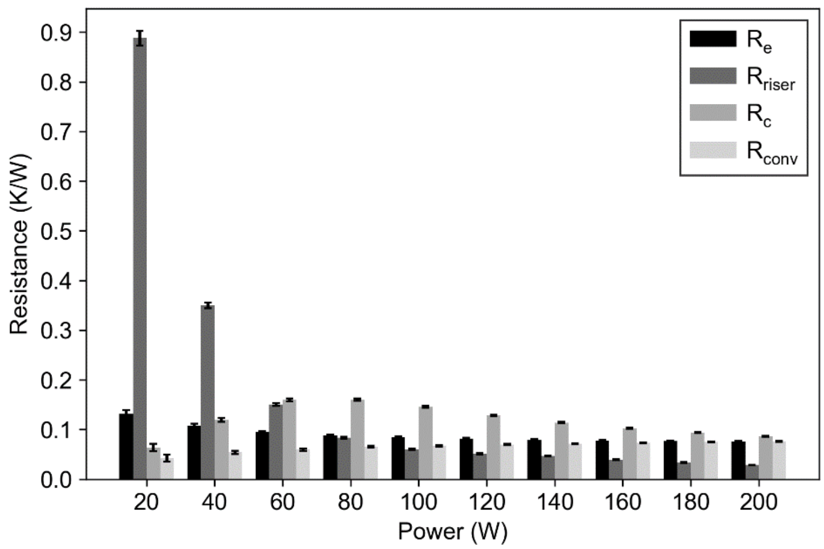

Figure 7-9: Comparison of thermal resistances of components with different input powers in operation with the machined heating surface and a 30 mL charge of water.

7.3.2.2 Stability

Figure 7-10 illustrates the effect of filling ratio on instabilities quantified by maximum fluctuations in the evaporator wall temperature. At a power input of 20 W, the maximum temperature fluctuation with a 20 mL charge of water was 3.4°C and 7.3°C lower than that with 30- and 40-mL charges, respectively. This distinct reduction in temperature fluctuations with a 20 mL charge can be explained by the low likelihood of geysering at low filling ratios. Low power inputs were enough to sustain evaporation without repeated condensation of bubbles in the riser, thanks to the low volume of liquid in the riser and the system altogether. However, the low liquid volume, in turn, caused increased temperature fluctuations at high powers (1.2°C higher than 30 and 40-mL charges) due to higher intermittent dry-out intensity. Both moderate and high charges, 30- and 40-mL, showed geysering and dry-out effects, with both instabilities occurring at a higher intensity with 40-mL charge.

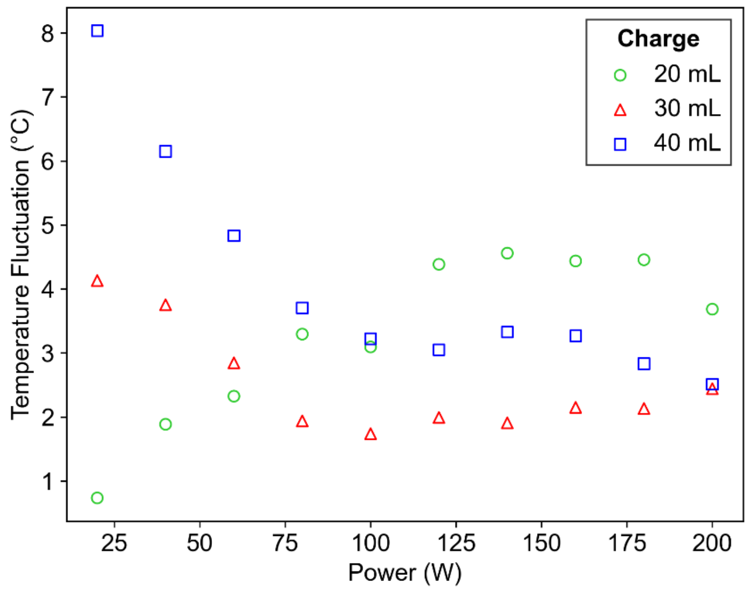

Figure 7-10: Maximum fluctuations in evaporator wall temperature in quasi-steady state with the machined heating surface and different charges of water.

7.3.3 Effect of Working Fluid

Working fluid is another parameter in thermosyphon design that can impact thermal and hydraulic performance and operational stability. In this section, water as a popular working fluid with good thermal properties for general applications and ethanol as a higher-pressure liquid are compared based on the thermosyphon thermal performance and stability.

7.3.3.1 Thermal Performance

Variation of the total thermal resistance of the thermosyphon loop with respect to input power is plotted in Figure 7-11 at different charges of water and ethanol. Thermal resistances were lower in operation with 30 mL than 40 mL of working fluid of either type. The total thermal resistance decreased as the input power was increased with both working fluids at all filling ratios, and its values were seen to converge at high powers. The decreasing trend and convergence are attributed to higher heat inputs improving the boiling effectiveness and reducing geyser occurrence with both working fluids. As geysering died out, riser resistance lost its dominance, as visualized previously in Figure 7-9. The remaining resistance components at high power inputs are the convection resistance, which is fluid-independent, evaporator resistance, which is limited by the evaporator conductivity, and the condenser resistance.

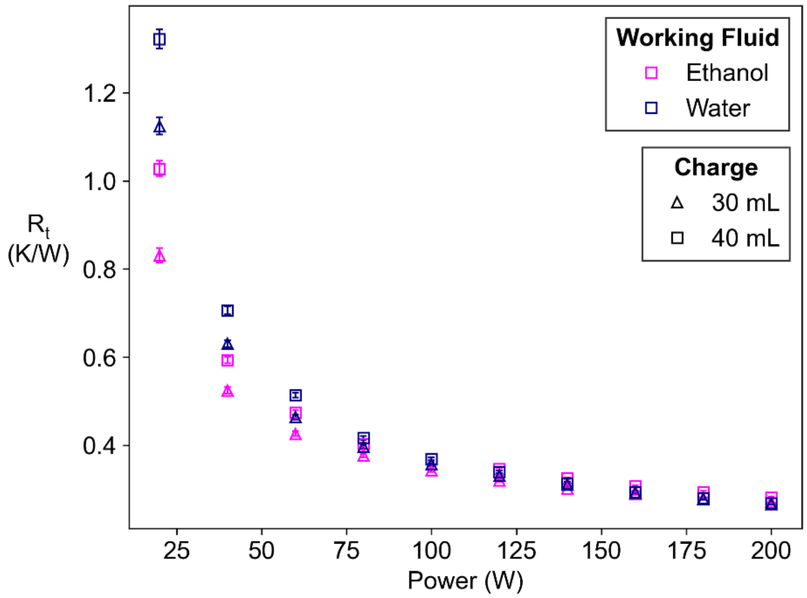

Figure 7-11: Total resistance of the system with the machined heating surface using water and ethanol as working fluids at different input powers and filling ratios.

Compared to operation with water, operation with ethanol achieved lower overall thermal resistances at both 30- and 40-mL charges until heating powers of 125 W. Lower resistances with ethanol are linked to it being a higher-pressure fluid than water, and thus creating a higher system pressure, which results in lower pressure drops and higher heat transfer coefficients in the evaporator [19], [21].

7.3.3.2 Stability

The condenser thermal resistance curve was found in Section 7.3.1.1 to be suggestive of geyser occurrence and is used in Figure 7-12 to compare the ranges of stable operation for the different working fluids. No geysering was observed with 20 mL of ethanol, and condenser resistance was found to be continuously decreasing with increasing power input. Resultingly, no peak was observed on the condenser resistance curve of the case. In contrast, geysering was seen at all filling ratios of water. Among all cases, those with ethanol are seen to become stable at lower power inputs, as represented in Figure 7-12, with peak condenser resistances shifted to the left.

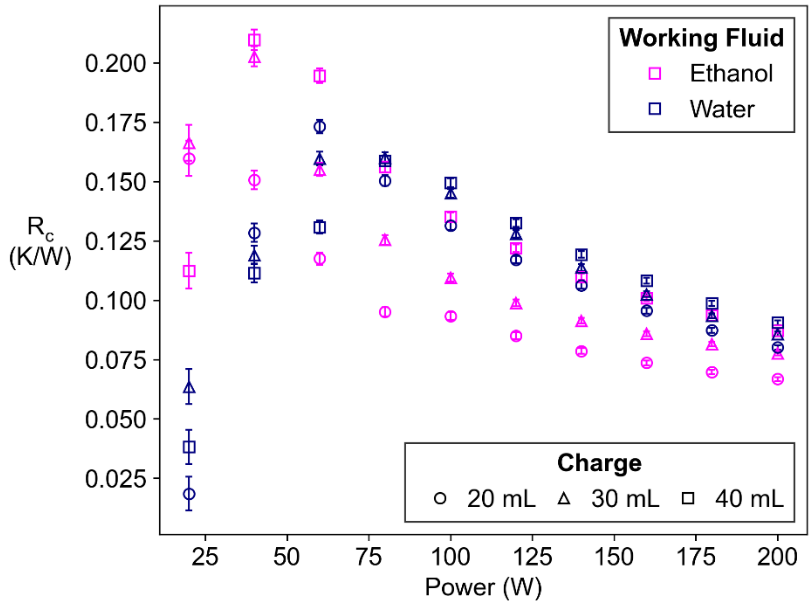

Figure 7-12: Variation of condenser resistance with respect to input power for different charges of water and ethanol in the loop using the machined heating surface.

Figure 7-13 is the plot of temperature fluctuation amplitudes in the machined evaporator with both working fluids. Fluctuations with any filling ratio of ethanol were lower than those with water, except for operation with 20 mL charge under 80 W power input, which is a unique case elaborated in Section 7.3.4.2. We speculate that the lower magnitude of instabilities and the end of geysering at lower power inputs with ethanol can be explained by its lower confinement number and smaller effective radius of nucleation, activating more nucleation sites [12]. The capability to produce smaller bubbles would increase the number of usable nucleation sites and facilitates the transition to effective boiling at lower power inputs than water.

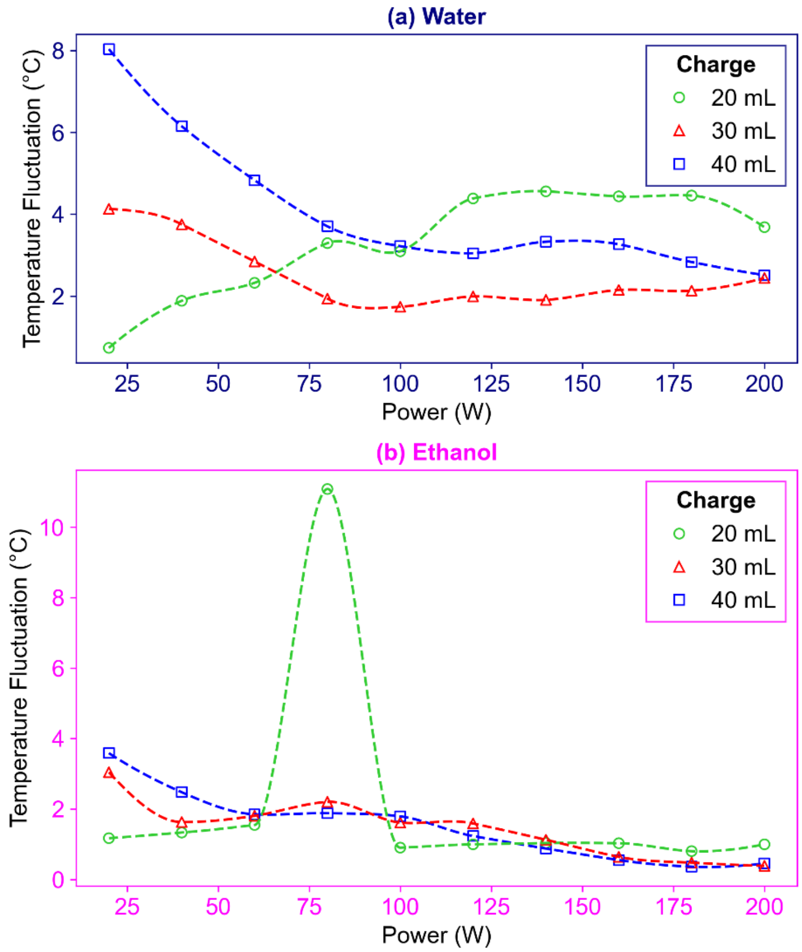

Figure 7-13: Maximum evaporator temperature fluctuation amplitudes with the machined heating surface and different filling ratios of water and ethanol.

7.3.4 Effect of Heating Surface

The evaporator material and manufacturing method has implications on the surface topology, distribution of active nucleation sites, roughness, and consequently, the boiling characteristics. In order to investigate their effect, machined and selective laser melted (printed) heating surfaces with the same geometry were tested with the experimental thermosyphon loop using both water and ethanol at low, moderate, and high filling ratios.

Figure 7-14 displays the variation of temperature in machined and printed heating surfaces with low and high filling ratios of water. With the machined heating surface and 20 mL of water, the temperature-time profiles of Figure 7-14 (a) got increasingly unstable as the input power was increased; whereas the maximum fluctuations were lower with the same charge of water for the printed heating surface, as seen in Figure 7-14 (b). In operation with 40 mL of water, a periodic cooldown event is visible in the temperature-time profiles of both heating surfaces. The event's frequency increased with input power and became indistinguishable from the constant fluctuations at 100 W input power. The temperature fluctuations for the printed heating surface with 40 mL of water at medium input powers were lower than those with the machined surface.

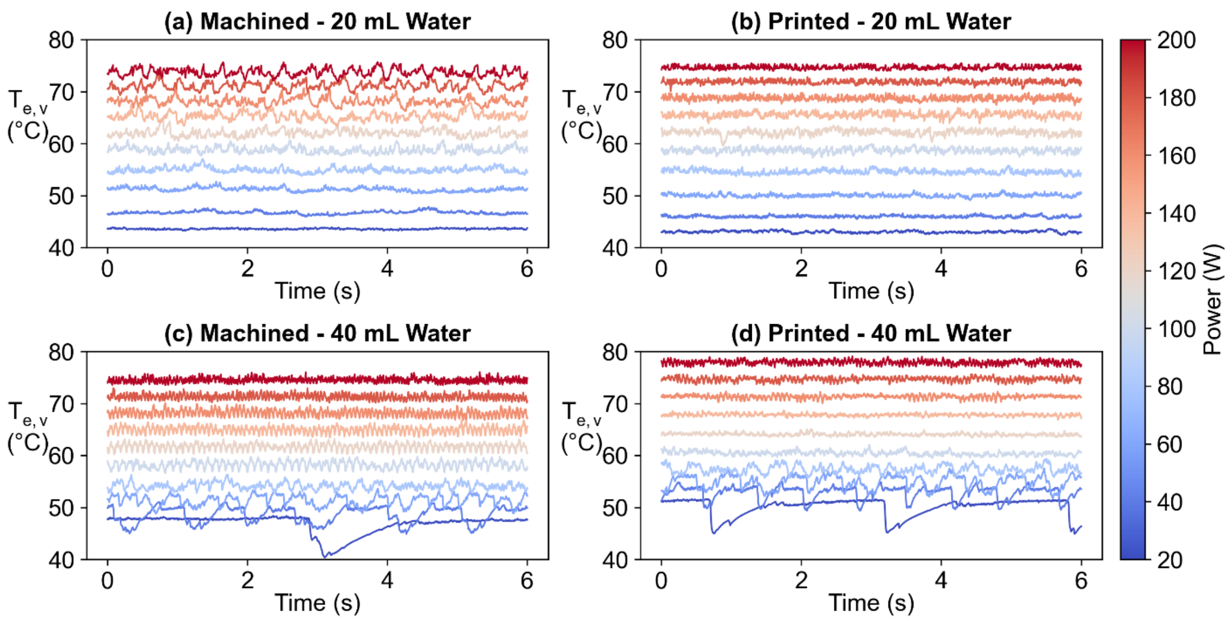

Figure 7-14: Variation of evaporator temperature with respect to time at different heating powers with different evaporator types and charges of water.

7.3.4.1 Thermal Performance

Variation of total thermal resistance with respect to input power in operation with machined and printed evaporators at different water and ethanol charges is shown in Figure 7-15. With both working fluids, the printed evaporator resulted in total resistances higher than those with the machined evaporator at low power inputs (0.23 K/W and 0.05 K/W difference at a power of 20 W with 30 mL of water and ethanol, respectively). As power was increased, filling ratios' effect on total resistance diminished, as explored earlier in Section 7.2.2; however, total resistance with printed evaporator remained slightly higher than the machined one.

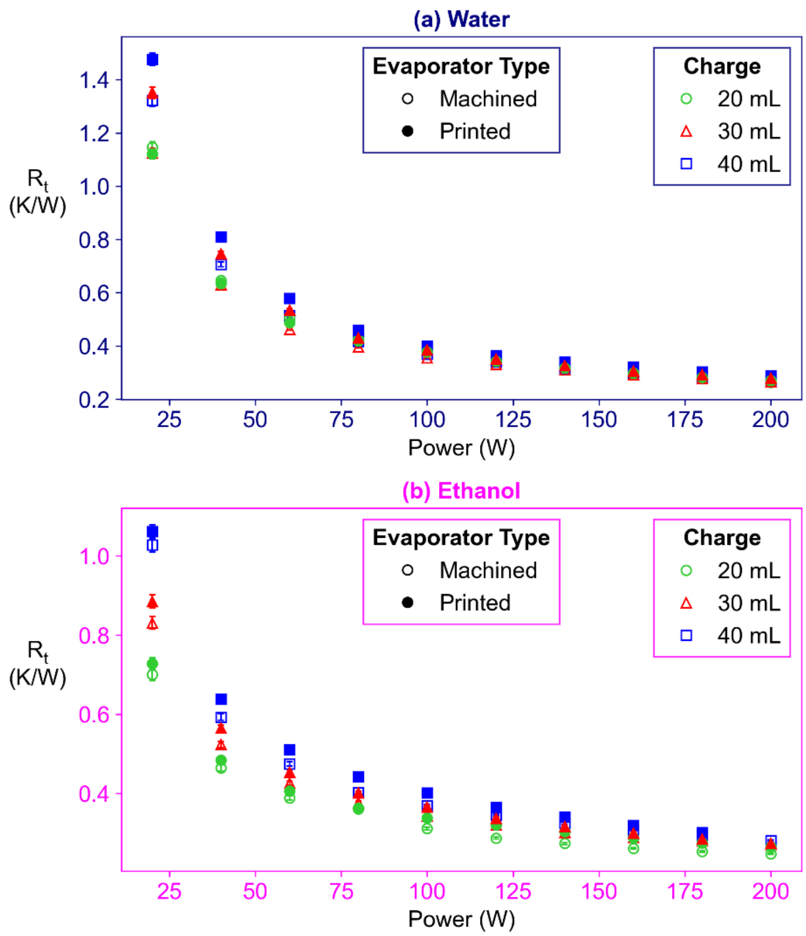

Figure 7-15: Variation of total thermal resistance with input power at different fill ratios with different evaporator types.

Total thermal resistances with printed and machined evaporators were found to differ primarily at high powers due to different evaporator thermal resistances. Figure 7-16 displays the evaporator thermal resistance progression with input power with the same variables as Figure 7-15.

The printed evaporator was observed to have a higher thermal resistance than the machined one at all power inputs and charges of both working fluids, which we believe is linked to its low thermal conductivity. Evaporator resistance is the summation of its boling and conduction resistances; and conduction resistance is believed to be the dominant component. In operation with water, resistances of both the machined and printed evaporators follow the same trend, and their difference remains roughly constant with respect to power input after 100 W, which we believe pertains to the difference in thermal conductivity of the evaporators. Reported values for the thermal conductivity of $AlSi_{10}Mg$ are in the range 103-119 W/mK [22]. In contrast, evaporator resistance with different charges of ethanol tends to converge towards the end of the input power range. This is believed to be due to the boiling heat transfer coefficient still actively improving with increased power inputs.

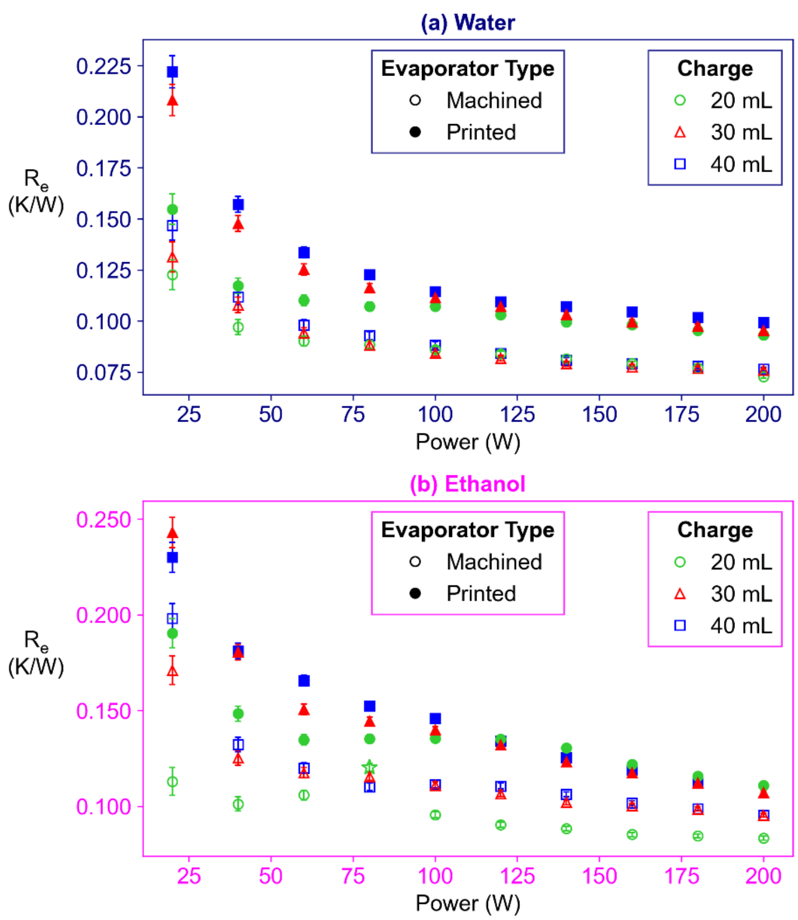

Figure 7-16**:** Variation of evaporator thermal resistance with input power at different fill ratios with different types of evaporator.

An exceptional event was observed at 80 W in operation with 20 mL of ethanol, where the machined evaporator resistance breaks the trend and is noticeably high. The data point is marked with a star (☆) in Figure 7-16, and the event is further discussed in Section 7.3.4.2.

7.3.4.2 Stability

Figure 7-17 illustrates the variation of maximum temperature fluctuations recorded during quasi-steady operation with different charges of water and ethanol. For 20- and 40-mL charges of water, maximum fluctuations were lower with the printed evaporator than the machined one at most tested power inputs, as can be seen in Figure 7-17 (a). The printed evaporator achieved the largest reduction in temperature fluctuations compared to the machined one during operation with 20 mL charge of water at the highest power inputs, up to 2.1°C at 200 W.

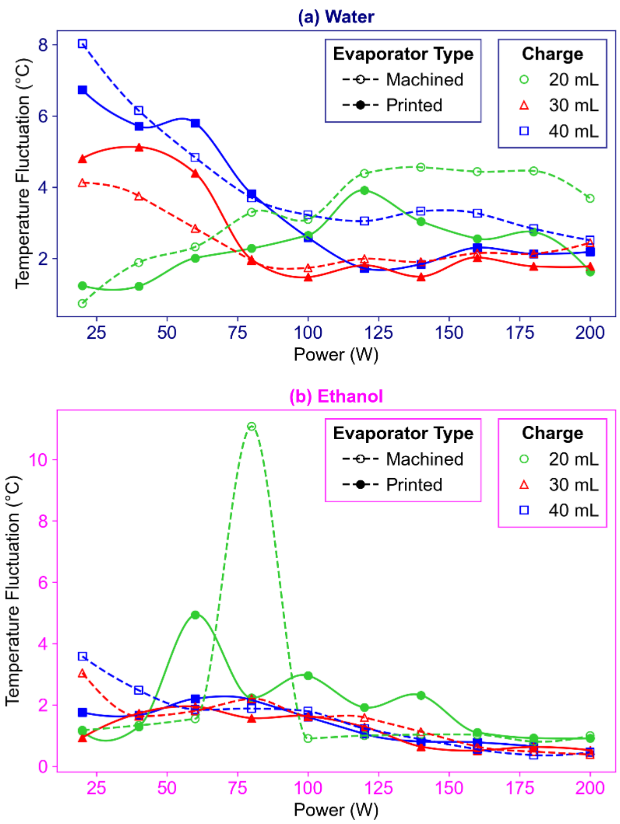

Figure 7-17: Maximum fluctuations in evaporator vapor temperature in quasi-steady state at different charges of water with different evaporator designs.

Stability of the evaporator temperature is believed to be governed by two parameters: surface topology and circulation mass flow rate.

Surface topology of the evaporator is related to the distribution and density of active bubble nucleation sites; a higher number of which would increase the boiling heat transfer coefficient, and resultingly, bubble generation rates and the mixture quality. On the other hand, increasing mixture qualities at a given power input will decrease the mass flow rates, as can be seen from the mass flow rate equation provided in Figure 7-4. Mass flow rate has implications on how often and how much the heating surface is wetted. Depending on the porosity and the resulting wettability of the surface, the wetting mass of liquid can have a role in absorbing heat and preventing dry-out. Low mass flow rates would lead to infrequent replenishment of liquid in the evaporator and could destabilize the temperature.

Circulation mass flow rates were predicted using the model introduced in Section 7.2.3. The model relies on predicting an evaporator outlet quality that gives the best agreement between calculated and experimental values of riser pressure drops.

Figure 7-18 shows the measured pressure drop for both surfaces with both working fluids at all fil ratios. Predicted pressure drops display a minimum with respect to input power, especially with 30- and 40-mL of water and 40 mL of ethanol in operation with both types of evaporators. Similar minima were also observed by Khodabandeh [20], and was attributed to the total pressure drop being the sum of frictional and gravitational pressure drops, which increase and decrease respectively as the input power increases. Predicted mass flow rates plotted in Figure 7-19 increase with higher charges of working fluids, in agreement with previous observations [12], [23]. It is worth mentioning that we conjecture that the mass flow rates in Figure 7-19 at low power inputs have a higher deviation from actual values as a result of neglecting subcooling in the prediction model.

The printed evaporator had lower temperature fluctuations in operation with water for most cases, as seen in Figure 7-17 (a). Especially in operation with 20 mL of water, the printed evaporator provided a distinct reduction of temperature fluctuations on the high end of the power input range, where the intermittent dry-out phenomenon occurred. Low fluctuations are attributed to higher mass flow rates achieved with the printed evaporator in comparison to those with the machined evaporator, as plotted in Figure 7-19 (a). Higher mass flow rates work favorably with the printed evaporator: working fluid wets the porous heating surface upon frequent contact, and even at dry-out conditions with little fluid in the evaporator, the absorbed liquid provides thermal inertia and prevents extreme temperature fluctuations at the evaporator. The effect of higher water mass flow rates with the printed evaporator on temperature fluctuations can also be seen by comparing the temperature-time profiles of Figure 7-14 (a) and (b) at high powers. Operation with high filling ratios also benefited from higher mass flow rates with the printed evaporator, and temperature overshoots were recovered more frequently, as can be seen by comparison of Figure 7-14 (c) and (d), particularly at low and moderate powers.

The printed evaporator had lower temperature fluctuations than the machined one in operation with ethanol, as shown in Figure 7-17 (b). However, the stabilizing effect of the printed evaporator with ethanol is speculated not to be linked to mass flow rates, which are lower with the printed evaporator than with the machined one, unlike in operation with water. Instead, we believe that surface topology was the dominating factor in reducing temperature fluctuations in the printed evaporator with ethanol. As a high-pressure fluid with an effective radius of nucleation smaller than water's, ethanol benefited from the surface roughness of the printed evaporator to a greater degree and achieved higher rates of boiling. Enhanced boiling resulted in higher evaporator outlet qualities, as verified by the lower mass flow rates plotted in Figure 7-19 (b), which are related to the exit quality by the relation $Q=\dot{m}h_{fg}\Delta x$.

Lastly, Figure 7-17 (b) displays an exceptionally high-temperature fluctuation at 80 W power in operation with the machined evaporator and 20 mL of ethanol. No such event was observed at lower powers or higher filling ratios. Mass flow rate predictions depicted in Figure 7-19 reveal that the instability arose from low circulation rates: the rate at 80 W is the minimum among those predicted for 20 mL of ethanol with the printed evaporator and resulted in a particularly strong dry-out. The low volume of fluid in circulation hardly accumulated in the heating surface, and the minimum mass flow rate lead to an extreme temperature overshoot. Flow rate and temperature fluctuation recovered to their steady values at higher powers.

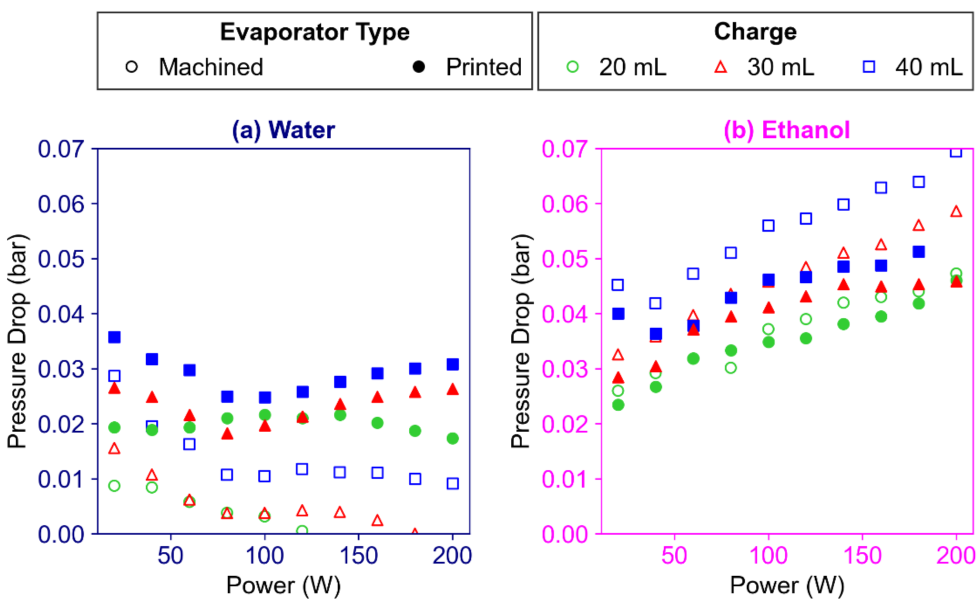

Figure 7-18: Riser pressure drops predicted by the model for water and ethanol with machined and printed evaporators in operation with different filling ratios.

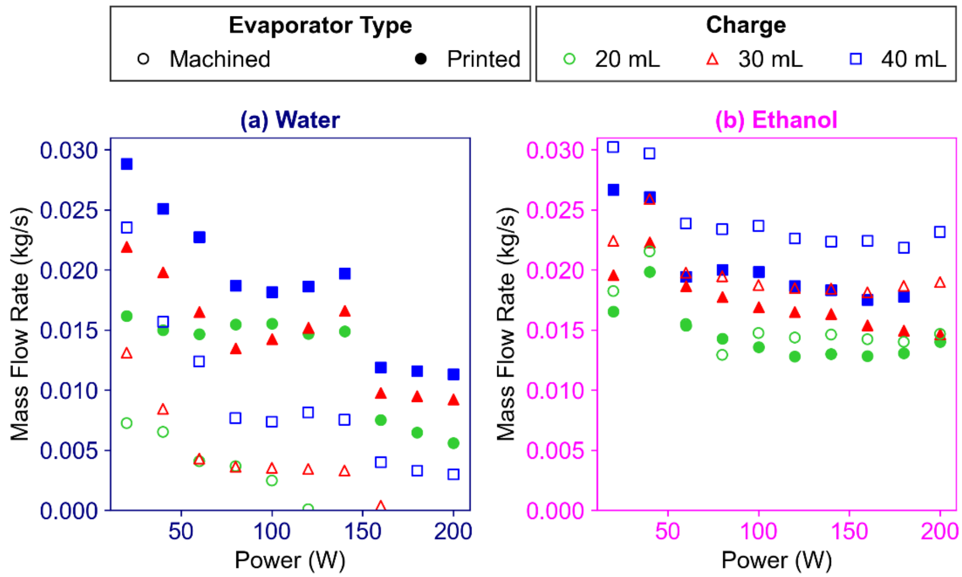

Figure 7-19: Mass flow rate predicted by the model for water and ethanol with machined and printed evaporators in operation with different filling ratios.

7.4 Summary & Conclusions

The two-phase closed-loop thermosyphon with different heating surfaces was observed using two working fluids at three filling ratios. Thermal resistances and maximum amplitudes of evaporator temperature fluctuations were used to quantify thermal performance and instabilities, respectively. Important observations include:

- Cycles with geysering required long “waiting periods” for the sufficient buoyancy force buildup in the evaporator the riser. Once achieved, they pushed the liquid column in the riser upwards, leading to effective circulation periods. During circulation, condenser resistance increased due to the low quality of the riser flow. More frequent circulations led to higher time-averaged condenser resistances.
- As input power was increased, circulations transition from intermittent to continuous, vapor fraction of the riser liquid column increased, and condenser resistance started to decrease.

Hence, the condenser resistance could be used as a monitor for the termination of geysering. No geysering was observed after the peak value of condenser resistance under operation with both water and ethanol.

- Geysering affected moderate and high filling ratios at low heat inputs, whereas dry-out was more prominent with low filling ratios at high heat inputs.
- Overall, thermal resistances were lower with ethanol than water due to having high system pressure with respect to ethanol, causing low-pressure drops and high heat transfer coefficient. Geysering terminated at a lower power input with ethanol and was not seen with its low filling ratios.
- Printed heating surface led to a higher evaporator and total resistances in comparison to the machined sample (up to 0.23 K/W higher total resistance in operation with 30 mL of water at 20 W power input). However, it achieved better temperature stability, with up to 2.1°C reductions in temperature fluctuation amplitude at 200 W input power with a 20 mL charge of water. Better stability was attributed to more frequent wetting in operation with water and increased active bubble nucleation sites in operation with ethanol.
- An extreme temperature overshoot was observed at 80 W heat load in operation with 20 mL of water using the machined heating surface. The event was explained by the local minimum in the predicted mass flow rate contributing to the existing susceptibility of low filling ratio to dry-out.

7.5 References

[1] D. Jafari, S. Filippeschi, A. Franco, and P. Di Marco, "Unsteady experimental and numerical analysis of a two-phase closed thermosyphon at different filling ratios," Exp. Therm. Fluid Sci., vol. 81, pp. 164–174, 2017, doi: 10.1016/j.expthermflusci.2016.10.022.

[2] D. Jafari, A. Franco, S. Filippeschi, and P. Di Marco, "Two-phase closed thermosyphons: A review of studies and solar applications," Renew. Sustain. Energy Rev., vol. 53, pp. 575–593, Jan. 2016, doi: 10.1016/j.rser.2015.09.002.

[3] T. F. Lin, W. T. Lin, Y. L. Tsay, J. C. Wu, and R. J. Shyu, "Experimental investigation of geyser boiling in an annular two-phase closed thermosyphon," Int. J. Heat Mass Transf., vol. 38, no. 2, pp. 295–307, 1995, doi: 10.1016/0017-9310(95)90019-5.

[4] G. Xia, W. Wang, L. Cheng, and D. Ma, "Visualization study on the instabilities of phase-change heat transfer in a flat two-phase closed thermosyphon," Appl. Therm. Eng., vol. 116, pp. 392–405, 2017, doi: 10.1016/j.applthermaleng.2017.01.096.

[5] H. Kuncoro, Y. F. Rao, and K. Fukuda, "An experimental study on the mechanism of geysering in a closed two-phase thermosyphon," Int. J. Multiph. Flow, vol. 21, no. 6, pp. 1243–1252, 1995, doi: 10.1016/0301-9322(95)00050-8.

[6] C. Tecchio, J. L. G. Oliveira, K. V. Paiva, M. B. H. Mantelli, R. Galdolfi, and L. G. S. Ribeiro, "Geyser boiling phenomenon in two-phase closed loop-thermosyphons," Int. J. Heat Mass Transf., vol. 111, pp. 29–40, 2017, doi: 10.1016/j.ijheatmasstransfer.2017.03.092.

[7] L. H. R. Cisterna, F. H. Milanez, and M. B. H. Mantelli, "Prediction of geyser boiling limit for high temperature two-phase thermosyphons," Int. J. Heat Mass Transf., vol. 165, p. 120656, 2021, doi: 10.1016/j.ijheatmasstransfer.2020.120656.

[8] B. Jiao, L. M. Qiu, Z. H. Gan, and X. B. Zhang, "Determination of the operation range of a vertical two-phase closed thermosyphon," Heat Mass Transf. und Stoffuebertragung, vol. 48, no. 6, pp. 1043–1055, 2012, doi: 10.1007/s00231-011-0954-x.

[9] M. S. El-Genk and H. H. Saber, "Determination of operation envelopes for closed, two-phase thermosyphons," Int. J. Heat Mass Transf., vol. 42, no. 5, pp. 889–903, 1999, doi: 10.1016/S0017-9310(98)00212-9.

[10] J. A. Boure, A. E. Bergles, and L. S. Tong, "Review of Two-Phase Flow Instability," Nucl. Eng. Des., vol. 25, pp. 165–192, 1973, doi: Doi: 10.1016/0029-5493(73)90043-5.

[11] Z. Tong and G. Zang, "Effect of the diameter of riser and downcomer on an CO2 thermosyphon loop used in data center," Appl. Therm. Eng., vol. 182, no. June 2020, p. 116101, 2021, doi: 10.1016/j.applthermaleng.2020.116101.

[12] A. Elkholy and R. Kempers, “Experimental investigation of geyser boiling in a small diameter two-phase loop thermosyphon,” Exp. Therm. Fluid Sci., vol. 118, no. May, p. 110170, 2020, doi: 10.1016/j.expthermflusci.2020.110170.

[13] R. Khodabandeh and R. Furberg, “Instability, heat transfer and flow regime in a two-phase flow thermosyphon loop at different diameter evaporator channel,” Appl. Therm. Eng., vol. 30, no. 10, pp. 1107–1114, 2010, doi: 10.1016/j.applthermaleng.2010.01.024.

[14] Y. Liu, Z. Li, Y. Li, Y. Jiang, and D. Tang, “Heat transfer and instability characteristics of a loop thermosyphon with wide range of filling ratios,” Appl. Therm. Eng., vol. 151, no. February, pp. 262–271, 2019, doi: 10.1016/j.applthermaleng.2019.02.031.

[15] Y. Liu, Z. Li, Y. Li, S. Kim, and Y. Jiang, “Experimental investigation of geyser boiling in a two-phase closed loop thermosyphon with high filling ratios,” Int. J. Heat Mass Transf., vol. 127, pp. 857–869, 2018, doi: 10.1016/j.ijheatmasstransfer.2018.07.018.

[16] G. C. Vieira, J. P. Flórez M, and M. B. H. Mantelli, “Improving heat transfer and eliminating Geyser boiling in loop thermosyphons: Model and experimentation,” Int. J. Heat Mass Transf., vol. 156, 2020, doi: 10.1016/j.ijheatmasstransfer.2020.119832.

[17] R. Khodabandeh and R. Furberg, “Heat transfer, flow regime and instability of a nano- and micro-porous structure evaporator in a two-phase thermosyphon loop,” Int. J. Therm. Sci., vol. 49, no. 7, pp. 1183–1192, 2010, doi: 10.1016/j.ijthermalsci.2010.01.016.

[18] Z. Tong, X. H. Liu, Z. Li, and Y. Jiang, “Experimental study on the effect of fill ratio on an R744 two-phase thermosyphon loop,” Appl. Therm. Eng., vol. 99, pp. 302–312, 2016, doi: 10.1016/j.applthermaleng.2016.01.065.

[19] F. Cataldo and J. R. Thome, “Experimental evaluation of the thermal performances of a thermosyphon cooling system rejecting heat by natural and forced convection,” Appl. Therm. Eng., vol. 127, pp. 1404–1415, 2017, doi: 10.1016/j.applthermaleng.2017.08.166.

[20] R. Khodabandeh, “Pressure drop in riser and evaporator in an advanced two-phase thermosyphon loop,” Int. J. Refrig., vol. 28, no. 5, pp. 725–734, 2005, doi: 10.1016/j.ijrefrig.2004.12.003.

[21] B. Palm and R. Khodabandeh, “Choosing working fluid for two-phase thermosyphon systems for cooling of electronics,” J. Electron. Packag. Trans. ASME, vol. 125, no. 2 SPEC., pp. 276–281, 2003, doi: 10.1115/1.1571570.

[22] EOS GmbH-Electro Optical Systems, “Material Data Sheet: EOS Aluminium AlSi10Mg,” pp. 1–5, 2014, [Online]. Available: http://gpiprototype.com/images/PDF/EOS_Aluminium_AlSi10Mg_en.pdf.

[23] F. Cataldo and J. R. Thome, “Experimental Performance of a Completely Passive Thermosyphon Cooling System Rejecting Heat by Natural Convection Using the Working R134a,” vol. 140, no. June, pp. 1–11, 2018, doi: 10.1115/1.4039706.

Chapter 8 Conclusions & Recommendations

8.1 Summary & Conclusions

Over the past decade, much effort has gone towards adopting additive manufacturing (AM) methods for heat transfer applications, especially for building novel heat exchangers and heat sinks. Among all the available AM methods, selective laser melting (SLM) using Al alloys and fused filament fabrication (FFF) with conductive polymer composites are the most popular and promising for heat transfer applications. However, previous work was high-level investigations of the thermal performance AM-devices, and there was a poor fundamental understanding of AM materials' behavior pertaining to heat exchange applications. This thesis addressed this gap by shedding light into the inherent connection between the fabrication processes of the AM components and their resulting thermal performance and exploring the exciting opportunities offered by AM methods to enhance the performance of two-phase heat exchange devices. This was achieved by accurately characterizing the fundamental thermal properties of the AM parts, either SLM or FFF, and specifically the effective conductivity and the convective pool boiling heat transfer from their surfaces. And finally, investigating the thermal performance of the closed-loop two-phase thermosyphon with additively-manufactured evaporators as one of the popular heat transfer applications. This section starts with a summary of the key outcomes of these studies and finally highlights the major contributions to knowledge related to this area of research.

In **Chapter 2**, a modified steady-state approach of the ASTM C177 standard is proposed and constructed for measuring the anisotropic thermal conductivity of polymer composites used by FFF. This device was employed to investigate the effect of the FFF printing parameters on the effective thermal conductivity, also to examine several PLA composites to address the discrepancy issue in the reported thermal conductivity values found in the literature for the materials used by the FFF technique. The isentropic nature in thermal properties was clear for all the materials, even with the pure PLA. Anisotropy of thermal conductivity was particularly significant for the carbon fiber composite, which showed an increase in the thermal conductivity by a factor of two in the printing direction compared to the other directions. This was attributed to the alignment of the fibers induced by the extrusion process through the nozzle.

The same apparatus was used in **Chapter 3** to characterize the difference in the effective thermal conductivity brought about by the input SLM variables, such as the laser power, hatch spacing, point-wise distance, and print orientation. To mitigate the effect of the contact resistance in the measured thermal conductivity, each sample was embedded with two well-calibrated RTDs, able to quantify the developed temperature gradient, and consequently, the thermal conductivity. It was demonstrated that changing these parameters can affect the effective thermal conductivity by up to 22%. The printing parameters are often grouped into a dimensionless number called the energy density, which was usually optimized in the literature for mechanical properties. However, it was found that it does not reflect the SLM process's nature on the resulting thermal properties. Also, it was observed that the thermal conductivity was not only influenced by the void fraction of the samples but also the intensity of melt pool contours existing in the microstructure had a substantial effect in distracting the heat flow.

The continuing performance enhancement in the pool boiling heat transfer field is mostly linked to the surface characteristics. AM methods can play an essential role in creating and tailoring customizable structures to control the bubble dynamic and enhance the heat transfer coefficient (HTC). Consequently, **Chapters 4 and 5** introduced two AM-based approaches to enhance the pool boiling performance. The first approach presented in **Chapter 4** was to attach low conductivity polymer fixtures to the top of the copper boiling surface. The fixture had a rectangles pattern, covering a part of the bare surface, creating a spatial surface temperature gradient inducing the generation of the bubbles at the uncovered area, even with low heat flux, which consequently enhanced the HTC. It was shown that fixtures with the smallest unit cell size outperformed other fixtures in terms of the HTC. However, it had a significant deterioration impact on the critical heat flux (CHF). This study was implemented using a rudimentary pool boiling rig, which served to highlight most of the associated experimental challenges associated with the pool boiling heat transfer field. In **Chapter 5**, a pool boiling apparatus was developed, addressing most of the pool boiling literature issues, such as the transient problem, the finite size heater, the measurement repeatability, etc. This apparatus considered some unique features, such as the capability to test at different surface orientations with a large visualization field of view and the ability to readily swap the surface. Also, it considered a careful measurement of the input thermal energy and quantification of the resulting uncertainty in the wall superheat. This device was then used to study the aging effect on the pool boiling heat transfer rate from bare copper surfaces, which was found to increase the HTC by 22%, while no effect was seen for the CHF.

Many studies have applied re-entrant cavities to enhance the boiling HTC due to its capability to provide stable bubble nucleation sites, even at lower heat fluxes. This endorsed their wide application in some commercial heat exchangers, such as Thermoexcle-E tubes, Turbo-B tubes, and Gewa-T tubes. However, all the re-entrant implemented in these studies used 2D-shaped channels or grooves, not cavities. In **Chapter 5**, SLM was employed to create 3D spherical re-entrant cavities, which can not be produced via conventional machining methods. It was shown that the 3D printed boiling surface with re-entrant cavities achieved a 285 % higher HTC compared to the printed surface without re-entrant cavities.

Lastly, in **Chapters 6** and **7**, the thermal performance of the two-phase loop thermosyphon was investigated with SLM evaporator and compared to another machined surface that shared the same configuration and geometry. It was observed that the SLM-3D printed evaporator achieved slightly higher thermal resistance pertains to the lower thermal conductivity of AlSi10Mg. However, it did enhance the evaporator wall temperature instabilities, which is very beneficial for control purposes of electronics cooling systems. This was believed to be a consequence of the increase of the circulation mass flow rate through the loop or the enhancement of the boiling heat transfer coefficient, depending on the used working fluid.

Considering the above, the most significant contributions to the knowledge of this research area are summarized below:

- Characterization of the FFF materials' thermal properties, either; pure or composites, and examining the effect of the printing parameters on their performance.
- Investigation of the SLM manufacturing parameters' impact on the effective thermal conductivity.
- Building a world-class pool boiling apparatus allows for the simultaneous flow visualization and characterization of boiling heat transfer characteristics for interchangeable surfaces.
- Investigating the effect of attaching 3D-printed FFF polymer fixtures on the heat transfer performance and characteristics.
- Studying the thermal performance and the associated instabilities for two-phase loop thermosyphon with several versions of machined evaporators as a baseline work towards achieving the last objective.

- Investigation of the effect of a novel additively manufactured heating surface on a two-phase loop thermosyphon's performance.

8.2 Recommendations & Future Directions

Several future studies can be performed to continue the investigations of the current work, as listed below:

- With respect to the polymer fixture used in Chapter 4, there is still future investigation needed to fully leverage the 3D-printing FFF technique to investigate the effect of employing hybridized or gradient fixtures with multiple layers designed and optimized to enhance the HTC and the CHF simultaneously. For instance, the bottom structure could be made optimally small for HTC purposes, and the top layer could consist of a larger-sized rectangular pattern to permit the bubbles to coalesce and escape. The use of high-temperature thermoplastics, such as PETG and PEI, could eliminate any long-term thermal creep that may occur in fixtures manufactured from PLA. Additionally, the effect of a confinement number using low-boiling-point organic working fluids and refrigerants should be investigated.
- Further investigations of the SLM re-entrant cavities effect on the CHF is necessary by testing different high-pressure fluids such as ethanol, FC 72, and HFE 7000. These studies should also broaden the geometrical parameters range examined, such as the pore diameter, cavity diameter, spacing, and boiling surface orientation. These parameters are expected to significantly impact the bubbles' coalescence behaviour, and consequently, both the CHF and the HTC.

- In relation to the thermosyphon studied in chapters 6 and 7, several SLM-evaporator structures can be investigated in future studies for their effect on thermal performance and operational stabilities. This study would involve replacing the existing condenser with a water-cooled one to further pronounce the evaporator resistance among the other thermal resistances. One of the novel AM structures, which is believed to improve the loop's thermal and hydraulic performance, is shown in Figure 8-1. This design consists of grids cube-shaped pores, forming a novel interconnected porous structure, which cannot be fabricated using the conventional methods. Besides, this study would include a broader range of fill ratio, working fluids, and height difference between the evaporator and the condenser sections.

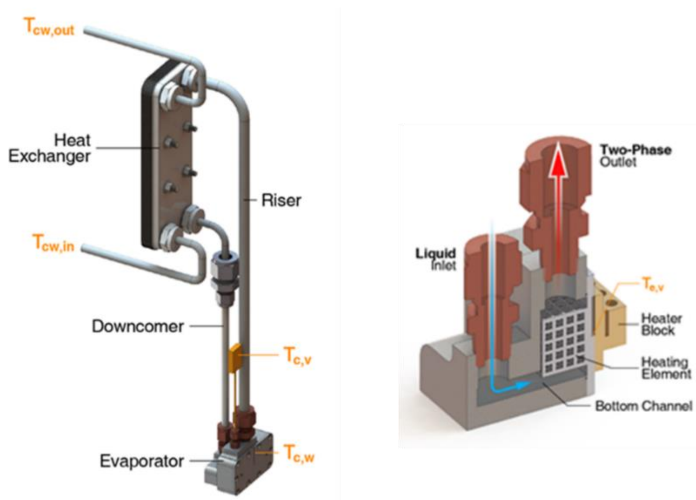

(a) (b)

Figure 8-1: (a) Layout of the proposed experimental setup redesign (b) Proposed evaporator.